ROCKBURST CONTROL USING DESTRESS BLASTING

By

Baoyao Tang

Department of Mining and Metallurgical Engineering

McGill University, Montreal, Canada

February 2000

A Thesis Submitted to the Faculty of Graduate Studies and Research in Partial Fulfilment of the Requirements for the Degree of Doctor of Philosophy

0-612-64678-5

ABSTRACT

One of the main problems facing mining engineers when dealing with deep, hard rock mines is to prevent and/or reduce rockburst hazard around mine openings. Rockburst is a phenomenon which is characterised by violent rock failure. The current research focuses on the assessment and control of rockbursts in deep, hard rock mines.

Strainbursts, or strain-type rockbursts, occur in the vicinity of mine openings and are generally provoked by high stress conditions in a brittle rock mass. A new theory has been developed for the assessment of the potential of violent rock failure by strainburst, in underground hard rock mines. In this theory, the mining-induced energy parameters are used to calculate the so-called burst potential index (BPI). When the BPI reaches or exceeds 100%, the method predicts a burst prone situation. One of the most commonly used methods to control strainbursts in hard rock mines is destress blasting.

Motivated by the lack of a dedicated analysis tool to help assess destress blasting, a new, geomechanical model was developed. The technique employs two newly introduced parameters, α, a rock fragmentation factor, and β, a stress dissipation factor, inside the modelled, fractured zone. Implemented in a 3-dimensional finite element code developed by the author, the new model simulates the damage zone induced by destress blasting of a mining face to help evaluate the efficiency of destress blasting. Extensive model verification and parametric studies have been undertaken. The effects of the destress blasting pattern, premining stresses and their orientation, and the two destress blasting factors (rock fragmentation factor, and stress dissipation factor) are studied. The model has been applied successfully to Canadian mine case histories. A detailed case study of a cut-and-fill mine stope involving crown and sill pillar destressing has been carried out. It is shown that the new method can be useful in the assessment of destress blasting in deep drift face development and the crown/sill pillar problems in cut-and-fill mine stopes.

RÉSUMÉ

Un des principaux problèmes auquel est confronté l'ingénieur des mines les mines profondes de roches dures est la prévention et la réduction des coups de terrain autour des excavations minières. Le coup de terrain est un phénomène qui est caractérisé par une violente rupture de roche. Cette recherche traite de l'estimation et du contrôle des coups de terrain dans les mines de roches dures.

Les coups de terrain se produisent aux alentours des excavations minières et sont généralement provoqués par des conditions de contraintes élevées dans les massifs rocheux peu fracturés. Une nouvelle théorie a été développée pour l'estimation du potentiel de rupture violente de la roche par les coups de terrain dans les mines souterraines de roches dures. Dans cette théorie, les paramètres d'énergie induite dans les mines sont utilisés pour calculer l'indice BPI (burst potential index). Quand le BPI atteint ou dépasse 100%, la méthode prédit une possibilité d'avoir une situation de coup de terrain. L'une des méthodes les plus couramment utilisées pour le contrôle des coups de terrain dans les mines de roches dures est le tir de relaxation.

Motivé par le manque d'un outil d'analyse pour l'evaluation des tirs de relaxation, un nouveau modèle géomécanique a été développé. La technique utilise deux nouveaux paramètres, α, un facteur de fragmentation de la roche, et β, un facteur de dissipation de contraintes, à l'intérieur de la zone fracturée modélisée. Introduit dans un code d'éléments finis développé par l'auteur, le nouveau modèle simule la zone de dommage induite par les tirs de relaxation de la face minière pour aider à évaluer l'efficacité des tirs de relaxation. Une vérification du modèle et des études paramétriques ont été menées. Les effets du schéma des tirs de relaxation, des contraintes initiales et leur orientation, et des deux facteurs de tirs de relaxations (facteur de fragmentation de la roche, et facteur de dissipation de contraintes) sont étudiés. Le modèle a été appliqué avec succès à des analyses sur des cas d'études de mines canadiennes. Un cas d'étude détaillé de tirs de relaxation dans les ouvertures minieres de type coupe et remblai a été mené. Cela a montré que la nouvelle méthode peut être utile dans l'estimation des tirs de relaxation dans les problèmes de développement de face de tunnel et des piliers horizontaux dans les ouvertures minières de type coupe et remblai dans les mines profondes.

ACKNOWLEDGEMENTS

It's a great pleasure to express my sincere gratitude to my supervisor Prof. Hani S. Mitri for his guidance and encouragement throughout the research and his financial support; without these supports, this thesis wouldn't have been a reality.

I would like to acknowledge the warmth and friendship of my friends at McGill University, specially of the numerical modelling group. Acknowledgements are especially due to Mr. Wilfrid Comeau and Mr. Joseph Marwan for their kindness and help during this project.

I am particularly indebted to my wife Yang Xia for her understanding, love and help all along the project. I would also like to express my special feelings to my son, Tian Hao, for the time I spent on my project which part of them should belong to him.

TABLE OF CONTENTS

CHAPTER 6

MODEL VERIFICATION AND PARAMETRIC STUDY

LIST OF FIGURES

LIST OF TABLES

NOTATION

a	Radius of the circular opening
[A]	Coefficient matrix
A_1, A_2	Area
B	Element strain-displacement matrix
B1, B2	Brittleness
{B}	Known vector
B_{er}	Burst-efficiency ratio
BIM	Brittleness Index Modified
BPI	Burst Potential Index
c	Cohesion
[D]	Stress strain relationship matrix
$[D_D]$	Stress strain relationship matrix of all elements in the destressed zone
D_t	Failure Duration Index
E	Elastic modulus
e_1	Stored strain energy due to induced stresses
e_2	strain energy caused by in situ stresses σ_0 in the surrounding rock mass
e_4	Total mining-induced strain energy calculated at the boundary of the opening
e_c	Critical strain energy
E_D	Energy dissipated in the cycle
E_D	Energy generated by the tremor in the rock mass
E_i	Isotropic elastic modulus
$\{E_D\}$	Elastic modulus in the destressed zone
E_k	Energy accumulated in the rock mass
E_k^0	Energy necessary for initiating rockburst
e_r	Seismic energy released
e_r^1	Seismic energy released in the first mining sequence
e_r^2	Seismic energy released in the second mining sequence
E_R	Elastic energy recovered during unloading
E_1	Elastic modulus in xoy plane
E_2	Elastic modulus in xoz plane

E_3	Elastic modulus in yoz plane
ERR	Energy release rate
ESR	Energy storage rate
ESS	Excess shear stress criterion
$\{F^b\}$	Element load vector due to body force
$\{F^q\}$	Element load vector due to the surface traction
$\{F^e\}$	Element load vector
$\{F^*\}$	Concentrated forces applied on the surface
$\{F_{\sigma_0}\}$	Load vector due to the initial stresses
$\{FB\}$	Initial stress ratio vector
G_1	Shear modulus in xoy plane
G_2	Shear modulus in yoz plane
G_3	Shear modulus in zox plane
I	Moment of inertia
[J]	Jacobian matrix
K	Horizontal to vertical stress ratio
K_1	Stiffness matrix of elements in the surrounding rock mass
$[K^e]$	Element stiffness matrix
K^i	The stiffness at the i^{th} mining sequence
$[K^m]$	Stiffness matrix of all elements in the zone which is mined out
k_{lm}	Mine stiffness
k_{pp}	Local stiffness
k_x	Horizontal (x direction) to vertical stress ratio
k_y	Horizontal (y direction) to vertical stress ratio
L	Length
l_i	Directional cosine for x-direction
L_{ZS}	Work used for breaking and crushing rock mass volume discharged to an opening
M	Bending moment
m_i	Directional cosine for y-direction
[N]	Element shape function
$[N^t]$	Array consists of the eight nodes shape function on the element side subjected to boundary traction
n_i	Directional cosine for z-direction
$N_i(x,y,z)$	Element nodal shape function
p	Vertical initial stress

P_i	External loading representing body forces in the rock mass
p_z	Initial vertical stress in the elementary volume
$\{q\}$	Distributed surface traction
Q	Shear force
r	Distance from the calculated point to the centre of the opening
R	One round of the face advance
R_a	Constraint support
R_b	Constraint support
RMR	Rock mass rating
S	Modelled domain boundary surface
S_m	Boundary surface area of the rock mass to be mined
S_0	Mine openings' boundary surface area
[T]	Transformation matrices
T_e	Energetic rockburst indicator
u	Displacement in x direction
u_i	Displacements
U_c	Strain energy stored in the rock mass surrounding the excavation
U_m	Stored strain energy in the mined rock.
v	Displacement in y direction
V	Volume of the modelled domain
V_c	Strain energy of the rock mass in the elementary volume
V_C	Elastic energy accumulated in the broken rock mass during rockburst
V'_c	Initial strain energy of the rock mass in the elementary volume
V_m	Volume of rock mass to be mined
V_o	Strain energy of volume change
V_0	Mine openings' volume
V_p	Strain energy of distortion
w	Displacement in z direction
W	work (or the variation of the potential energy in the system) done by the shifting of external and gravitational forces working on the convergence and deformation of the rock mass
W_i	Integration weight factor
W_{et}	Burst Liability Index

W_k	Kinetic energy
W_r	The amount of the released energy
W_s	Energy dissipated through supporting system
W_t	Potential energy
x	Global co-ordinate
{x}	Unknown vector for linear equation grooups
y	Global co-ordinate
z	Global co-ordinate
x'	local co-ordinate
y'	local co-ordinate
z'	local co-ordinate
ΔP	Load vector
ΔW_k	Change in seismic energy
ΔW_t	Change in potential energy
α	Coefficient of vertical stress concentration
$\{\alpha\}$	Rock fragmentation factors
β	Coefficient of energy concentration
$\{\beta\}$	Stress dissipation factors
θ	Strike
$\{\delta^e\}$	Element nodal displacements vector
ε	Strain
$\{\varepsilon'\}$	Strain tensor related to the local co-ordinate system
ε_1	Major strain
ε_f	Deformation at failure
φ	Dip
ϕ	Shear angle taken from the failure surface in Mohr's diagram
ϕ'	Angle from the vertical radial direction clockwise to the calculated radial direction
ϕ_1	Energy of particle ejected at failure in a uniaxial compression test
ϕ_0	Maximum energy stored in loading
ϕ_s	Static friction angle
$\rho_{,r}$	Average density of broken rock mass (assumed to be 2.5 t/m^3)
ξ	Local co-ordinate
ξ_i,	Local co-ordinate at integration point
η	Local co-ordinate

η_j	Local co-ordinate at integration point
ζ	Local co-ordinate
ζ_k	Local co-ordinate at integration point
σ	Stress
σ^i	Stress at the i[th] mining sequence
$\{\sigma'\}$	Stress tensor related to the local co-ordinate system
σ_0	Initial (in situ) stresses
$[\sigma^{0e}]$	Element initial stress matrix
σ_1	Major principal stress
σ_2	Intermediate principal stress
σ_3	Minor principal stress
σ_D	Post destress remaining stress
σ_{D_i}	Stress tensor in the destressed zone
σ_{ind}	Mining induced stress
σ_r	Radial stress around the circular opening
σ_t	Tangential stress around the circular opening
$\sigma_z(x,y,z)$	Vertical stress in the elementary volume
σ_c	Uniaxial compressive strength
σ_n	Normal stress at the slipping point
σ_0	Mean applied stress
σ_t	Uniaxial tensile strength
σ_x	Normal stress in x direction
σ_y	Normal stress in y direction
σ_z	Normal stress in z direction
σ_x^0	Initial normal stress in x direction
σ_y^0	Initial normal stress in y direction
σ_z^0	Initial normal stress in z direction
τ_{xy}	Shear stress on xoy plane
τ_{yz}	Shear stress on yoz plane
τ_{zx}	Shear stress on zox plane
μ_s	Static friction factor
γ	Body force per unit volume
τ_e	Shear stress available to produce a seismic event once failure has started
τ	Shear stress at the initiation point
τ_d	Dynamic resistance at this point

μ	Dynamic friction factor
υ	Beam deflection
ν	Poisson's ratio
v_0	Average velocity of broken rock mass ejected to an opening during rockburst

CHAPTER 1

INTRODUCTION

1.1 GENERAL

Rock mass instabilities have always been a safety hazard in underground mines. Underground rock mass instabilities are of many types. Among those are the well known rockburst phenomena that can have severe consequences such as damage to the underground workings, equipment, and as a result can cause long delay of the mining operation. But most of all, the occurrence of rockburst in underground mines can cause injuries and even fatalities among the mine workers. Today, mining engineers are able to design different mine support systems against ground fall with a relatively high degree of confidence. Unfortunately, this has not been always the case when dealing with rockburst-prone ground.

The first report about rockburst seems to have emerged from Kolar Gold Field in India at the end of the 19^{th} century, where the mining depth was still under 500 m (Morrison, 1942; Blake, 1972). The problem started to be noticed in the Witwatersrand mines in South Africa a few years later (Cook et al., 1966). Some East European countries such as Russia, Chechslovk also faced the problem (Petukhov, 1987, 1990). China also reported the rockburst phenomenon as early as 1933 at the SL Coal Mine and more than 2000 rockbursts had taken placed since 1949 (Tan, 1986; Mei and Lu, 1987; Lu et al, 1993). In the United States, the first rockburst seems to have occurred in 1904 at the Atlantic Mine in the copper district in Michigan (Bolstad, 1990).

Detailed records of rockburst incidents in Canadian mines including related damage, injuries and fatalities are best illustrated by the records of the Ontario Ministry of Labor. From 1928 to 1990, nearly 4000 rockbursts and 57 associated fatalities were reported to the Ministry or its predecessor, the Department of Mines (Hedley, 1992). There has been less documentation of rockbursts in Quebec mines although incidents of rockbursts and related fatalities are probably no less frequent than in Ontario mines.

With the persistence and (sometimes) growth of the problem, research efforts were made worldwide and principally in the regions touched by rockbursts. The analytical studies originally from South Africa set the paces on subsequent rockburst research. The post-failure studies on rocks, stress analysis, and the energy approach in the unstable equilibrium analysis (Cook, 1965; Diest, 1965; Cook et al., 1966; Salamon 1970,1974) are important notions that are still in use in present research investigations.

1.2 CLASSIFICATION OF ROCKBURST MECHANISMS

Rockbursts and other seismic events that may occur within rock masses due to mining activities are associated with unstable equilibrium states that may involve one of two fundamental mechanisms (Brown, 1984):

- slip on pre-existing discontinuities; or
- fracturing of intact rock.

Ortlepp (1992) suggested the classification of main rockburst mechanisms as follows:

- Strainbursting
- Buckling
- Pillar or face crushing
- Shear rupture events
- Fault-slip events

Hedley (1992) classified rockbursts into three categories:

- Inherent bursts to emphasize the pre-mining stresses were high enough to cause failure when the initial development openings were driven,
- Induced bursts to represent pillar and crush bursts caused by mining operations transferring and concentrating stress on the remaining structures such as pillars.
- Fault-slip burst represent slippage suddenly occurring along a geological weakness plane.

In the present thesis, rockburst mechanisms are grouped into three broad categories as shown in Figure 1.1. They are:

- strainbursts and
- fault-slip bursts
- combined mechanisms.

It is noted that the majority of rockbursts are of the strainburst type, which appears to be of great significance for deep hard rock mines.

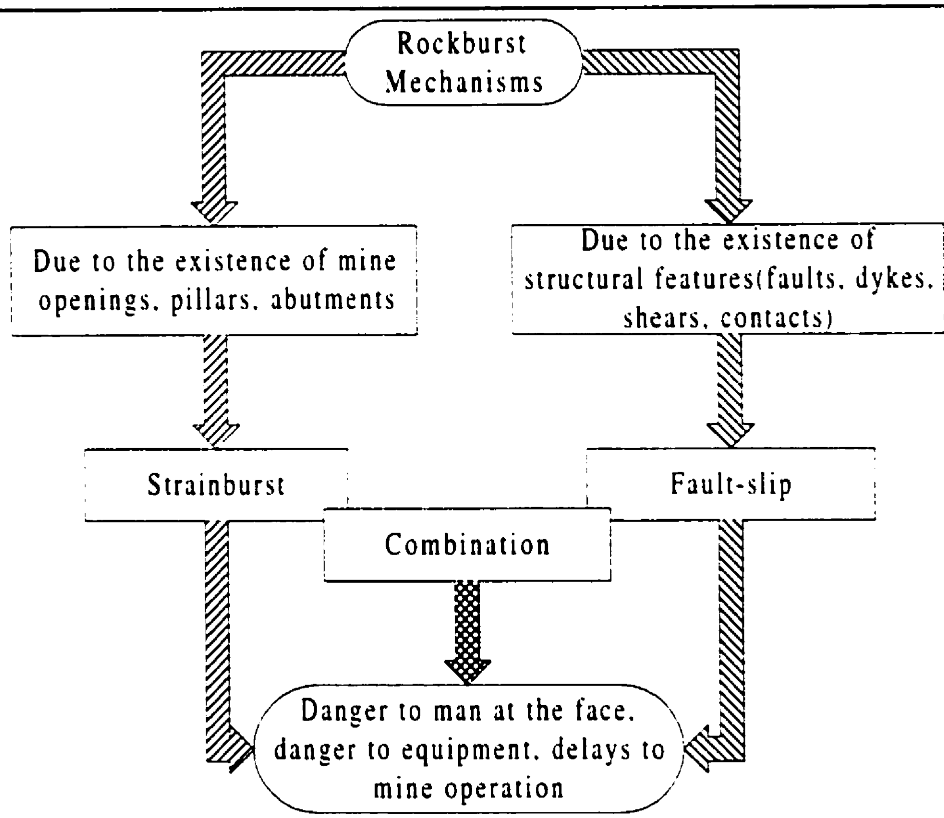

Figure 1.1 Flowchart illustrating the classification of rockburst mechanisms

Strainbursts are associated with the release of strain energy in the form of seismic energy in highly stressed volume of brittle rock around mine openings, and are therefore related to the creation of an adverse geometry in areas that are prone to rockbursting (Mitri *et al.*, 1993). Thus, the problem is dependent on the size, shape and the location of a mine opening or a pillar as well as the mining induced stresses and mining sequences. The significant amount of energy stored in highly stressed, brittle rock surrounding an opening or within a pillar can result in the sudden creation of fractures within the intact rock and explosive displacement of large portions of rock mass into underground openings. For the fault-slip burst, shearing on distinct geological features (i.e. faults, dykes, and shears) is usually considered to be the mechanism associated with the problem. It is expected that, in general terms, the magnitude of fault-slip type seismic events (ranging from 2.5 to 5.0) is larger than the strainburst type events (ranging from –0.2 to 2.5) (Ortlepp, 1994). Nevertheless, this has no relevance to the amount of damage that can result from either type of rockburst, since this is a function of the distance between the seismic event and the opening, the extent of local rock mass fracturing, and the pre-installed support. Thus, both types of rockburst are of equal significance in terms of the potential danger to the mineworkers at the face, damage to equipment and delays to the mine operation.

A statistical analysis of the relationship of geologic features to seismic events was carried out for Lucky Friday Mine, Idaho (Scott, 1990). A set of 746 events that occurred from 1982 to 1986 at depth 1600 to 1800m was analysed together with geologic information about each event. Preliminary results indicated that 29% of the seismic events occurred on strike-slip or bedding plane faults, whereas 71% of the events were not associated with identified faults.

Although strainbursts generally involved only small amounts of rock, they accounted for the great majority of rockburst accidents at relatively shallow depth at which mining then took place (Ortlepp, 1982, 1983). Examples of such phenomena are crown pillar bursts in overhand cut-and-fill mining, face bursts at development headings at depth, and floor bursts commonly encountered with shaft sinking.

1.3 ROCKBURST ALLEVIATION AND CONTROL METHODS

In general, there are three principal methods of controlling rockbursts, as follows:

- Artificial ground support

- Alternative mining methods and/or mining sequences, and
- Ground preconditioning

Theses approaches can be classified into two broad categories: 'strategic' and 'tactical' (Salamon, 1983). The strategic approach is to try to diminish the possibility of encountering rockburst-prone ground, or to reduce the severity of the rockbursts. The available techniques include optimizing the shape and orientation of the development openings, layout of permanent pillars and the use of backfill. The tactical approach is to accept some rockbursting is inevitable, but seeks to limit the extent of the damage or to control the timing of a rockburst.

1.3.1 Alternative Mining Methods and/or Mining Sequences

Although rockbursts have been known to mining engineers since the beginning of the century and considerable research into their occurrence, mechanisms and behavioural characteristics has been undertaken, there seems that no certain method of prediction or prevention of rockbursts has yet emerged. Early experiences in combating rockbursts were gained primarily in South Africa (Whittaker *et al.*, 1992).

Mining and excavating in the rockburst prone area can be made less cumbersome by changing the geometry and orientation of the openings, layout of the pillars and the stope, mining sequences and use of backfill, etc (Hedley, 1992).

Efforts have been made to reduce the hazardous occurrence of rockbursts. These have relied on the traditional approaches of engineers: observations, experiences and reasoning followed by practical trials (Salamon, 1983). The application of the longwall mining method in deep hard rock mines prone to rockbursts might be considered a result of these efforts. This method not only allows more mineral to be recovered, but also considerably reduces high stress concentrations induced by mining due to its simple layout and hence reduces the possibility of rockbursts in comparison to the room and pillar mining approach (Salamon, 1993). The introduction of stablizing pillars large enough to reduce convergence of the mined-out area has reduced the total seismicity and the occurrence of rockbursts in South African gold mines (Ortlepp, 1984).

Some notable studies have been reported on the phenomenon of rockbursts (Cook *et al.*, 1966; McGarr and Wiebols, 1977; Robson, 1940; Morrison, 1942; Dickout, 1972). Although considerable attention was devoted to collating observed data on rockbursts, particularly during the early stages of research into rockbursts, it was appreciated that more detailed investigations were necessary in order to identify and clarify the role of the principal factors.

1.3.2 Ground Support

In some cases, it is impossible to prevent rockbursts from occurring, either because of very high stress conditions or past mining practices that may have created a layout, which is rockburst prone. Under rockburst conditions, it becomes increasingly important for the support system to provide and maintain complete area coverage of the retaining/ holding function, in order to avoid violent unravelling of the rock mass. Based on South African experience, it is now clear that mine openings can be designed to survive fairly large rockburst events, using cable lacing support systems (McCreath *et al.*, 1992). Designing of support systems for burst-prone ground has three components. It is important to understand what the demand on the support systems is likely to be, to know what the capacity of different support systems are and to assess the hazard that is posed by the potential for rockbursts. The support system firstly should reinforce the rock mass in order to control the failure of the rock. When this is not successful, it then has to hold the failed rock and control the amount of the displacement that occurs. And finally, it has to retain the failed rock and absorb the energy with which this material is being forcibly driven. The first two functions, reinforcing and holding, are accomplished within the volume of the rock mass, usually by bolts or rebars or cables, while the third function is accomplished only on the surface of the rock mass, usually by mesh or increasingly by shotcrete (McCreath et. al. 1992).

There have been many publications on ground support in burst prone conditions in the last two decades. Among them the followings may be the representatives: Blake and Cuvelier (1988); Davidge, et al. (1988); Hedley, et al. (1983); Roberts and Brummer (1988); McCreath and Kaiser (1992); Ortlepp (1992); Brummer and Kaiser (1995); Stacey, *et al.* (1995). Some traditional support systems were ineffective in controlling rockburst damage, such as concrete lining and conventional timber posts and beams. The installations of stronger and more rigid systems, such as mechanical bolts and rebar, were successful in controlling damage from smaller magnitude rockbursts, but were ineffective against larger events. It was realized that the rigidity of support was contributing to the problem. This led to the introduction of supports with yielding characteristics, for example, the friction type supports, steel mesh, steel or plastic fibre shotcrete, yielding bolts, etc.

Jeager (1992) reported two new support units for the control of rockburst damage: rapid yield hydraulic prop and cone bolt tendon. The prop, which yields at 3 m/s, has a 30% lower mass than existing props and a variable yield force, can be blasted-on and be used in support systems which are always close to the stope face where most of the casualties and dilution occur. The cone bolt tendon is used for the support of tunnels under rockburst conditions. The cone bolt tendon can yield more than 0.5 m at a force of 80 kN. It was found that the cone bolts were no more difficult to install than other full column grouted tendons. The cone bolts fulfil a long realized need for the better control of rockburst damage in tunnels.

Stacey *et al.* (1995) reported their test results based on the static tests on the energy absorbing capacity of reinforced shotcrete. The mesh-reinforced shotcrete has sufficient energy-absorbing capacity to contain rockbursts of significant magnitude. Even a 50-mm thick mesh-reinforced shotcrete layer has greater energy-absorbing capacity than fully grouted 16-mm rebar. Fibre-reinforced shotcrete has energy absorbing capacities of the same order as, or better than, those of 16-mm rebar. However, the performance of the fibre-reinforced shotcrete is erratic. CRRP (1996) stated from actual observations that both mesh and fibre-reinforced shotcrete can survive ground motions of 1.5-2.0m/sec.

But even the best support systems based on optimal combinations of holding/reinforcing and tough-retaining elements will be limited to energy absorption capacities of roughly $50KJ/m^2$ (CRRP, 1996). In some situations, rockbursts may be so severe that they generate violent ejection of rock despite any reasonable support system (i.e., exceeding $50KJ/m^2$). In these cases the maximum practical support limit is reached and a combination of strategic mine-design measures such as modified destressing must be adopted to alter the conditions leading to rockbursts.

1.3.3 Ground Preconditioning

The development of local stress concentrations, increasing the potential of the rockburst hazard, requires the use of temporary preventive actions. These actions are connected with a particular location and time of their realisation. The task relies upon changing the physical-mechanical properties (first of all the strength) of the rock environment, usually through weakening (failure) of its structure. The basic preventive techniques used for this purpose are destressing and torpedo blasting (blasting in roof strata with large charges of explosives) (Adams, et al., 1993; Landriault and Oliver, 1992; Lightfoot, 1993; Lightfoot, et al., 1996; Toper, et al., 1997; Boler and Swanson, 1993).

Landriault *et al.* (1992) reported destress slot concept for bulk mining at depth. The conceptual solution consisted of creation of a destress envelope in the orebody large enough to allow the drilling and blasting of VRM panels to be conducted in a stress relaxed section of the rock mass (See Figure 1.2). The destress or relaxation envelope

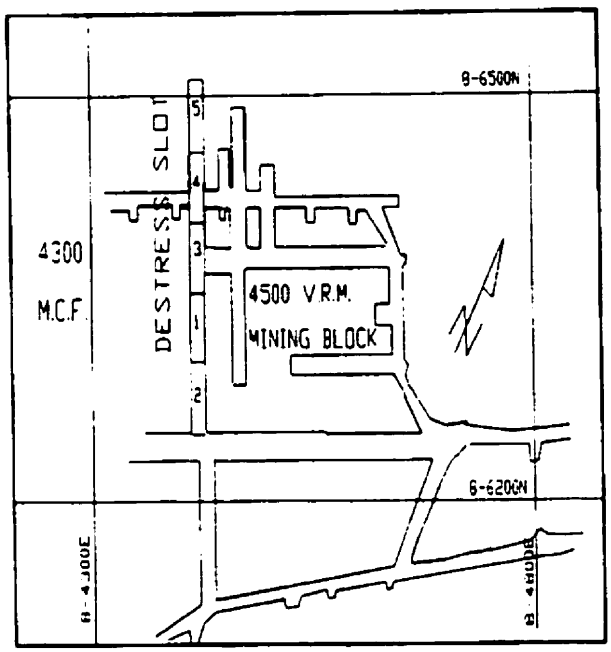

Figure 1.2 6600 level plan showing destress slot mining sequence at Creighton Mine (After Landriault *et al.*, 1992)

would be created through a combination of rock mass failure around the excavation perimeter and stress shadowing brought about by the changing excavation geometry resulting from the mining. They utilized this concept on an actual production scale in 400 orebody at Creighton Mine between 6600 and 6800 levels. The concept accompanied by proper sequencing of the panels mined, will allow the relaxation zone to be passively extended as mining progresses without bursting problems generally associated with unfavourable geometry of an excavation at depth.

In addition to reducing the stress in a particular mine structure, a well designed destress blasting also results in modifying the rockmass properties of the structure so that its mode of failure is changed. Since rockburst is almost exclusively associated with brittle rocks that behave elastically and which have the potential to fail violently when their strength is exceeded, it is obvious that by destress blasting of such a rock mass, one attempts to change its failure mode from brittle to ductile. Thus destress blasting should not only result in the reduction of stress in the zone but should also promote yield type of failure.

The first documented experiments undertaken into the use of explosives for destressing the rock ahead of a deep level mine face in South Africa were at ERPM in the 1950's (Roux, *et al.*, 1957, and Hill and Plewman, 1957). This involved a system of 3m long holes of a normal diameter drilled at regular intervals into the stope face. The preconditioning holes were drilled approximately once every week in replacement of the normal 1m long production holes. A considerable reduction in face bursting and subsequent accident statistics was reported. In the late 1980s destress blasting was again re-evaluated for the South African gold mines (Rorke and Brummer, 1988; Rorke *et al.* 1990; Adams, *et al.*, 1993; Lightfoot *et al.*, 1996; Toper, *et al.*, 1997).

In North American mines, destressing is more widely practiced and apparently more successful (Hedley, 1992). Detressing of sill pillar was done on a regular basis in the mine Coeur d'Alene district of northern Idaho. Blake (1972) and Board and Fairhurst (1983) reported instrumented field trials. It was reported that preconditioning significantly reduced seismic activity during mining (Blake, 1982).

In Canadian mines, destressing is normally practiced in sill pillars in thin, steeply-dipping orebodies such as those at Campbell Red Lake Mine, Dickenson Mine (now Red Lake Mine), Falconbridge Mine (Moruzi and Pasieka, 1964), and Kirkland Lake (Cook and Bruce, 1983; Hanson, et al, 1987). At Inco's Creighton Mine, destress blasting is in regular use in driving development openings, and in pillars which is a form of preconditioning (Oliver, *et al.*, 1987; MacDonald, et al., 1988; O'Donnell, 1992).

Mitri et al. (1988) used a series of finite element numerical simulations to address the issue of the optimum design and location of a destress blast, and the volume of the blasted rock in overhand cut-and-fill in typical Canadian Precambrian Shield conditions. They reported the results of six different models in which sequential mining was done from the premining state to the stage where critical safety levels were detected in the stope back, at which stage, destress blasting was modelled. These results, taken in context, show that destress blasting can be modelled using numerical procedures. Mitri et al. (1990) adopted Salamon's energy approach to calculate mining-induced strain energy in the rock mass using finite elements. The technique was applied to Campbell Redlake mine, Balmetown, Ontario, to evaluate the effectiveness of destress blasting by examining mining induced energy changes before and after the blasting (Mitri et al., 1993).

1.4 SCOPE AND OBJECTIVES

1.4.1 Research Scope

As described in section 1.3, in some mining situations, the only way which could reduce the risk of rockburst is to transfer the high stresses in a mine face abutment to a relatively far area ahead of the face. This can be achieved by destressing the adjacent surrounding rock, such as for the mine drift, ramps, crosscut, and shafts development, etc, through destressing the crown/sill pillars in stope.

Despite the apparent success of the destress blasting technique there appears to be a fundamental absence of dedicated design-analysis method and modelling technique. It is therefore essential to develop an analytical tool for quantifying the effects of mining openings geometry and mining sequence on the burst potential. At what kinds of situations should the destress blasting method be used to control the rockburst? And what kind of destress blasting pattern is more suitable for the specific situation? And what is the effectiveness of a destress blasting? Why are some of the destress blasting practices successful, but some others are not?

To address the above questions is the target of this doctoral research. Knowledge of the exact mechanism of a rockburst-related seismic event is often difficult to obtain, and it is still the subject of extensive research. Current models in both seismology and rock mechanics consider simplified mechanisms for the unstable release of energy (Mandl, 1988).

Trying to model the detailed process of failure at a mining face, or along a structural feature according to a proposed mechanism would be very complex, and possibly scale-dependent, with only limited practical applications. A simple representation of the rockburst mechanism, which makes mechanical sense, but avoids detail, is usually a more sound approach to the problem.

The current research will focus on the assessment and control of strainbursts using destress blasting method in the deep, hard rock mine environment.

1.4.2 Objectives

The main objective of this research project is to develop a dedicated method for the simulation and evaluations of destress blasting to help better understanding rockburst control using destress blasting. More specifically, this research aims to:

- Develop a methodology to identify mining situations which call for the use of destress blasting.
- Develop a new geomechanical model to simulate the destress blasting.
- Develop a 3-dimensional finite element model to implement the new methodology and geomechanical model.
- Perform model verification and parametric study.
- Use the new developed model to do back analysis

1.5 THESIS OUTLINE

Chapter 1 discusses the scope and objectives of the thesis.

Chapter 2 presents the literature review on the evaluation of rockburst potential.

Chapter 3 reviews destress blasting practice in hard rock mines. The geomechanical effects of destress blasting are discussed.

Chapter 4 presents the new methodology to evaluate the burst potential using mining induced energy

Chapter 5 presents the proposed numerical model for destress blasting. A finite element model ***e-z tools3D*** is developed by the author. This chapter explains the modelling procedure of the mining sequences and destress blasting. The rock failure is also discussed with the newly introduced energy parameters. The element isoparametric test is presented in the chapter.

Chapter 6 deals with the model verification and parametric study. The effects of varying destressing patterns, rock fragmentation factor, stresses dissipation factor, and the initial stresses are studied in detail.

Chapter 7 gives a detailed description of destress blasting case studies; namely of a cut-and-fill mine stope as well as the discussion of the whole model and its results.

Chapter 8 presents the general conclusions of this doctoral thesis as well as the recommendations for the further research.

CHAPTER 2

LITERATURE REVIEW ON THE EVALUATION OF ROCKBURST POTENTIAL

2.1 INTRODUCTION

Rockburst may cause damage to underground openings and equipment. This results in a cost increase and a loss of productivity for the operator. Bláha (1990) reported that the production cost in coal mines in the Ostrava-Karviná region in Poland increased by 100% when the mined area became burst-prone. On the safety issue, Salamon (1983) noted that in 1979, 62% of fatalities in South African mines could be attributed to rockburst and rockfalls. In the first half of 1996 only, there were more than 35 fatalities associated with rockbursts in South African mines (Ryman-Lipinsky and Bakker, 1997).

As stated in Chapter 1, before any action is taken to fight rockburst, the first thing is to recognize the rockburst potential. Many different methods are utilized for the estimation/prediction of rockburst hazard. Generally these methods may be described as seismological and rock mechanics methods. The literature review aims to screen the different tools available for the evaluation of rockburst potential in underground mines.

2.2 ROCKBURST POTENTIAL EVALUATION USING ROCK MECHANICS METHODS

In the case of rockbursts, the engineer can examine various alternative sequences or designs by comparison of the relative seismic potential of each design. Stress, energy and stiffness approaches can be applied using numerical models for the determination of this seismic potential. Critical values of the model output parameter can be obtained using back-analysis and forward modelling can then be conducted with a higher degree of confidence. The results can be applied for the selection of mining method, excavation sequence, access to the stopes and identification of areas with hazard for rockburst (CRRP, 1996).

2.2.1 Stress Method

2.2.1.1 Hard rock behaviour under uniaxial compression

Extensive laboratory research work was undertaken which was aimed at clarifying the behaviour of rock under stress and in particular, identifying and examining the deformation characteristics and the mechanism of failure of brittle rocks (Cook,1965; Cook *et al.*, 1966; Hoek and Bieniawski; 1965a and 1965b; Martin, 1996; Shao *et al.*, 1996; Tang, 1997, Chen et al., 1997; Wu, et al., 1997).

Figure 2.1 shows a typical stress-strain relationship for a rock specimen subjected to uniaxial compression. Some phase boundaries are added. The first phase, curved upward, is associated with the reversible closure of microcracks; in dense rocks with very low

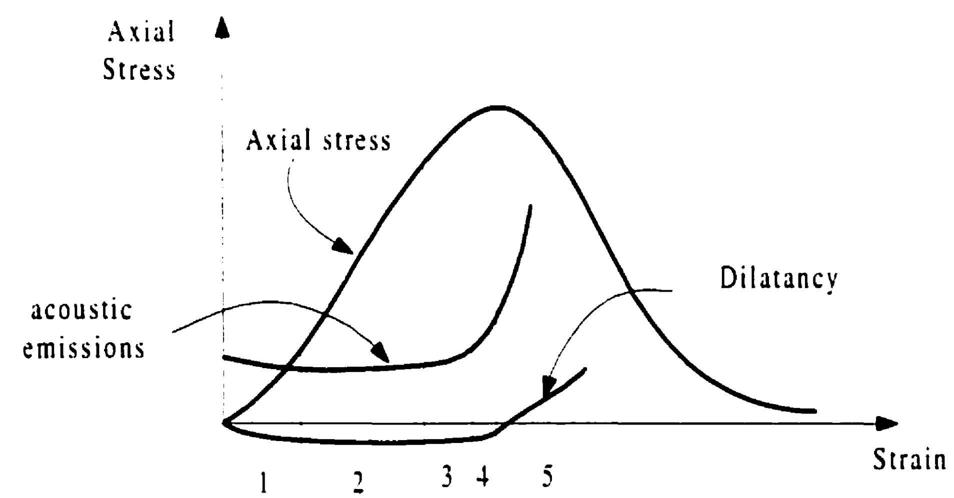

Figure 2.1 Schematic stress-strain curve of low porosity, brittle rocks under uniaxial compression (after Bieniawski, 1967)

porosity, this phase is almost non-existent. Then follows a linear phase due to the elastic response of the rock, which extends up to the microfracturing threshold where stable crack propagation starts. The onset of microcrack growth, which precedes the peak strength, commonly begins above 50% of the ultimate load, as shown by studies on volumetric measurements, acoustic emissions, wave velocity, etc. (e.g., Paterson, 1978; Hakami, 1988; Cox and Meredith, 1993; Chen et al., 1997). When approaching the peak strength, the size and density of cracks increase, and cracks interaction becomes more important, and unstable crack propagation can be initiated.

Damage accumulation during crack propagation leads to a rapid increase in dilation and eventually to strain localisation. It is known that, for brittle materials such as rocks, localisation associated with loss of homogeneity of strain field, usually occurs in the vicinity of the peak load (e.g., Wawersik et al., 1990). In the post peak phase, localisation phenomena become more important, and usually produce a gradual reduction of the sample cohesion with increasing inelastic strain. This causes a pronounced softening of the material, which is a progressive decrease of strength as strain accumulates.

One important aspect of the rock behaviour, used with several indices, is that inelastic strain can develop in the pre-peak regime and can dissipate energy by microcracking.

2.2.1.2 Brittleness of Rocks

The brittleness of rocks is sometimes evaluated from two different empirical (and more or less arbitrary) concepts such as (Hucka and Das, 1974):

$$B_1 = \frac{\sigma_c - \sigma_t}{\sigma_c + \sigma_t} \tag{2.1}$$

$$B_2 = \sin\phi \tag{2.2}$$

Where:

σ_c is the uniaxial compressive strength, σ_t is the uniaxial tensile strength, and ϕ is the shear angle taken from the failure surface in Mohr's diagram. Rockburst potential seems to increase with larger brittleness values

2.2.1.3 Failure Duration Index (Dt)

Wu and Zhang (1997) proposed to monitor the time of failure of coal samples during an uniaxial compression test (stress rate between 0.5 to 1.0 MPa/s). The Dt index is the time between peak strength and complete break-down. The authors proposed the following values of proneness:

Table 2.1 Indicative values for the Dt index (after Wu and Zhang, 1997)

Dt value	Bursting proneness
Lower than 50 ms	Strong
Between 50 and 500 ms	Medium
Larger than 500 ms	None

2.2.1.4 Activity index

Tao (1988) proposed an index that considers the uniaxial compressive strength σ_c and the major principal stress σ_1 in the region of the opening. His experience in Chinese mines led to the following classification of risk:

Table 2.2 Rockburst potential classes (after Tao, 1988)

Class	σ_c/σ_1	Bursting activity	Comments
1	>13.5	No	No acoustic emission
2	13.5-5.5	Low	Weak acoustic emissions
3	5.5-2.5	Average	Loud acoustic emissions
4	<2.5	High	Very loud acoustic emissions

Where σ_1 is the major principal stress, σ_c is the uniaxial compress strength.

2.2.1.5 Excess Shear Stress (ESS)

The South African experience shows that the notion of energy release rate (ERR) is not suited for fault-slip type rockbursts. Ryder (1987) proposed a similar criterion, the excess shear stress criterion (ESS), that could be applied to this type of rockbursts. This criterion is based on the energy available when passing from static resistance (before slip movement) to the dynamic resistance (during slip).

The static resistance τ_s of the discontinuity can be estimated with a Mohr-Coulomb criterion such as:

$$\tau_s = c + \mu_s \sigma_n \tag{2.3}$$

with $\mu_s = \tan\phi_s$ (2.4)

where c is the cohesion, μ_s is the static friction factor, σ_n is the normal stress at the slipping point, and ϕ_s is the static friction angle. Once the motion has started, the value of ESS is given by:

$$\text{ESS} = \tau_e = |\tau| - \tau_d \tag{2.5}$$

where τ_e is the net shear stress available to produce a seismic event once failure has started, τ is the shear stress at the initiation point, and τ_d is the dynamic resistance at this point and given by:

$$\tau_d = \mu\sigma_n \tag{2.6}$$

$$\text{with } \mu = \tan\phi \tag{2.7}$$

where μ is the dynamic friction factor, and ϕ is the dynamic friction angle. Ryder (1987) suggested these average values of τ_e to produce significant seismic events:

$\tau_e \equiv 5\sim10$ MPa for an unstable movement along a pre-existing discontinuity;

$\tau_e \equiv 20$ MPa for a shear failure of intact rock.

In theory, the larger ESS value brought by the progression of the opening towards the discontinuity, the larger surface of the discontinuity would be involved, and the larger would be the seismic event produced. In practice however, back analyses performed showed that not all positive ESS situation yielded seismic events. This could be due to lack of accuracy on the data and/or stress involved (Ryder, 1987). Gill and Aubertin (1988) note that this absence of rockbursts for positive ESS confirms the fact that the discontinuity post-peak stiffness and the rock mass stiffness on both sides of the discontinuity may play a major role in the process, or maybe τ_e should not be assumed; rather it should be assessed by laboratory testing.

2.2.1.6 Stress State

The rockburst potential can be estimated based on the relative stresses in the rock mass. These stresses can be examined with the speed of acoustic waves. Mining can induce conditions which promote rockbursting by inducing high stress level due to the geometry of openings and the mining sequence. This technique can then be used to monitor the conditions which promote rockbursting by inducing high stress level due to the geometry of openings and the mining sequence. This technique can then be used to monitor the stress state induced by mining (Singh, 1989). The continuous monitoring of the electric resistance changes in the rock mass has been used to predict the frequency of rockbursting (Stopinski and Dmowska, 1984). This monitoring facilities the observation of the effects of tectonic stresses and mining induced stresses. These observations can also indicate the location and necessity for applying a destress blasting technique to the rock mass (Singh, 1989).

2.2.2 Energy Method

As mining is a progressive activity, the excavations are modified in shape and enlarged with time. It is logical, therefore, to examine the strain energy changes resulting from specific changes in the mining geometry (Srinivasan *et al.*, 1997). Since rockbursts are the result of a violent release of energy it is natural that an analysis of energy be used to explain the mechanics of violent rock failure. Initially only the energy stored within the rock was considered as the source of the liberated energy. Later it was realized that there was a change in potential energy of the surrounding rock mass because of mining operations.

Cook (1963) was the first to point out the significance of energy changes in the rock masses in deep underground mines due to mining, and the link between excess potential energy and the damage due to rockbursts. Following Cook's contributions, several researchers investigated the link between energy release rates and rockburst hazards. In the meantime, theoretical studies were carried out by Salamon (1964a, 1964b, 1964c, and 1984) who successfully applied the theory of elasticity to the simulation of the behaviour of the rock mass surrounding mining excavations. His theory provided a sound foundation for the energy approach to mine design and furnished rockburst research with an acceptable theoretical basis. He assumed that the rock mass surrounding mining excavations behaved as a linear elastic solid but was not necessarily homogeneous or isotropic. Based on the theory, Mitri *et al.* (1993) introduced the concept of mining-induced strain energy, which provided an efficient method for the study of the stress configuration around underground openings induced by mining and made a detailed study of the energy balance resulting from progressive mining activity in deep underground hard rock mines.

2.2.2.1 Energy Balance

Since 1960, many measurements of rock displacement have been performed and they suggest that the rock mass mechanical behaviour in rockburst situation is essentially of elastic nature (Ortlepp, 1983). Then the energy balance is usually performed using elastic laws. It could be shown that using elastic laws to evaluate the energy available for rockbursting is a conservative approach since the energy dissipated by micro fracturing in the pre-peak range is neglected, hence, the stress and energy concentration around opening is overestimated.

Ortlepp (1983) and Obert and Duvall (1967) discussed the importance of mining-induced strain energy in the context of rockbursts in South African hard-rock tabular mining. Recognizing that energy is required to cause rockburst damage and to generate the associated seismic waves, Ortlepp (1983) proposed a study of the energy balance in the rock mass during mining as a means of gaining insight into some of the fundamental aspects of the problem. Some of the questions he proposed are: What is the source of the energy? How is it stored? Why is it liberated sporadically when stoping is a regular cyclic process? How is it triggered? His theoretical developments follow the same trend as those of Blake (1972).

When an opening is created or modified, the stored strain energy equilibrium is changed. Let stage I be the initial situation before the creation of the opening: the stage following the creation (or modification) of the opening will be called stage II, as shown in Figure 2.2. The energy balance is concerned with the transition between stage I and stage II.

When an opening is created, energy becomes available and is provided from two sources. The first one is the work W (or the variation of the potential energy in the system) done by the shifting of external and gravitational forces working on the convergence and deformation of the rock mass. The second source is the stored strain energy U_m in the mined rock. The sum of these energies $(W+U_m)$ is the total energy available when passing from stage I to stage II.

This energy can be dissipated in two ways. A portion of this energy will be dissipated

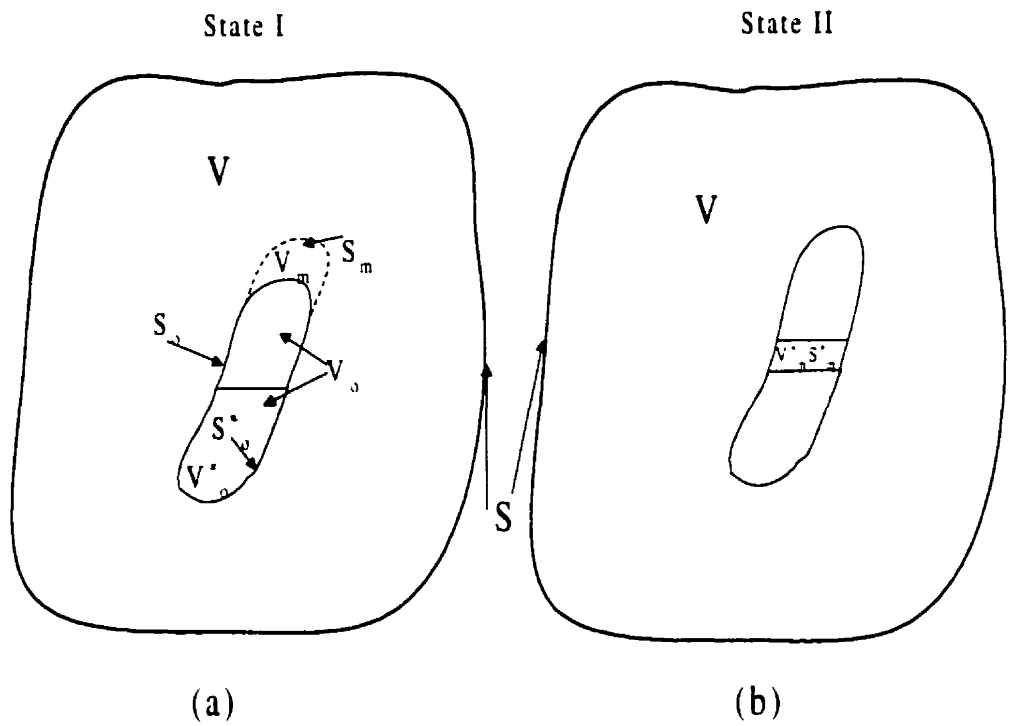

Figure2.2 Mining configuration and notations in the reference state, i.e. in state I (a) and after additional mining, i.e. in state II (b) (after Salamon, 1984)

with an increase in the strain energy U_c stored in the rock mass surrounding the excavation. It is also possible that the pressure on support elements surrounding the opening increase; this work W_r is the second way of energy dissipation.

If the rock mass is considered as an ideal elastic continuum, then no energy is dissipated through fracturing of inelastic deformation of the rock. With this simplification in mind, the sum $(U_c + W_r)$ is the total energy dissipated during the mining of the opening.

It is obvious that the total energy dissipated cannot be larger than the energy available $(W + U_m)$. Considering that the stored strain energy in stage I in the mined rock (U_m) is not available anymore and since U_m>0, then (Salamon, 1984)

$$W + U_m > U_c + W_s \tag{2.8}$$

This inequality implies the existence of an excess of energy that must be dissipated when passing from stage I to stage II. This energy is referred to as the released energy W_r. Then, one can write:

$$W_r = (W + U_m) - (U_c + W_s) > 0 \tag{2.9}$$

and

$$W_r \geq U_m > 0 \tag{2.10}$$

The amount of the released energy W_r, when larger than the stored strain energy in the mined rock (U_m) in stage I, produces a wave (kinetic energy) that propagates from the new limits damped by minor flaws in the rock mass (the latter not being perfectly elastic). This kinetic energy W_k will be dissipated by the damping process. Since there is no other way to dissipate the energy, then:

$$W_r = U_m + W_k \tag{2.11}$$

and

$$W_k = W - (U_c + W_s) \geq 0 \tag{2.12}$$

2.2.2.2 Energy Parameters

The change in potential energy W is the driving force behind the other energy components. If it can be reduced the other energy components are correspondingly reduced. Support, such as backfill, has two beneficial effects. It will reduce the change in potential energy by reducing volumetric closure in the excavations; and by absorbing energy, less energy is available to be released as seismic energy. There are some other energy terms in common use. Based on the energy balance, an incremental approach can be used to follow the changes due to mining. The mining of an underground orebody usually implies the widening of excavations by increments. This leads to an energy release rate by unit surface, used when the opening geometry is regular (or two-dimensional analysis), or a volumetric energy release rate, used for irregular geometry openings (or three-dimensional analysis).

Stacey and Page (1986) provided a way to evaluate, in a preliminary manner, this energy release rate (the symbol ERR is commonly used in the literature). This ERR has become a rockburst prediction tool in South African gold mines (Salamon, 1993). Spottiswoode

(1990) notes that ERR is one of the most used parameters for stope design in deep underground South African mines. Ryder (1987, 1988) in introducing the notion Excess Shear Stress ESS for the prediction of fault-slip rockburst observed that ERR has been found to correlate well with depth of face fracturing, hangingwall conditions, and the decrease in seismicity observed after the introduction of stabilizing pillars in a number of deep mines. It is the preferred criterion used in current designs of stabilizing pillar and backfill systems. Energy release rate (ERR) is now a very useful measure for the design of stope face shapes and investigation of stope interaction and the design of stabilizing pillars for tabular orebodies in South African mines. It has been found (Ortlepp, 1983) that the energy release rate and incidence of seismic activity are statistically associated, although they are not mechanistically related. Experience shows that continuum mechanics, even when applied to discontinuous material, often provides correct results, and it is mathematically much simpler than the theory of discontinua (Gibowicz *et al.* 1994). There is also evidence to suggest that in some cases, under the same rockmass conditions, rockbursts will occur with machine excavation but not with drill and blast excavation (Ortlepp *et al.*, 1994).

This can be attributed to the increased ERR associated with blasting thus relieving the excavation boundary of some of the strain energy in the rock. The need to better

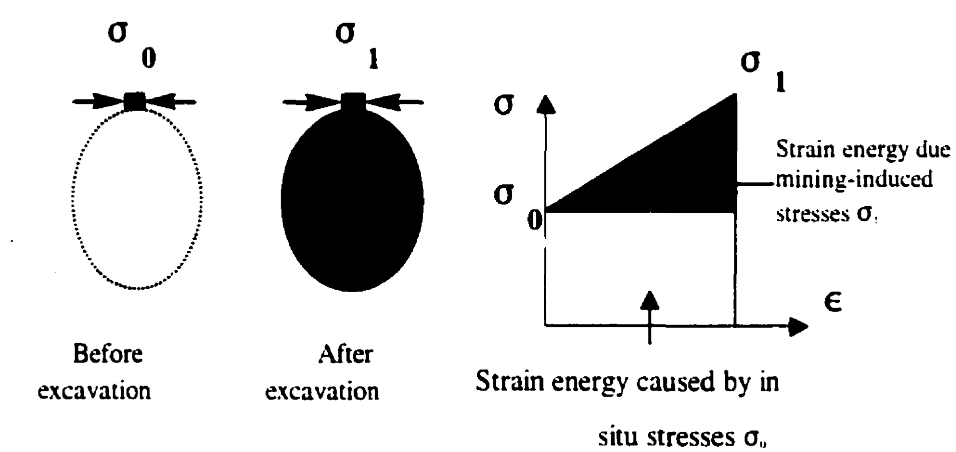

Figure 2.3 Mining-induced Strain Energy (after Mitri et al., 1996a)

as shown in Figure 2.3 (Mitri *et al*, 1996a). The idea is based on the assumption that rockburst phenomena can be attributed to the sudden release of energy in a volume of highly stressed rock. Thus, mining-induced strain energy may serve as an indicator of rockburst potential, rather than simply relying on mining-induced stress concentration. The concept is graphically illustrated in Figure 2.4.

Later, Mitri (1996b) explained how the mining-induced strain energy is related to the

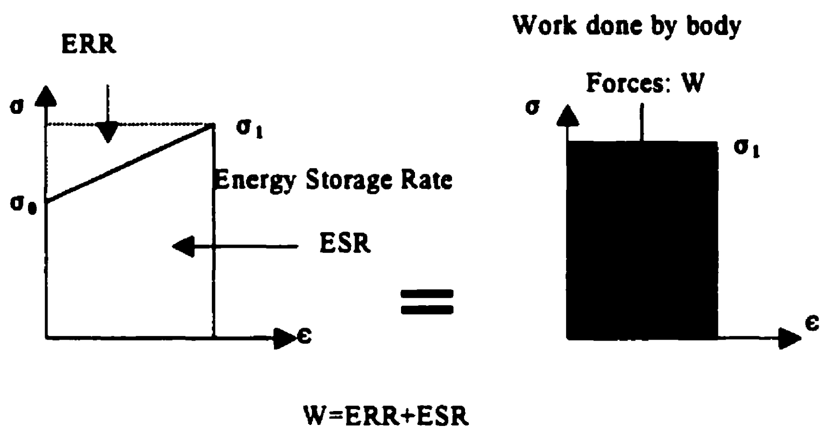

Figure 2.4 Application of the Concept of Change of Potential Energy(Mitri, 1996a)

energy storage rate (ESR) and the energy release rate (ERR) using a finite element modelling approach. Simulation of a crown-pillar case study showed that strainburst phenomena could be examined with this approach.

2.2.2.3 Indices Based on Stored Elastic Strain Energy

Several indices are based on the elastic energy recovered in a loading-unloading test.

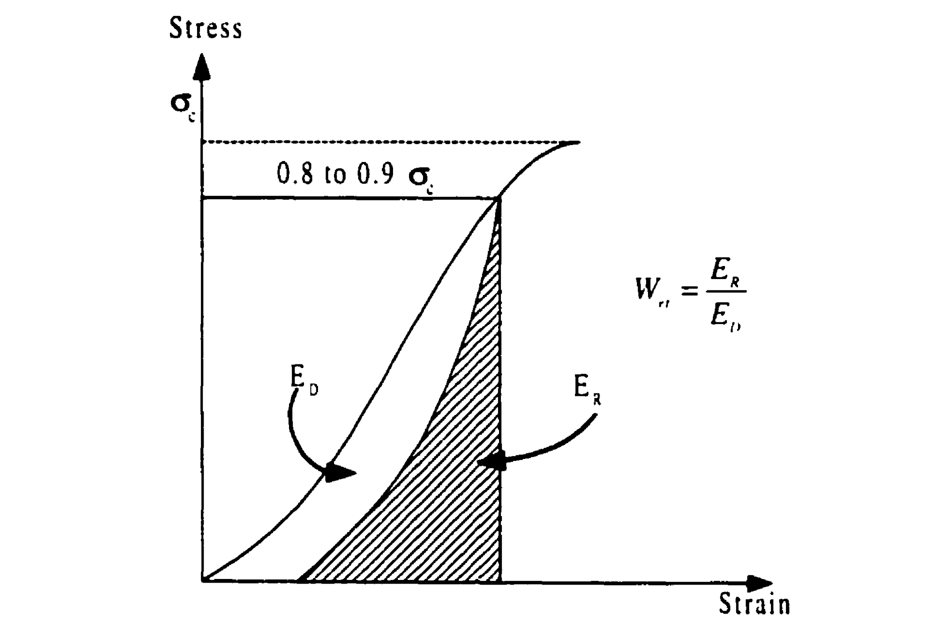

Figure 2.5 Calculation of W_{et} index from a uniaxial compression stress-strain curve (after Kidibinski, 1981)

Among these is the Burst Liability Index or W_{et} Index proposed by Neyman et al. (1972) for coal mines. This index is determined with a uniaxial compression test by:

$$W_{et} = \frac{E_R}{E_D} \tag{2.13}$$

where E_R is the elastic energy recovered during unloading which can be calculated by the area under the unloading curve, and E_D is the energy dissipated in the cycle which can be calculated by the area between the loading and unloading curves (Figure 2.5). The load during the test must attain between 80% and 90% of the uniaxial compressive strength. The larger the value of the index, the less the rock can dissipate energy via stable propagation and the larger is the rockburst potential. Stewarski (1987) also proposed the Rock Dynamic Index that is determined by the same ratio but for a loading test on Hopkin's bar.

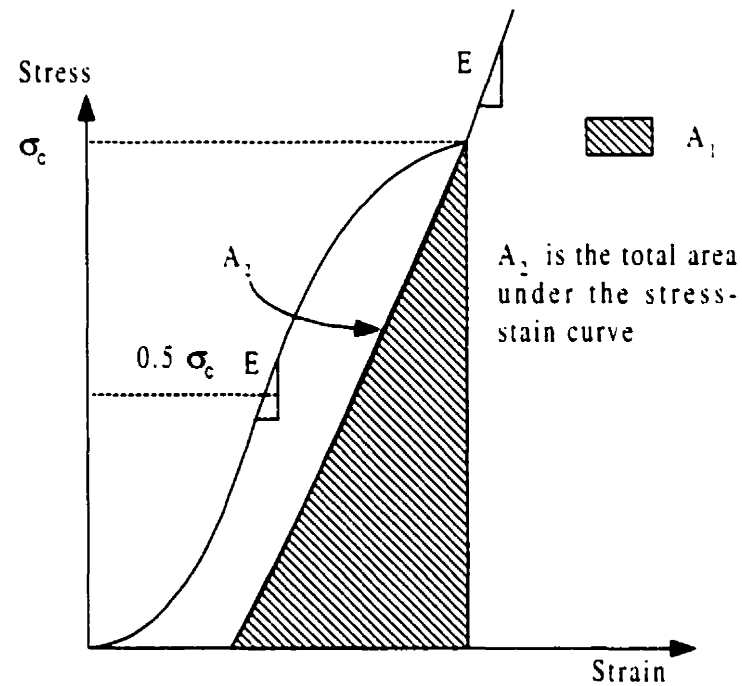

Figure 2.6 A schematical representation of the BIM value determination from a uniaxial compression test results (after Aubertin and Gill, 1988)

However, to achieve 80% to 90% of the strength with W_{et} index is a problem since this strength can be known, a priori, only in a probabilistic manner. Moreover, the size of the hysterisis and the value of the index are directly influenced by the relative value of the load attained (Hueckel, 1987). To eliminate this problem, Aubertin and Gill (1988) proposed the Brittleness Index Modified (BIM). To calculate the value of this index, a uniaxial compression test is carried out up to failure. The area under the loading curve (A_2) is easy to evaluate (Figure 2.6). A_2 is then compared to the area under the curve corresponding to the deformation modulus of the rock (A_1) taken at 50% of the peak strength. The value of this index is then determined by (Aubertin and Gill, 1988):

$$BIM = \frac{A_2}{A_1} > 1.0 \tag{2.14}$$

The smaller the value of the BIM, the higher is the rockburst potential. Aubertin et al (1994) also proposed a classification of the proneness of the rock for rockbursting:

Table 2.3 Indicative values of BIM as related to bursting liabilities (after Aubertin et al., 1994)

BIM	Bursting liabilities
Between 1.0 and 1.2	High
Between 1.2 and 1.5	Moderate
Above 1.5	Low

The BIM has also been related to the ratio of pre-peak modulus to the post-peak modulus and can be used to find the post-peak modulus when it was not determined in laboratory testing.

Motyczha (see Kidybinski, 1981) proposed a Burst-efficiency ratio which is given by:

$$B_{er} = \frac{\phi_1}{\phi_0} \tag{2.15}$$

where ϕ_1 is the energy of particle ejected at failure in a uniaxial compression test, and ϕ_0 is the maximum energy stored in loading and given by (also, Mitri, 1996a):

$$\phi_0 = \frac{\sigma_c \varepsilon_r}{2} \tag{2.16}$$

where σ_c is the uniaxial compressive strength, and ε_r is the deformation at failure.

Hou and Jia (1988) presented a factor that combines drilling observations with in situ stresses. The mean length of drilling core is associated to the in situ stress and then classified. The rockburst potential is evaluated from this class.

Mitri (1996a) suggested the calculation of pillar skin strainburst using an index based on strain energy which is given by:

$$S.L. = \frac{e_s}{e_c} \tag{2.17}$$

Where e_s is the total mining-induced strain energy calculated at the boundary of the opening (pillar skin) and e_c is the critical strain energy given by equation 2.16.

2.2.2.4 Rockburst Hazard Based on 3D Stress Field Analysis

Tajdus et al. (1997) proposed several rockbursts indicators for the evaluation of rockburst potential for Polish underground coal mines:

a). Coefficient of vertical stress concentration

$$\alpha = \frac{\sigma_z(x, y, z)}{p_z} \tag{2.18}$$

where $\sigma_z(x.y.z)$ is the vertical stress in the elementary volume, p_z is the initial vertical stress in the elementary volume.

b). Coefficient of energy concentration:

$$\beta = \frac{V_c}{V_c'} \tag{2.19}$$

where V_c is the strain energy of the rock mass in the elementary volume and V_c' is the initial strain energy of the rock mass in the elementary volume, with:

$$V_c = V_o + V_p \tag{2.20}$$

Where V_o is the strain energy of volume change given by:

$$V_o = \frac{1-2v}{6E}\left[\sigma_x^2 + \sigma_y^2 + \sigma_z^2 + 2(\sigma_x\sigma_y + \sigma_y\sigma_z + \sigma_z\sigma_x)\right] \tag{2.21}$$

and V_p is the strain energy of distortion given by:

$$V_p = \frac{1+v}{6E}\left[(\sigma_x - \sigma_y)^2 + (\sigma_y - \sigma_z)^2 + (\sigma_z - \sigma_x)^2 + 6(\tau_{xy}^2 + \tau_{yz}^2 + \tau_{zx}^2)\right] \tag{2.22}$$

The initial elementary strain energy of the rock mass can be obtained by

$$V_c' = \frac{p_z^2\left(1 - \nu - 2\nu^2\right)}{2E(1-\nu)} \tag{2.23}$$

where E is the elastic modulus and ν is the Poisson's ratio.

c). <u>Ratio of effective stress to rock strength:</u>

$$W_b = \frac{\sigma_0}{\sigma_c \; or \, \sigma_t} \tag{2.24}$$

where σ_0 is the mean applied stress, σ_c is the uniaxial compressive strength and σ_t is the uniaxial tensile strength.

d). <u>Energetic rockburst indicator:</u>

$$T_r = \frac{E_k}{E_k^0} \tag{2.25}$$

where E_k is the energy accumulated in the rock mass and E_k^0 is the energy necessary for initiating rockburst. Based on the energy balance, E_k is given by:

$$E_k = V_C + E_D - L_{ZN} \tag{2.26}$$

where V_C is the elastic energy accumulated in the broken rock mass during rockburst, which is a sum of initial and induced stresses, E_D is the energy generated by the tremor in the rock mass and L_{ZN} is the work used for breaking and crushing rock mass volume discharged to an opening. The minimum energy necessary for initiating a rockburst E_k^0 can be estimated by

$$E_k^0 = \frac{1}{2}\rho_{sr} v_0^2 \tag{2.27}$$

where ρ_{sr} is the average density of broken rock mass (assumed to be 2.5 t/m^3) and v_0 is the average velocity of broken rock mass ejected to an opening during rockburst (estimated at 10 m/s by Filcek, 1980). Thus, $E_k^0 = 1.25\times10^5\ J/m^3$. Then, the energetic rockburst indicator is given by:

$$T_e = \frac{V_C + E_D - L_{ZV}}{E_t^0} \qquad (2.28)$$

If $T_e<1$, then the rock mass is not capable of rockbursting; if $T_e \geq 1$, then a rockburst is possible (the probability of occurrence increases with the value of T_e). From their experience in Polish coal mines, Tajdus et al (1997) have combined the preceding indices to provide the following limits:

- When in a given region the following conditions are fulfilled: $\alpha \geq 1.5$; $\beta \geq 1.5$; rock mass is close to failure $W_h \approx 1$ and $T_e < 1$, then the probability of rock tremors occurrence is very high.
- If the following conditions are fulfilled: $\alpha \geq 2$; $\beta \geq 3$; rock mass is close to failure $W_h \approx 1$ and $T_e \geq 1$, then there is a probability of rockburst occurrence.

2.2.3 Stiffness Method

An analogy based on stiffness difference between the rock sample and the loading system was used to explain the rockburst mechanism. This analogy has been integrated in the local mine stiffness coefficient approach for predicting stability of mine pillars (e.g., Starfield and Fairhurst, 1968; Starfield and Wawersik, 1968; Salamon, 1970; Zipf, 1996).

Gill *et al.* (1993) and Simon *et al.* (1995) devised a methodology for evaluating rockburst potential of highly stressed pillars, which included the use of numerical stress analysis, intact rock properties, geomechanical classifications of rock masses and other site investigation data. The methodology is based on the comparison of post-peak stiffness (or unloading stiffness) of the pillar in question with that of the host wall rock (see Figure 2.7). It includes up to four steps: zoning, identification of vulnerable rock structures, stability analysis and a stiffness comparison when a strain or pillar burst is expected as shown in Figure 2.8. A similar approach has been adopted by Zipf (1996) to examine cascading pillar failure in room-and-pillar mines using the boundary element method.

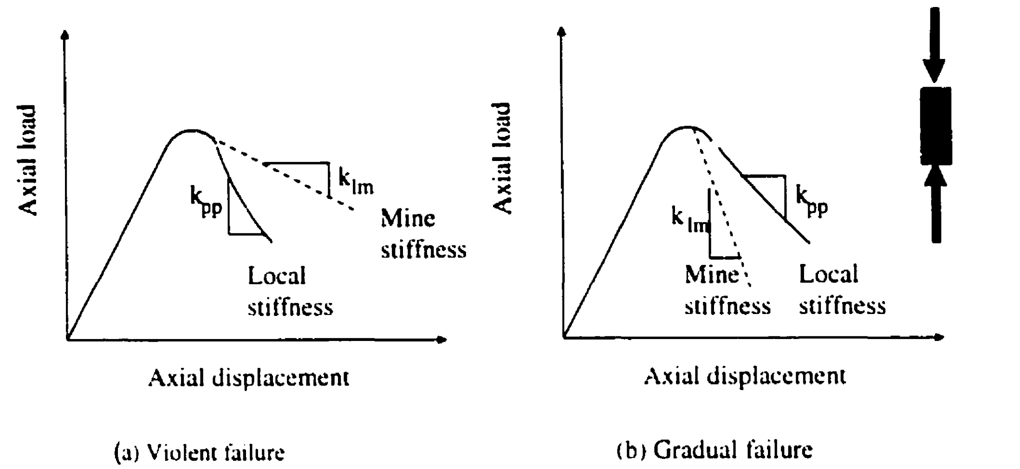

Figure 2.7. Mode of failure determined by comparison between sample and testing(after Cook, 1965)

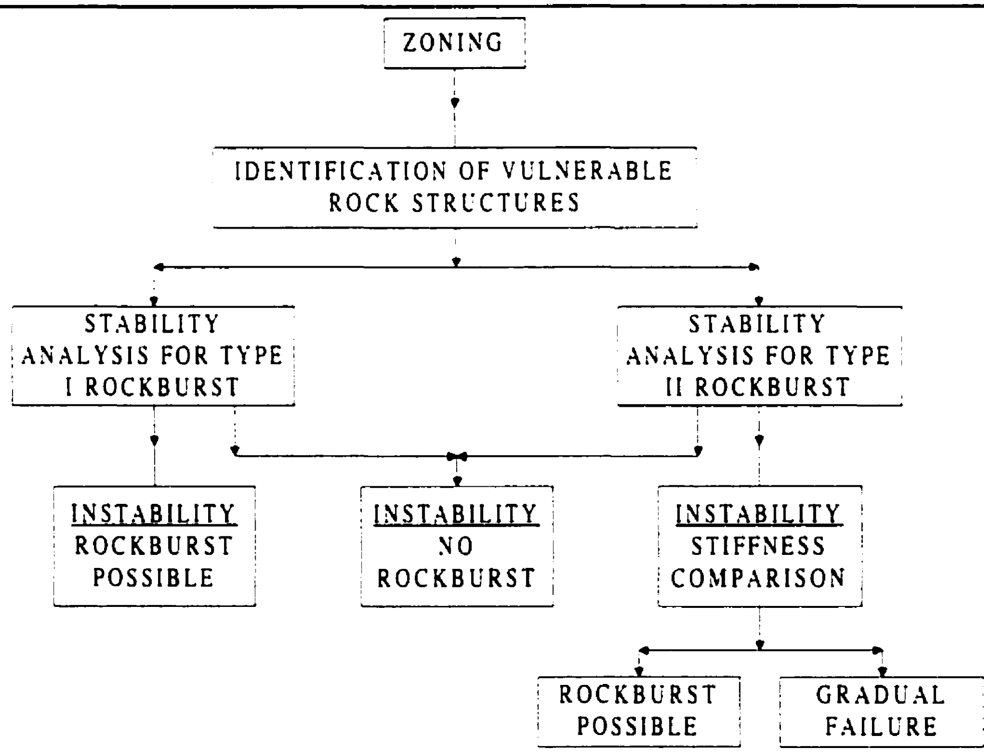

Figure 2.8 Diagram showing the methodology to evaluate the rockburst potential (after Gill and Aubertin, 1988)

2.3 SEISMOLOGICAL METHODS

2.3.1 General Overview

The seismological techniques that were developed to study global earthquakes have obvious application to rockbursts and mining-induced seismicity. A major portion of rockburst research was directed to establish what these techniques could bring to the understanding of the rockburst problem. The primary objective was to use seismology to provide an insight into the behaviour of the source of the seismic events and to provide three-dimensional information about the conditions and properties of the rock mass through which the seismic signals pass. The secondary objective was to contribute to support design and numerical modelling. Through identifying the parameters that control the magnitude, frequency and direction of the energy generated by the events, one can anticipate the severity of damage to excavations and so can be designed appropriate support systems. The properties of the rock mass identified by the seismological analysis could be used to help calibrate numerical models and provide an independent corroboration of modelling results.

In addition to the improvement in event location, accuracy and the ability to improve the design of the sensor array, the application of full waveform seismic monitoring has provided two important benefits. Firstly, it has indicated that large seismic events occur on pre-existing structures and secondly, it has allowed the classification of rockbursts and seismic events by magnitude. This allows the use of the changing distribution of small and large events to indicate the variations in the stress regime and to track these changes in space and time.

In many cases, particularly close to the surface of excavations; mining-induced seismic events generate a dramatic loss of cohesion and shear failure on a multiplicity of planes. So that the failure of the rock mass is better described as a function of a volume of the rock mass than as a failure of a single discontinuity within the rock mass (CRRP, 1996).

Rockburst research has focused basically on two fields - prediction and control. The first studies on prediction focused on acoustic and microseismic emission monitoring. The relation between microseismic emission rate and stress state was first verified in 1938 in the United States (Bolstad, 1990). However, it is with the work of Obert and Duvall in the 1940's (see Obert and Duvall, 1967) that this technique really started.

In a stable elastic homogeneous and isotropic domain, no acoustic or microseismic emission should theoretically occur. Daihua and Miller (1987) note that there is little acoustic emission in an uniaxial compression test until the load reaches a certain level, that is 75% to 80% of the peak strength (50% for Paterson, 1978), which shows that the rock specimen has an elastic behaviour. However, heterogeneity and anisotropy in rock masses will create some local instabilities (Salamon, 1974; Jaeger and Cook, 1976).

Mine microseismicity is highly influenced by local geology and tectonics - i.e., by heterogeneity and discontinuities, and the interaction between gravitational, tectonic and induced stresses at a local and regional scale (Gibowicz, 1990). It is usually assumed (see for example Blake, 1982) that at the scale of rock masses, one finds the same phenomenon as in laboratory tests.

Microseismic events can be recorded by sensors strategically located in a mining region and connected to a data acquisition system. During an event, the computer program locates the position and the amplitude of the event by analysing arrival times at each sensor. It is then possible to locate regions where there is strong microseismic activity. These regions are then considered as burst-prone (Blake, 1972).

Microseismic monitoring can also be used for other purposes than localization. Experience showed that microseismic activity could be related to the ERR and bursting activity; an increase in ERR will usually produce an increase in microseismic activity (Gay et al., 1982), and in periods preceding rockbursts, there is often a high increase of number of seismic events (Jaeger and Cook, 1976). For example, a 17 month experiment in a South African mine where a warning was issued for an increased seismicity showed an 80% success in predicting rockbursts (Glazer, 1997). However, half of these rockbursts occurred more than 4 days after the warning was issued (only 27% occurred within 24 hours).

Microseismic monitoring in the mining industry has been used widely in Canada and worldwide. Canada in particular has spent a lot of efforts in that field (Calder et al., 1986; Daihua and Miller, 1987; Hedley and Udd, 1987; Hasegawa et al., 1989, 1990; Young et al., 1989, 1990; Hedley, 1991, 1992; Plouffe et al., 1993; Beghoul et al, 1996).

Nevertheless, the relative high cost for the purchase, installation, maintenance and use of this technique makes it a tool that is not easily available for small mines like several in the province of Quebec. Moreover, it is hardly a predictive method but rather a monitoring tool (Simon, 1999).

2.3.2 Stochastic Methods

Kijko(1997) demonstrated the power of statistical tools in describing, analyzing and predicting seismic activity induced by mining. Although the occurrence of mine tremors is not strictly a random process, a statistical approach to the analysis of seismic events in mines provides a reasonable basis for seismic-hazard assessment. Essentially two types of approaches are possible:

- The first approach is the assessment of seismic hazard, understood as an estimation of the mean probability (over space and time) of the occurrence of a seismic event with a certain magnitude within a given time interval.
- The second approach is a continuous evaluation of hazard as a function of time or the amount of extracted rock.

2.3.3 Deterministic Methods

Chavan, *et al.* (1993) reported their new concept and method of analysis for predicting rockbursts based on the data obtained through mine closure measurements and seismic network. The method involves recognition of simple regularity patterns, qualification of closures, delineation of stopes prone to bursting and arriving at the date of occurrence of the event. The technique has been tried a number of times and is found to be very successful. It is an alternative theory for the prediction of rockbursts from the mine closure measurements with respect to the location, intensity, and day of the burst. They found that ground movements caused due to stoping activity are not uniform but erratic in nature. The method permits an estimation of the intensity of the rockburst being predicted.

Srinivasan, *et al.* (1997) established linear empirical relations relying on correlation seen between the seismic energy released due to rockbursts, total tonnage of ore mined out and total number of rockbursts, as well as seismic events in some shallow and deep workings currently active at Kalar Gold Field. This deterministic model, although not free from certain limitations at present, has been applied to predict rockburst activity with some success. Its major limitation is the inability to describe the exact location of a predicted impending seismic event.

CHAPTER 3

DESTRESS BLASTING PRACTICE IN HARD ROCK MINES

3.1 DESTRESS BLASTING PRACTICE AND PROBLEMS

Destress blasting was conceived as a rock fracturing technique to stress-relieve potential rockburst zones in deep mines. It was first developed and widely used in the Witwatersrand gold mines in South Africa in the 1950s (Roux et al., 1957; Gay et al., 1982; Salamon, 1983). The concept of destress blasting evolved from the observation that the zone of highly fractured rock immediately surrounding some deep underground openings seemed to offer some shielding to both the occurrence of and damage from rockbursts. By extending and maintaining this zone of fractured rock ahead of a face, it was argued that both the occurrence and effects of rockbursts should be reduced (Figure 3.1).

The effectiveness of the concept was tested in the field and involved destress blasting 32 stopes over a 19 month period at the East Rand Proprietary Mines Ltd. The results were encouraging. Among the parameters monitored before and after the destress blasting were the incidence of rockbursts, severity of bursts, time (relative to shifts), and casualties. Improvements ranged from 34% for the first parameter to 100% for the last (Roux et al., 1957).

Although this initial success was repeated in other parts of the world, it was noticed that rockbursts continued to occur as mines got deeper. This was the immediate reason for stopping these costly and massive destress blasting programs. For the South African mining environment at least, it became obvious that maintaining a 3m thick fractured or destressed zone ahead of an advancing face of kilometres in extent did not provide a large enough buffer against the occurrence of and damage from large close-by rockbursts. Also, there was no real advantage in extending the fracture zone by a few meters either economically or in terms of safety.

However, successful destress blasting programs have been reported over the years (Dickhout, 1962; and Moruzi and Pasieka, 1969). The Coeur d'Alene mining district of Idaho reported successful destress blasting program (Blake, 1972; Blake, 1971). It seems that cooperative effort by the US Bureau of Mines and the mining companies has shown that for certain mining geometry, sill pillars in particular, destress blasting could be effective in improving rockburst control.

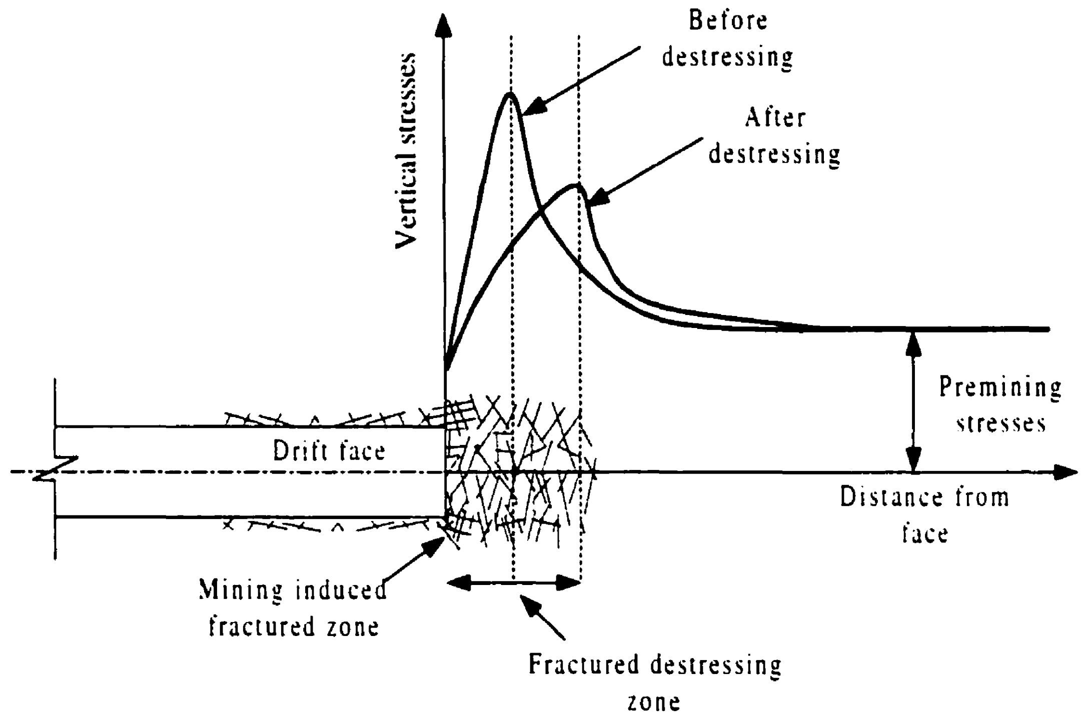

Figure 3.1 Stress profile ahead of a destressed face

Although destress blasting is one of the best techniques of controlling rockbursts, (Blake, 1982; Roux et al., 1957; William and Cuvellier, 1988; Oliver et al., 1987 etc), it has received mixed success in its application mainly because of the following factors:

1. There is a wealth of information about the topic world-wide; however, this information is scattered and is not easily available to the mine site engineer in a coherent form.

2. While the principle of destress blasting is well understood, its successful application is hampered by the lack of a dedicated design tool that is readily capable of simulating the mine conditions before and after destress blasting.
3. In the absence of a better understanding, destress blasting can be unnecessarily costly due to excessive number of drill holes, too much explosives and too many interruptions to the mining cycle.

In addition to reducing the stress in a particular mine structure, successful destress blasting should also result in modifying the material properties of the structure so that its mode of failure is changed. Since rockbursting is almost exclusively associated with brittle rocks, that behave elastically and show a potential for violent failure when their strength is exceeded, it is obvious that by destress blasting of such a rock mass, one is attempting to change its failure mode from brittle elastic to ductile plastic. Thus destress blasting should not only result in the reduction of stress in the zone but should also promote yield type of failure.

Destress blasting in mine development has been applied in zones of high stress and brittle rock. The driving of development headings - drifts, raises and shafts is often accompanied by popping, rock spalling and occasionally face ejection rockbursts. This is often caused by high stress concentrations ahead of the face. The problem is usually alleviated by drilling and blasting long holes ahead of the face and in the pillars between multiple headings. Many variations of the procedure exist as will be seen in the review of case histories to follow.

Destress blasting of crown/sill pillars has been tried in several mining areas of the world but has been most successful in the Coeur d'Alene district of Idaho (Karwoski et al., 1979) where the narrow steeply dipping Ag-Pb-Zn veins are mined by an overhand horizontal cut-and-fill method which results in the creation of rockburst prone pillars. Pillar stresses do not usually approach critical levels until pillar heights have been reduced to about 15 m, at which time, destress blasting is carried out if it is felt that further mining would result in rockbursts. The destressing procedure for stope faces and rib pillars during silling operations was described by Oliver (Oliver et al., 1987). Some uncertainties and constraints about pillar destress blasting are:

- The use of hand held drilling equipment limits the size and length of destress holes.
- The usual practice of waiting for the pillar to be as small as possible before destress blasting can result in increased exposure time to possible on-shift bursting.
- Any misfires occurring during destress blasting could prove hazardous during subsequent mining. The time and care necessary to ensure that there are no misfires or to take care of any, constitute expense and delay which can be costly.
- Timing is critical. Destress blasting carried out too early may allow stresses to rebuild to the extent of causing on-shift bursting; carried out too late, it may result in increased exposure time to possible on-shift bursting.
- Destress blasting procedures cause production delays, which have to be balanced against the cost of safety of the mining operation.
- It is difficult to assess the quantity of explosives required for adequate destress blasting.

In the study conducted by Ineris-École Des Mines, Nancy, France, (Al-Heib et al., 1994, Bigarre, 1996), a review of the various destressing methods, and useful monitoring methods presently available was made. It is pointed out that fracture patterns around fully confined blastholes are dependent on the orientation of the major principal stress (Rorke & Brummer, 1990). A useful part of this report is the appendix containing non-critical resumés of significant reports of destress blasting. In a complementary report a mechanical method used in a French coal mine is described and results analysed.

Simon et al. (1998) presented the main results of numerical and experimental investigation on the effect of destress blasting on the rockburst potential of an horizontal pillar below a stope (sill pillar) at Sigma Mine, Val d'Or, Quebec.

3.2 MINING SITUATIONS WHICH CALL FOR DESTRESS BLASTING

In general, destress blasting can be regarded as a tactic measure of strainburst control in all mining situations, which lead to the creation of high stresses in stiff, brittle rock at the boundary of mine openings. With this notion in mind, several mining situations can benefit from destress blasting as a means for the control or even elimination of rockburst hazard. Some of those situations are illustrated in Figure 3.2.

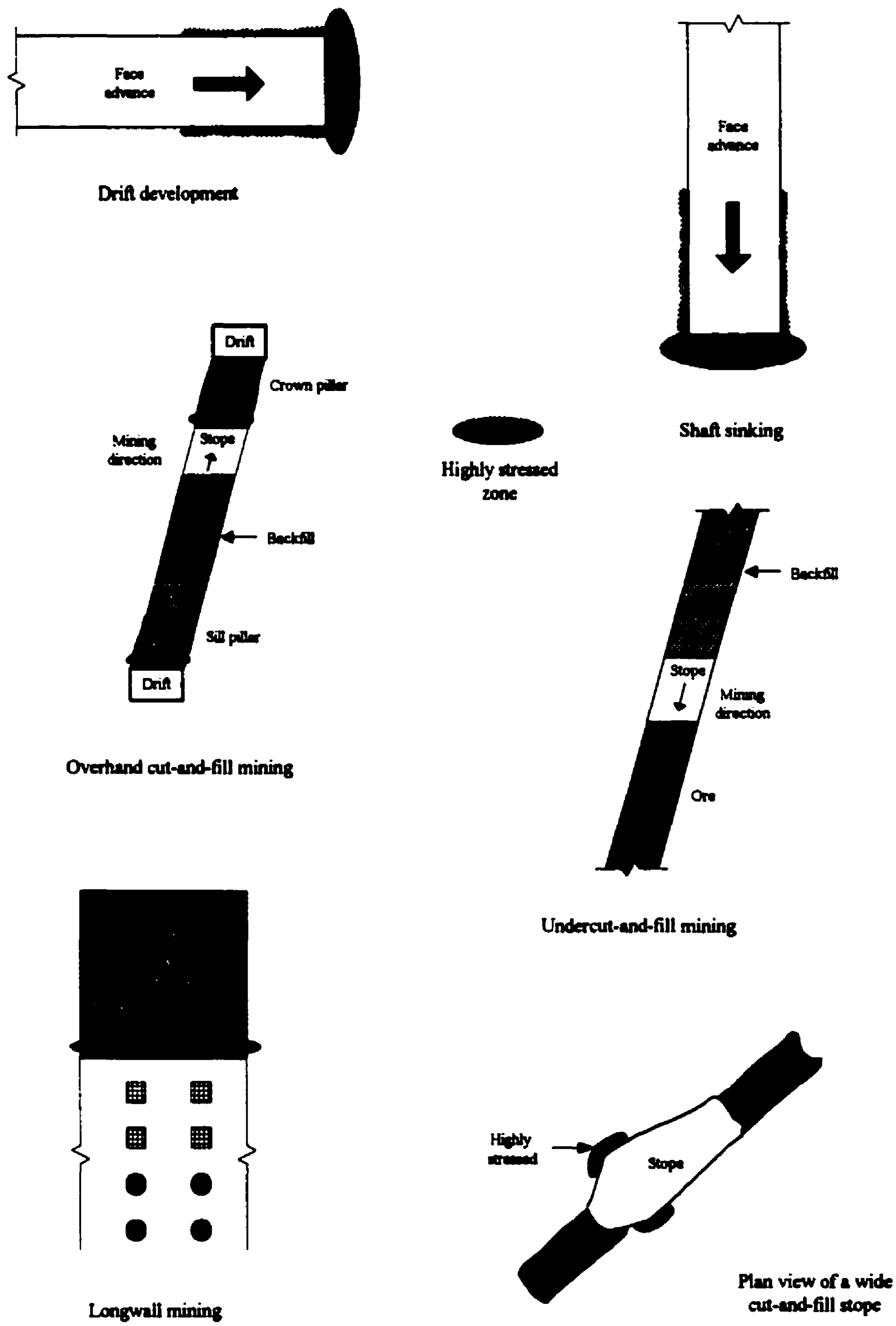

Figure 3.2 Some mining situations, which may benefit from destress blasting

Drifting at depth- Ramps, drifts and cross cuts developed at depth in hard rock mines may be prone to face bursts, floor bursts or a combination thereof. The presence of high mining-induced stresses in a brittle rock mass makes it more likely for rockburst to occur. Detsress blasting can result in shifting the high stresses away from the face and drift corners.

Shaft sinking at depth-Floor burst, wall spalling and spitting are among the commonly observed strainbursts in deep shaft sinking in hard rock. The integration of floor destressing in the mining cycle can have beneficial effects on the reduction of on-shift seismic events, and the conditions of the walls and floor.

Crown pillar destressing- In conventional cut and fill, upward mining of small lifts of 2-3 m eventually leads to the development of high stresses in the crown pillar, particularly, at the skin, i.e. immediately above the working area.

Sill pillar destressing- Several mining methods rely on sill pillars to keep the integrity of the mine structure. Examples of sill pillars are found in cut-and-fill stopes, shrinkage stopes and sublevel stoping. In the latter, regional sill pillars are found between the main levels.

Undercut and fill mining- In this method, mining progresses downwards, while the stope back is backfilled and supported by a timber frame. As the ore vein becomes thinner under the stope, high stresses develop in the floor, and the situation becomes prone to floor bumps.

Longwall mining- Mining of large, relatively flat tabular ore deposits, by longwall methods inevitably leads to high mining-induced stresses at the working face. The method relies on external supports such as cribs and packs to help control the roof to floor convergence. Nevertheless, high stresses still occur at the face. The severity of face rockburst will depend primarily on the depth and overburden pressure, but other factors like length of unsupported span, rock type, and the strength of the support will also play an in important role.

3.3 LITERATURE REVIEW ON REPORTED DESTRESS BLASTING CASE STUDIES

A comprehensive survey of destress blasting trials to control hazards associated with rockbursts was conducted. This covers papers on rockbursts and destress blasting practice in hard rock mines. Most of the literature deals with metal mines in Northern Ontario, South African gold mines, the Kolar Gold Fields in India, and the Coeur d'Alene mining district in Idaho, United States.

Table 3.1 reports the list of mines which practiced destress blasting. The collected information include a wide range of information from the name and location of the mines, to the specific details of destress blasting. As can be seen from the Table 3.2, considerable amount of blasting related data is not reported, such as the type and quantity of explosive. A more detailed review of selected case studies is described in the following section.

Table 3.1 Summary of reported destress blasting studies

Company	Mine	Location	Minerals recovered	Ore type	Dimensions	Host rock
Goldcorp	CRLM	Balmertown, ON	Gold, AU	Quartz sulphide veins	Variable	Andesite
Kinross Gold	Macassa	Kirkland Lake, ON	Gold, AU	Siliceous Syenite		
Falconbridge Ltd	Strathcona	Onaping, ON	Copper-Nickel-cobalt	Massive Sulphide Veins	1600x1600x 2000	Gneiss
Falconbridge Ltd	Falconbridge	Sudbury, ON	Zinc-copper-silver			
Hecla	Lucky Friday	Idaho, USA	Lead-silver	Lead-silver		
Hecla	Star	Burke, Idaho	Lead-zinc-silver	Sulphalerite and galena		Revette quartzite
CMC and ASARCO	Galena	Wallac, Idaho		Mineralized quartzite		Quartzite
Inco	Creighton	Copper Cliff, ON	Nickel-copper-cobalt	Massive Sulphide		
LKAB	Malmberget	Sweden	Iron	Reddish Grey Leptite		
Boliden	Laisvall	Sweden	Lead	Lead ore		
Sumtomo Corp.	Besshi	Niihama, Japan	Copper	Cupriferous Pyrite	1300mx2.5m	

Continued for Table 3.1

McWatters	Sigma			Quartz-tourmaline		Diorite
Beijing	Mentougou	Beijing, China	Coal			
Fushun	Longfeng	Fushun, China	Coal			
Kailuan	Tangshan	Tangshan, China	Coal			
Deyang	Tianchi	Deyang, China	Coal			
Boliden	Pyhäsalmi	Finland	Iron			
	Lake Shore	USA	Gold			
	Kerr Addison	Kirkland Lake, ON				
ERPM	ERPM	South Africa	Gold			
VRRE	Vaal Reefs	S. Africa	Gold			
WDL	South Mine	S. Africa	Gold			
KGM	Libanon	S. Africa	Gold			
DCL	WDGM	S. Africa	Gold			
DRD	Blyvooruitzich	S. Africa	Gold			

Table 3.2 Detailed information of reported destress blasting studies

Mine	Mining M.	Destress Blasting (DB)											
		Classification					Layout				Explosives		
		FRE	Zone	Level	Depth (m)	Date	N. H	H.D (mm)	H.L (m)	S (m)	Type	P.F (kg/m^3)	E.M (Kg)
CRLM	C&F		C. Pillar	1102E'B'	450			45		1.8	ANFO	0.2	
CRLM	S.B (8m)		Chutes	1421W				45			ANFO	0.09	
CRLM			Drift	1470				45	2.5	0.3-1.2	AMEX		
CRLM	C&F		C. Pillar	1902-1802	810			44	6	1.8	ANFO	0.2	
CRLM	10 m stopes		Vein	1604				45		1.4		0.7	
CRLM	O.H. C&F & U.H. C&F	RO	Sill Pillar	1800	1300	1980	28	44	6	1.8	ANFO	0.2	
Macassa	O.H. C&F		Footwall	1800	1400-2150		14	63.5	16.8		ANFO	0.14	
Macassa	O.H. C&F	Ex	Shaft 3		1524		6	50.8	27.43		Primaflex		
Macassa	O.H. C&F	Ex	Shaft 3		1524		4	35	3.66		Powermex 5000		
Macassa	O.H. C&F	Ex	C. Pillar		1524	1962	2		19.5+3 2.3	7.62	AMEX II		

Continued for Table 3.2

Strathcona	C&F		Access Ramp	25-32-C9 25-34-DO	2375-2500		66	76.2	5.5	2.13	M.F 3000	0.115 - 0.138	
Falconbridge	C&F	EX	H.W (raise)	3850	1174	1963	3						9.8-19.6
Falconbridge	C&F	EX	H.W (raise)	3850	1174	1963	2	50.8	16.8		ANFO		
Galena	C&F	EX	F.W	3700	1128	1970		48	6	1.5	ANFO		
Galena	C&F	Ro		4300-4600	1500	1990	11		4-10	1.5	ANFO		125
Lucky Friday	U.H. C&F	EX	C. Pillar	4900	1620		58		24	3	Apex 340	0.6	6.4
Star	O.H. C&F	EX	# 7, 10	7700	2350			102	30	2.3			
Star	O.H. C&F	EX	# 8, 9, 12	7900	2400			102	30	2.3	Tovex 500		
Star	O.H. C&F	EX	Grouse	7700	2050			29-57	5-8	2-3	ANFO		
Terra Tek	U.H. C&F						29	57	10.7	3			
Creighton	M C&F M C&F	RO	Cross-Cut	5400	1645	1960's	1	67	14	-			
Creighton	M C&F	RO	Cross-Cut	6000-7000	1820-2130		4	32-41	3-5.5		ANFO		
Creighton	VRM	RO	Drift		2010		4				ANFO		
Creighton	VRM	RO	Drift		2130		6	32-41	3.6		ANFO		
Creighton	Sill Drifting	RO	Drift		2073		2	43	3.6-6		ANFO		

Continued for Table 3.2

Creighton	Sill Drifting	RO	Drift		2073		4	43-54	3.6-7.3		ANFO		
Creighton	VRM	RO	Drift		2134		6	43	3.6-7.3		ANFO		
Creighton	VRM	RO	Drift		2195		10	43			ANFO		
Cresent		RO	Sill and C. Pillar	3100					10.7	3.1-1.5	Dynamite		
Cresent		RO	Sill and C. Pillar	3300					10.7	3.1-1.5			
Cresent		RO	Sill and C. Pillar	3500					10.7	3.1-1.5			
Malmberget	Drifting	EX	Drift		815		3		6-7		Bonagel		1
Laisvall													
Pyhäsalmi	C&F	EX	Pillar	645-660				89	10	.8	TNT	1460	
Pyhäsalmi	C&F	EX	Pillar	615-630				64	10	.5	TNT	1460	
G		RO	Roadway		1200			42-50	3M				
G		RO	Roadway				7	32-35	2.5-3	10 m			
Besshi			Footwall	28		1969	64		10	3			128
Sigma	C&F	EX	Sill Pillar	3400	1500	1996	15	38.1	8.5	1.2	ANFO	0.15/0.2	
Longfeng	Longwall		Face						4-6	3-5			
Lake Shore	C&F	EX	Raise	3950	1204	1963	2	38.1	16.8	2.4			

Continued for Table 3.2

Kerr Addison									3	1.5	ANFO		
ERPM	Longwall	EX	Drift Face										
Vaal Reefs	Longwall	EX	Fault		675		12	60	12				
Vaal Reefs	Longwall	EX	Fault		2500		3	60					
WDL	Longwall	RO		WDLS 87-49W				38-42	2- 2.2 5		ANFO		
Libanon	Longwall	RO	Pillar	25-55W							ANFO		
WDGM	Longwall	RO	Stope	32-12W				76	3.5- 5	8	ANFO		
BGM	Longwall	RO	Stope	18-13W				76	30		ANFO		
BGM	Longwall	RO	Pillar	30-24W				76	10		ANFO		
BGM	Longwall	RO	Stope	17-24W	1900			89	18		ANFO		
BGM	Breast M.	RO	Face	17-24W	1900	09/9 2			17. 0		ANFO		150
BGM	Breast M.	RO	Face	17-24W	1900	10/9 2			17. 0		EMUL		125
BGM	Breast M.	RO	Face	17-24W	1900	11/9 2			22. 0		ANFO		150
BGM	Breast M.	RO	Face	17-24W	1900	11/9 2			14. 0		ANFO		75
BGM	Breast M.	RO	Face	17-24W	1900	12/9 2			22. 0		ANFO		150

Continued for Table 3.2

BGM	Breast M.	RO	Face	17-24W	1900	01/93			15.0		ANFO		75
BGM	Breast M.	RO	Face	17-24W	1900	01/93			18.0		ANFO		118
BGM	Breast M.	RO	Face	17-24W	1900	01/93			10.0		ANFO		50
BGM	Breast M.	RO	Face	17-24W	1900	02/93			15.0		ANFO		75
BGM	Breast M.	RO	Face	17-24W	1900	03/93			15.0		ANFO		95
BGM	Longwall	RO	Face	17-24W	1900	03/93			10.0		ANFO		75
BGM	Breast M.	RO	Face	17-24W	1900	03/93			17.0		EMUL		81
BGM	Breast M.	RO	Face	17-24W	1900	04/93			15.0		ANFO		81
BGM	Breast M.	RO	Face	17-24W	1900	05/93			14.0		EMUL		93
BGM	Breast M.	RO	Face	17-24W	1900	06/93			16.0		ANFO		100
BGM	Breast M.	RO	Face	17-24W	1900	06/93			14.5		ANFO		100
BGM	Breast M.	RO	Face	17-24W	1900	07/93			10.0		ANFO		43
BGM	Breast M.	RO	Face	17-24W	1900	08/93			13.5		ANFO		100

Continued for Table 3.2

BGM	Breast M.	RO	Face	17-24W	1900	09/93			18.0		ANFO		125
BGM	Breast M.	RO	Face	17-24W	1900	11/93			13.5		EMUL		100
BGM	Breast M.	RO	Face	17-24W	1900	12/93			16.5		ANFO		100

<u>Company</u>

KGM=Kloof Gold Mining Co. Limited

CMC=Coeur d'Alene Mines Corporation

ERPM=East Rand Proprietary Mines Ltd

VRRE=Vaal Reefs Reefs Expl. & Mining Limited

DCL=Driefontein Consolidated Limited

DRD=Durban Roodepoort Deep Limited

<u>Mine</u>

BGM=Blyvooruitzicht Gold Mine

CRLM=Campbell Red Lake Mine

ERPM=East Rand Proprietary Mines

LGM=Libanon Gold Mine

WDGM=West Driefontein Gold Mine

<u>Mining Methods</u>

U.H. C&F=Underhand Cut-and-fill

O.H. C&F=Overhand Cut-and-fill

S.B= Shrinkage boxholes

<u>DB Classification</u>

Zone

H.W=Hanging wall; F.W=Footwall; S.&C. P.= Sill and Crown Pillar

FRE=Frequency

EX=Experimental; RO=Routine

Zone

C. Pillar=Crown Pillar

Explosives

Continued for Table 3.2

WDLS=Western Deep Levels South Mine WDL=Western Deep Levels	M.F=Magnafrac S = Hole spacing; P.F. = Powder factor; N.H = Number of holes; H.D = Hole diameter; H.L = Hole length

3.4 SELECTED CASE HISTORIES

3.4.1 Star-Morning Mine, Hecla Mining Co., Burke, Idaho (Karwoski et al., 1979), (Figures 3.3, Figure 3.4)

In this case, the destress blasting trial was done in and near a sub-vertical, narrow, ore vein, mined using a timbered, overhand, cut and fill mining method. The test zone was divided into two adjacent test panels totalling 79.24 meters long and 24.38 meters high (12.19 m above and below the access level). In one panel (half the total area i.e. 39.62 m

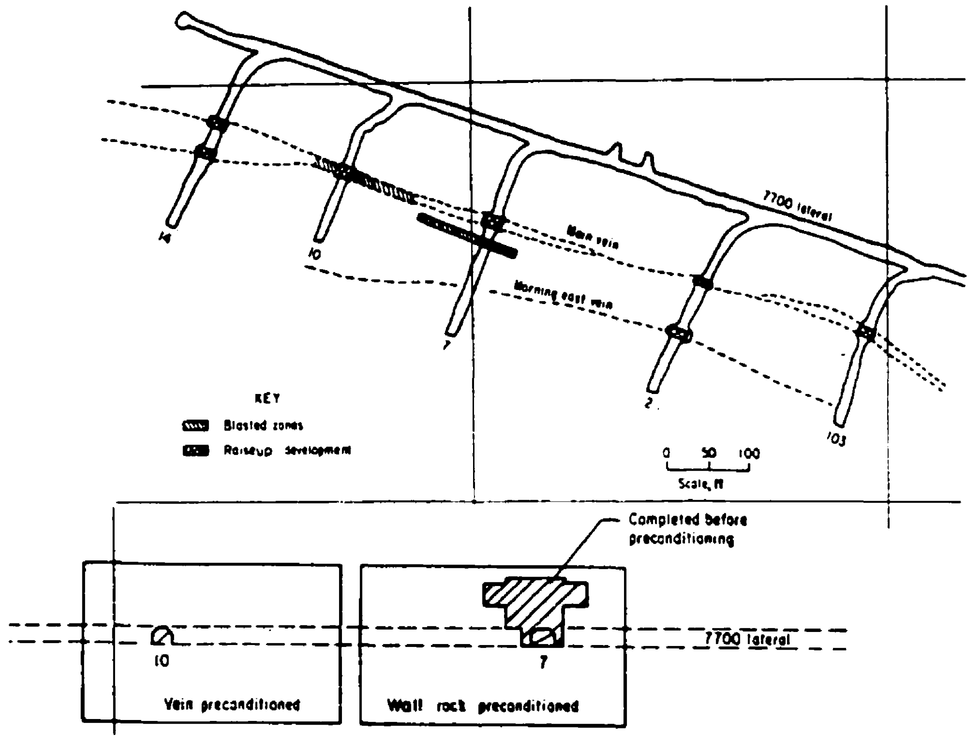

Figure 3.3 Locations of Destress Blasting, Level 7700, Star-Morning Mine, Hecla Mining Co. (after Karwoski et al., 1979)

x 24.38 m) the destress blasting was done outside the ore vein, while in the other panel the destress blasting was carried out in the ore vein. Seismic tests showed that the wall rock had a higher P-wave velocity than the ore. In general it was found that the best results occurred where the destress blasting was done in the ore vein. This was determined by monitoring the seismic activity during mining of the vein.

Destress blastholes of 102 mm and 92 mm diameter were drilled in a fan pattern covering the panel area around access crosscuts either in mid plane of the ore or parallel to the vein. Explosives used were TROJAN slurry (1400 kg/m^3) and pourable gel (1470 kg/m^3), and ANFO (770 kg/m^3). Ignition of the blastholes was at 100ms intervals and 42.69-gr./m detonating cord was used as a tracer in the blastholes. This tracer cord was detrimental as it ejected the stemming. The in vein panel consumed about 2141.52 kg of explosive (2.199 kg/m^2) while the out of vein consumed about 1916.8 kg (1.1955 kg/m^2). Drilling and blasting the destress holes was carried out over a six month period in the latter half of 1976.

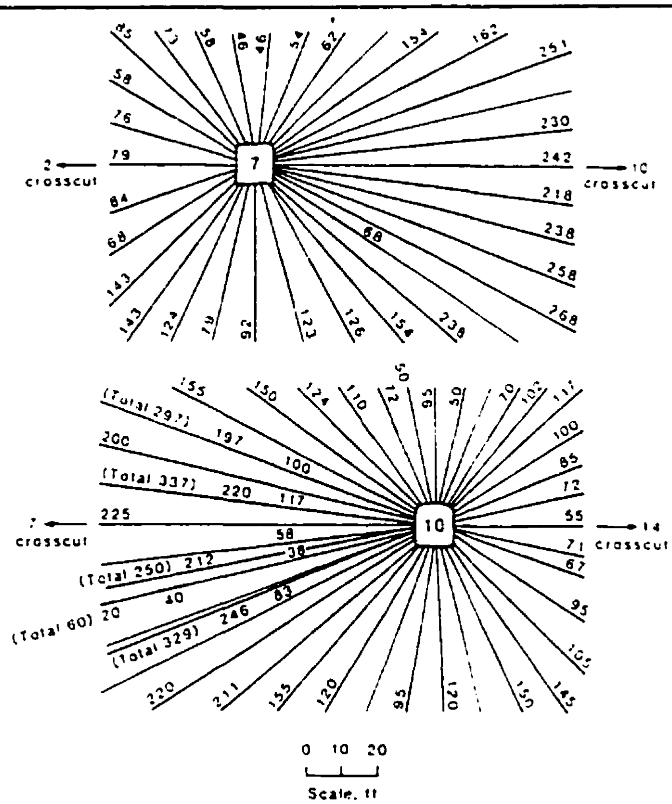

Figure 3.4 Destress blasting drillholes and loading patterns for the 7700 level, Star-Morning (after Karwoski et al., 1979)

Mining the destressed vein, from the 3rd floor for the out of vein panel and from the 1st floor for the in vein panel out a total of 10 floors, was carried out to September, 1977. Mining the in vein panel disclosed that the destress blastholes had increased in diameter to 203 mm (a 51 mm wide halo representing rock completely powdered and removed by the blast) with a 152 mm wide halo of crushed rock about the enlarged hole. No radial cracking around the blastholes was observed in the ore but it showed signs of being fractured and fissured by the blasting possibly by extension of existing defects.

3.4.2 Macassa Mine, (Hanson et al., 1987), (Figure 3.5)

This trial concerns a stope crown pillar, in a steeply dipping ore vein. where a line of destress blastholes are drilled on the mid-plane of the pillar. This was done after about

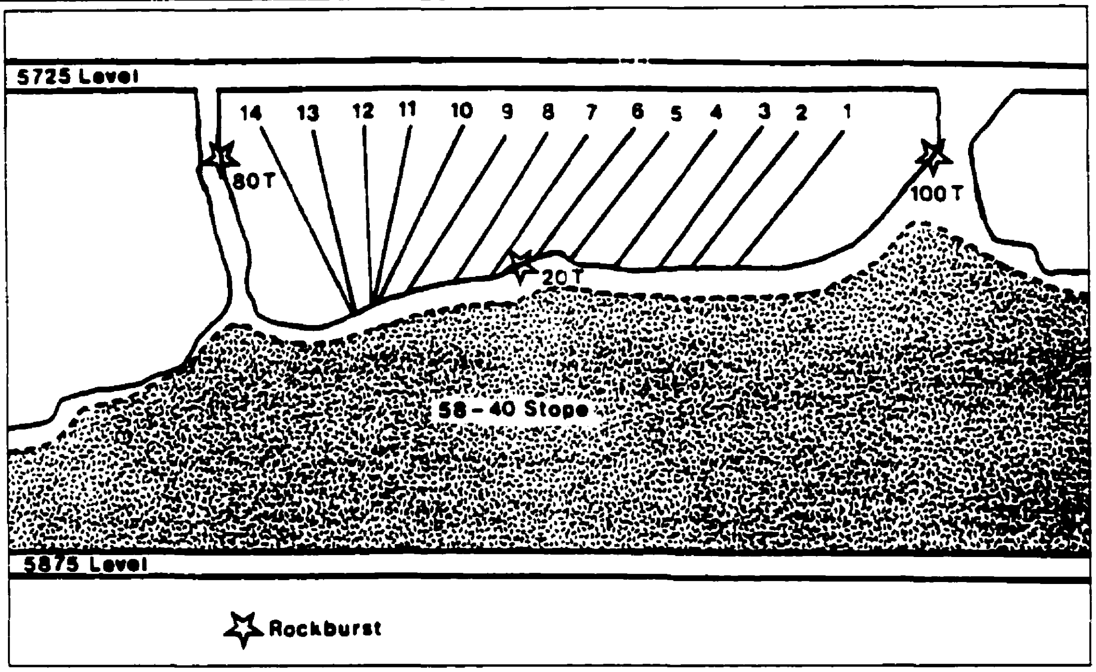

Figure 3.5 Layout of destress holes in the 58-40 crown pillar at the Macassa Mine (after Hanson et al., 1987)

60% of the stope being mined by the cut-and-fill method. Stress measurement indicated that the vertical stress was equal to the overburden pressure more or less. i.e. 0.026 MPa/m. The maximum and minimum horizontal stresses were 1.62 and 1.14 times the vertical stress respectively. Stress on the pillar was so high that some blastholes could not be loaded with explosives. The blastholes were fired on separate delays with about 45 kg/del. Seismic event location and convergence, before and after the destress blast, were used to monitor the results. Simulation of the process was done using linear and non-linear NFOLD numerical simulations.

Pillar failure was noted to progress from the edges towards the centre. Post blast seismic activity was located mainly in the destressed (presumably failed) part of the pillar, which is inconsistent with current thought on the operating mechanism. Only part (50%±) of the pillar was destressed. When the numerical model is well calibrated by the failure observations and convergence measurements it correctly predicted the results. This requires material properties such as a 60 degree angle of internal friction and a cohesion of 50 MPa. The numerical model predicts load transfer to adjacent backfilled stopes which is not confirmed by the convergence measurements.

3.4.3 South Africa, (Lightfoot et al. 1996; Toper et al., 1998), (Figure 3.6)

These reports concern destress blasting in the sub-horizontal, deep, gold reef ores in South Africa. The trials reported on, which are presently being incorporated into the operational procedures, were done on border pillars surrounding a reef being mined, probably already preconditioned by mining induced stresses. Two types of drilling geometry were evaluated:

1. Destress blasthole drilled parallel to the advancing face, and
2. Destress blastholes drilled perpendicular to the advancing face.

Proper tamping of the destress blastholes was found to be very important and somewhat difficult to obtain in the short, face-perpendicular, sub-horizontal holes. Monitoring of results included convergence and horizontal displacements, seismic event location, tomography and ground penetrating radar. Numerical modelling was used to analyse the collected data.

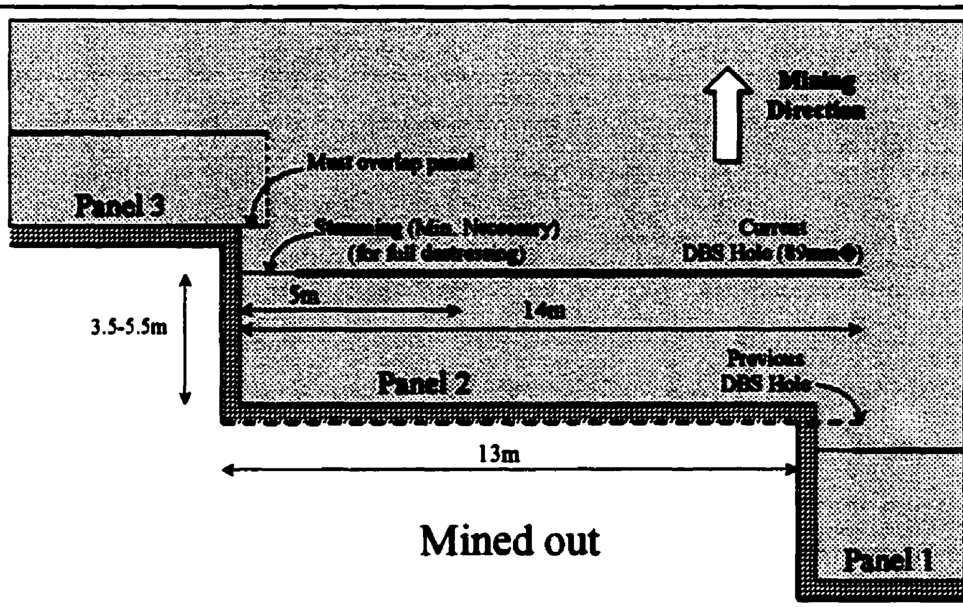

Figure 3.6a Face-parallel destress blasting at Blyvooruitzicht Gold Mine, South Africa (after Lightfoot et al. 1996; Toper et al., 1998)

No new fracture planes were observed after destress blasts. Displacement on existing geologic planes showed-up as crushing or gouge of varying thickness. The destressing mechanisms proposed are: shake-up of existing stressed planes causing slip by shearing of locked-up protuberances, and gas penetration of existing stressed planes reducing the effective stress and thus the shear resistance. Seismic events after destressing migrated away from the destressed area which is consistent with the currently held, basic, destressing mechanism. It was found that destressing should not be carried out too far ahead of the mining face as the load may revert to the destressed rock in the face with undesirable results. It was also found that too long a delay in resuming mining after destressing allowed the stresses to build up again in the destressed rock, i.e. evidence of consolidation of fissured but otherwise strong rock.

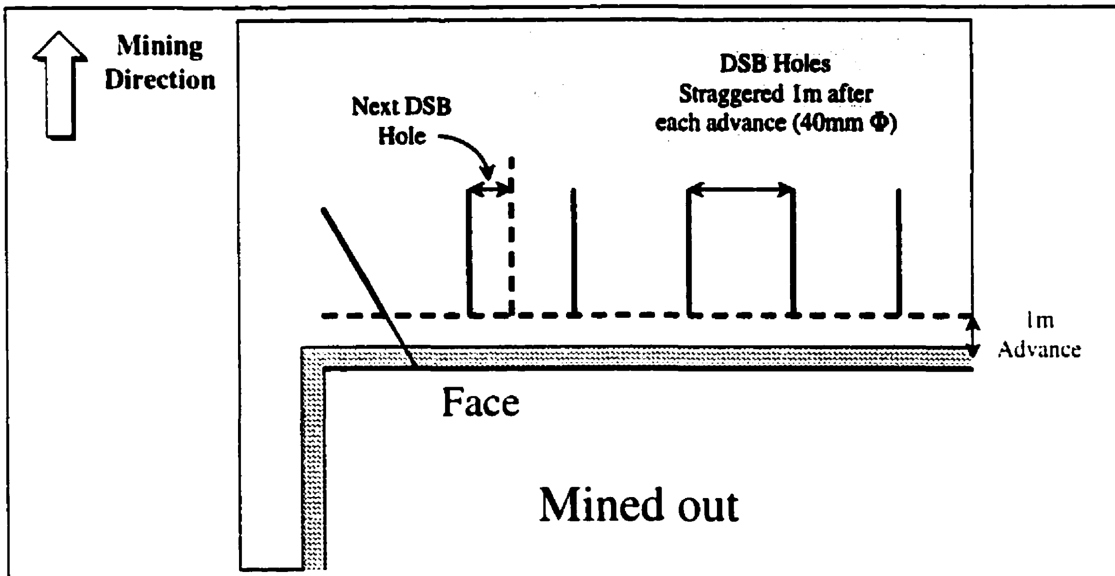

Figure 3.6b Face-perpendicular destress blasting at Blyvooruitzicht Gold Mine, South Africa (after Lightfoot et al. 1996; Toper et al., 1998)

Ground penetrating radar showed that the damage zone around destress blastholes extended for a radius of 1.5 meters. This helped in optimising the blasthole layout. No description of the damage zone around destress blastholes was given. Modelling used step functions of 500 and 1000 MPa explosion gas pressures injected into the fractures. A rating system was devised relating immediately recorded seismic energy to quantity of explosives used, number of post blast seismic events, largest magnitude of post blast events, spatial migration of seismic events and convergence. This rating system also takes into account whether production blasts occur on the same day in another panel.

3.4.4 The use of destressing at Inco's Creighton mine, (O'Donnell, 1992), (Figures 3.7, Figure 3.8)

This section describes the problems, the methods and the results achieved while preparing to mine the 400 orebody, a massive sulphide deposit dipping at 65 degrees, with a strike length of 183 meters and a thickness of 122 meters. Three mining methods were envisaged for this orebody: sub-vertical blasthole mining on the hangingwall side, cut-and-fill in the centre and undercut-and-fill on the footwall. The stopes were originally aligned along the strike for the blasthole mining and changed to across the strike for the cut-and-fill mining. The VRM method was introduced to negate the undesirable effects of cut-and-fill mining in burst prone ground.

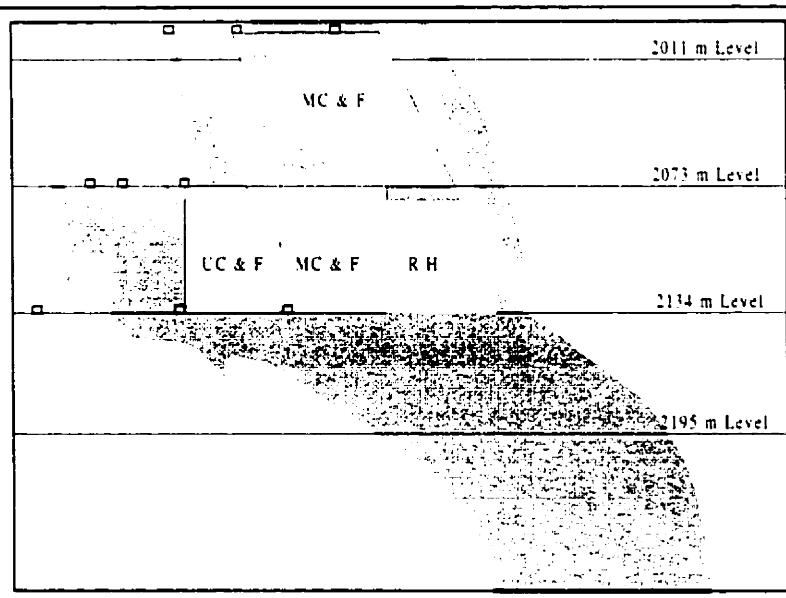

Figure 3.7a: Section 4400, indicating the proposed mining methods at Inco's Creighton (after O'Donnell, 1992)

The section describes three cases where destress blasting was applied during excavation of the sill drifts in preparation for mining the ore blocks. Sill drifts were 4.3m wide and 3.7 meters high with variable spacing as low as 3 meters. The first case described is on the 2073 level (2073 meters below surface), the second on the 2134 level and the third on the 2195 level, where the VRM mining was introduced increasing the height of the sill drifts to 4.6 meters. Far field stresses were: 100 MPa in the E-W direction, 79 MPa in the N-S direction, with a vertical stress of 62 MPa. The uniaxial compressive strength of the footwall rock varied from 175 to 250 MPa while that of the hangingwall rock was approximately 160 MPa, no value was given for the ore. Primary support was supplied by 1.8 m x 15 mm mechanical bolts and number 4 gauge, 10 cm x 10 cm welded wire mesh to mid-wall. Destress blastholes were generally 43 mm diameter. Long destress blastholes were started at 54mm diameter and completed at 43mm. ANFO was used as the explosive at the bottom of the destress blastholes in lengths of 0.9 and 1.5 meters and were always fired on the first delay of the round. Figure 10 shows the layout of the drifts which are relatively close together giving extraction rates of 67 to 75% in the sill.

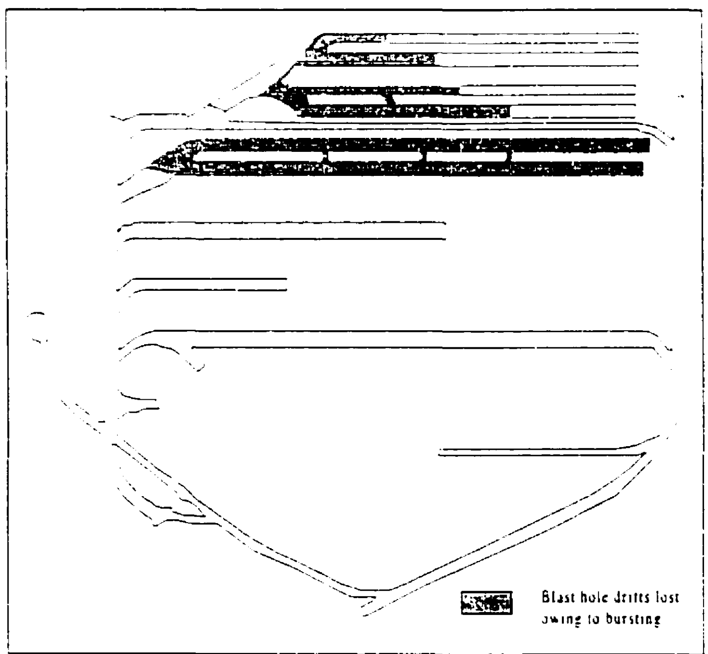

Figure 3.7b: Sill-cut MC&F units on 2073m level at Inco's Creighton Mine (O'Donnell, 1992)

The first attempt at the 2073 level, over the hangingwall block had the drifts and stopes running parallel to the major principal stress. Minimal destressing using only two top-corner holes the same length as the round drilled (3 m ±) outward at 30 degrees gave inadequate results forcing the abandonment of this area in 1979. Sill drifting was resumed over the cut-and-fill blocks with no change in the support but with the addition of two face perpendicular destress blastholes at mid face, two rounds long (6 meters), loaded with 1.5 meters of ANFO at the bottom. While better results were obtained, minor bursts occurred and additional destress blastholes were added in the pillars between the drifts, drilled horizontally 3 meters long at mid-wall at 45 degrees to the direction of driving, the bottom 0.9 meters being loaded with ANFO. Certain problems were encountered executing the face perpendicular destress blastholes due to the necessity of drilling using two diameters (54 and 43 mm).

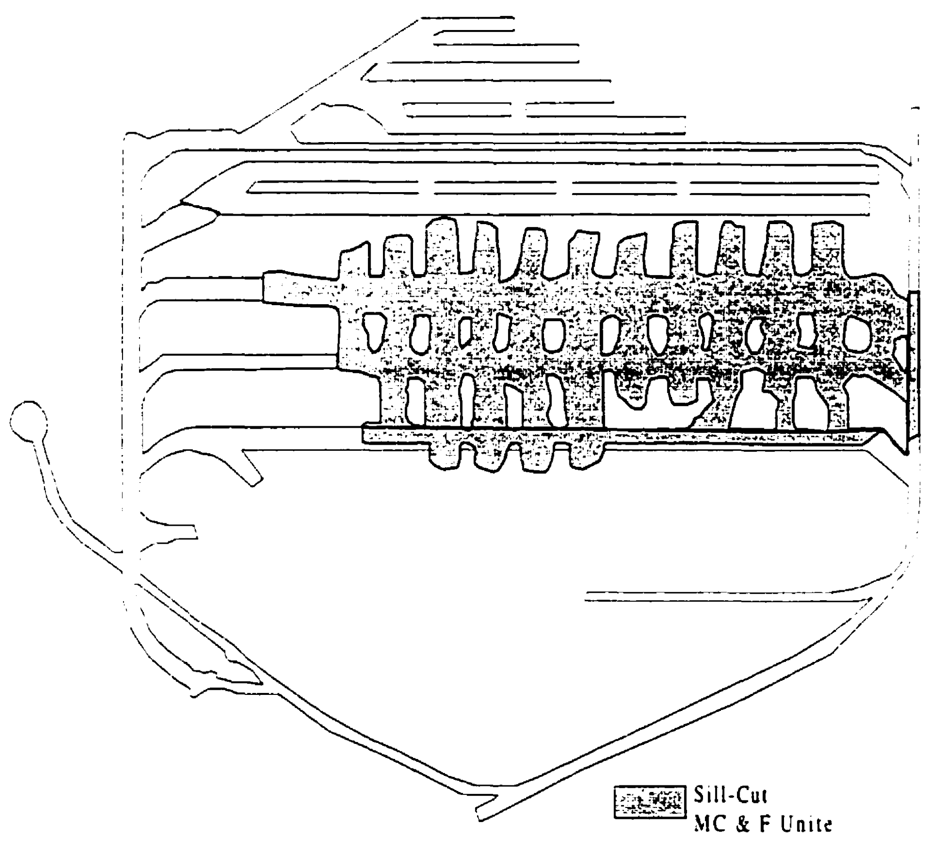

Figure 3.7c Blasthole drifts on 2073m level lost Mine owing to bursting at Inco's Creighton (after O'Donnell, 1992)

Bursting continued, 14 bursts releasing 210 tons of failed ore and causing delays, subsequent to further production development in the drifts (mining footwall slots and tram drifts) so the support was increased. The mesh was carried to the floor and the mechanical bolts were replaced with 1.7-meter split sets and 1.8-meter resin grouted rebars. This combination of increased destressing, pillars considered not destressed enough being reblasted, and increased support finally gave very good results with most of the bursts occurring with the blasts.

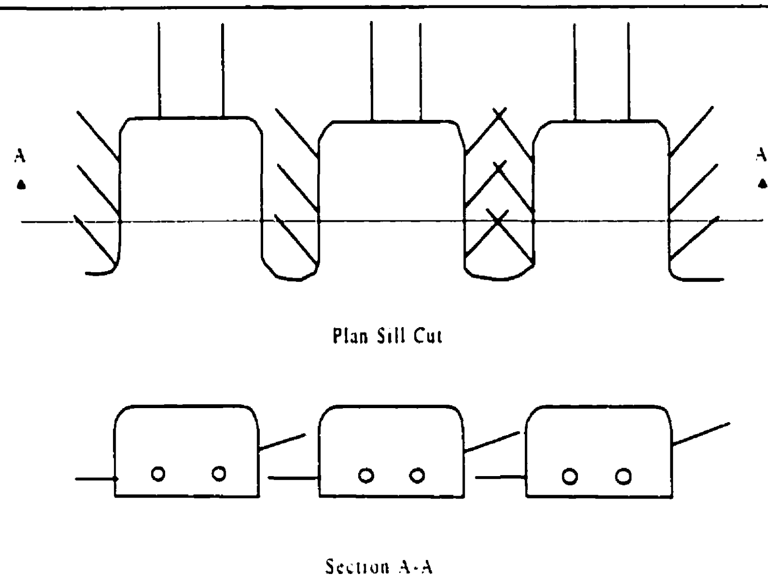

Figure 3.8a Destress patterns of MC&F units on 2073 m level (after O'Donnell, 1992)

The same procedure was adopted for the 2134 level sill drifting. In addition, the mining of the stope drifts would proceed en echelon and the additional development and pillar isolation would be done at the end of the week to allow a weekend for stress readjustment and bursting. During 2134 level sill mining only one of eleven bursts releasing 214 tons of failed ore, occured during working hours. Cut-and fill stope mining was carried out to crown pillar failure and VRM mining used to mine the crowns. The 2195 level sill mining followed the 2134 level procedures with adjacent drift faces en echelon being carried three rounds (3 x 3.6 meters) apart. Four additional destress blastholes for a total of 10 per round were used, two for the bottom face corners and two in the pillars due to the increased pillar height. ANFO loading in the corner and pillar holes was reduced from 0.9 to 0.6 meters. Support was also increased in two stages using mechanical bolts (backs) and split sets (ribs) in the first stage (1.2 x 0.6 meter pattern) and, when convergence had stabilized, stiffer resin grouted rebar on a 1.2 meter square pattern in the backs. Large back spans and high ribs were cable bolted.

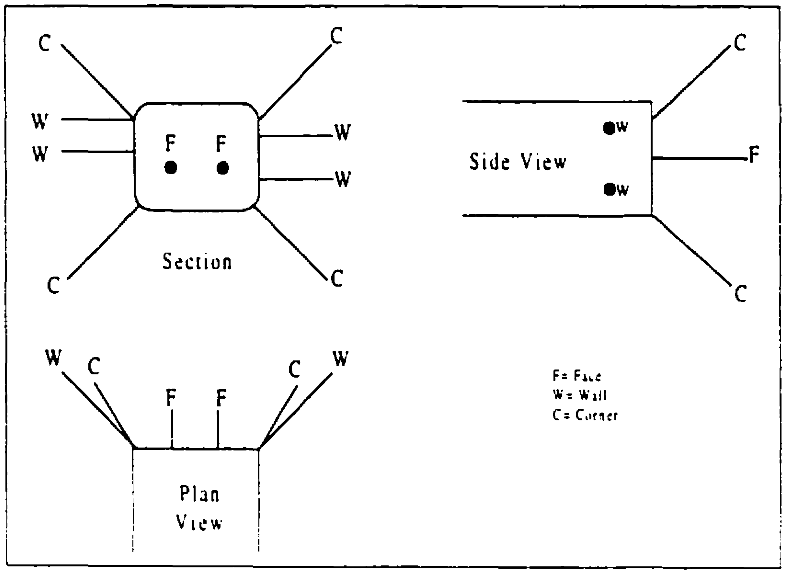

Figure 3.8b Drift destressing patterns, 2195m level, Creighton mine (after O'Donnell, 1992)

VRM mining, to June 1991, was used exclusively for the 2134 – 2195 stopes with the center stope being first and the only one having a crown pillar. These latest procedures resulted in no lost time due to bursts and 85% occurring with the blast. Breakthrough destressing, when drift faces from opposite ends of a drift are four rounds (14.6-meters ±) apart, was used. This involves drilling 7.3-meter face perpendicular blastholes in each drift face and blasting the bottom 3.7-meters in each.

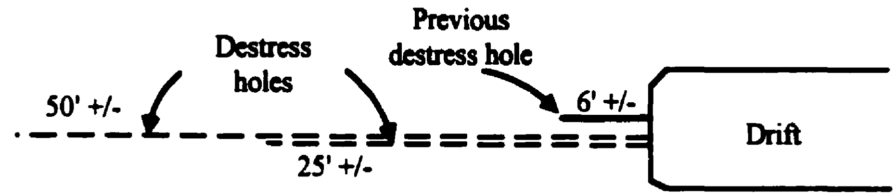

Figure 3.8c Development heading destressing at Inco (after Dickout, 1963)

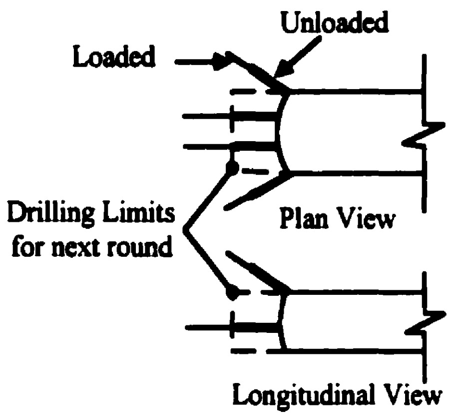

Figure 3.8d Development heading destressing at Inco (after Oliver et al.,1987)

3.4.5 Destress blasting at Campbell Red lake mine, (Makuch et al., 1987), (Figure 3.9)

This report is mainly concerned with the mathematical analysis of a destress blast similar to the previous trial. Monitoring methods are similar with the addition of blast vibration monitoring. All destress blastholes were fired on the same delay using a powder factor of 0.7 kg/m^3 as opposed to the 'normal' production powder factor of 2.1 kg/m^3. Blastholes were 45mm diameter on 1.4 meter centres with 1.5 meters of stemming. Analysis neglects the gas energy of the explosive and uses a constant power law to establish stress wave energy attenuation. It was proposed that destress blasting is most effective when the pillar is close to failure or in other words preconditioned.

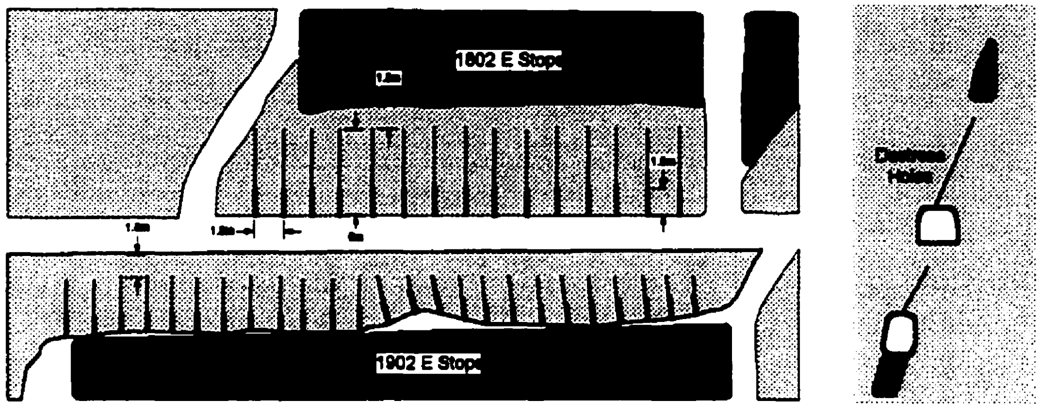

Figure 3.9 Layout of distress holes in the 1902 and 1802 crown and sill pillars at the Campbell Mine (after Makuch et al., 1987)

3.4.6 Destress blasting experiments at the Pyhäsalmi mine Finland, (Hakami et al., 1990)

This report describes three tests of destress blasting done on the center plane of stope pillars some 10 m thick by 5 m wide, between levels 645 and 660 for the first two tests and levels 615 and 630 for the third test. The first two tests used 89 mm diameter blastholes about 10 meters long while the third used 64 mm blastholes about 11 m long. The blastholes broke through from level to level. The explosive used was a cap sensitive TNT sentisized slurry of 1460 kg/m^3 and 7200 m/s velocity. In the first two tests it was poured into the blastholes while the third test used cartridges of a similar explosive. Blast hole spacing for the first test was 0.8 m and 0.5 m for subsequent tests.

Instrumentation used included rock bolt load cells, vibrating wire strain cells, extensometers, an endoscope and a seismograph for the third test. Diamond drilling was used to sample the rock adjacent to the tests before and after the blasting. RQD values were calculated for these test holes. Inspection holes were included along with the blastholes and in the same plane.

Results of these tests were considered inconclusive but promising. While there were many instruments installed, little data from these are given in the report. The reader is referred to other internal reports by one of the authors. Modulus and strength data, which show significant destressing effect, is given for the first test taken from the diamond drill core but not fit the other tests. Serious damage was done to the drift floors and backs (cratering) because no stemming was used in most of the blastholes. The endoscope inspection results are given in detail but it seems this was not done before-and-after. While it seems that cracking extended between the blastholes (not confirmed), cracking was also noted perpendicular to the plane of the blastholes. This confirms the beliefs of this author as well as those expressed by INERIS in France. Inspection holes in the test plane showed damage and breakouts after the blasts. In the second test, which was more extensive as all holes were not fired at once, the holes were blocked and required redrilling after the first blast. It was felt that the test zone was not as highly stressed as other area of the mine due to the fact that breakouts did not occur in the test blastholes as is common in other areas. This may have had a significant effect on the possibility of getting reliable results from the instrumentation. RQD values generally but not always showed deterioration after blasting.

3.5 CONCLUSION

Of all the case histories the South African-SIMRAC trials appears to be the most carefully executed and monitored. Observations of damage around fully charged and fully confined blastholes show that considerable powdery fines are produced which will inhibit gas flow. Gas expanded fractures around blastholes should also show signs of propping by fine particles swept into the fracture by the gas flow. Crushing and powdering of the rock has been definitely observed as reported by the USBM report.

One thing clearly identified in the SIMRAC report is the displacement on existing, appropriately oriented, fracture planes which coincides with modulus softening and convergence measurements. Understanding how to create this condition using explosives may well be the key to the success of destress blasting.

The mental picture one has of the destress blasting effect on rocks is that they are 'softened'. Practically, this refers to a reduction of the modulus so that the blasted rock can only support a reduced load with respect to the neighbouring rock. The SIMRAC report states that these failure planes exhibited gouge zones after destress blasting when no gouge existed before.

The principal monitoring methods are visual observation of fracture patterns, convergence and seismic event measurement and location. In addition, blasting vibrations, measurement of absolute stress and stress change, ground penetrating radar, tomography and the usual geomechanical rock properties have all been proven useful in preparing and analysing destress blasting trials. Digital recording of seismic events should be carried out at the highest sampling rate possible so as to be able to evaluate the seismic energy content of the event.

Destress blasting is considered successful when it succeeds in triggering a major seismic event in or near the destressed area immediately after the blast and/or no important seismic events causing delays occur during the mining process. The magnitude of the seismic event recorded at the time of the blast should be at least equal to the explosive energy in the blast. The results reported by INCO, gained over twelve years of mining, confirm the previous comments and conclusions that a better understanding of the mechanisms involved in bursting and destressing will lead to better numerical modelling and the prediction of the most cost effective solution.

CHAPTER 4

EVALUATION BURST POTENTIAL USING MINING INDUCED ENERGY

4.1 INTRODUCTION

Before a destress blasting program is commissioned, it is important first to assess the need for it. As a strainburst control technique, destressing can only be useful and effective if the mining zone in consideration was highly prone to burst. As mentioned earlier in Chapter 3, several techniques and methods have been developed since the sixties in an attempt to assess rockburst potential of underground rock structures. Several of these techniques are based on the energy balance around excavations. Among those is the Energy Release Rate (ERR) that was developed in South Africa (Cook et al., 1966). With the evolution of numerical modeling tools over the past decades, this technique, along with similar concepts, has been often used in the assessment of rockburst potential (e.g., Cook, 1978; Bolstad, 1990, Mitri et al., 1993; Mitri, 1996a).

A simple methodology to assess strainburst potential using a finite element modeling approach is presented in this Chapter. It leads to the calculation of the ERR and another index called the total mining induced energy storage rate or ESR. The calculations take into consideration the geomechanical properties of the rockmass, in situ stress conditions as well as the mine geometry. Such energy parameters can help identify areas of higher energy release and/or storage due to mining activity, and hence the location and potential of strainbursts. Based on the energy balance approach reviewed in detail by Salamon (1970, 1974, 1983, 1984), as well as by Budavari (1983), Walsh (1977), Brady and Brown (1985), and Hedley (1992), the current methodology is developed to assess the rockburst potential of underground openings before and/or during the mining activities. The methodology follows these steps:

1. Determine in situ geomechanical data
2. Laboratory testing to determine the rock mechanical properties such as E, ν, σ_c, e_c
3. Energy analysis with the help of a numerical modeling tool.

4.2 ENERGY RELEASE RATE (ERR) AND ENERGY STORAGE RATE (ESR)

4.2.1 Energy Release Rate (ERR)—Advantages And Limitations

Based on the energy balance, an incremental approach can be used to follow the changes due to mining. The mining of an underground orebody usually implies the widening of excavations by increments. This leads to an energy release rate by unit surface (dW_r/dS), used when the opening geometry is regular, or a volumetric energy release rate (dW_r/dV), used for irregular geometry openings. Stacey and Page (1986) provided a way to evaluate, in a preliminary manner, this energy release rate (the symbol ERR is commonly used in the literature). Observations of the incidence of violent rock failures at two South African mines (5000' and 9000' deep) indicated that such failures increase with the spatial rate of energy release or ERR (Hodgson and Joughin, 1967). Salamon (1974) showed that for elastic conditions the relations among the energy components apply to any mining configuration. Also, when mining takes place in very small steps, the limiting conditions are:

$$\Delta W_t \cong \Delta U_c,\ \Delta W_r \cong \Delta U_m,\ and\ \Delta W_k \cong 0 \qquad (4.1)$$

The above relations imply that when mining takes place in very small steps, no or little seismic energy (ΔW_k) is released. Furthermore, Salamon (1983) demonstrated this point by considering a case of a circular opening subject to hydrostatic field stress; refer to Figure 4.1. As can be seen from the figure, the kinetic energy released decreases as the number of mining steps increase.

As a result, ERR became one of the most used parameters for stope design in deep underground South African mines (Cook, 1978, Spottiswoode, 1990). Although the ERR has gained wide acceptance in South Africa, Salamon (1993) pointed out that it must be used with caution, and that it can be only of limited value in combating the rockburst hazard, because:

(1) the magnitude of ERR only depends on the virgin field stress, the elastic properties of the rocks and the layout of the mining excavation, i.e. it is independent of the

geological structure, the presence of flaws (discontinuities) in the rock mass and the potential instability of these flaws,

(2) ERR alone is unable to recognize failure. The latter reason has been a motivating factor for the present development of a new theory for the calculation of the so-called Burst Potential Index (BPI), based on energy considerations, which is described herein.

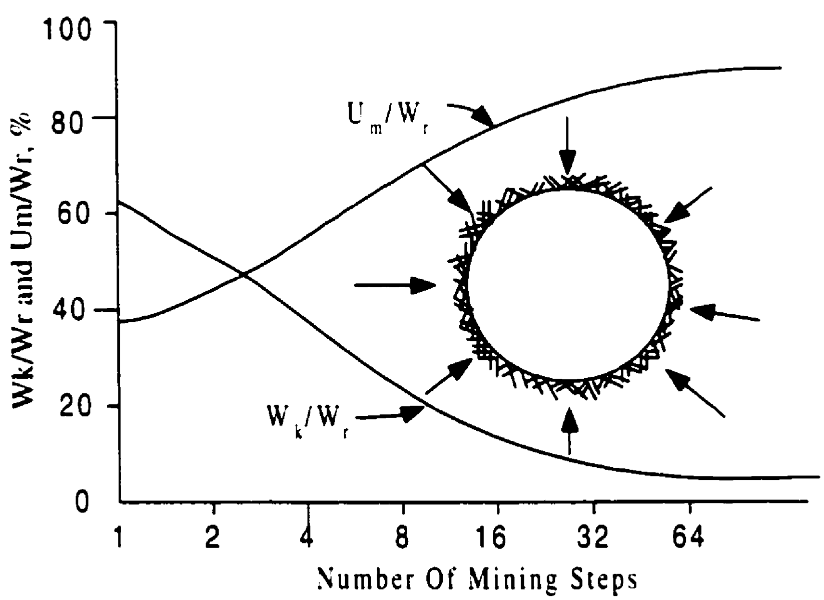

Figure 4.1 Variation of energy released with the number of mining steps (after Salamon 1983)

4.2.2 Present Approach

The need to better understand rockburst phenomena, particularly pillar and strainbursts, has motivated the researchers to expand on the concept of mining-induced strain energy density around mine cavities (Mitri *et al.*, 1993). Referring to Figure 4.2, the premining state of stress before any excavation is made is σ_0. These stresses are in balance with the initial external loading P_0 representing the body forces in the rock mass, or simply its own weight in this case. The loading of the problem is initiated by the unbalance created by the removal of the rock mass inside the boundary. The initial stresses stored in the excavated volume disappear (due to mining) and as a result, an out-of-balance load,

$\Delta P = P_1 - \int B^T \sigma_0 dV$, is induced. This induced load causes displacements u_1, strains ε_1, and stresses σ_1 around the excavation in order to reach state of equilibrium as per the following relation:

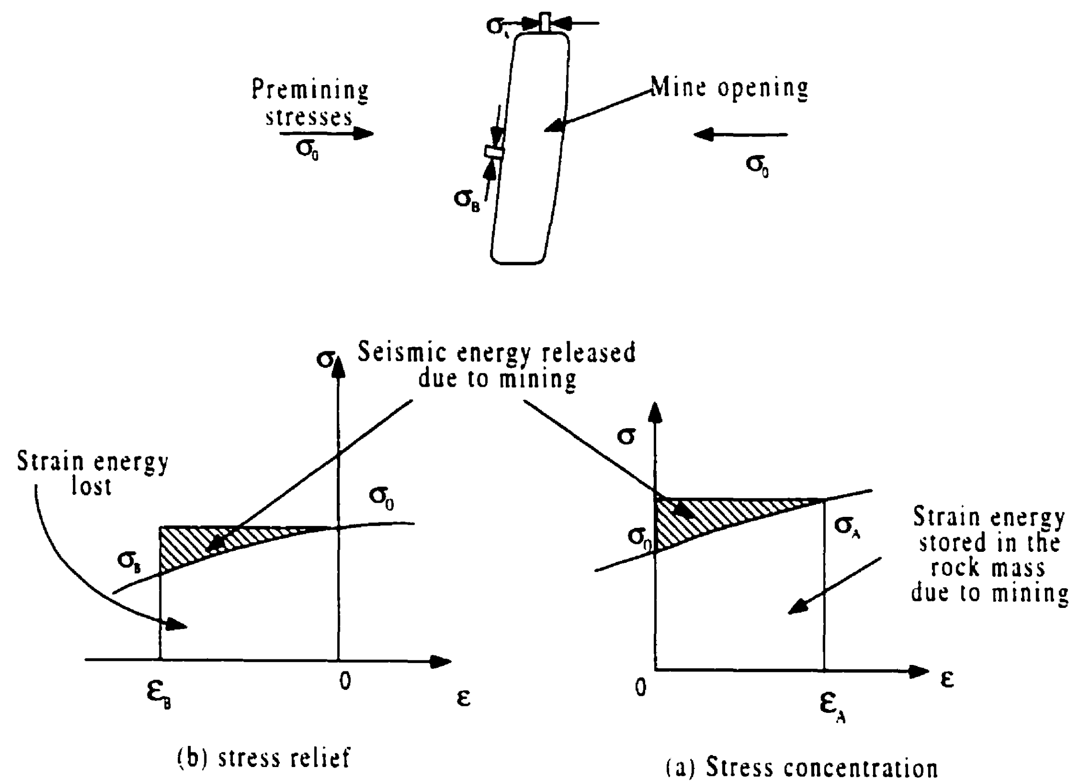

Figure 4.2. Definition of mining-induced energy components (after Mitri et al., 1999)

$$P_1 = K_1 u_1 + \int B^T \sigma_0 dV \qquad (4.2)$$

where, in finite element terms,

P_1 = external loading representing body forces in the rock mass

K_1 = stiffness matrix of elements in the surrounding rock mass

B = element strain-displacement matrix

σ_0 = initial (in situ) stresses

When equilibrium is reached, the external load P_1 becomes in balance with the induced internal stresses $\sigma_{ind} = \sigma_1 - \sigma_0$, i.e.

$$P_1 = \int B^T(\sigma_1 - \sigma_0)dV + \int B^T \sigma_0 dV \tag{4.3}$$

Multiplying both sides of Equation (4.3) by the displacements u_1, one obtains the work done by induced load $u_1^T P_1$, or W in Equation (2.8). Thus the work done by the external load is

$$W = \int \varepsilon_1^T(\sigma_1 - \sigma_0)dV + \int \varepsilon_1^T \sigma_0 dV \tag{4.4}$$

Part of the work is stored as strain energy due to induced stresses, e_1, in the surrounding rock mass. This can be easily shown to be given by:

$$e_1 = \frac{1}{2}\int \varepsilon_1^T \sigma_{ind} dV \tag{4.5}$$

As appears from Equation (4.4), the strain energy caused by in situ stresses σ_0 in the surrounding rock mass, e_2, can be expressed as

$$e_2 = \int \varepsilon_1^T \sigma_0 dV \tag{4.6}$$

Hence the total energy stored in the surrounding rock mass, U_c (Equation 2.8), due to mining, is $e_1 + e_2$ and the storage rate, ESR, is

$$ESR = \frac{d}{dV}(e_1 + e_2) \tag{4.7}$$

Since body forces existed before any excavation took place, the kinetic energy released, W_k, in this process must cause a seismic effect, and thus be referred to as "seismic energy release". Applying Equation (2.12) can form this:

$$e_r = W - (e_1 + e_2) \tag{4.8}$$

which, after substitution gives

$$e_r = \frac{1}{2}\int \varepsilon_1^T(\sigma_1 - \sigma_0)dV \qquad (4.9)$$

Thus the seismic energy release rate, ERR, can be obtained from

$$ERR = \frac{d}{dV}(e_r) \qquad (4.10)$$

To summarize, the total strain energy stored in the surrounding rock mass due to a mining step, U_c, is equal to $e_1 + e_2$, while the seismic energy released, e_r, is given by Equation (4.8). The summation of all energy components is then $e_1 + e_2 + e_r$ as illustrated in Figure 4.2. This can be shown to be equal to the work done by the body forces or the own weight of the surrounding rock mass, W, which is calculated from:

$$W = \int u_1^T \gamma \, dV \qquad (4.11)$$

where γ is the body force per unit volume.

4.3 EFFECT OF MINING SEQUENCES

Let us now suppose that the excavation of Figure 4.2 is to be created in two steps, as illustrated in Figure 4.3. Since the behaviour of the rock mass is linear elastic, the state of stress and strain at the end of the two mining steps must be the same as when mining in one step. Moreover, the total strain energy stored in the rock mass should be the same. However, the amount of seismic energy released is significantly smaller when mining in two steps. From Equation (4.9), it can be seen that the seismic energy released in the first mining step is:

$$e_r^1 = \int \frac{1}{2}(\sigma_1 - \sigma_0)\varepsilon_1 dV \qquad (4.12)$$

whereas mining in the second step results in the release of:

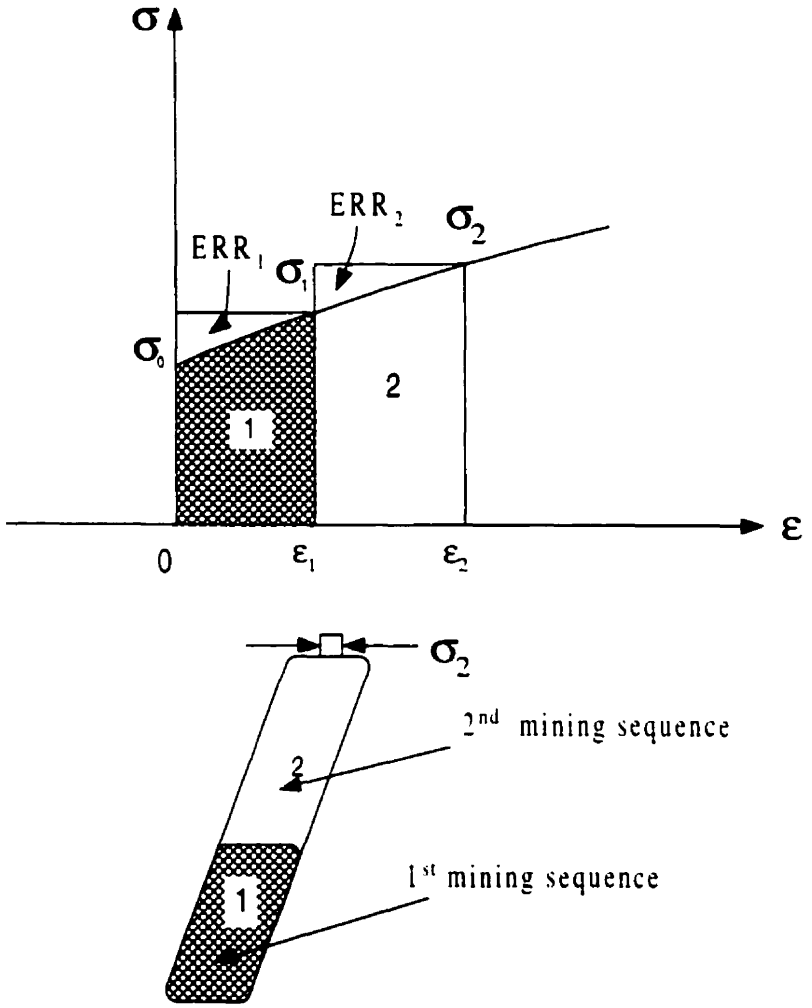

Figure 4.3 Energy components when mining in sequences (after Mitri et al., 1999)

$$e_r^2 = \int \frac{1}{2}(\sigma_2 - \sigma_1)\varepsilon_2 dV \qquad (4.13)$$

Adding the above two quantities, it can be seen that there is significantly less seismic energy released when mining in two steps than in one step. It can be shown that the reduction in seismic energy release when mining in two steps, instead of one, is given by $\int \varepsilon_1(\sigma_2 - \sigma_1)dV$.

Supposing that the occurrence of strainburst depends, at least partly, on the amount of seismic energy released due to mining, it may be concluded, in the light of the above, that the potential for strainburst hazard is reduced when mining in small steps. The hatched rectangular area shown in Figure 4.4 represents this reduction in "seismic energy".

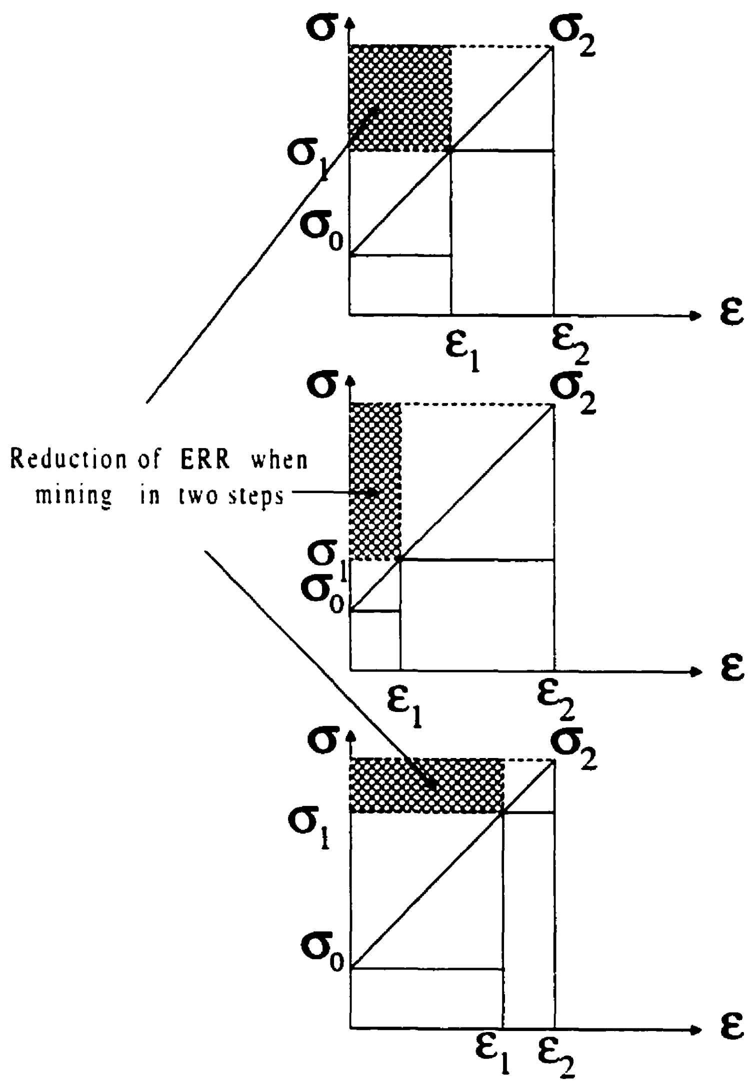

Figure 4.4 Reduction of energy released when mining in sequences (after Mitri et al., 1999)

Furthermore, the maximum reduction of seismic energy (maximum area of the hatched rectangle) can be achieved by making two mining steps leading to equal stress increments, i.e. the optimum mining sequence would be the one which satisfies the condition (refer to Figure 4.4):

$$\sigma_2 - \sigma_1 = \sigma_1 - \sigma_0 \tag{4.14}$$

Since mining is a continuous process, it is possible to design the mining sequences to satisfy the above condition. It should be noted that mining in equal size lifts does not necessarily result in equal stress (and energy) increments. In general, when mining in sequences, three strain energy components can be calculated after each mining step. These are illustrated in Figure 4.5 for ith mining step of a given mining sequence.

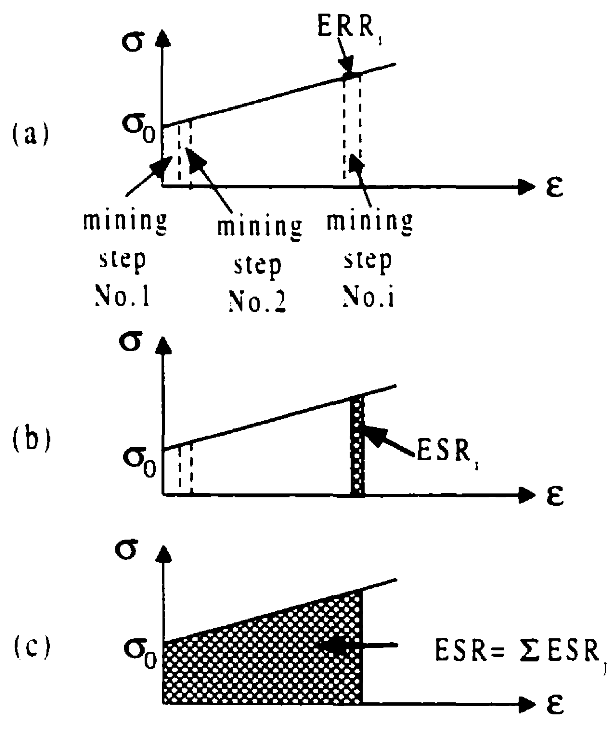

Figure 4.5 Energy components for ith mining step (after Mitri et al. 1999)

ESR$_i$ = mining-induced strain energy in the rock mass after a given mining step, = $\frac{d}{dV}(e_1 + e_2)$;

ERR_t = energy release rate after a given mining step;

ESR = total mining-induced strain energy stored in the rock mass from the beginning of the mining process.

4.4 BURST POTENTIAL INDEX (BPI)

The present approach permits the calculation of mining-induced energy stored in the rock mass. Following the line of thought that rockburst is due to sudden release of energy from a volume of highly stressed rock, it can be supposed that violent failure will take place when the energy stored in the rock mass exceeds a critical value, thus rendering the rock material to its post-peak (unstable) range. In a uniaxial test the recoverable energy, E_R, is determined by the triangular area defined by $\frac{1}{2}(\sigma_c + \sigma_0)\cdot(\varepsilon_p - \varepsilon_0)$, where E is the tangent modulus. The critical energy, e_c, is then defined by the portion of the recoverable

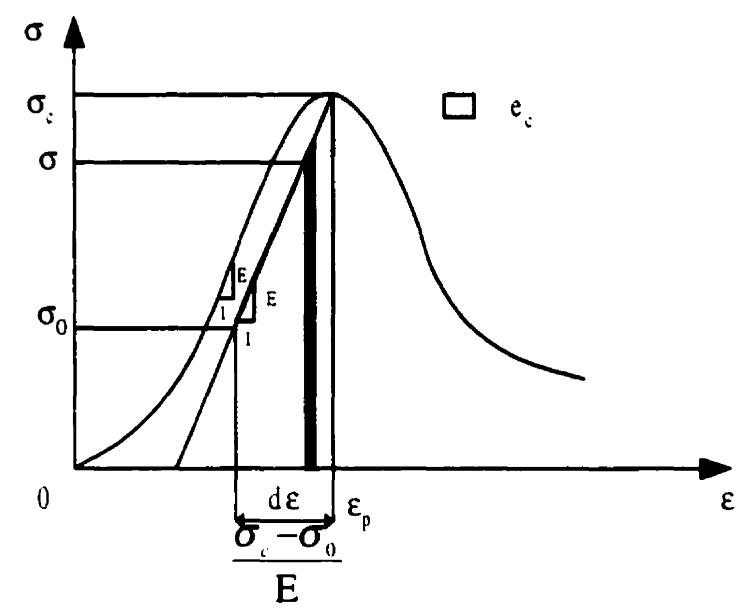

Figure 4.6. Definition of critical energy stored in a uniaxial test

energy which is bounded by the initial stress σ_0 and the peak stress σ_c, as shown in Figure 4.6. Thus:

$$e_c = \frac{\sigma_c^2 - \sigma_0^2}{2E} \tag{4.15}$$

where ε_p, is the uniaxial peak strain, and ε_0, is the premining strain. A burst potential index (BPI), can then be defined as,

$$BPI = \frac{ESR}{e_c} \times 100\% \tag{4.16}$$

It may be argued that the above burst potential index calculation is limited in its application to the uniaxial loading condition, which is not the case inside the rock mass surrounding the mine stopes. While this is theoretically true, strainburst problems in reality are often associated with failure which takes place at the pillar skin, or at least is triggered at the skin, where stress concentration, as well as energy stored are the highest. In such cases, the state of stress at the skin is biaxial, and violent failure will be controlled by the major principal stress, σ_1, parallel to the excavation boundary (since the stresses normal to the boundary must be zero). Also, it is to be noted that equations (4.15) and (4.16) consider not only the strength of the rock (σ_c), but also its ability to deform (E); and hence its "strain energy storage capacity". This aspect is thought to be important in the assessment of rockburst potential, and in effect, more representative than conventional rock failure criteria, which consider only the rock strength parameters.

All the equations deduced in the model are based on linear elastic rock behaviour. Actually, around mine openings, there exist naturally fractured zones as shown in Figure 3.1. Part of the ESR in Figure 4.4 will be released through fracturing the surrounding rock, which actually is a time-dependent phenomenon (COMRO,1988). The fracturing leads to the increase of energy released, but the seismic released energy has not been changed. That means the formation of the fractured zone in computing the ERR can be neglected. The computed ESR value in this model is higher than the value in reality, and so is the BPI, i.e. it is conservative from design point of view.

4.5 CASE STUDY

The BPI theory described above has been implemented in 2-dimensional and 3-dimensional finite element codes. The 3-dimensional code is new, and is developed by the author. This is described, together with a new theory for destress blasting in Chapter 5. An existing 2-dimensional code called ***e-z tools/2D***, has been developed to implement the BPI theory. ***e-z tools/2D*** perform static analysis of linear elastic materials. It has been used exclusively in rock mechanics applications. Detailed information on the ***e-z tools/2D*** is available elsewhere (Mitri, 1993).

In the following, a case study is presented to demonstrate the application of the BPI to underground opening. The 2-dimensional code is used herein. Figure 4.7 shows the vertical section of a cut-and-fill stope in a Canadian mine. The mine uses conventional and mechanized cut-and-fill methods, and also does some long hole mining. In the cut and fill method, ore is removed in small lifts of approximately 1.80 m and the stope is

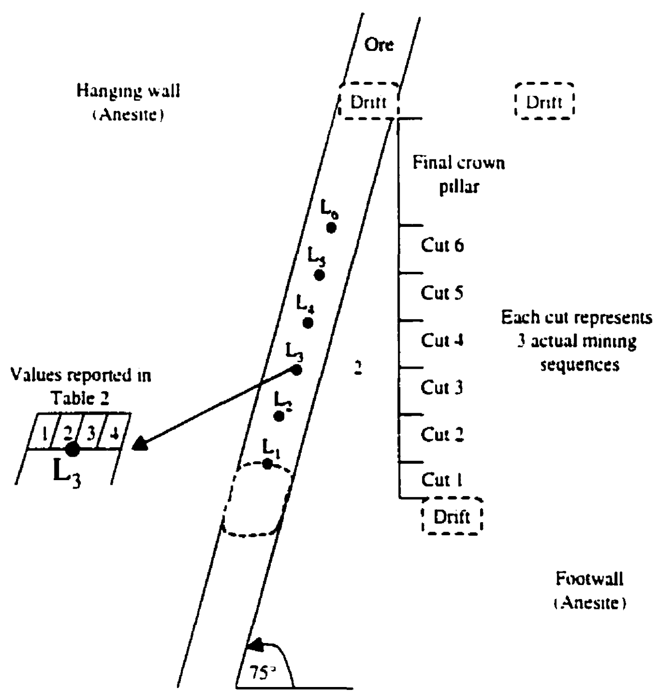

Figure 4.7 Cross-section of a cut-and-fill stope 18-1361 Goldcorp's Red Lake Mine

then filled with hydraulic backfill. The mine reported a crown pillar failure shortly after the removal of the last (18th) mining lift. Production was stopped subsequently and the stope was abandoned.

The geology of the section analysed comprises the ore body, a mineralized sulphide vein, which is 6-feet wide, dipping at 75°. Both the footwall and hanging wall are andesite. Although there are 18 mining lifts that took place in the stope, numerical modeling was carried out by simulating eight mining steps as follows: six mining steps representing 18 lifts by grouping every 3 lifts into one mining step, plus two other mining steps to simulate the initial conditions and access drifts. These are presented in Table 4.1

Table 4.1 Model sequences

First	Static analysis of the model with no excavations.
Second	The overcut and the two footwall drifts.
Third	First mining cut simulated. The first cut of the stope is mined.
Fourth	Second mining cut simulated. The second cut of the stope is mined.
Fifth	Third mining cut simulated. The third cut of the stope is mined.
Sixth	Fourth mining cut simulated. The forth cut of the stope is mined.
Seventh	Fifth mining cut simulated. The fifth cut of the stope is mined.
Eighth	Sixth mining cut simulated. The sixth cut of the stope is mined.

At each step of the analysis, stresses, displacements and strain energy parameters (ERR, ESR) are computed at the centre of each element in the mesh. A gradual increase in the strain energy storage rate around the excavation is expected between excavation step1 and step5, the change in ESR between step 6 and step 8 is expected to be significantly greater as we reach the lower skin of the crown pillar.

4.5.1 Geomechanical Properties

The relevant geomechanical properties of the rock masses used in this analysis are shown in Table 4.2.

Table 4.2. Geomechanical Properties

Properties	Mineralized sulphide vein	Andesite
Unit weight γ	0.027 MN/m^3	0.029 MN/m^3
Poisson's ratio ν	0.20	0.28
Elastic modulus E	76 Gpa	80 GPa
Uniaxial strength σ_p	180 MPa	174 MPa

4.5.2 In Situ Stresses

The principal stresses at the Red Lake Mine are summarized below. The strike of the ore is generally N126°E and dips 64° SW.

- $\sigma_1 = 8.80 + 0.0422$ MPa /m of depth perpendicular to strike of the ore body
- $\sigma_2 = 3.64 + 0.0276$ MPa /m of depth parallel to strike of the ore body
- $\sigma_3 = 0.029$ MPa /m depth

Thus, the natural stress tensor at depth of 981m can be calculated as:

- $\sigma''_x = 31.83$ MPa
- $\sigma''_y = 52.001$ MPa
- $\sigma''_z = 33.779$ MPa (out of plane of the section)

The material properties for both types of rock in the model were considered homogeneous, isotropic and linearly elastic. The influence of hydraulic backfill was assumed to be negligible. This is a reasonable assumption as already stated by others (e.g. Mitri, 1996a; Lu et al., 1993). From the above data, the critical strain energy storage, e_c, (Equation 4.15) is calculated for each mining step in the analysis.

4.5.3 Results and Discussion

ESR and BPI results at 6 monitoring levels L_1 to L_6 along the stope successive backs were monitored as shown in Figure 4.8. Level L_6 is the centre of the skin element at the bottom of the final crown pillar and level L_1 is the centre of the skin element at the top of cut # 1. The intermediate levels, L_2, L_3, L_4, and L_5 are located at the centre of the upper skin element of cuts # 2,3,4,5.

The values of ESR and BPI at these points are shown in Table 4.3 for the four finite elements spanning the stope back. It can be seen from Table 4.3 that the values of the monitored locations rise gradually as the excavation approaches the final crown pillar, and substantially after cuts #5 and #6. The increase of the ESR and BPI values at monitoring points at the lower end corner of the crown pillar is noteworthy. ESR and BPI values have been used to study the failure mechanism of the crown pillar as shown in Figure 4.8 and the results are listed in Table 4.4. Considering the limitation that the present analysis is only linear elastic, and stress redistribution due to skin fracturing is not accounted for, it may be more realistic to consider the average results for the first two rows of elements in the immediate back after each cut. From Table 4.4, it can be shown that the average BPI for the entire stope back rises substantially from 102% after cut #5 to 136% after cut#6, at which point, the pillar is reported to have failed by a rockburst.

Table 4.3: ESR and BPI values in the stope back after each cut

Cut	Level	Element 1		Element 2		Element 3		Element 4	
		ESR Mj/m^3	BPI %	ESR Mj/m^3	BPI %	ESR Mj/m^3	BPI %	ESR Mj/m^3	BPI %
1	L_1	0.08	39.94	0.067	33.45	0.092	45.92	0.105	52.42
2	L_2	0.130	64.80	0.110	54.83	0.150	74.76	0.170	84.73
3	L_3	0.220	109.50	0.187	93.10	0.187	93.10	0.286	142.30
4	L_4	0.221	109.70	0.188	93.30	0.254	126.10	0.287	142.43
5	L_5	0.290	143.70	0.333	165.01	0.333	165.01	0.376	181.90
6	L_6	0.373	184.60	0.318	157.35	0.318	157.35	0.482	238.50

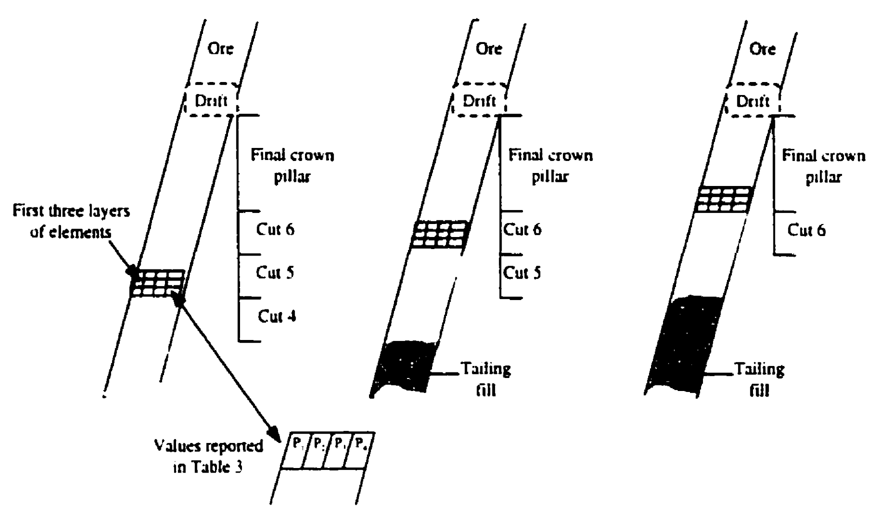

Figure 4.8 First three layers of elements

4.5.4 Conclusion

A simple numerical modelling technique is presented and employed to assess the strainburst potential in a cut-and-fill mine stope. From the results obtained, it can be seen that the BPI is a useful tool in predicting crown pillar strainburst in cut-and-fill mining. It was shown that as the mining sequence progresses upwards thus reducing the size of the pillar, the magnitudes of ESR and BPI increase. Those were particularly highest at the corners of the stope back, which indicates a possible shear failure mechanism. The average burst potential index (BPI) in the bottom two rows of elements in the crown pillar is 136%, after cut #6, when it actually failed by a rockburst. The present analysis is only linear elastic. A more realistic approach is to consider a time-dependent analysis, which will consider the progressive development of skin extension fractures at the stope back.

Table 4.4. ESR and BPI in the crown pillar for cut 4, 5 and 6

Cut	Layer	P_1		P_2		P_3		P_4	
		ESR Mj/m^3	BPI %	ESR Mj/m^3	BPI %	ESR Mj/m^3	BPI %	ESR Mj/m^3	BPI %
4	3	0.060	29.80	0.060	29.80	0.028	13.90	0.028	13.90
	2	0.093	46.20	0.093	46.20	0.060	29.80	0.093	46.20
	1	0.222	110.20	0.190	94.30	0.255	126.60	0.287	142.40
5	3	0.092	45.60	0.092	45.60	0.090	44.60	0.052	25.77
	2	0.133	65.90	0.133	65.90	0.114	56.50	0.133	65.90
	1	0.295	146.20	0.214	106.10	0.254	125.90	0.376	186.32
6	3	0.066	32.66	0.118	58.390	0.118	58.390	0.066	32.66
	2	0.158	78.18	0.158	78.180	0.104	51.460	0.158	78.18
	1	0.381	188.52	0.330	163.29	0.431	213.30	0.482	238.50

CHAPTER 5

PROPOSED NUMERICAL MODEL FOR DESTRESS BLASTING

5.1 INTRODUCTION

This chapter describes a 3-dimensional numerical modeling technique for the simulation of destress blasting in hard rock mining operations at depth. The technique employs two newly introduced parameters, α, a rock fragmentation factor, and β, a stress dissipation factor, inside the modeled, fractured zone. The model is based on the theory presented in Chapter 4 to help assess strainburst potential and hence, the need for a remedial solution such as drift destressing. Basically, when the burst potential index (BPI) approaches or exceeds 100%, the method suggests that rockburst is imminent and destress blasting may be required. Destress blasting is simulated by modifying the deformation properties of the rockmass and the post-blast state of stress in the destressed zone using the above mentioned parameters α and β. The technique, based on incremental analysis, permits the simulation of actual mining activities, i.e. mining and destressing.

5.2 NEW GEOMECHANICAL MODEL FOR DESTRESS BLASTING

Destressing is a technique that aims to reduce the stress field in the rock mass immediately ahead of the mining face to reduce the potential of face burst. This is achieved by blast-induced fractures resulting in a release of strain energy in the fractured zone.

Destress blasting in mine development has been applied in zones of high stress in brittle rock. The driving of development headings, raises and shafts is often accompanied by rock noise due to popping, spalling and occasionally face ejection rockbursts. This is often caused by high stress and energy concentrations in the face. The problem is usually alleviated by drilling and blasting long holes ahead of the face and in the pillars between multiple headings.

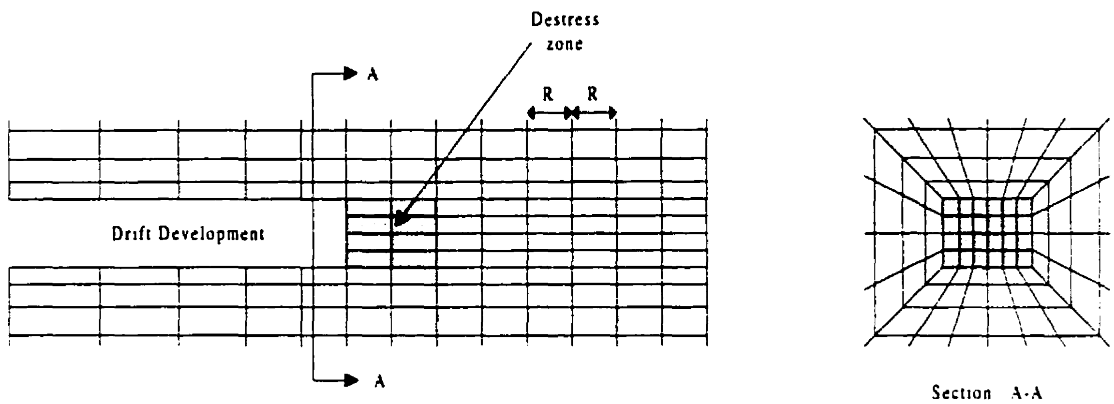

Figure 5.1 Finite element mesh for a drift development

Figure 5.1 shows the finite element mesh of a drift development in elevation and cross section. The first step required is to calculate the stress and energy parameters for the initial conditions (Figure 5.2a). If the initial conditions indicate the need for destressing, then destress blasting will be carried out. To model the destressed area, based on the idea that the rock is to be 'softened', we introduce the rock fragmentation factor $\{\alpha\}$, which ranges from 0 to 1. This means that the rock property in the destressed zone is reduced from E_i to E_{Di}

$$E_{Di} = \alpha_i \times E_i \qquad (5.1)$$

or $\{E_D\} = \{\alpha\}^T \cdot [I] \cdot \{E\}$

Where $\{\alpha\}^T = \{\alpha_x, \alpha_y, \alpha_z\}$, $\{E\}^T = \{E_x, E_y, E_z\}$, $[I]$ is the 6×6 unit matrix.

The stress dissipation factor $\{\beta\}$ in the destressed zone is also introduced. It represents the instantaneous drop in stresses due to blasting. Thus, the residual stress in the destressed zone immediately after blasting, σ_{Di} can be expressed as:

$$\sigma_{Di} = (1-\beta_i) \times \sigma_i. \qquad (5.2)$$

or $\{\sigma_D\} = \{1-\beta\}^T \cdot [I] \cdot \{\sigma\}$

where $\{\sigma\}^T = \{\sigma_x, \sigma_y, \sigma_z, \tau_{xy}, \tau_{yz}, \tau_{zx}\}$ is the mining induced stress before destressing,

and $\{1-\beta\}^T = \{(1-\beta_x), (1-\beta_y), (1-\beta_z), (1-\beta_{xy}), (1-\beta_{yz}), (1-\beta_{zx})\}$

To fulfill the task required above, we must first define the zone or finite elements to be destressed and the factors {α} and {β}. In practice, in situ measurements, such as dilatometer, extensometer, microseismic monitoring, should be used to help determine appropriate value for {α} and {β} and the extent of the destressed zone.

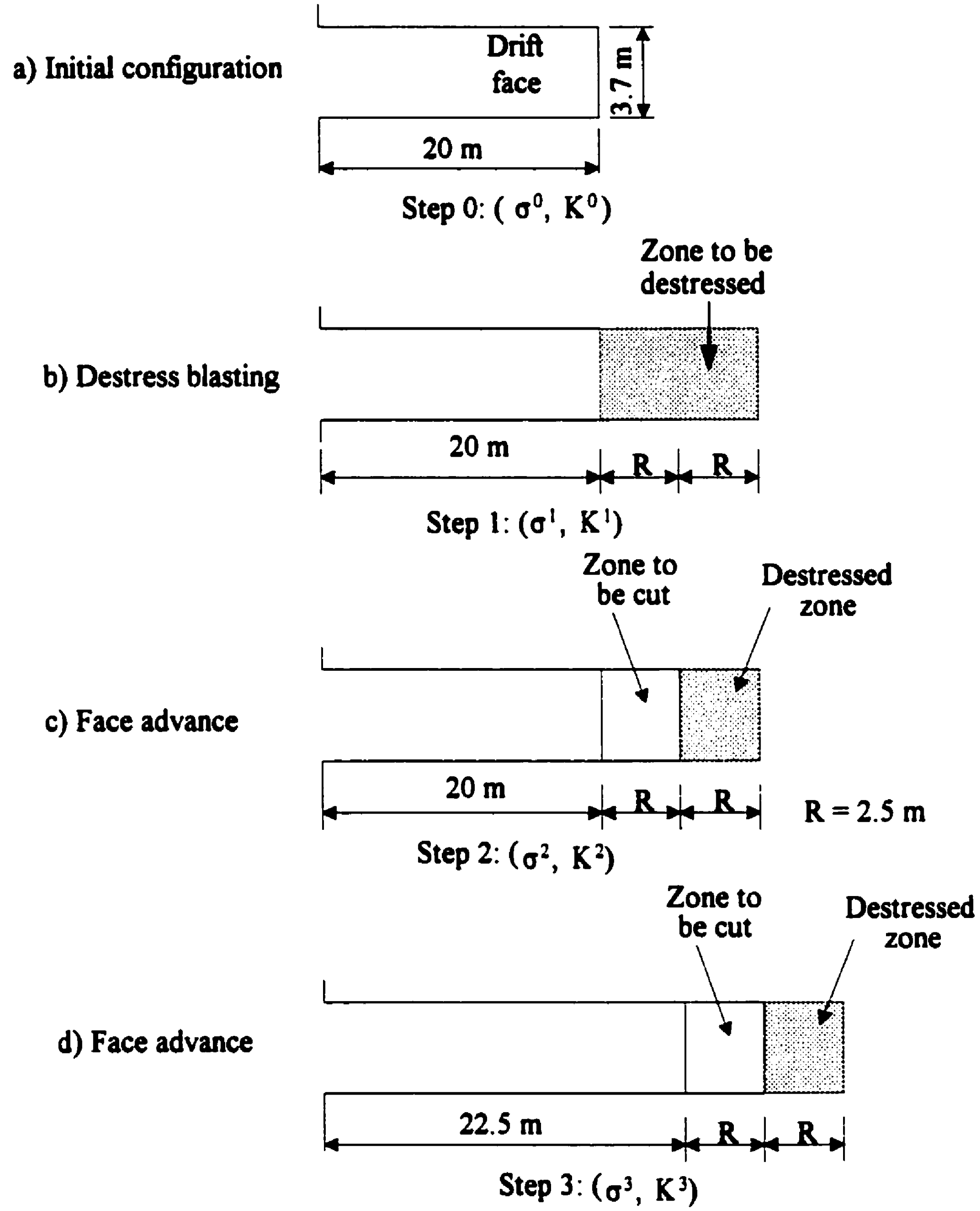

Figure 5.2 Steps for modeling destress blasting and face advance

Based on the modified rock properties and stresses, we can reconstruct the global stiffness matrix [K^1] and the load vector {ΔP}. The element stiffness matrix of the destressed zone is reduced to:

$$[K^1] = \int_V [B]^T \cdot [D_D] \cdot [B] \cdot dV \tag{5.3}$$

where [D_D] is the stress strain relationship matrix of all elements in the destressed zone and the load vector {ΔP} is calculated from the following equation:

$$\{\Delta P\}^1 = \int_V [B]^T \cdot (1-\beta)\sigma' \cdot dv \tag{5.4}$$

As shown in Figure 5.2c, the next step is to model the face advance. The stiffness matrix is updated according to the following equation;

$$[K^2] = [K^1] - [K^m] \tag{5.5}$$

where [K^m] is the stiffness matrix of all elements in the zone which is mined out. The new load vector resulting from the removal of elements in the zone mined out is solved by

$$\Delta P^2 = \int_V [B]^T \cdot \{\sigma\}^1 \cdot dV - \int_{\text{all elements removed}} [N]^T \cdot \{\gamma\} \cdot dV \tag{5.6}$$

When carrying out analysis, a global co-ordinate system (x, y, z) is generally adopted. This does not usually coincide with the coordinate system (x', y', z') introduced in Figure 5.3. The linking of the global coordinate system with the coordinate system related to the orientation of the anisotropy may be achieved using two angles. These describe the direction of a contour (strike θ) and the slope of the line of dip (dip φ) to the global coordinate system.

The stress {σ'} and the {ε'} in the coordinate system related to the orientation of the local coordinate (x', y', z') may be computed from the stresses and strains in the global coordinate system with the aid of the transformation matrices [T] and [T^*] respectively (Lekhnitskii, 1963):

$$\{\sigma'\} = [T] \cdot \{\sigma\} \tag{5.7}$$

$$\{\varepsilon'\} = [T^*] \cdot \{\varepsilon\} \tag{5.8}$$

The components of the vectors $\{\sigma\}$ and $\{\varepsilon\}$ may also be related in a similar manner to Equation 5.9 with the aid of a matrix in the case of transverse isotropy.

$$\{\sigma\} = [D]\{\varepsilon\} \tag{5.9}$$

Such a matrix is initially only valid in the chosen coordinate system (x', y', z'), and should therefore also be denoted by ', as are the stress and strain vectors in this system. Thus

$$\{\sigma'\} = [D] \cdot \{\varepsilon'\} \tag{5.10}$$

The matrices contains the angles θ and φ in the following form:

$$[T] = \begin{bmatrix} l_1^2 & m_1^2 & 0 & 2l_1m_1 & 0 & 0 \\ l_2^2 & m_2^2 & n_2^2 & 2l_2m_2 & 2m_2n_2 & 2n_2l_2 \\ l_3^2 & m_3^2 & n_3^2 & 2l_3m_3 & 2m_3n_3 & 2n_3l_3 \\ l_1l_2 & m_1m_2 & 0 & l_1m_2 + l_2m_1 & m_1n_2 & n_2l_1 \\ l_2l_3 & m_2m_3 & n_2n_3 & l_2m_3 + l_3m_2 & m_2n_3 + m_3n_2 & n_2l_3 + n_3l_2 \\ l_3l_1 & m_3m_1 & 0 & l_3m_1 + l_1m_3 & m_1n_3 & n_3l_1 \end{bmatrix} \tag{5.11}$$

$$[T^*] = \begin{bmatrix} l_1^2 & m_1^2 & 0 & l_1m_1 & 0 & 0 \\ l_2^2 & m_2^2 & n_2^2 & l_2m_2 & m_2n_2 & n_2l_2 \\ l_3^2 & m_3^2 & n_3^2 & l_3m_3 & m_3n_3 & n_3l_3 \\ 2l_1l_2 & 2m_1m_2 & 0 & l_1m_2 + l_2m_1 & m_1n_2 & n_2l_1 \\ 2l_2l_3 & 2m_2m_3 & 2n_2n_3 & l_2m_3 + l_3m_2 & m_2n_3 + m_3n_2 & n_2l_3 + n_3l_2 \\ 2l_3l_1 & 2m_3m_1 & 0 & l_3m_1 + l_1m_3 & m_1n_3 & n_3l_1 \end{bmatrix} \tag{5.12}$$

in which

$l_1 = \sin\theta$, $m_1 = \cos\theta$, $n_1 = 0$,

$l_2 = \cos\varphi \cos\theta$, $m_2 = -\cos\varphi \sin\theta$, $n_2 = -\sin\varphi$

$l_3 = -\sin\varphi \cos\theta$, $m_3 = \sin\varphi \sin\theta$, $n_3 = -\cos\varphi$.

Equation 5.7, and Equation 5.8 may be substituted in to 5.10:

$$[T]\{\sigma\}=[D']\cdot[T^*]\cdot\{\varepsilon\} \tag{5.13}$$

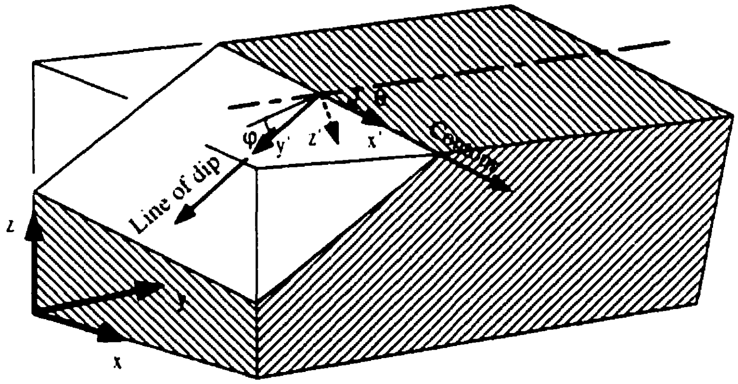

Figure 5.3 Relationship between the fixed global coordinates and those related to orientation of a local plane of isotropy

Multiplication by $[T]^{-1}$ gives

$$\{\sigma\}=[T]^{-1}[D']\cdot[T^*]\cdot\{\varepsilon\} \tag{5.14}$$

Since $[T]^{-1}=[T^*]^T$, the following is thus obtained from equation 5.10:

Where [D'] is given as:

$$\{\sigma\}=[D]\cdot\{\varepsilon\} \tag{5.15}$$

in which

$$[D]=[T^*]^T[D']\cdot[T^*] \tag{5.16}$$

Equation 5.15 describes the relationship between stresses and strains in an arbitrary global coordinate system which forms the angles ϕ and φ defined in Figure 5.3 with the coordinate system (x', y', z') related to the local. In certain circumstances the inverse of equation 5.15 is also of interest. Appropriate rearrangement yields

$$\{\varepsilon\}=[T]^T[D']^{-1}\cdot[T\ ]\cdot\{\sigma\} \tag{5.17}$$

where for the case of orthotropy in terms of stresses and both normal and shear strains in a three-dimensional element (referring Figure 5.4), $[D']^{-1}$ is defined as Equation 5.18.

$$[D']^{-1} = \begin{bmatrix} \frac{1}{E_1} & -\frac{\nu_1}{E_1} & -\frac{\nu_2}{E_2} & 0 & 0 & 0 \\ -\frac{\nu_1}{E_1} & \frac{1}{E_3} & -\frac{\nu_3}{E_3} & 0 & 0 & 0 \\ -\frac{\nu_2}{E_2} & -\frac{\nu_3}{E_3} & \frac{1}{E_2} & 0 & 0 & 0 \\ 0 & 0 & 0 & \frac{1}{G_1} & 0 & 0 \\ 0 & 0 & 0 & 0 & \frac{1}{G_2} & 0 \\ 0 & 0 & 0 & 0 & 0 & \frac{1}{G_3} \end{bmatrix} \tag{5.18}$$

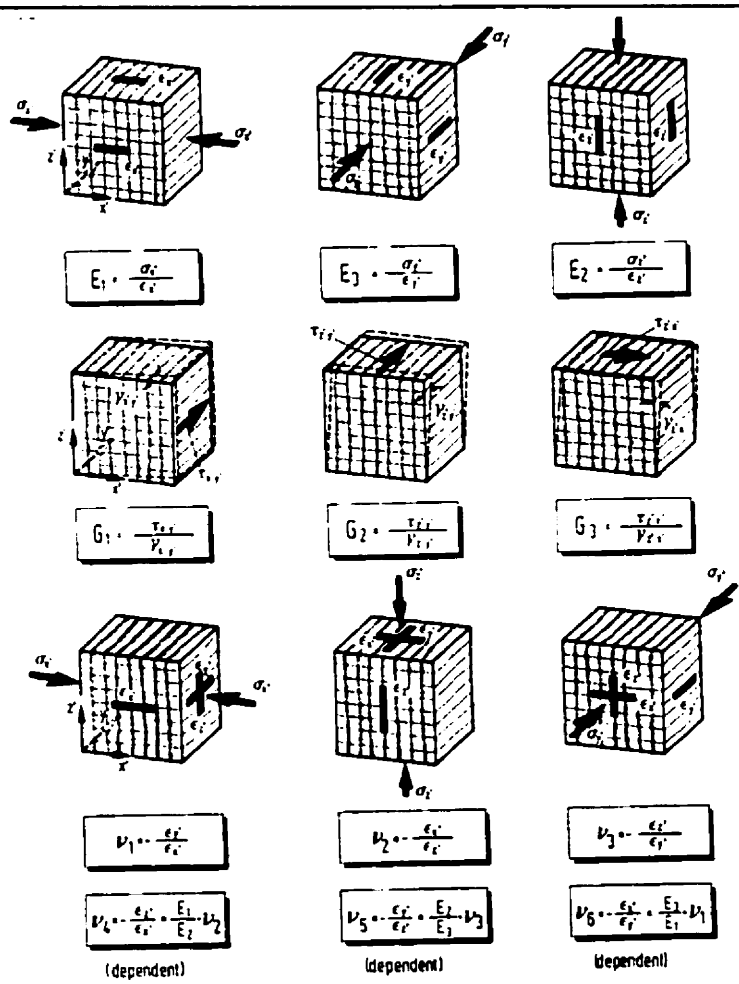

Figure 5.4 Definition of elastic constants for the case of orthotropy in terms of stresses and both normal and shear strains in a three-dimensional element (after Wittke, 1990)

A further simplification in the $[D']^{-1}$ matrix arise when the rock mass has only one dominant joint set. In this case there is a symmetry of elastic properties about an axis (parallel to the normal to the joint set), say the x direction. The six elastic constants of transverse isotropy are defined as follows (see Figure 5.5). For the case of transverse isotropy and planar fabric in terms of stresses and both normal and shear strains in a three-dimensional element, the stress strain relationship can be defined as follows:

$$[D']^{-1} = \begin{bmatrix} \frac{1}{E_1} & -\frac{\nu_1}{E_1} & -\frac{\nu_2}{E_2} & 0 & 0 & 0 \\ & \frac{1}{E_1} & -\frac{\nu_2}{E_2} & 0 & 0 & 0 \\ & & \frac{1}{E_2} & 0 & 0 & 0 \\ & & & \frac{1}{G_1} & 0 & 0 \\ & & & & \frac{1}{G_1} & 0 \\ & & & & & \frac{1}{G_2} \end{bmatrix} \tag{5.19}$$

$$[D'] = \begin{bmatrix} E_1\frac{1-n\nu_2^2}{(1+\nu_1)m} & E_1\frac{\nu_1+n\nu_2^2}{(1+\nu_1)m} & E_1\frac{\nu_2}{m} & 0 & 0 & 0 \\ E_1\frac{\nu_1+n\nu_2^2}{(1+\nu_1)m} & E_1\frac{1-n\nu_2^2}{(1+\nu_1)m} & E_1\frac{\nu_2}{m} & 0 & 0 & 0 \\ E_1\frac{\nu_2}{m} & E_1\frac{\nu_2}{m} & E_2\frac{1-\nu_1}{m} & 0 & 0 & 0 \\ 0 & 0 & 0 & \frac{E_1}{2(1+\nu_1)} & 0 & 0 \\ 0 & 0 & 0 & 0 & G_2 & 0 \\ 0 & 0 & 0 & 0 & 0 & G_2 \end{bmatrix} \tag{5.20}$$

where $n = {}^{E_1}\!/_{E_2}$, $m = (1-\nu_1-2n\nu_2^2)$

Once the global system of equilibrium equations is solved for the displacements $\{\Delta u^2\}$, strain, stresses and energy parameters ESR, ERR, and BPI can all be computed.

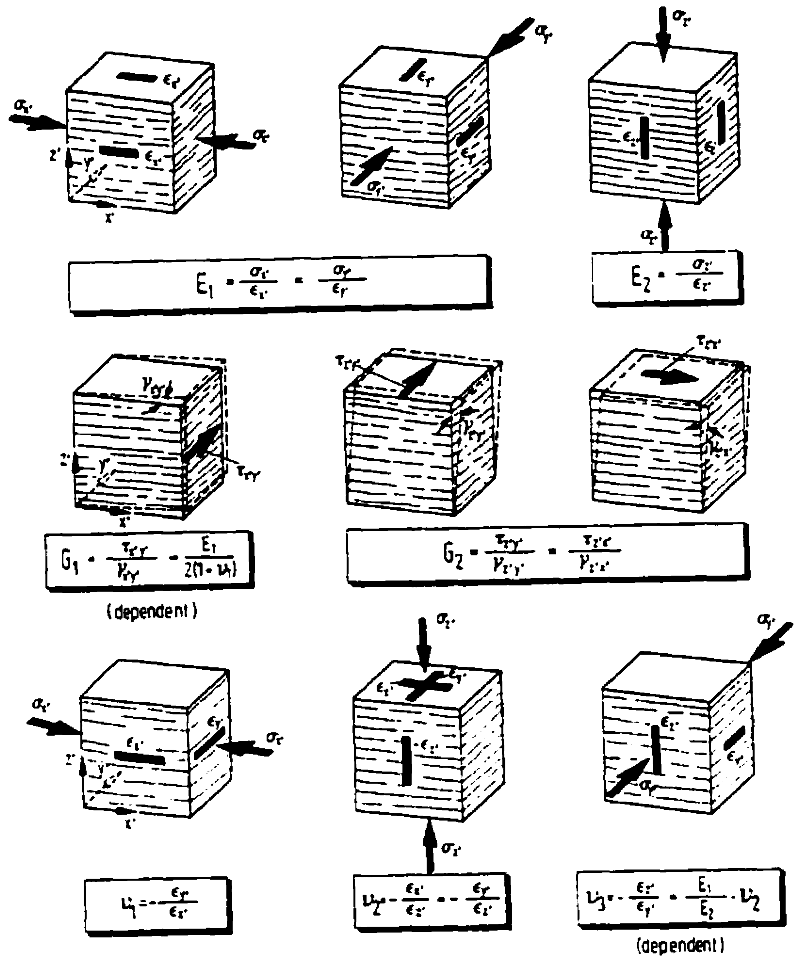

Figure 5.5 Definition of elastic constants for the case of transverse isotropy and planar fabric in terms of stresses and both normal and shear strains in a three-dimensional element (after Wittke, 1990)

To recap, referring to Figure 5.6, the suggested procedure for numerical modelling of destress blasting in mine drift developments is described as follows:

- model the initial drift configuration (Figure 5.2a) to assess the potential for face burst using the burst potential index (BPI), and hence determine the need for destress blasting,
- model destress blasting for a given $\{\alpha\}$ and $\{\beta\}$ (Figure 5.2b), while varying the blasting pattern. Assess the effectiveness of each pattern through comparison of post-blasting stress distributions,

- model face advance (Figure 5.2c), while examining the post-blast stresses, both ahead and behind the face,
- model face advance (Figure 5.2d), while destress blasting one round ahead of the drift face.

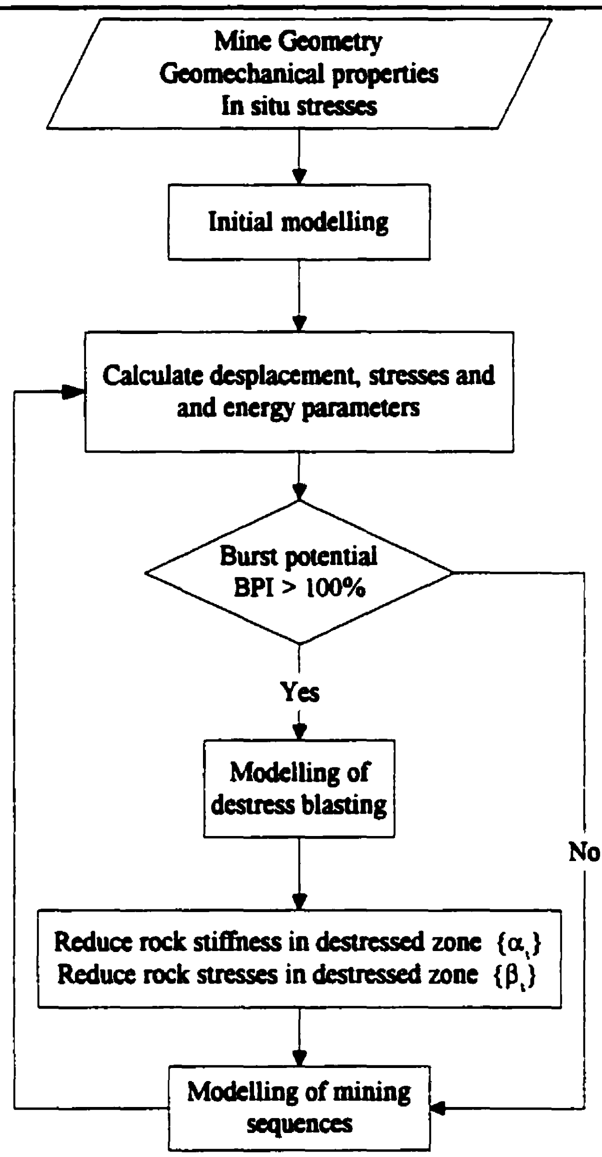

Figure 5.6 Flowchart of the model procedure for destress blasting

5.3 FINITE ELEMENT EQUATIONS

5.3.1 General

Based on the numerical algorithm for destress blasting as well as the rock mass constitutive law described in the last section, a finite element model ***e-z tools 3D*** has been developed by the author. In this section, the details of the finite element formulation are presented. The model employs piece-wise linear elastic algorithm. ***e-z tools 3D*** uses the 8-node and the 20-node isoparametric brick elements (Figure 5.7).

Underground openings in rock, such as caverns, drifts, and shafts, represent a considerable portion of the construction volume in this field. The three dimensional state of stress and strain in the vicinity of a temporary working face is in most cases of important, although a cavity is normally supported. In the cases of both shafts and drifts, the stresses due to the dead weight of the overburden and any tectonic loading in the rock mass have to be diverted around the opening. This stress redistribution takes place largely in the rock, which consequently experiences deformations due to the alterations in stress. As a rule, the support and lining, consisting of anchors, shotcrete, reinforced concrete etc., plays only a secondary role (Wittke, 1990). It is for this reason that a knowledge of states of stress and strain in the rock mass is of the utmost importance when assessing the stability of underground openings and an appropriate description of the rock mass stress-strain behaviour is indispensable.

Computation procedures to assess the stability of underground openings must therefore be able to handle general three-dimensional states of stress, and anisotropic rock mass characteristics. In this context, the finite element method has come very much to the forefront in recent years (Pande et al., 1990; Wittke; 1990, Beer, 1992; Mitri, 1993, 1996a; Yu et al., 1996). Such a computational procedure has been developed and will be presented in this Chapter.

5.3.2 Element Shape Functions

As discussed earlier, the displacements are calculated at the nodes. Displacements at any point within the element are related to the displacements of the nodes (u, v, w) through shape function as in Equation 5.21.

$$
\begin{aligned}
u &= \sum_{i=1}^{m} N_i(\xi,\eta,\zeta)\cdot u_i \\
v &= \sum_{i=1}^{m} N_i(\xi,\eta,\zeta)\cdot v_i \\
w &= \sum_{i=1}^{m} N_i(\xi,\eta,\zeta)\cdot w_i
\end{aligned}
\tag{5.21}
$$

where m is the number of nodes for each element which is 8 or 20.

The determination of these functions is based on the fact that the coordinates of certain points are known in both coordinate systems. This is the case for the nodal points of the element (Figure 5.6).

- Linear shape function for 20-node for corner nodes, or the shape function for 8-node

$$NL_i = \frac{1}{8}(1+\xi_i\xi)(1+\eta_i\eta)(1+\zeta_i\zeta),\ \text{i=1,8} \tag{5.22}$$

- Shape function for mid-side nodes:
    - For the nodes on the palne $\xi o \eta$

$$N_i = NA_j;\ NA_j = \frac{1}{4}(1-\xi^2)(1+\eta_i\eta)(1+\zeta_i\zeta),\ \text{j=1,4; i=13,16} \tag{5.23}$$

- For the nodes on the plane $\eta o \zeta$

$$N_i = NB_j;\ NB_j = \frac{1}{4}(1-\eta^2)(1+\xi_i\xi)(1+\zeta_i\zeta),\ \text{j=1,4; i=10, 12,20,18} \tag{5.24}$$

- For the nodes on the plane $\xi\ o\zeta$

$$N_i = NC_j;\ NC_j = \frac{1}{4}(1-\zeta^2)(1+\xi_i\xi)(1+\eta_i\eta),\ \text{j=1,4; i=9,11,19,17} \tag{5.25}$$

- For each corner node the final shape function is

$$N_i = NL_i - \frac{1}{2}(N(NK(i,1)) + N(NK(i,2)) + N(NK(i,3))) \qquad (5.26)$$

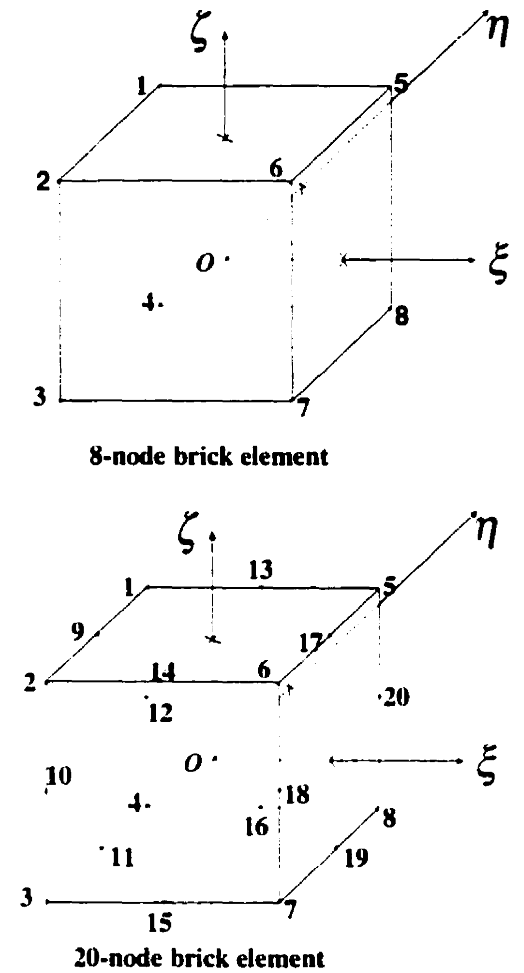

Figure 5.7 Element numbering

5.3.3 Element Displacements and Strains

Referring to Figure 5.7, Equation 5.21 can be expressed as follows:

$$\{\delta\} = \begin{Bmatrix} u \\ v \\ w \end{Bmatrix} = \sum_{i=1}^{m} N_i(\xi, \eta, \zeta) \begin{Bmatrix} u_i \\ v_i \\ w_i \end{Bmatrix} \qquad (5.27)$$

where m equals to 8 or 20 respectively for 8-node and 20-node element.

The sum of this equation may also be represented by the product of a matrix [N] and a vector $\{\delta^e\}$, the components of which are formed from the displacements of all the element's nodal points:

$$\{\delta^e\}=\{u_1,v_1,w_1,u_2,v_2,w_2,\cdots,u_m,v_m,w_m\}^T \tag{5.28}$$

The matrix [N] contains the known shape functions and consists of a series of m matrices:

$$[N]=[\,[N_1],[N_2],[N_3],\cdots,[N_m]\,] \tag{5.29}$$

in which, $[N_i]=N_i\cdot\begin{bmatrix}1&0&0\\0&1&0\\0&0&1\end{bmatrix}$.

So Equation 5.34 can be presented in the following form:

$$\{\delta\}=\begin{Bmatrix}u\\v\\w\end{Bmatrix}=[N(\xi,\eta,\zeta)]\cdot\{\delta^e\} \tag{5.30}$$

Further more the strain vector can be written in the following way:

$$\{\varepsilon\}=\begin{Bmatrix}\varepsilon_x\\\varepsilon_y\\\varepsilon_z\\\gamma_{xy}\\\gamma_{yz}\\\gamma_{zx}\end{Bmatrix}=\begin{Bmatrix}\frac{\partial u}{\partial x}\\\frac{\partial v}{\partial y}\\\frac{\partial w}{\partial z}\\\frac{\partial u}{\partial y}+\frac{\partial v}{\partial x}\\\frac{\partial v}{\partial z}+\frac{\partial w}{\partial y}\\\frac{\partial u}{\partial z}+\frac{\partial w}{\partial x}\end{Bmatrix}=\begin{Bmatrix}\sum_{i=1}^{m}\frac{\partial N_i}{\partial x}u_i\\\sum_{i=1}^{m}\frac{\partial N_i}{\partial y}v_i\\\sum_{i=1}^{m}\frac{\partial N_i}{\partial z}w_i\\\sum_{i=1}^{m}(\frac{\partial N_i}{\partial y}u_i+\frac{\partial N_i}{\partial x}v_i)\\\sum_{i=1}^{m}(\frac{\partial N_i}{\partial z}v_i+\frac{\partial N_i}{\partial y}w_i)\\\sum_{i=1}^{m}(\frac{\partial N_i}{\partial z}u_i+\frac{\partial N_i}{\partial x}w_i)\end{Bmatrix} \tag{5.31}$$

A matrix [B] is introduced to simplify the form of Equation 5.38, this resulting from the series of matrices [B_i]:

$$[B]=[[B_1],[B_2],[B_3],\cdots,[B_m]] \tag{5.39}$$

The following is valid for [B_i], i = 1, m at the same time:

$$[B_i]=\begin{bmatrix} \frac{\partial N_i}{\partial x} & 0 & 0 \\ 0 & \frac{\partial N_i}{\partial y} & 0 \\ 0 & 0 & \frac{\partial N_i}{\partial z} \\ \frac{\partial N_i}{\partial y} & \frac{\partial N_i}{\partial x} & 0 \\ 0 & \frac{\partial N_i}{\partial z} & \frac{\partial N_i}{\partial y} \\ \frac{\partial N_i}{\partial z} & 0 & \frac{\partial N_i}{\partial x} \end{bmatrix} \tag{5.32}$$

Then Equation 5.31 can be expressed in the following format:

$$\{\varepsilon\}=[B]\cdot\{\delta^e\} \tag{5.33}$$

Replace Equation 5.33 into 5.9 can be written into Equation 5.34, expressing the stress vector within the element in terms of nodal point displacements:

$$\{\sigma\}=[D]\cdot[B]\cdot\{\delta^e\} \tag{5.34}$$

5.3.4 Element Stiffness Matrix and Equilibrium Equation

It can be shown that the element stiffness matrix is given by

$$[K^e]\cdot\{\delta^e\}-\{F^e\}=0 \tag{5.35}$$

in which

$$[K^e]=\int_{V^e}[B]^T[D]\cdot[B]\cdot dV \tag{5.36}$$

$$\{F^e\} = \int_{V^e} [B]^T \{\sigma^0\} dV + \int_{V^e} [N]^T \{p\} \cdot dV + \int_{S^e} \{N'\}^T \{q\} \cdot dS + \{F^*\} \tag{5.37}$$

Transforming the variables from global coordinates (x, y, z) into local coordinates (ξ, η, ζ) with the relationship

$$dV = dx\,dy\,dz = \det[J]\,d\xi\,d\eta\,d\zeta \tag{5.38}$$

$$[J] = \begin{bmatrix} \Sigma \frac{\partial N_i}{\partial \xi} x_i & \Sigma \frac{\partial N_i}{\partial \xi} y_i & \Sigma \frac{\partial N_i}{\partial \xi} z_i \\ \Sigma \frac{\partial N_i}{\partial \eta} x_i & \Sigma \frac{\partial N_i}{\partial \eta} y_i & \Sigma \frac{\partial N_i}{\partial \zeta} z_i \\ \Sigma \frac{\partial N_i}{\partial \xi} x_i & \Sigma \frac{\partial N_i}{\partial \eta} y_i & \Sigma \frac{\partial N_i}{\partial \zeta} z_i \end{bmatrix} \tag{5.39}$$

Equation 5.36 becomes:

$$[K^e] = \int_{-1}^{1} \int_{-1}^{1} \int_{-1}^{1} [B]^T [D] \cdot [B] \cdot \det[J] \cdot d\xi \cdot d\eta \cdot d\zeta \tag{5.40}$$

This integration can be implemented using Gauss Quadrature.

$$[K^e] = \sum_{i=1}^{n} \sum_{j=1}^{n} \sum_{k=1}^{n} [B(\xi_i, \eta_j, \zeta_k)]^T [D] \cdot [B(\xi_i, \eta_j, \zeta_k)] \cdot \det[J(\xi_i, \eta_j, \zeta_k)] \cdot W_i \cdot W_j \cdot W_k \tag{5.41}$$

where for the 20-node element (n = 3), the $3\times3\times3$ integration points are located at ξ_i, η_j, ζ_k = $\sqrt{0.6}$, 0, $-\sqrt{0.6}$, and the weighted factors at each integration point are W_i, W_j, W_k = $\frac{5}{9}, \frac{8}{9}, \frac{5}{9}$ with $i, j, k = \overline{1,3}$.

And for the 8-node element (n = 2), $2\times2\times2$ integration points are located at ξ_i, η_j, ζ_k = ± 0.57735, and the weighted factors at each integration point are W_i, W_j, W_k = 1.0 with $i, j, k = \overline{1,2}$.

<u>5.3.5.1 Consistent Load Vector Due To Initial Stresses</u>

A numerical integration is also necessary to determine the first three members of the element load vector.

$$\{F_{\sigma^0}\} = \int_{V^e} [B]^T \{\sigma^0\} dV = \int_{-1}^{1}\int_{-1}^{1}\int_{-1}^{1} [B]^T [\sigma^{0e}] \cdot \{N^0\} \cdot \det[J] \cdot d\xi\, d\eta\, d\zeta \tag{5.42}$$

where $\{N^0\} = \{N_1 \quad N_2 \quad N_3 \quad \cdots \quad N_{20}\}^T$

$$[\sigma^{0e}] = \begin{bmatrix} \sigma_x^1 & \sigma_y^1 & \sigma_z^1 & \tau_{xy}^1 & \tau_{yz}^1 & \tau_{zx}^1 \\ \sigma_x^2 & \sigma_y^2 & \sigma_z^2 & \tau_{xy}^2 & \tau_{yz}^2 & \tau_{zx}^2 \\ \vdots & & \cdots & \cdots & & \vdots \\ \vdots & & \cdots & \cdots & & \vdots \\ \sigma_x^m & \sigma_y^m & \sigma_z^m & \tau_{xy}^m & \tau_{yz}^m & \tau_{zx}^m \end{bmatrix} \tag{5.43}$$

So,

$$\{F_{\sigma^0}\} = \sum_{i=1}^{n}\sum_{j=1}^{n}\sum_{k=1}^{n} [B(\xi_i, \eta_j, \zeta_k)]^T [\sigma^{0e}] \cdot \{N^0(\xi_i, \eta_j, \zeta_k)\} \det[J] \cdot W_i W_j W_k \tag{5.44}$$

5.3.5.2 Consistent Load Vector Due To Body Forces

$$\begin{aligned} \{F^b\} &= \int_{V^e} [N]^T \begin{Bmatrix} p_1 \\ p_2 \\ p_3 \end{Bmatrix} dV = \int_{-1}^{1}\int_{-1}^{1}\int_{-1}^{1} [N]^T \begin{Bmatrix} 0 \\ 0 \\ \gamma \end{Bmatrix} \det[J] \cdot d\xi\, d\eta\, d\zeta \\ &= \sum_{i=1}^{n}\sum_{j=1}^{n}\sum_{k=1}^{n} [N(\xi_i, \eta_j, \zeta_k)]^T \cdot \begin{Bmatrix} 0 \\ 0 \\ \gamma \end{Bmatrix} \det[J(\xi_i, \eta_j, \zeta_k)] \cdot W_i W_j W_k \end{aligned} \tag{5.45}$$

where the [N] matrix is defined by Equation 5.29.

5.3.5.3 Consistent Load Vector Due To Boundary Traction

The consistent load vector due to boundary traction is computed along each side of the element using the following formula:

$$\begin{aligned} \{F^t\} &= \int_{S^k} \{N^t\}^T \{q\} dS = \frac{1}{H} \int_{-1}^{1}\int_{-1}^{1} \{N^t\}^T \{q\} \cdot \det[J] \cdot ds\, dt \\ &= \frac{iw}{H} \sum_{l=1}^{n}\sum_{m=1}^{n} \{N^t(r_i, s_j, t_k)\}^T \{q\} \cdot \det[J(r_i, s_j, t_k)] \cdot W_l \cdot W_m \end{aligned} \tag{5.46}$$

in which

iw is the weight factor for 20-node is 2.0 and for 8-node is 1.0

$[N^t]$ is the array consists of the eight nodes shape function on the element side subjected to boundary traction,

$\{q\}$ is the array consists of the eight nodal pressures,

H is the average thickness on the boundary traction direction.

r_i, s_j, t_k will take the value of ξ_i, η_j, ζ_k respectively depending on the direction of the boundary traction, one of the three will take the value ± 1, the rest will be the same as before.

Up to now, the consistent load vectors due to body forces, initial stresses and boundary tractions can all been numerically computed. The concentrated forces can be directly added to the global load vector.

$$\{F\}=\{F_{\sigma^0}\}+\{F^b\}+\{F^t\}+\{F^c\} \tag{5.47}$$

5.4 FLOWCHART AND NUMERICAL ALGORITHM

In this section, the programming technique and structure of the ***e-z tools 3D*** program is described through several flowcharts. First, the main structure of ***e-z tools 3D*** is divided into 5 steps. Then the detail of programming for each step is discussed and its flowchart is presented.

5.4.1 General Flowchart

The computation process in ***e-z tools 3D*** follows into five basic steps. They are:

- Data reading and preparation (calculation of the global degree-of-freedom and the global stiffness matrix);
- Calculate the element stiffness matrix and load vector, then assemble them into their respective global arrays;
- Solve the system of equations to determine the nodal displacements;
- Calculate stresses and energy parameters, and hence the Burst Potential Index (BPI) to determine if destress blasting is needed;
- Safety level calculation and transfer of data into postprocessor required format to view the results.

Figure 5.8 presents the general flowchart of ***e-z tools 3D*** which illustrates the above mentioned steps. Referring to Figure 5.2, if destress blasting is needed, the program will repeat the five steps based on the stress state after the initial configuration. Since the commercial software HyperMesh is used as the pre- and post-processor, the translation of files, from and to HyperMesh, before and after each computation of ***e-z tools 3D*** is needed. For the different purpose of analysis, ***e-z tools 3D*** employs 2 sets of equation solvers: **Gauss Seidel** and **Gauss Elimination**. When the problem to be analyzed is relatively large the former equation solver (define IGS = 1) is recommended. And when the problem is relatively small (define IGS = 2) and with predicted large deformation, the latter one is recommended.

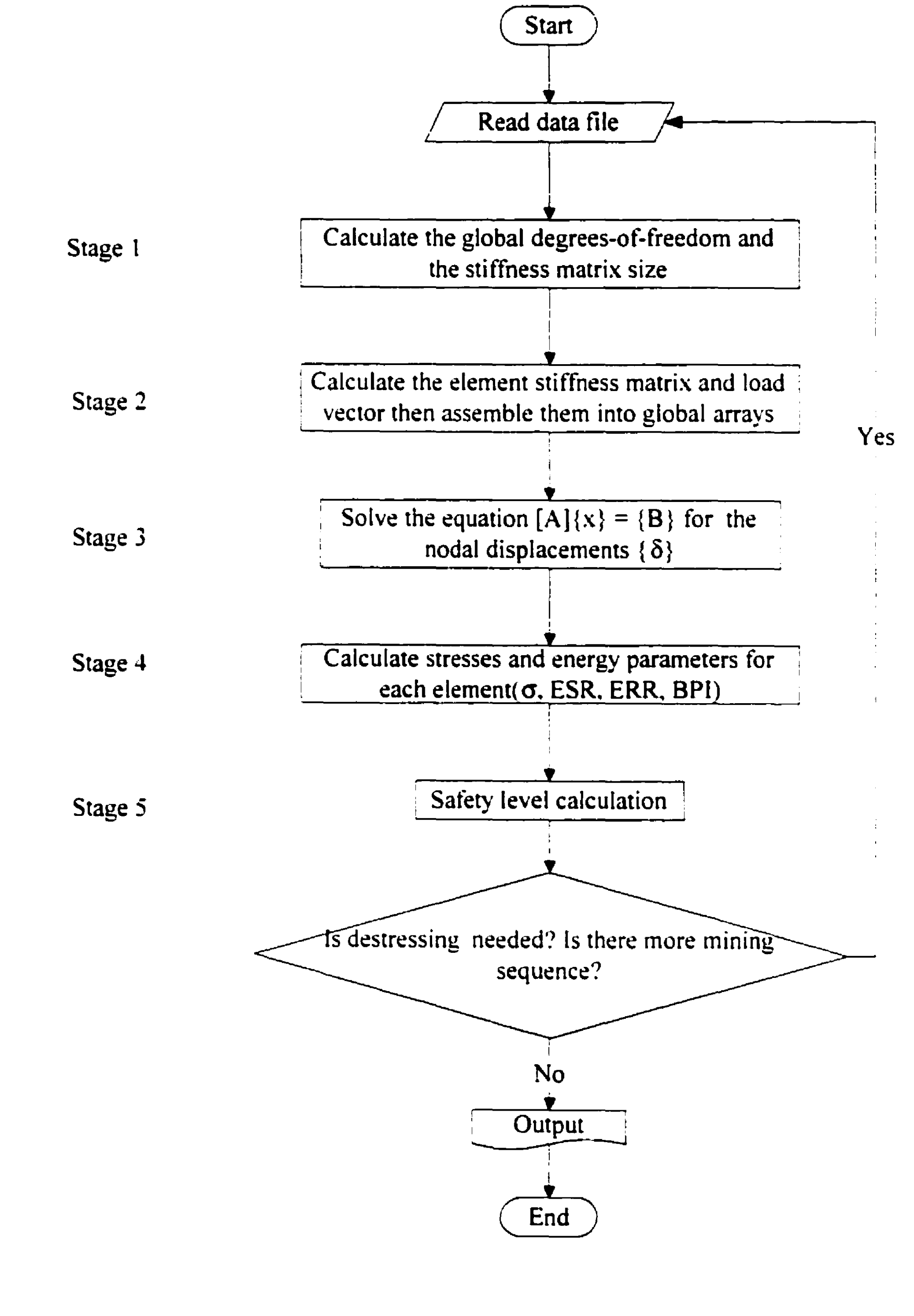

Figure 5. 8 General flowchart of ***e-z tools 3D***

A complete description of the input data is given in the Appendix.

5.4.2 Model input Parameters

Except for the graphic information of the finite element model from the preprocessor, to carry on the calculation, the following data are needed for the input data file of ***e-z tools 3D***:

Materials properties which include elastic modulus {E}, Poisson's ratio {ν}, unit weight {γ}, uniaxial compressive strength {σ_c}, coherent force of the material C, geomechanical constant m for RMR, geomechanical constant s for RMR, friction angle ϕ.

In situ stress data which include initial stresses array at the original point of the model {σ_0}, initial stresses angle θ (strike 0^0 to 360^0), φ (dip -90^0 to 90^0, referring to Figure 5.3), initial stress ratio {FB}.

5.4.3 Global Degrees-of-Freedom and the Size of the Stiffness Matrix

Figure 5.9 gives the detailed flowchart of the first model step, whereas Figure 5.10 gives the second step flowchart. Since the three-dimensional analysis makes the problem much larger than the two-dimensional analysis, optimizing the global stiffness matrix storage becomes very important for the efficient computation. In ***e-z tools 3D***, for the different equation solvers, the global stiffness will be stored into two forms: upper skyline format for Gauss Elimination and lower skyline format for Gauss Seidel.

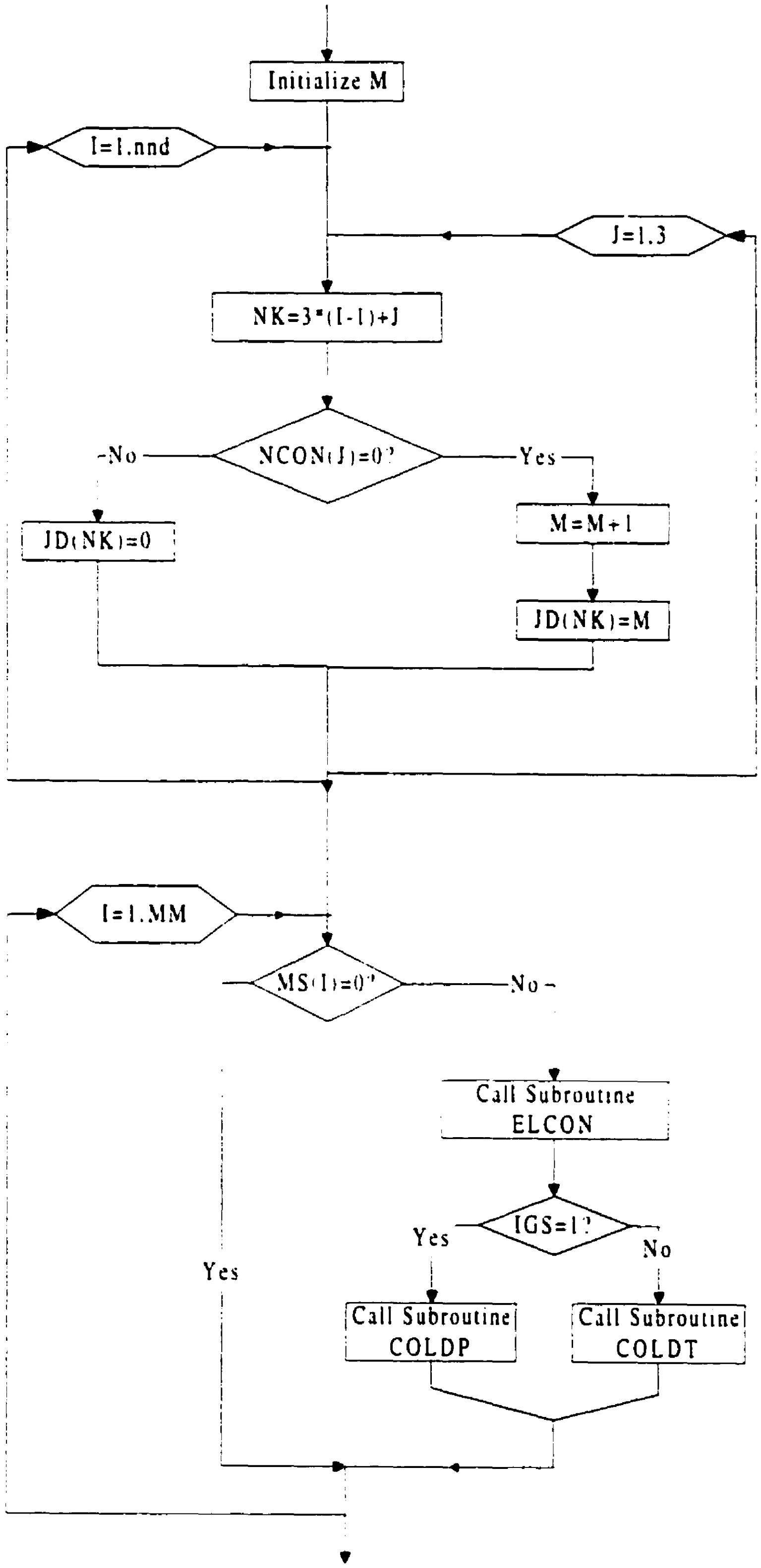

Figure 5. 9 Flowchart details of Step1 for ***e-z tools 3D***

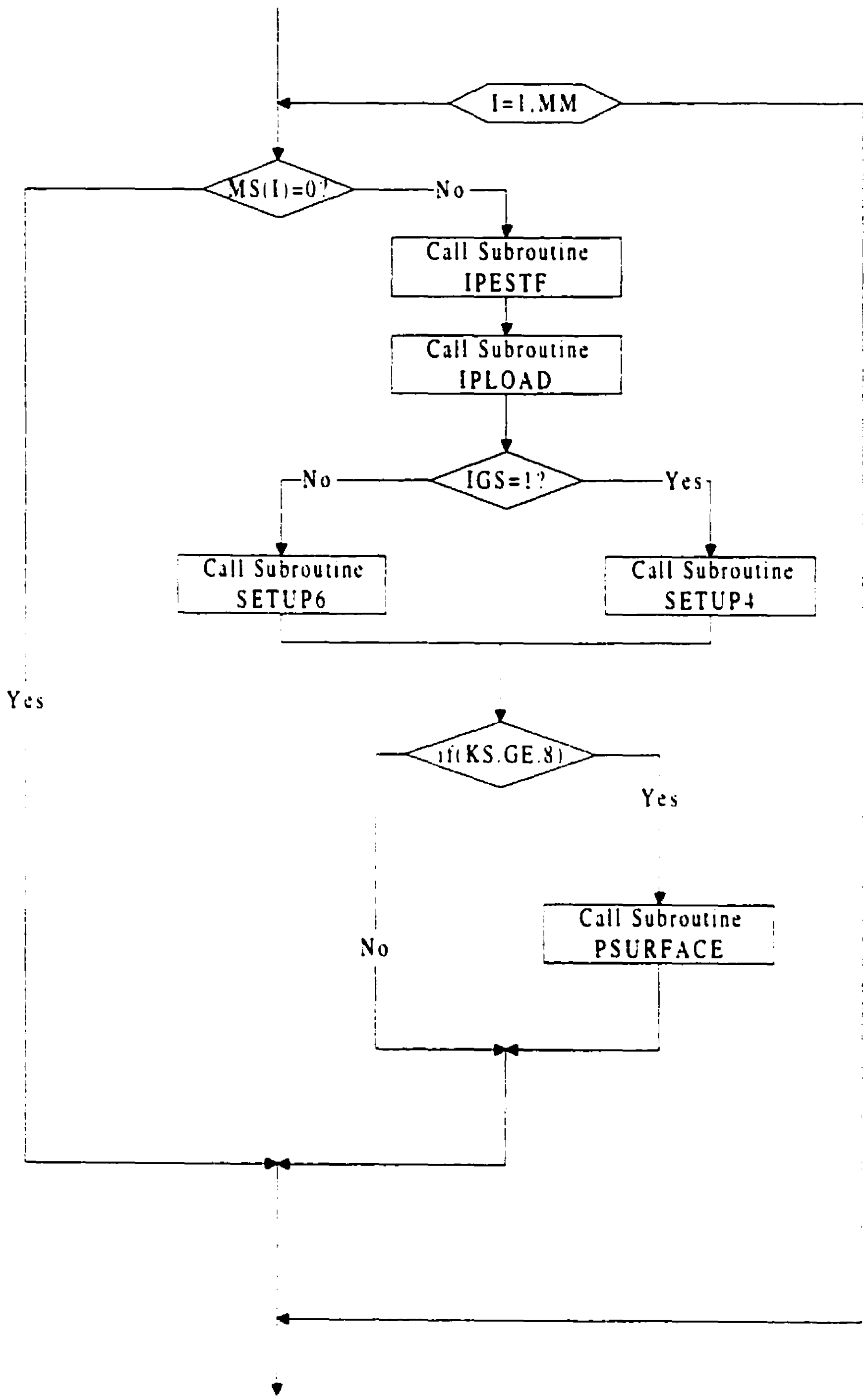

Figure 5.10 Flowchart details for Step2 in ***e-z tools 3D***

5.4.4 Element Calculation for Stiffness and Load Vector

The calculations of the stiffness matrix and load vector are carried on any single element and setup the global stiffness matrix and load vector. Figure 5.10 shows the general flowchart of step 2 in ***e-z tools 3D***. Subroutine IPESTF (refer to Figure 5.11) gives the element stiffness matrix for both isotropic and anisotropic materials. Inside the subroutine IPESTF, subroutine ANIDMAT, which is a routine to calculate the stress-strain relationship matrix, and subroutine IPLQBJ, which is used to calculate the shape function, strain-displacement relationship matrix and Jacobian matrix, are called. The subroutine IPLOAD (refer to Figure 5.12) calculates the load vector due to gravity and initial stresses. For the different equation solver the subroutine SETUP4 is used for the Gauss Seidel and the subroutine SETUP6 is used for Gauss Elimination. If any of the elements is subjected to the surface traction, the subroutine PSURFACE will be called to calculate the load vector due to surface traction. Theses operation will be repeat until all the elements have been calculated.

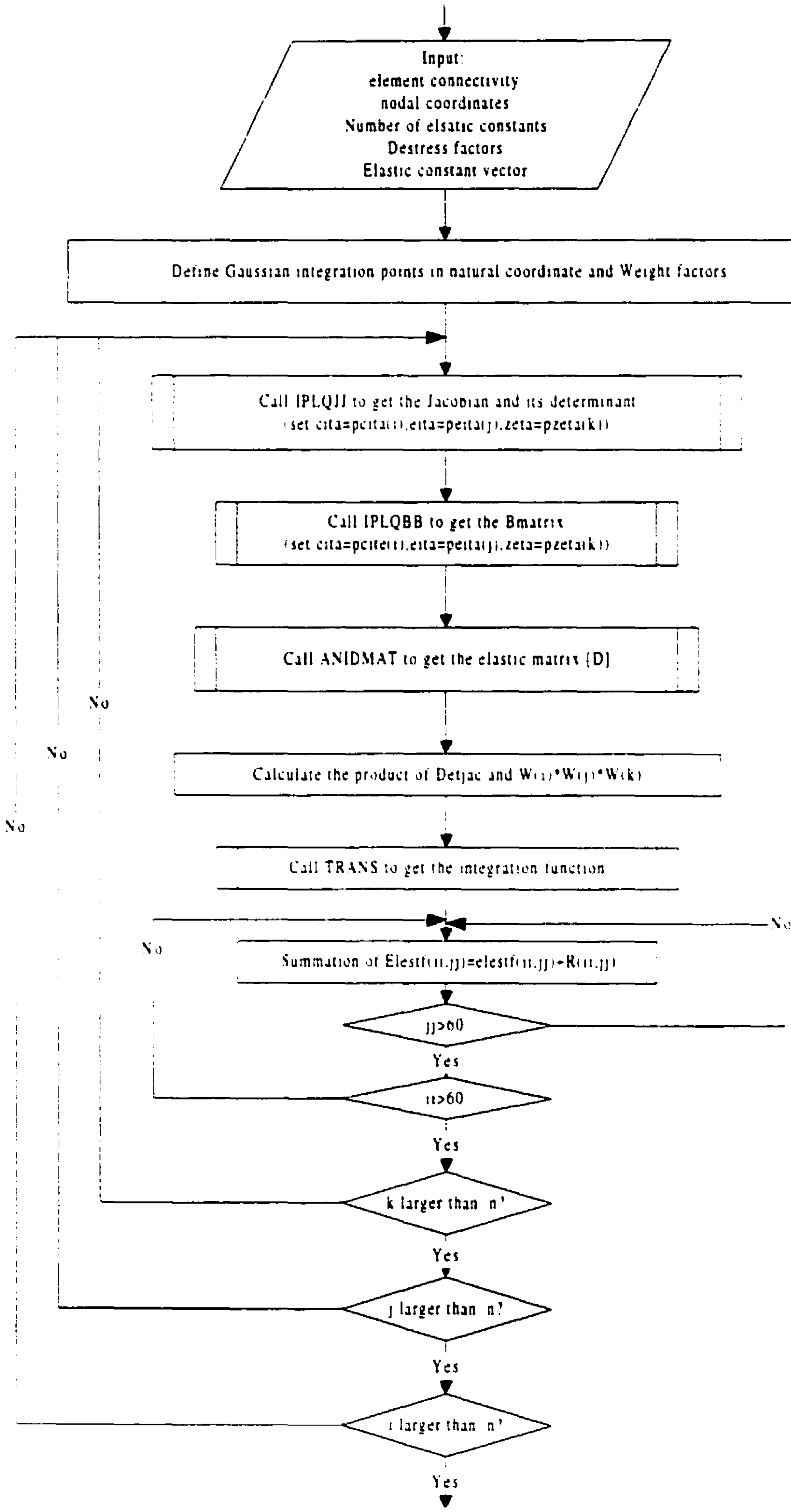

Figure 5.11 Flowchart for the element stiffness matrix calculation

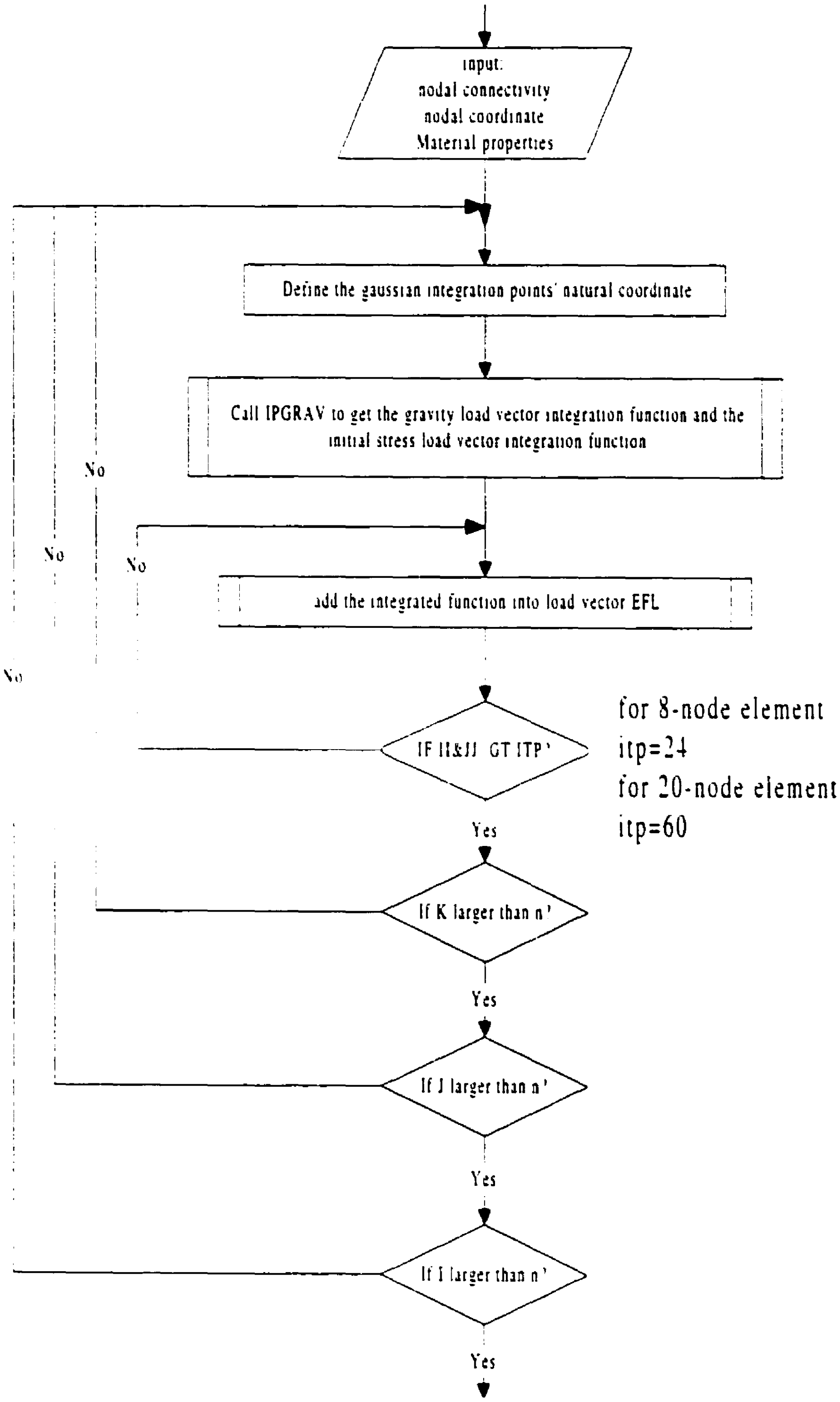

Figure 5.12 Flowchart of element load vector due to gravity and initial stresses

5.4.5 Strain, Stresses and Energy Parameters

After solving the equation [A] {x} = {B}, a vector of unknowns is obtained. But they need to be translated into the nodal point displacements. The subroutine NDISP is called to implement this task. With the known nodal displacements, the strains distribution and the stresses increments in the current mining sequence inside the elements can be calculated on the designated integration points, which is carried out by calling subroutine STRENG. Then subroutine ENGPRT is called to calculate the energy parameters ESR and ERR and the total stress on the designated integration points (see Figure 5.13). If there are some elements belonging to the destressed zones, the subroutine UPDESR and GETESR are called to calculate the energy parameters' changes which just follows the definition shown in Figure 5.14 as for the possible changes in the destressed zone.

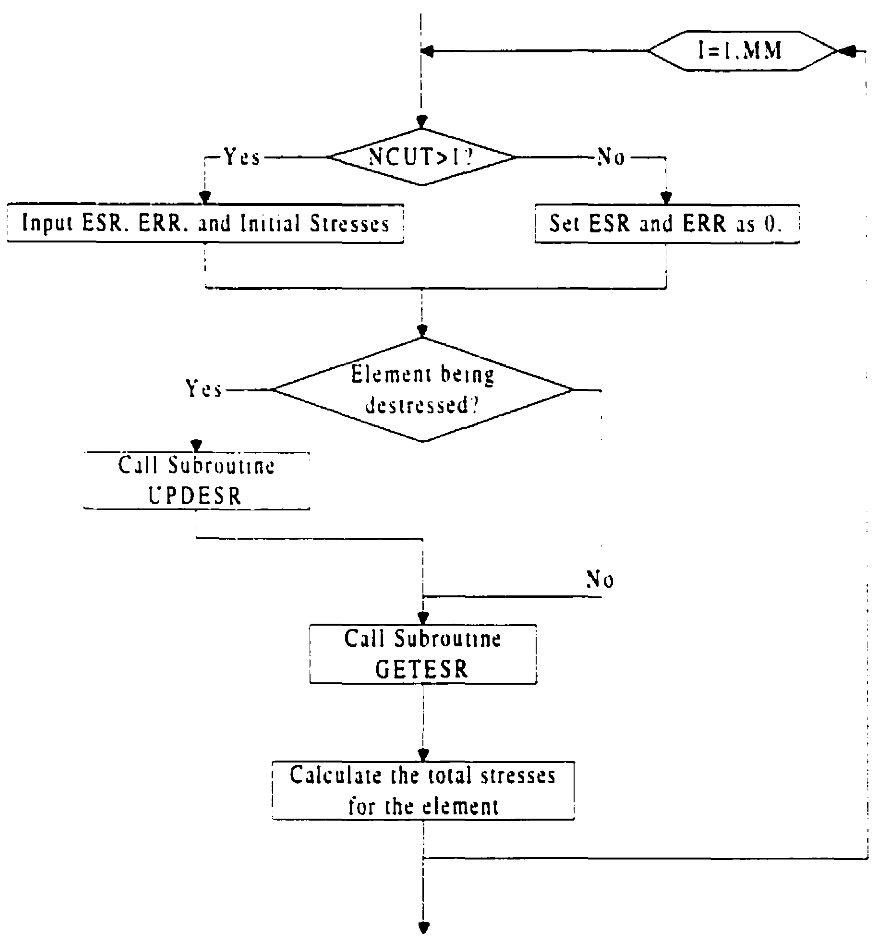

Figure 5.13 Flowchart for the stresses and energy parameters

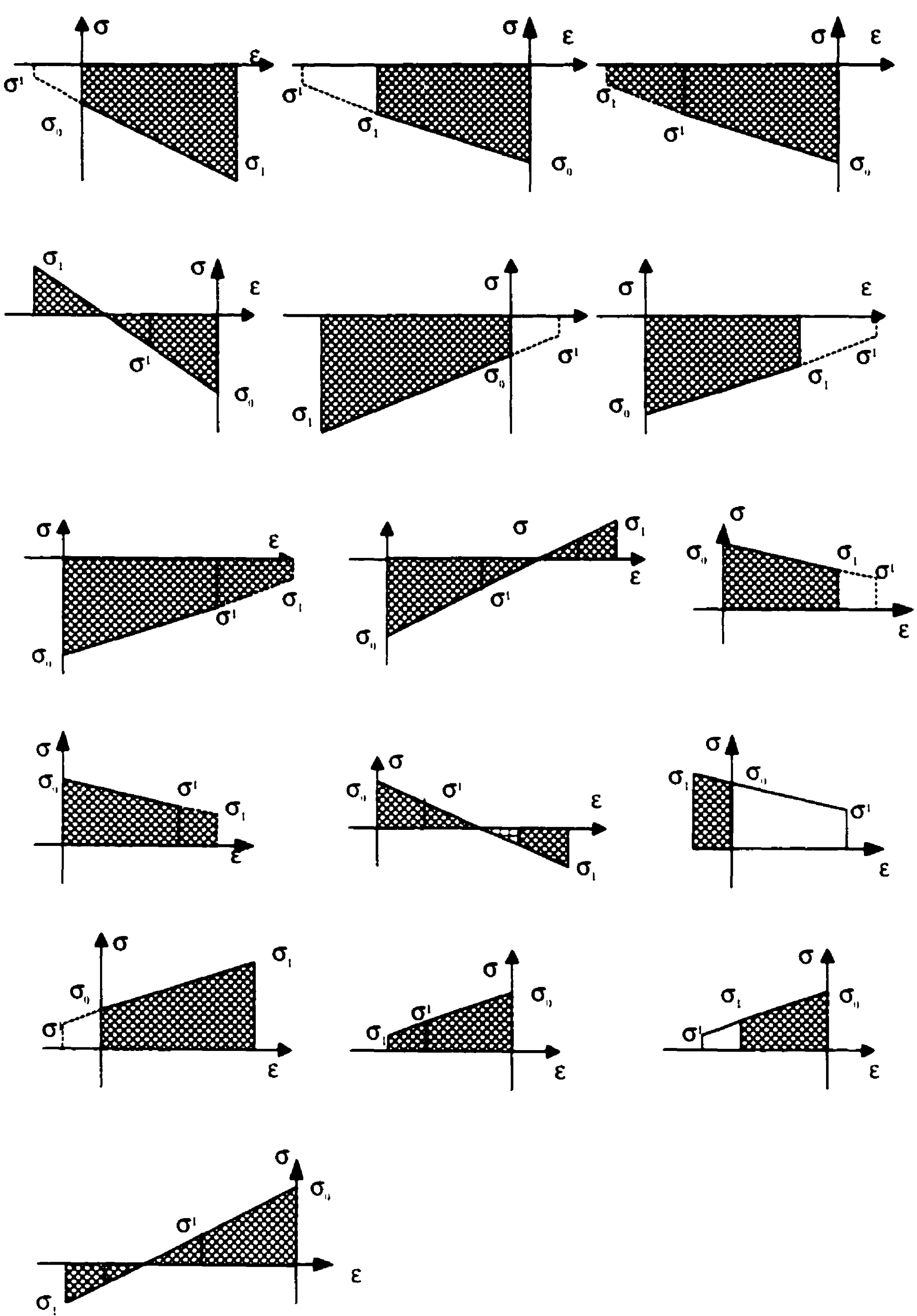

Figure 5.14 Possible ESR reduction and increase from the initial state of stress σ^0

5.5 ISOPARAMETRIC ELEMENT TEST

In this section, a test of the isoparametric element for ***e-z tools 3D*** is described. A fixed-end beam subjected to uniformly distributed load is compared with the analytical results. The load is applied to the different directions to test the element isoparametric.

For a fixed-end beam subjected to uniform load over the entire span (Figure 5.15a), the reactions yield:

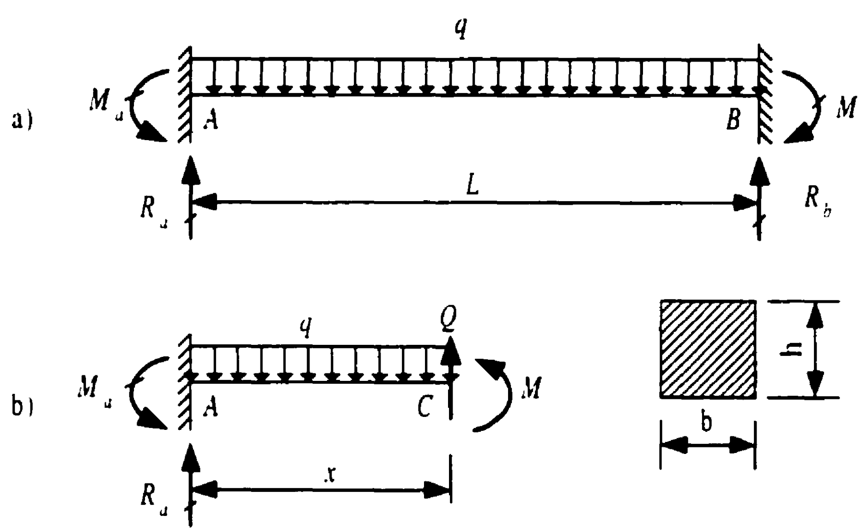

Figure 5.15 Fixed-end beam with a uniform load

$$M_a = M_b = \frac{qL^2}{12}, \quad R_a = R_b = \frac{qL}{2} \tag{5.48}$$

So the bending moment at any point along the beam is defined as follows (Figure 5.15b):

$$M = R_a x - M_a - \frac{1}{2} q x^2 \tag{5.49}$$

The differential equation of the deflection curve becomes

$$EIv'' = -M = M_a + \frac{1}{2} q x^2 - R_a x \tag{5.50}$$

After integration and applying the boundary condition (when y = 0, υ =0, and when y = L, υ = 0), this equation yields

$$EI\upsilon = \frac{qL^2}{24}y^2 + \frac{qy^4}{24} - \frac{qL}{12}y^3 \tag{5.51}$$

The normal stress in the beam are expressed as

$$\sigma_x = \frac{M \cdot z}{I} \tag{5.52}$$

in the above equations $I = \int z^2 dA$ is the moment of inertia of the cross-sectional area with respect to y axis, that is the neutral axis,

M_a, M_b, M are the bending moments at end A, end B, and at any point,

R_a, R_b are the vertical reactions of the supports at end A and end B,

z is the vertical distance from the axis of the beam to the calculated point,

q is the uniform load acting on the beam,

L is the span of the beam,

υ is the beam deflection.

Based on Equation 5.51 and 5.52, the deflection and normal stress along the beam are plotted in Figure 5.17 and 5.18 with the data input as follows:

E = 78 GPa, ν = 0.15, L = 25m, b = 1m, h = 1m, γ = 0.028MN/m^3.

For the same problem, a file is prepared for ***e-z tools 3D*** as shown in Figure 5.16) with distributed load in z-direction. The model results of the vertical displacements and normal stresses are plotted in Figure 5.17 and Figure 5.18 also. For the condition that load is applied in the x direction, the results are presented in Figure 5.19 and Figure 5.20 respectively for displacement and normal stress which are plotted together with the analytical results. Comparison between the analytical and numerical model results under different loading directions for the vertical displacements and the normal stresses show excellent agreement.

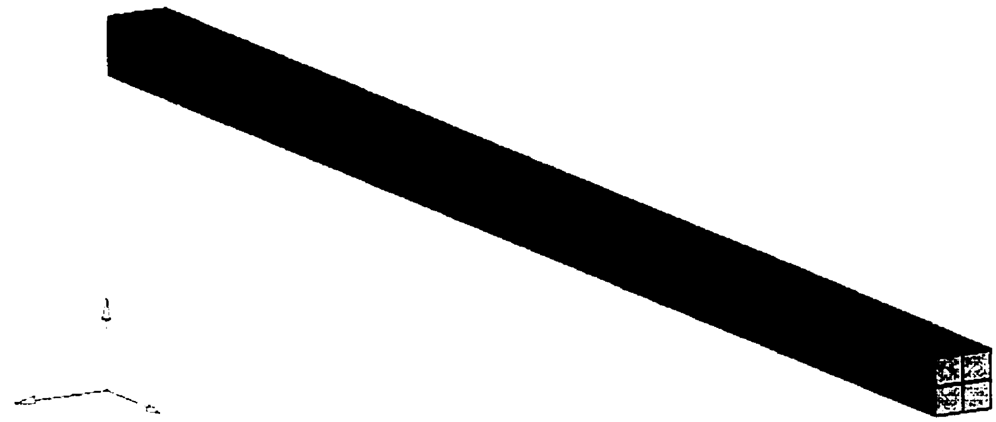

Figure 5.16 Finite element mesh for the tested beam with 64 20-node elements

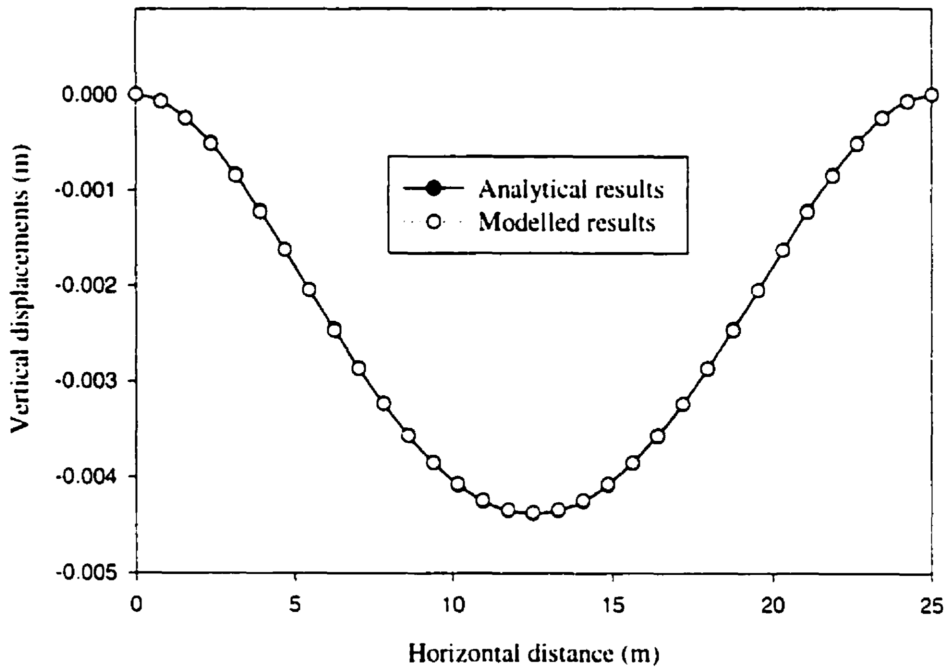

Figure 5.17 Vertical displacement distribution along the fixed-end beam under a uniform load

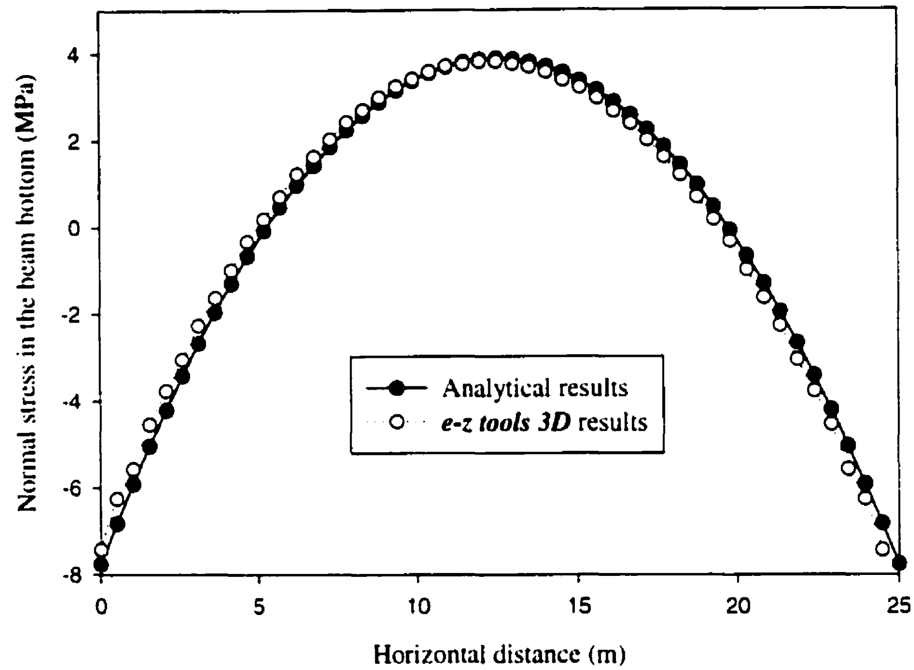

Figure 5.18 Stress distribution along the fixed-end beam under a uniform load

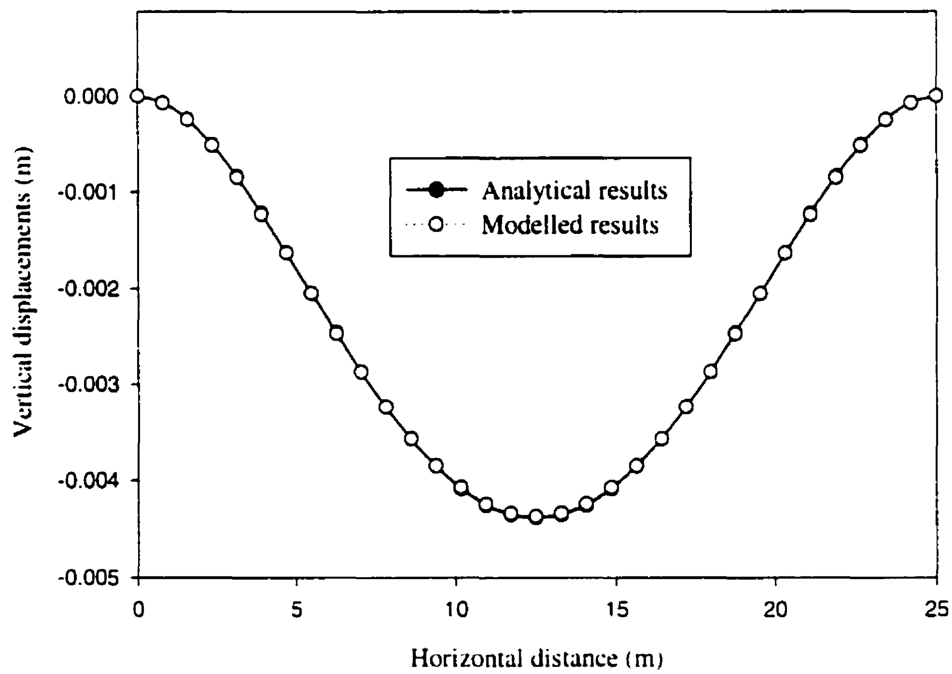

Figure 5.19 Horizontal displacement distribution along the fixed-end beam under a uniform load applied in x direction

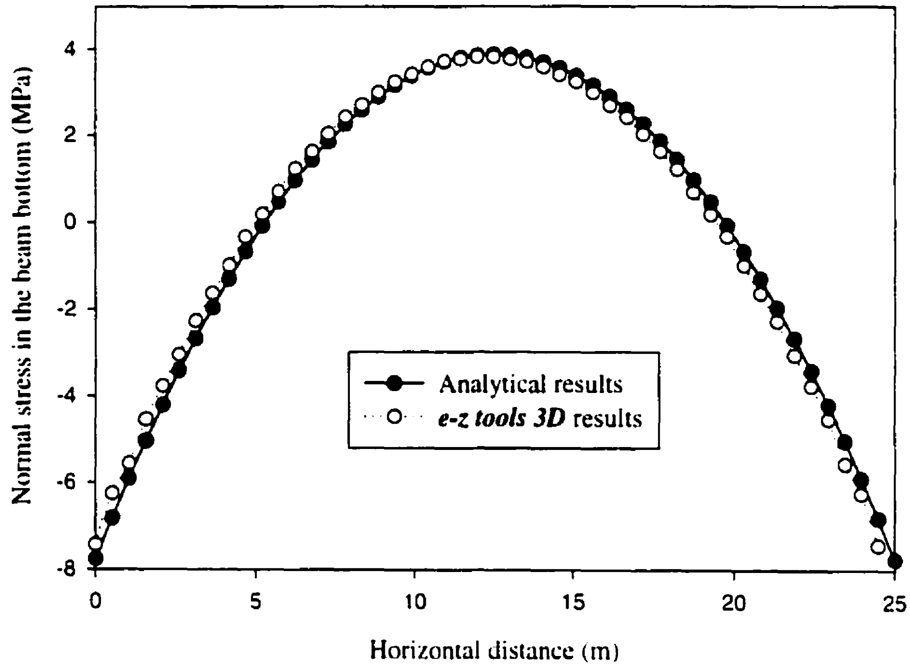

Figure 5.20 Stress distribution along the fixed-end beam under a uniform load applied in x direction

5.6 MODEL FEATURES AND LIMITATIONS

5.6.1 Model Features

- 8-node or 20-node isoparametric brick elements
- 100,000 8-node elements or 25,000 20-node elements
- Up to 16 geomaterials
- Isotropic / orthotropic materials
- Modelling of initial stresses, body forces and surface traction loading
- Computation of energy release and storage parameters (ERR, ESR)
- Modelling of mining sequences (piecewise linear)
- Calculation of burst potential index (BPI)
- Modelling of destress blasting

- Modelling of ground support (backfill, props, cribs)
- Safety level calculation (Mohr-Coulumb, Hoek-Brown)
- Mesh generation and data visualization using HyperMesh®.

5.6.2 Model Limitations

- Number of elements handled is limited by the computer hardware (speed, memory and hard disk storage)
- Static analysis only
- Linear elastic analysis only
- No time-dependent behaviour

CHAPTER 6

MODEL VERIFICATION AND PARAMETRIC STUDY

6.1 INTRODUCTION

In this chapter, the verification and sensitivity analysis of the finite element model, ***e-z tools 3D***, developed by the author, are described. The model verification involves two tests. For the model sensitivity analysis, four aspects are considered.

In the first verification test of the model, the modelled stress results calculated around the circular opening are compared with those obtained from the classical method with the hydrostatic loading condition. The second verification a horizontal-to-vertical ratio $k=0$.

For the parametric study, a typical Canadian hard rock drift configuration is adopted. First three destress blasting patterns are analyzed and compared. The destressing pattern No. 2 is then chosen for subsequent, detailed parametric study on the destress model parameters $\{\alpha\}$, $\{\beta\}$, the angle between major principal horizontal initial stress and the development direction θ. A summary of the model parametric study and parametric values is shown in Table 6.1.

Table 6.1 Parametric values for the model sensitivity analysis

Purpose	model	α	β	Pattern	θ	k_x	k_y
Study the effect of the different destress blasting patterns	1	0.4	0.4	1	90^0	2.0	1.4
	2	0.4	0.4	2	90^0		
	3	0.4	0.4	3	90^0		
Study the effect of change of α	4	0.05	0.4	2	90^0	1.8	1.4
	5	0.1	0.4	2	90^0		
	6	0.15	0.4	2	90^0		
	7	0.2	0.4	2	90^0		
	8	0.4	0.4	2	90^0		
	9	0.6	0.4	2	90^0		
	10	0.8	0.4	2	90^0		
Study the effect of change of β	11	0.4	0.1	2	90^0	1.8	1.4
	12	0.4	0.2	2	90^0		
	13	0.4	0.3	2	90^0		
	14	0.4	0.5	2	90^0		
	15	0.4	0.8	2	90^0		
	16	0.4	1.0	2	90^0		
Study the effect of change of θ	17	0.2	0.6	2	0^0	1.8	1.4
	18	0.2	0.6	2	30^0		
	19	0.2	0.6	2	45^0		
	20	0.2	0.6	2	60^0		
	21	0.2	0.6	2	90^0		

6.2 MODEL VERIFICATION

One of the earliest analytical solutions for the two-dimensional distributions of stresses around an opening in an elastic body was published in 1898 by Kirsch (Hoek & Brown, 1980) for the simplest cross-sectional shape, the circular hole. Jeager and Cook (1976) fully discussed the Kirsch equations, as they are known today. The final equations (Equation 6.1) presented using a system of polar coordinates in which the stresses are defined in terms of the tractions acting on the faces of an element located by radius r and a polar angle ϕ. Although ***e-z tools 3D*** is a three-dimension model, the two-dimensional analytical solutions can still be used to verify the model when a circular drift is modelled without considering the face affection which can be approximated as plane strain state.

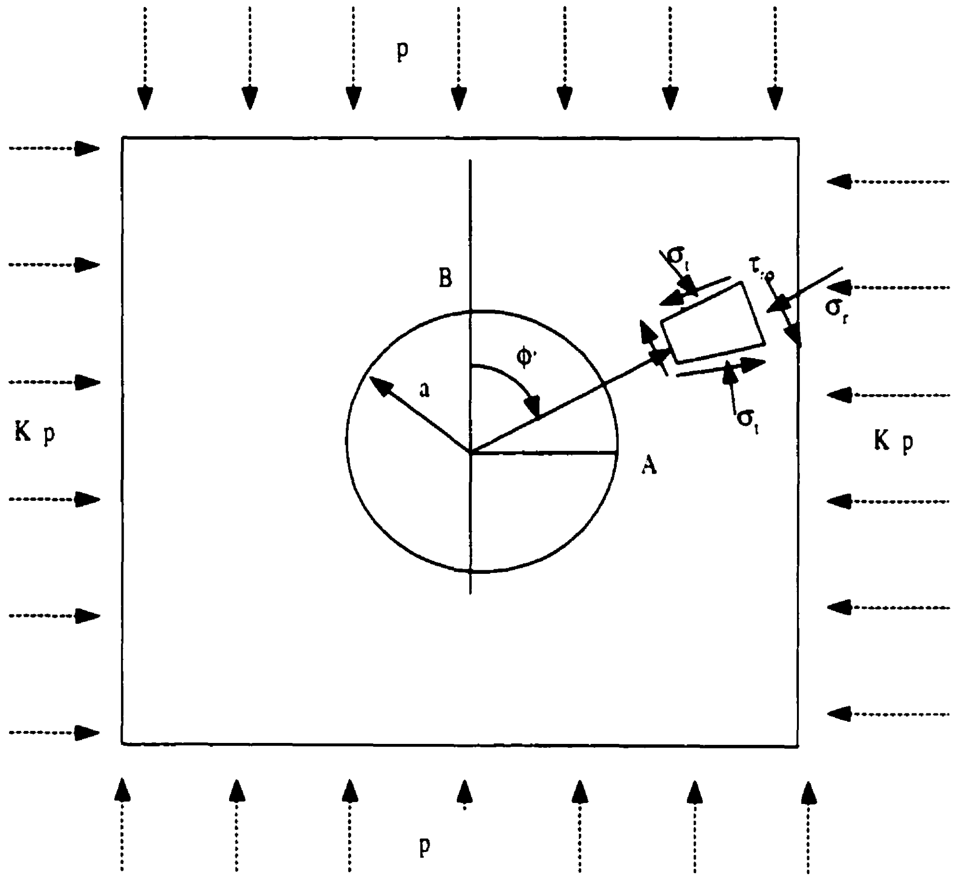

Figure 6.1 Circular opening in a biaxial stress field

$$\sigma_r = \frac{p}{2}\left[(1+K)\left(1-\frac{a^2}{r^2}\right)-(1-K)\left(1-4\frac{a^2}{r^2}+\frac{3a^4}{r^4}\right)\cos 2\phi\right]$$
$$\sigma_t = \frac{p}{2}\left[(1+K)\left(1+\frac{a^2}{r^2}\right)+(1-K)\left(1+\frac{3a^4}{r^4}\right)\cos 2\phi\right] \quad (6.1)$$

where σ_r is the radial stress around the circular opening,

σ_t is the tangential stress around the circular opening,

K is the horizontal to vertical stress ratio,

p is the vertical initial stress,

a is the radius of the circular opening, r is the distance from the calculated point to the centre of the opening,

ϕ' is the angle from the vertical radial direction clockwise to the calculated radial direction.

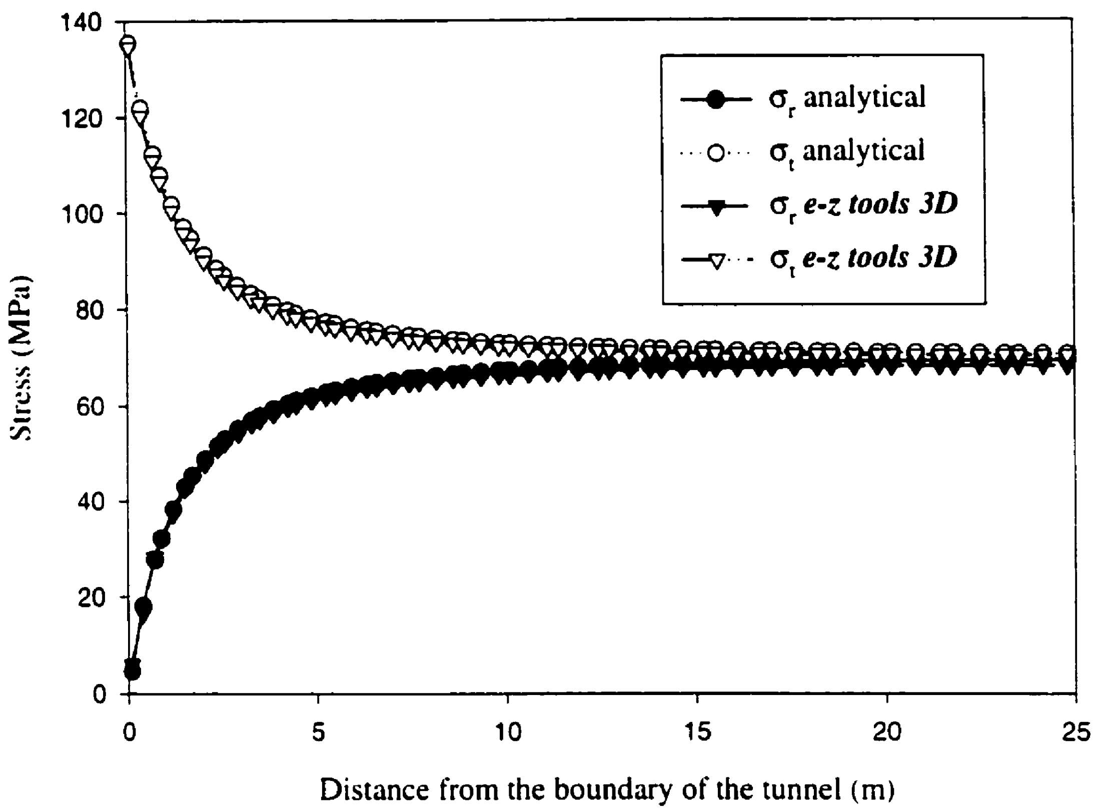

Figure 6.2 Tangential and radial stress distribution around the circular opening at $\phi = 90^0$, under hydrostatic pressure of 70 MPa

To compare with the model results, the analytical calculation points are coincident with the element integration points in the radial direction, but there is a slight difference in the tangential direction as shows in. Figure 6.2 and 6.3 present the stresses distributions along the radial line at $\phi = 90^0$ (vertical direction) and $\phi = 0^0$ (horizontal direction) respectively with hydrostatic stress condition (K = 1). And Figure 6.4 and 6.5 show the stress distributions when K = 0. The results near the opening boundary also are presented in Table 6.2 for K = 1 and Table 6.3 for K = 0. These results show excellent agreement between the analytical and ***e-z tools 3D*** solutions. When k = 1, the difference between the

Table 6.2 Peak stress comparison of circular opening (K = 1, a = 2.5m)

	Calculated position (r/a)	σ_t/p		σ_r/p	
		Analytical	*e-z tools 3D*	Analytical	*e-z tools 3D*
Point A	1.0348	1.9338	1.9214	0.066	0.0848
Point B	1.0348	1.9338	1.9270	0.066	0.0854

stress concentration factors for tangential stress at point A is 0.0124, and at point B is 0.0068. For radial stress the difference at point A and B are 0.0188 and 0.0194 respectively. These differences are mostly affected by the finite element mesh density.

Through the model verification, some basic conclusions on the finite element model ***e-z tools 3D*** can be obtained. They are:

- The model is mathematically correct,
- Physically true, i.e., it reflects the elastic behaviour of the structural materials.

Based on the two conclusions drawn above, the next important step is to perform the parametric study to better understand the model response to variation of input parameters.

Table 6.3 Peak stress comparison of circular opening (K = 0, a = 2.5m)

	Calculated position (r/a)	σ_t/p		σ_r/p	
		Analytical	*e-z tools 3D*	Analytical	*e-z tools 3D*
Point A	1.0348	2.7751	2.7215	0.0926	0.13574
Point B	1.0348	-0.8412	-0.8023	-0.0265	-0.05071

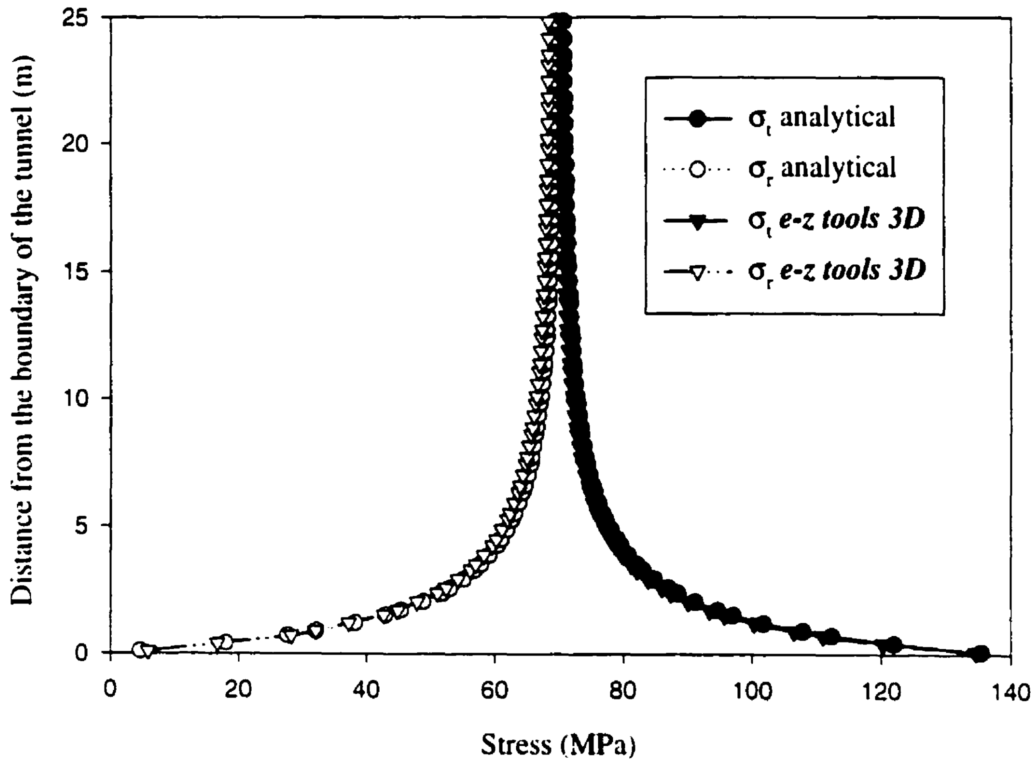

Figure 6.3 Tangential and radial stress distribution around a circular opening under hydrostatic pressure of 70 MPa at $\phi = 0^0$

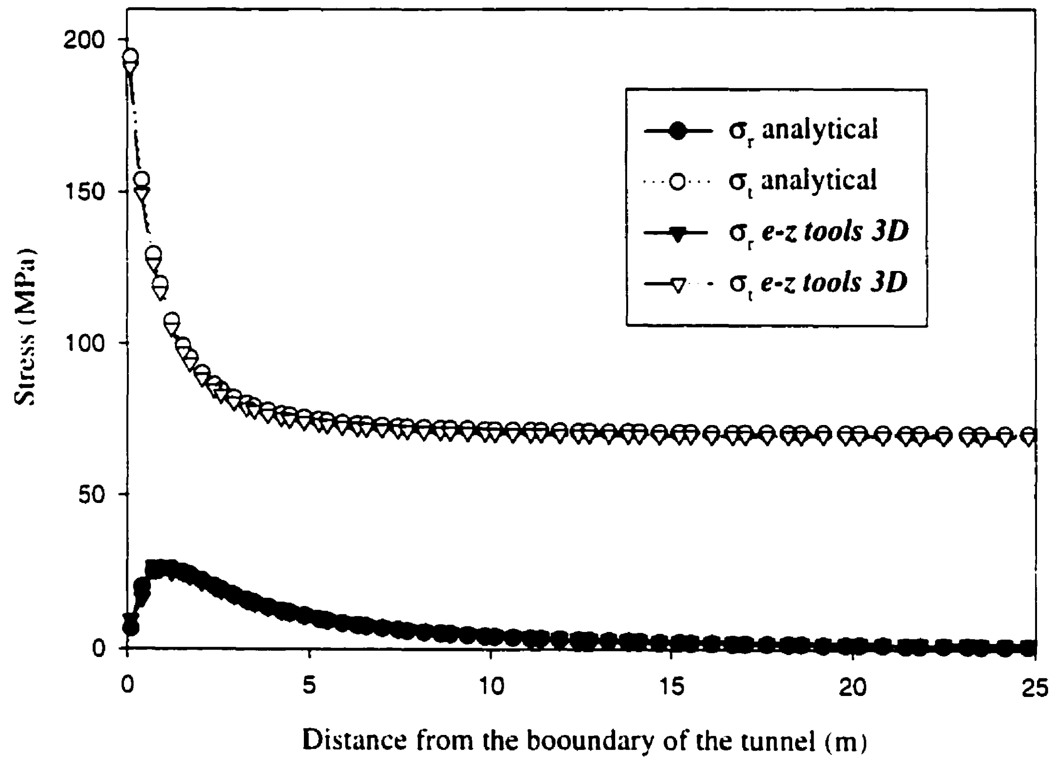

Figure 6.4 Tangential and radial stress distribution around the circular opening under vertical pressure of 70 MPa with k = 0 at $\phi = 90^0$

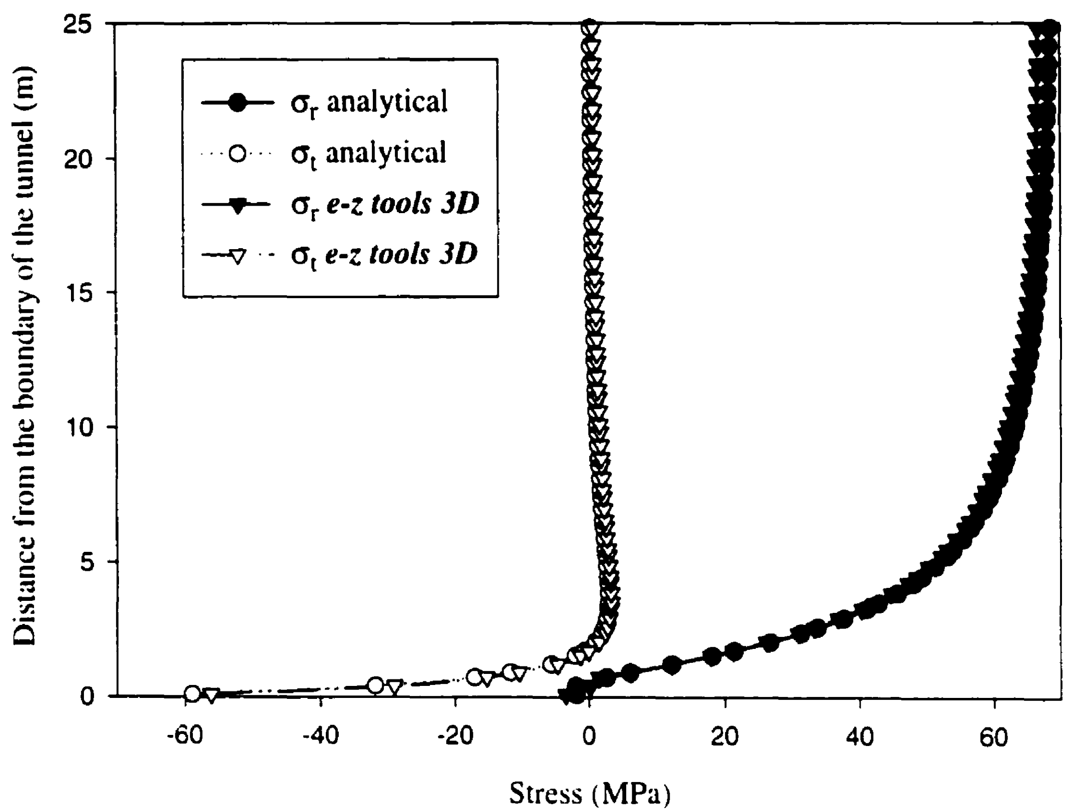

Figure 6.5 Tangential and radial stress distribution around the circular opening under vertical pressure of 70 MPa with k = 0 at $\phi = 0^0$

6.3 MODEL PARAMETRIC STUDY ON DESTRESS BLASTING PATTERNS FOR DRIFT DEVELOPMENT

6.3.1 Problem Definition

In this section, numerical model ***e-z tools 3D*** is applied to the problem of drift development at depth in hard rock mining; refer to Figure 5.2 and Figure 5.6. This problem is commonly found in Canadian mines. The drift is 4.3m wide by 3.7m high and is situated 2156m (7000 ft) below surface. A case study is carried out using different destress blasting patterns for a given α and β. The finite element mesh is shown in Figure 6.13.

Referring to Figure 6.6, after the second face advance, the rests of the face advances are just the repetition of the second face advance. So in the following parametric study, the results will be only presented for the initial configuration and the situation after two face advances.

The rock mass is assumed to be homogeneous, isotropic and linear elastic. The relevant geomechanical parameters are:

Unit weight $\gamma = 0.028$ MN/m^3

Poisson's ratio $\nu = 0.15$

Elastic modulus $E = 78$ GPa

Uniaxial compression strength $\sigma_c = 180$ MPa

Rock fragmentation factor $\alpha = 0.4, 1.4$

Stress dissipation factor $\beta = 0.6$

The horizontal to vertical in situ stress ratios are:

$K_{xx} = 2$ and $K_{yy} = 1.4$

The natural stress tensor at depth of 2152m (7000 ft) is:

$\sigma^0_y = 120.52$MPa

σ^0_x = 84.36MPa

σ^0_z = 60.26MPa (Vertical)

Three different destress blasting patterns have been selected for the simulation; they are shown in Figure 6.7. The selection of such blasting patterns is based on the literature survey of destress blasting practice in hard rock mines (Chapter 3). The destress patterns used are:

- All -perimeter destressing (pattern 1)
- Full-face-and-corner destressing (pattern 2)
- Wall -and-corner destressing (pattern 3)

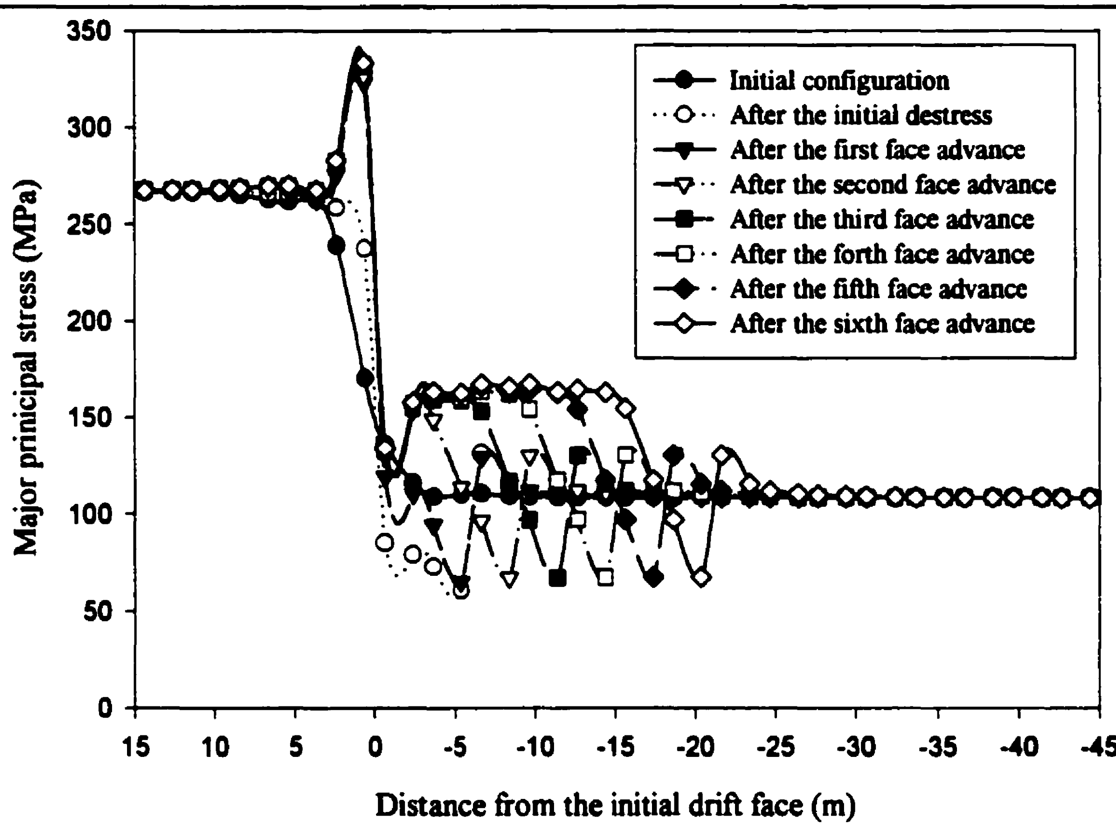

Figure 6.6 The demonstration of the results repetition due to six face advances

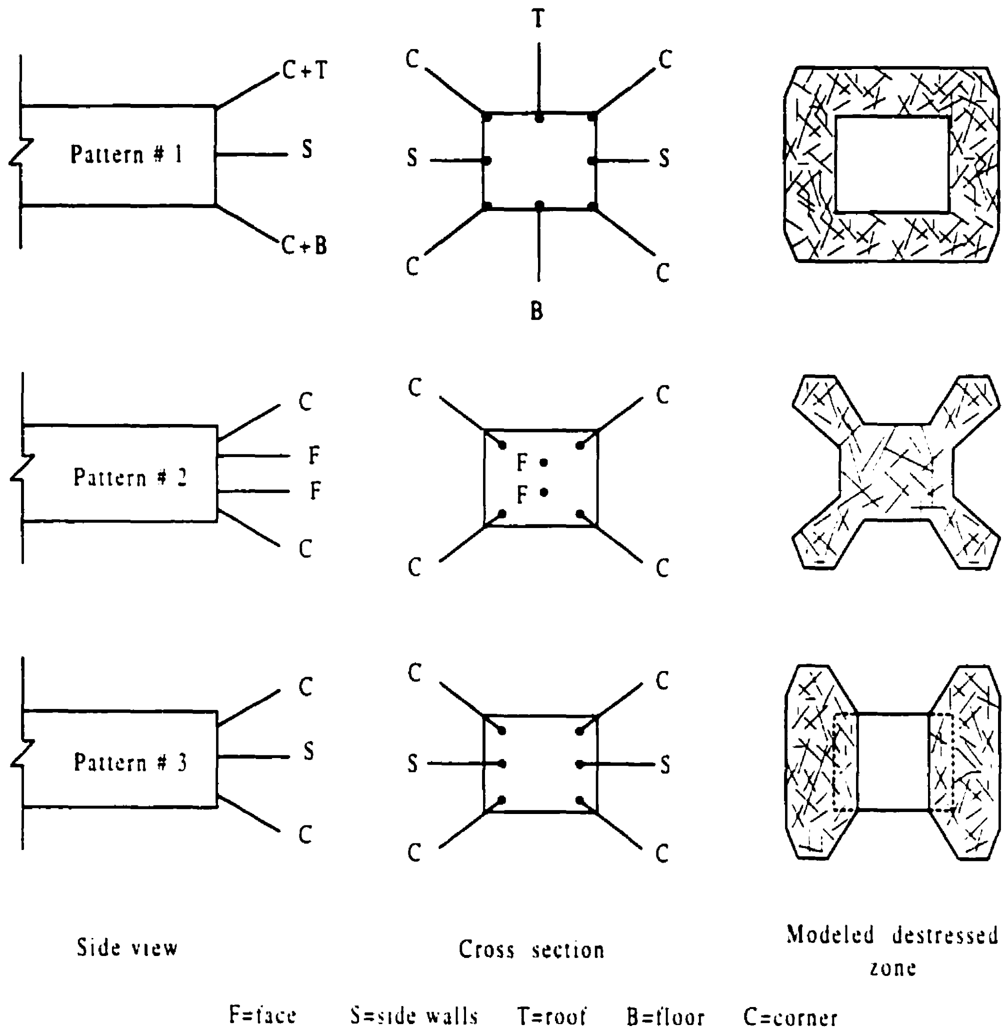

Figure 6.7 Destress blasting patterns

6.3.2 Numerical Results

Modeling of the initial drift configuration (Figure 5.2a) shows that the Burst Potential Index (BPI) is quite high, and can be as much as 174 % in the drift corners some distance behind the drift face; see Figure 6.8. This suggests that destress blasting is required. The computations were done for the four modeling sequences depicted in Figures 5.2a, 5.2b, 5.2c, 5.2d, i.e. before destressing, after destressing, and after one face advance, after two face advances respectively.

The major principal stress contours in the drift face before and after destressing are shown in Figure 6.9a and 6.9b for blasting pattern 1. As can be seen, destressing has caused stress reduction in the face. Also, it is observed that the maximum stress is found in the drift corners. A comparison of the major principal stresses along the drift corners, before and after destressing is shown in Figure 6.10. It is evident that the principal stress drops significantly ahead of the face. Table 6.4 summarizes the results of maximum face stresses for all three patterns. It is found that the maximum face stress is nearly horizontal and is reduced from 248.83 MPa to 153.21 MPa for blasting pattern 1, 156.29 MPa for pattern 2, and 180.29 MPa for pattern 3.

Furthermore, it appears from the numerical modeling results that the maximum stress in the drift is found along the corners behind the face. The major principal stress profiles along the longitudinal axis of the drift are computed for the corner stress in the drift back, both behind and ahead of the drift face. The results are shown in Figures 6.11 and 6.12. As is evident from the results, blasting pattern 1 appears to be more effective in terms of reducing the stresses ahead of the face.

Table 6.4 Maximum face stresses before and after destressing

Pattern	Maximum face stress	
	Before (MPa)	After (MPa)
Pattern 1	248.83	153.21
Pattern 2	248.83	156.29
Pattern 3	248.83	180.29

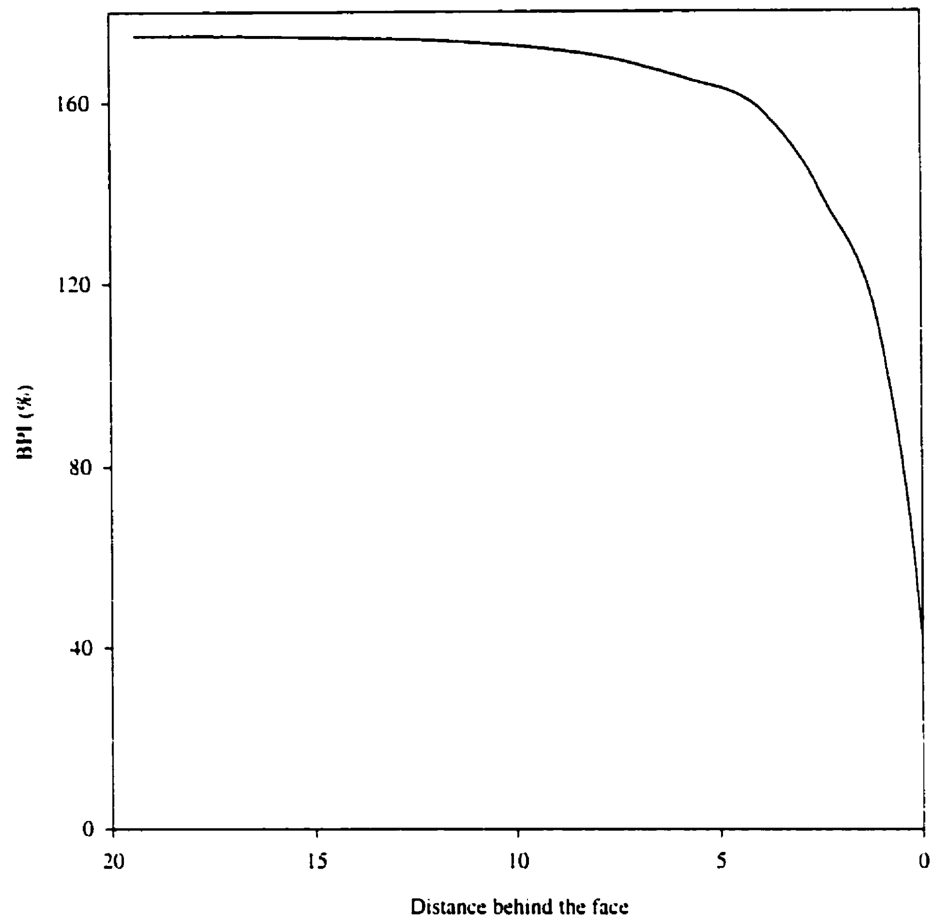

Figure 6.8 Burst potential index (BPI) behind the face-initial configuration

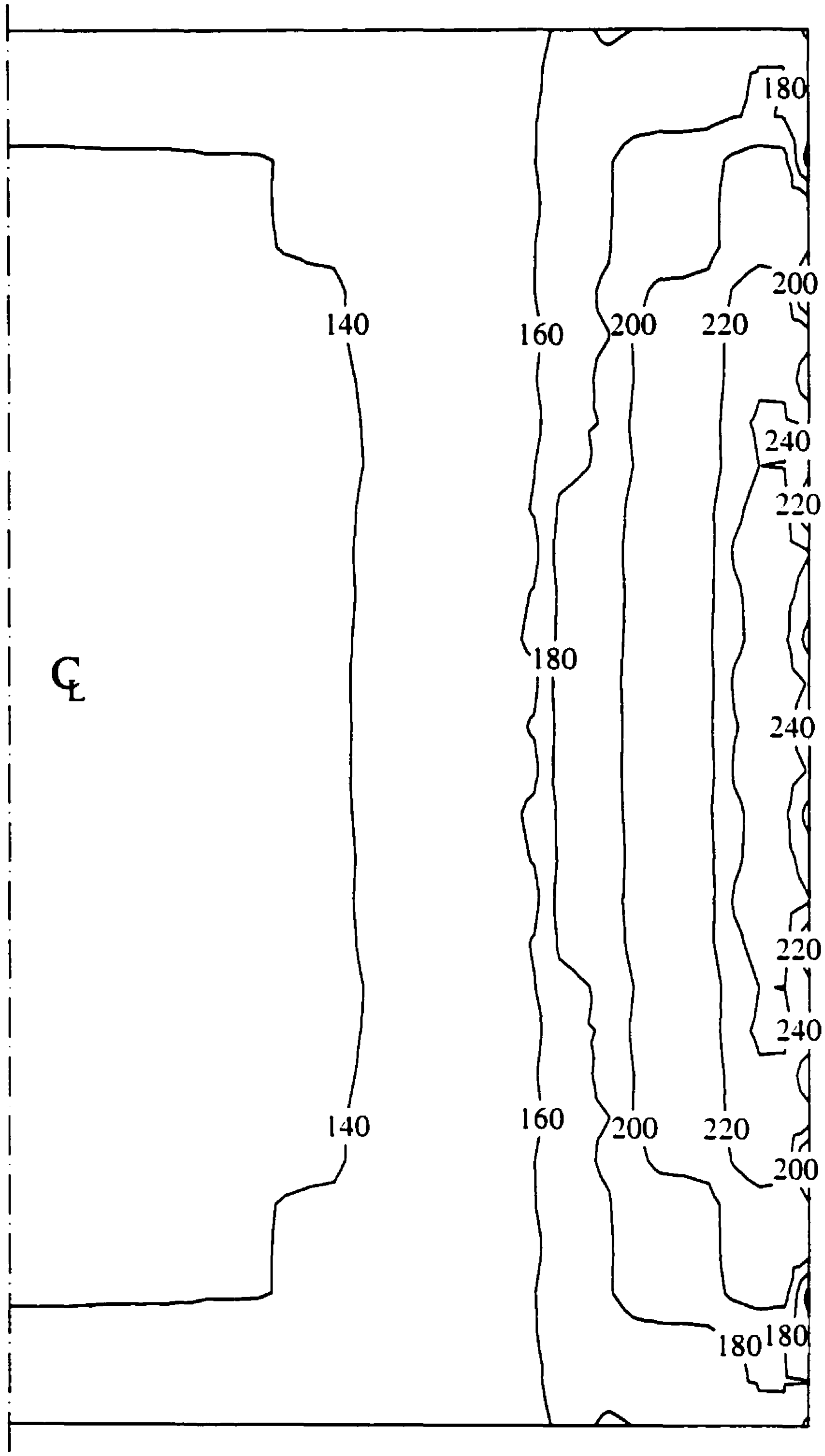

Figure 6.9a Major principal stress distribution in the face before destressing

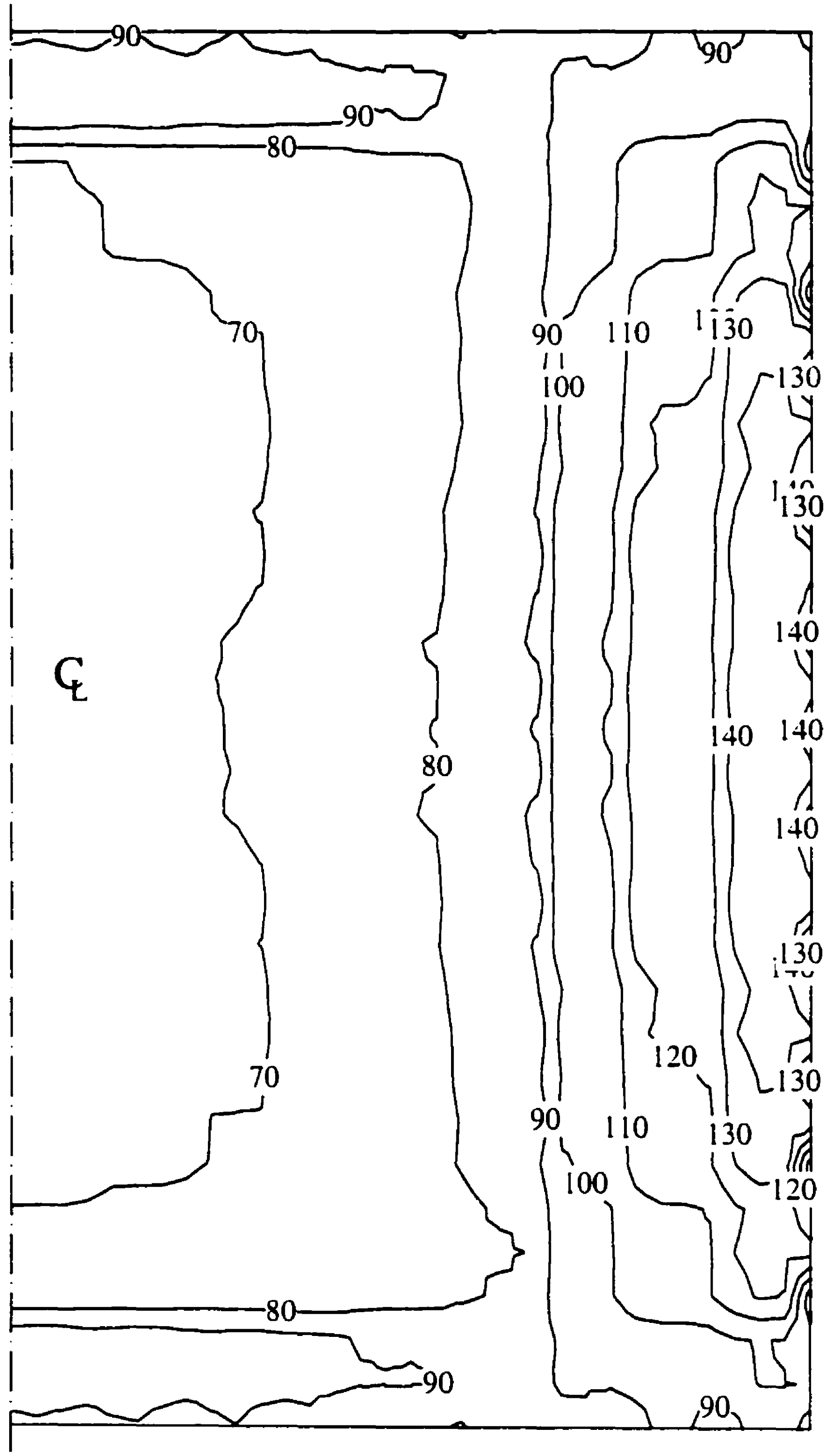

Figure 6.9b Major principal stress distribution in the face after destressing

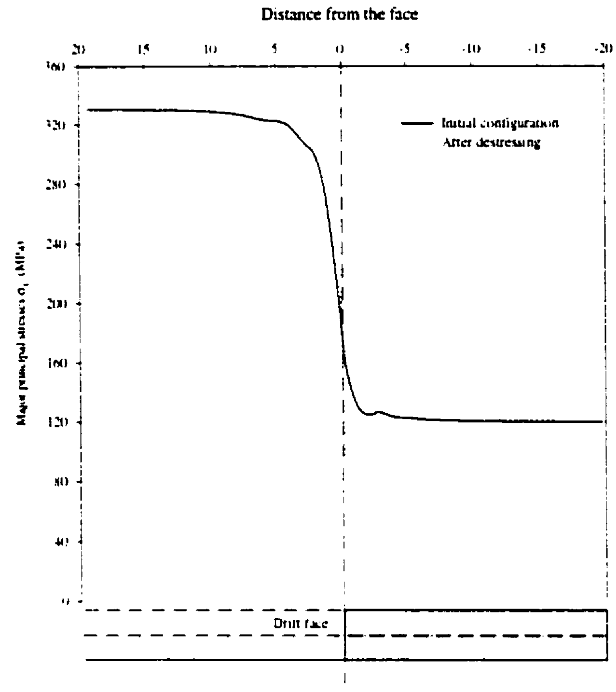

Figure 6.10 Major principal stress distribution for blasting pattern 1

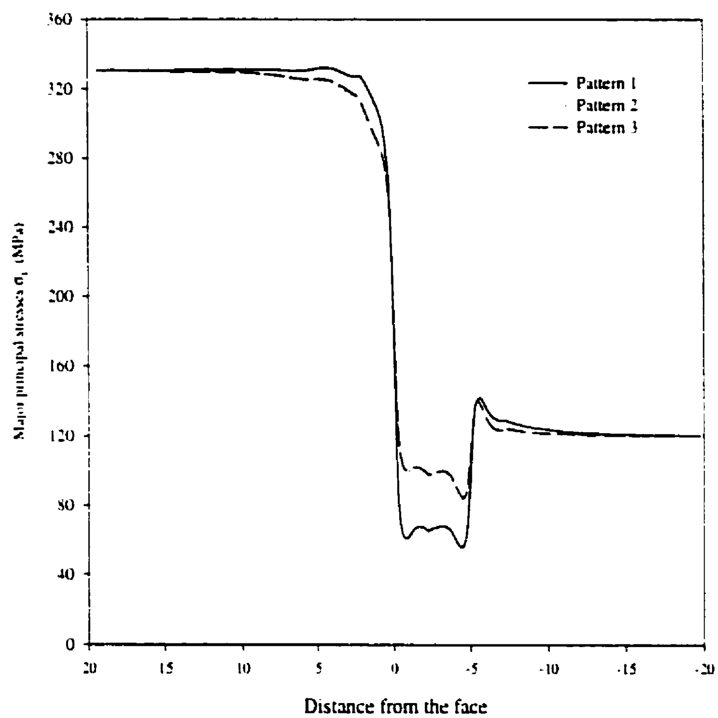

Figure 6.11 Major principal stress distribution after destress blasting

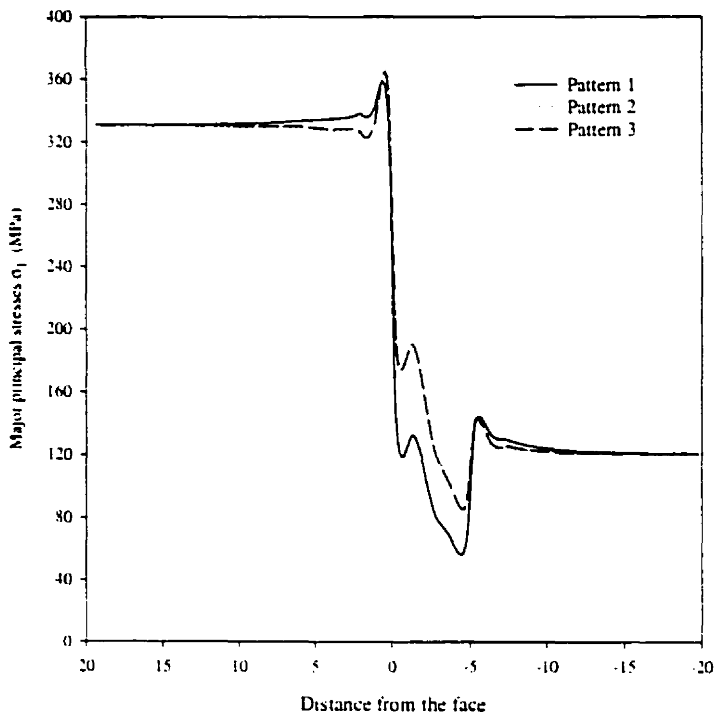

Figure 6.12 Major principal stress distribution after face advance

6.4 EFFECT OF THE ROCK FRAGMENTATION FACTOR α

As destress blasting is aimed to reduce the field stress around mining openings, this is achieved by blast-induced fractures resulting in a release of strain energy in the fractured zone. The brittle to ductile transition is accomplished through fundamental changes in both inelastic behaviour and failure mode. The micromechanical processes are extremely complex, involving the interaction of a multiplicity of defects (e.g., microcracks, voids, dislocations, and mechanical twins) (Evan, et al., 1990). Although one cannot expect any theory to model exactly the destress blasting mechanisms, there are at least some empirical models that can approximate the process. The rock fragmentation factor $\{\alpha\}$ is one of them abstracted from our current understanding to the destress blasting. In this section the effect of the various values of $\{\alpha\}$ is presented using the same drift problem described in section 6.3. Due to the symmetry of the problem, half of the opening is

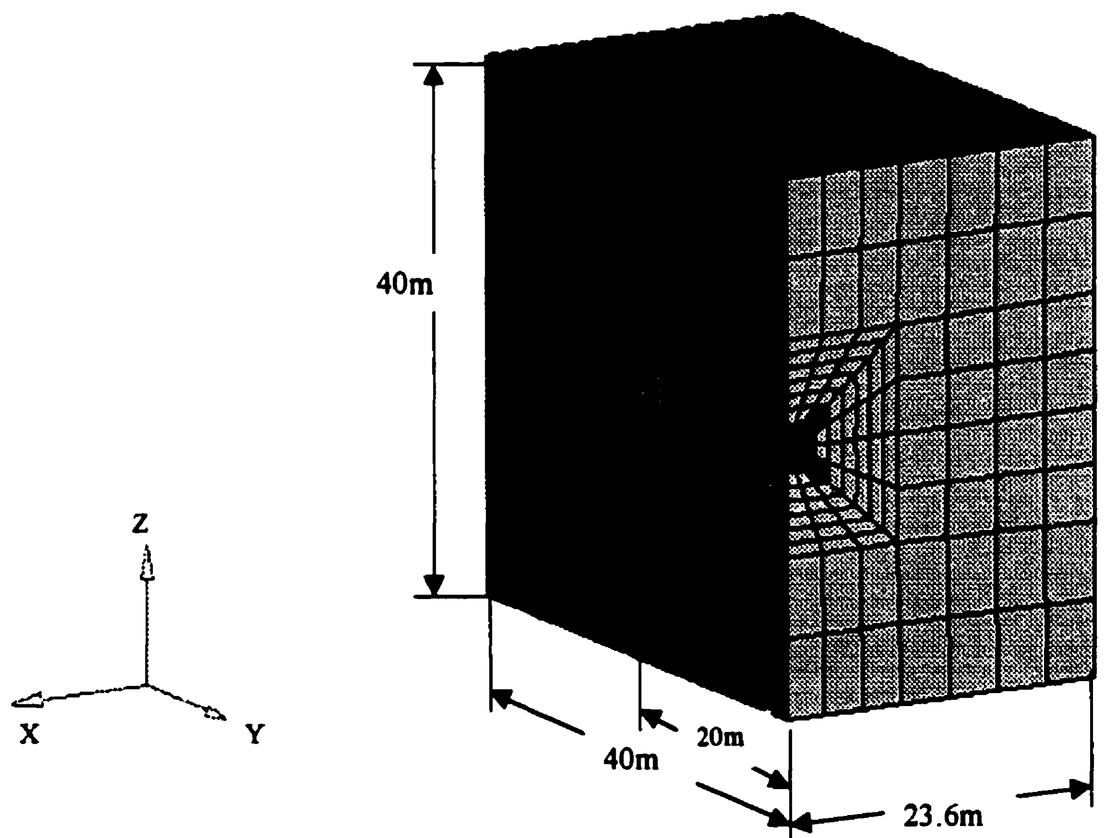

Figure 6.13 Finite element mesh for the parametric study

simulated (see Figure 6.13).

The feature points and sections along the drift are defined as shown in Figure 6.14. The major principal stresses at feature points on the first two sections, before destress blasting, are shown in Table 6.5. The stress distribution along the lines passing by points B_i, C_i, A_i, in Figure 6.14, are plotted in Figure 6.15, Figure 6.16, and Figure 6.17 respectively. Figure 6.18 presents the major principal stress contour just in front of the drift initial face.

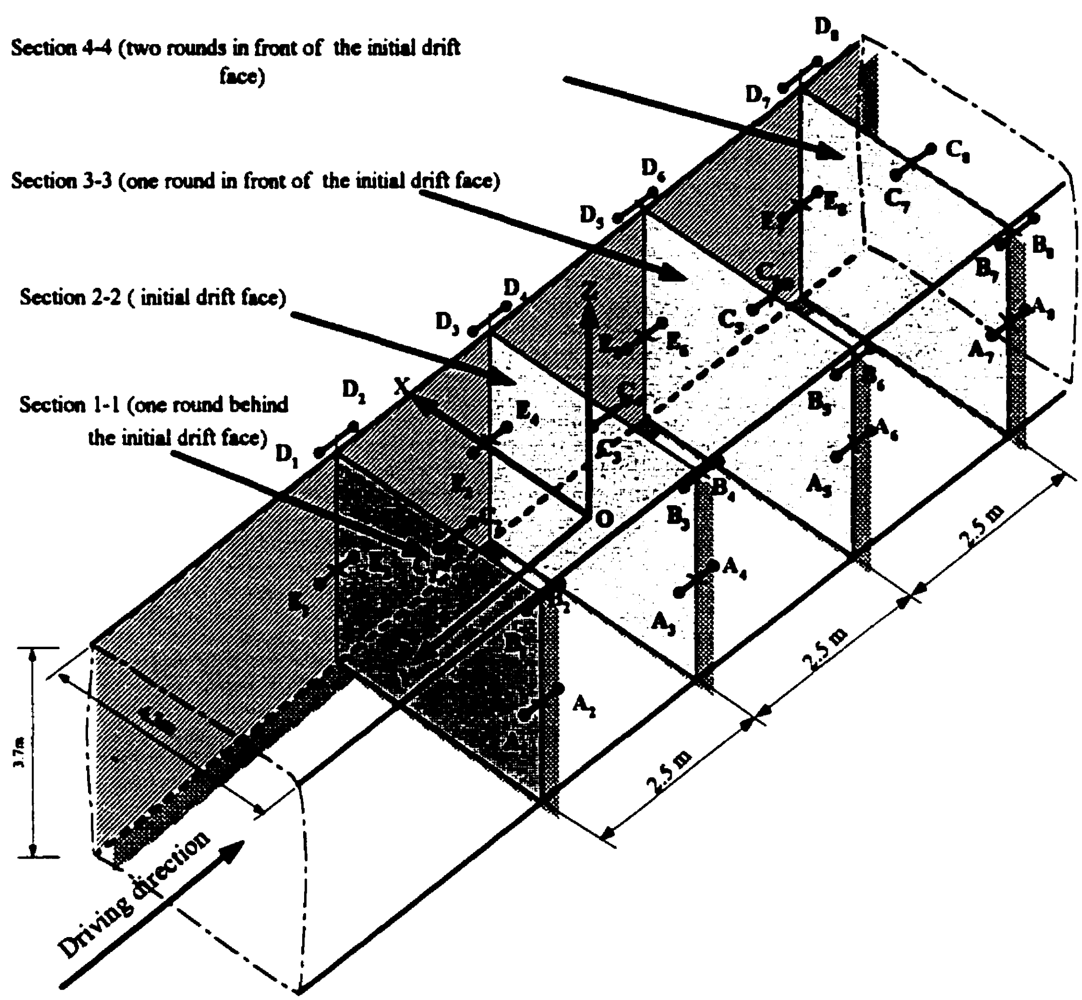

Figure 6.14 Feature points definition for the drift development

Table 6.5 Major principal stress at feature points before destress blasting

Point	σ_1 (MPa)	ESR (MJ/m^3)	Point	σ_1 (MPa)	ESR (MJ/m^3)	Point	σ_1 (MPa)	ESR (MJ/m^3)
A_2	62	-7.5×10^{-2}	A_3	164.6	1.4×10^{-2}	A_4	120.5	-8.6×10^{-4}
B_2	248.7	0.1894	B_3	173.1	9.5×10^{-2}	B_4	137.6	1.9×10^{-4}
C_2	121.66	1.5×10^{-2}	C_3	143.1	3.2×10^{-2}	C_4	124.6	2.1×10^{-2}

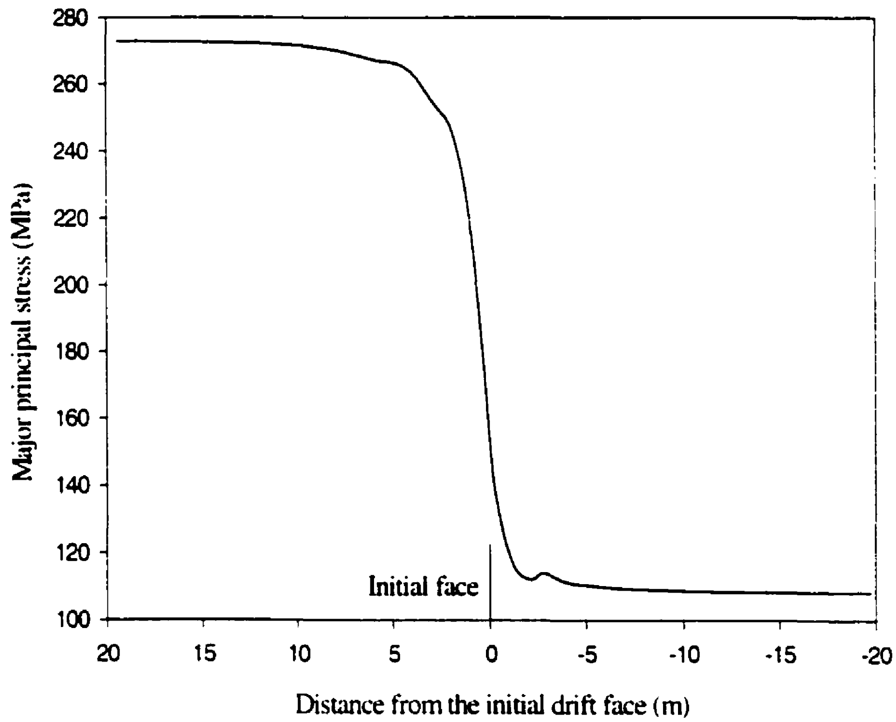

Figure 6.15 Major principal stress distribution along the line passing by points B_i before destress blasting

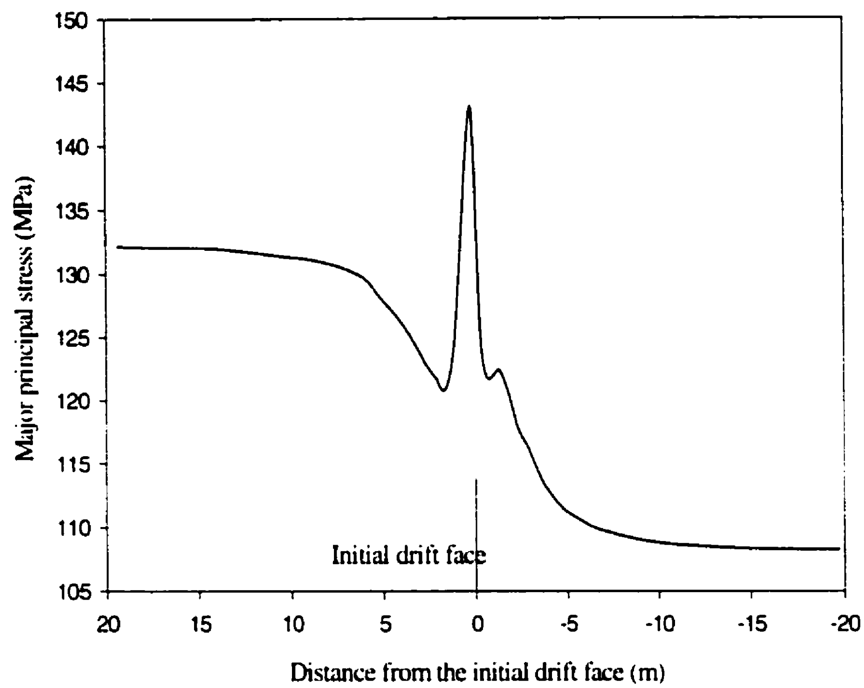

Figure 6.16 Major principal stress distribution along the line passing by points C_1 before destress blasting

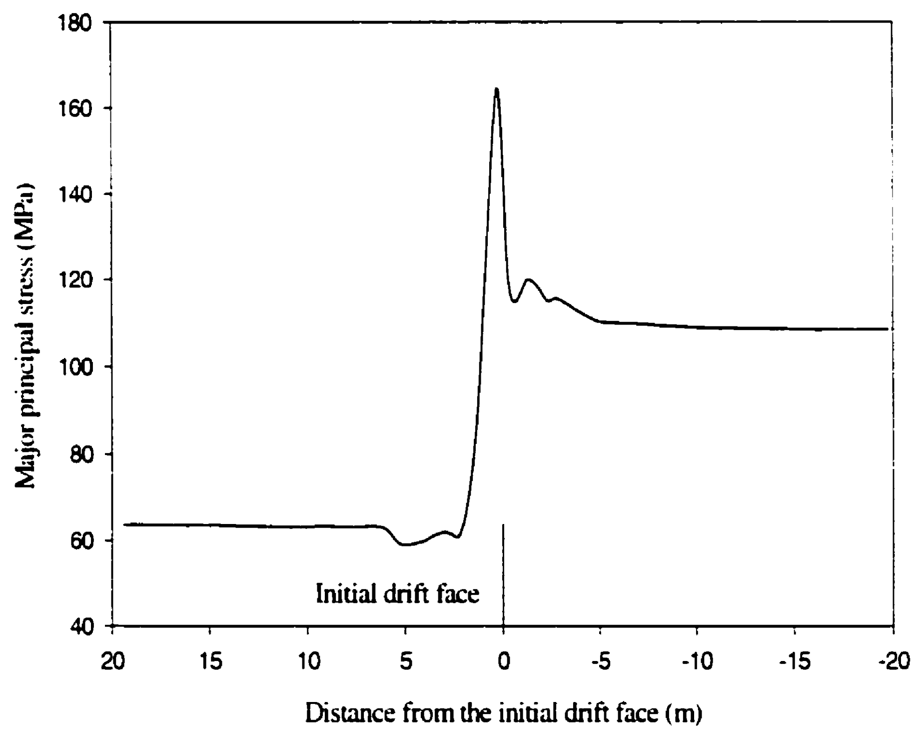

Figure 6.17 Major principal distribution along the line passing by points A_1 before destress blasting

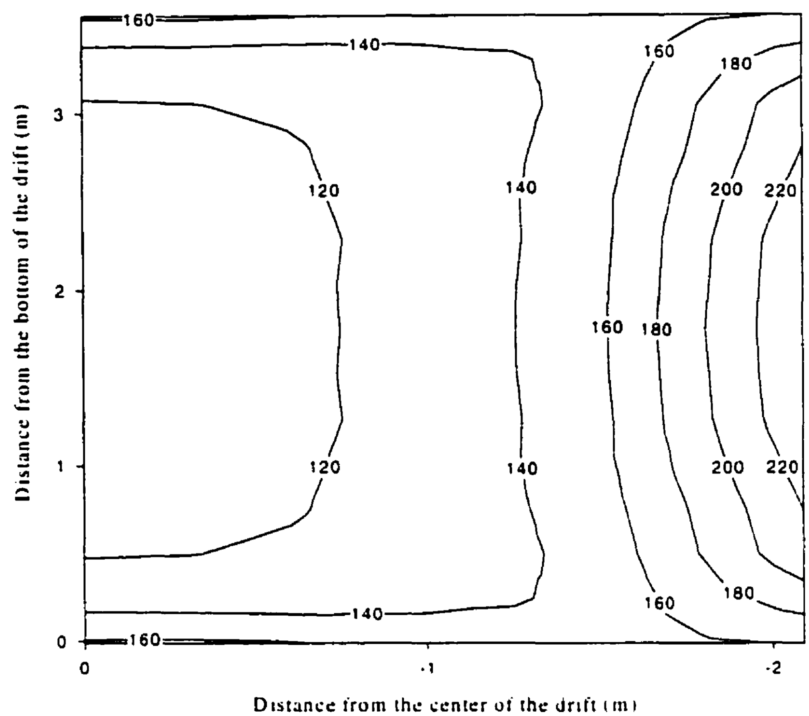

Figure 6.18 Major principal stress contours just in front of the drift initial face before destress blasting

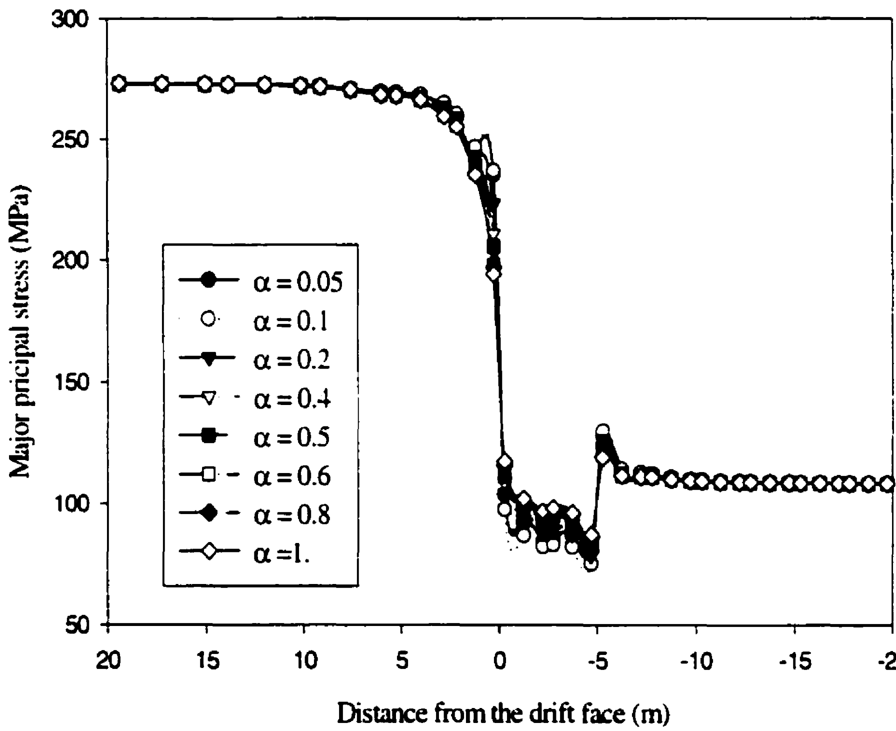

Figure 6.19 Variation of the major principal stress along the line passing by points B_i with α

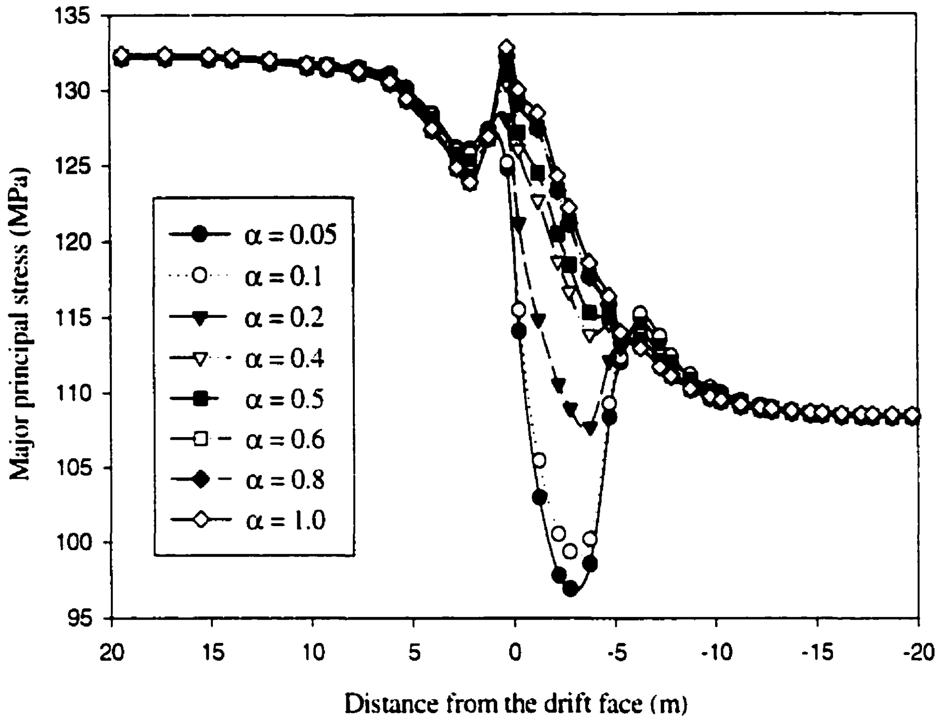

Figure 6.20Variation of the major principal stress along the line passing by points C, with α

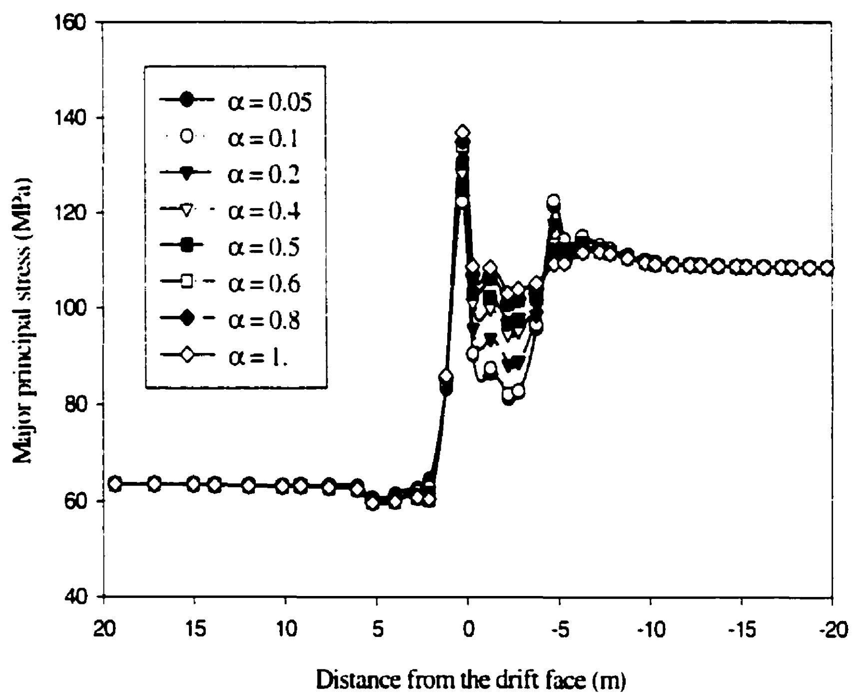

Figure 6.21 Variation of the major principal stress along the line passing by points A, with α

Table 6.6 Major principal stress changes at feature points vs. rock fragmentation factor α just after two face advances while destress blasting

Feature points σ_1(MPa)									
	One round behind the drift face			Just behind the drift face			Just in front of the drift face		
α	A6	B6	C6	A7	B7	C7	A8	B8	C8
0.05	50.6	127	79.3	108	106.4	106.8	85.7	110	95.9
0.1	50.8	133	80.7	113	106	111.4	91	109	97.8
0.2	53.7	160	89.7	120	121.7	116.7	97	115	107.3
0.4	56.9	194	99.5	128	140.5	122.5	103.6	120	116.5
0.5	58	205	102	132	146	124.4	105.6	121	119.1
0.6	60.3	230	108	140	157.2	128.2	109.6	122	123.6
0.8	60.5	232	109	141	159.3	128.8	109.2	123	123.9
1	61.5	244	111	145	164.4	130.5	111	123	125.6

Referring to Table 6.1. rock fragmentation factor {α} has been varied from 1.0 to 0.05 with $\beta = 0.4$ and $\varphi = 0^{0}$. $\theta = 0^{0}$. The decrease of α represents rock mass stiffness reduction due to destressing. The stress variations with the changes of the rock fragmentation factor α are plotted in Figure 6.19 to Figure 6.21 along the lines passing by B_i, C_i, A_i respectively. Figure 6.19 shows that the reduction of α has a great effect on σ_1 at the corner points. When α is larger than 0.4 the effect on the major principal stress is less obvious than when α is smaller than 0.4. Figure 6.20 shows the slight affection at the top center point. And Figure 6.21 presents the influence of the rock fragmentation factor at the side points of the drift referring to Figure 5.2. Table 6.6 gives the major principal stress changes at feature points vs. rock fragmentation factor after two face advances and destress blasting.

Figure 6.22, Figure 6.23 and Figure 6.24 shows the major principal stress distribution after two face advances along the lines passing by points A_i, B_i and C_i respectively which show the decrease of the principal stress behind the drift face. However, on section 4-4, the variation of the rock fragmentation factor α has much more influence on the major principal stress at the top and side than at the corner. This can also be seen from Figure 6.19 to Figure 6.24 that the major principal stress has a downward trend with the decrease of α. Comparing Figure 6.18 and Figure 6.25, a substantial reduction is seen in the major principal stress in front of the drift face after destressing.

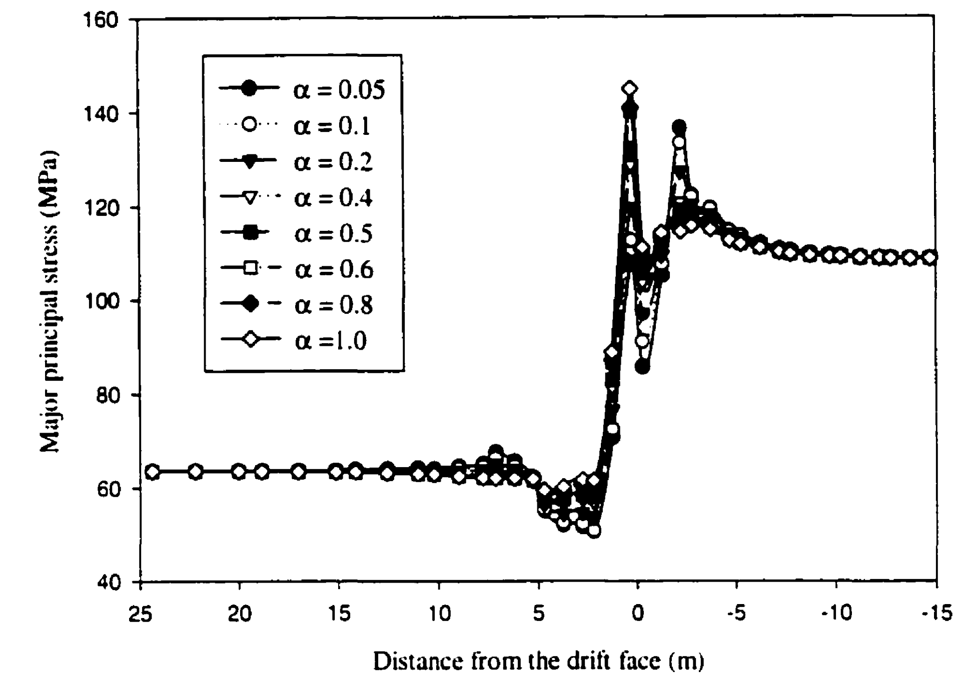

Figure 6.22 Variation of the major principal stress along the line passing by points A_i with α after two face advances

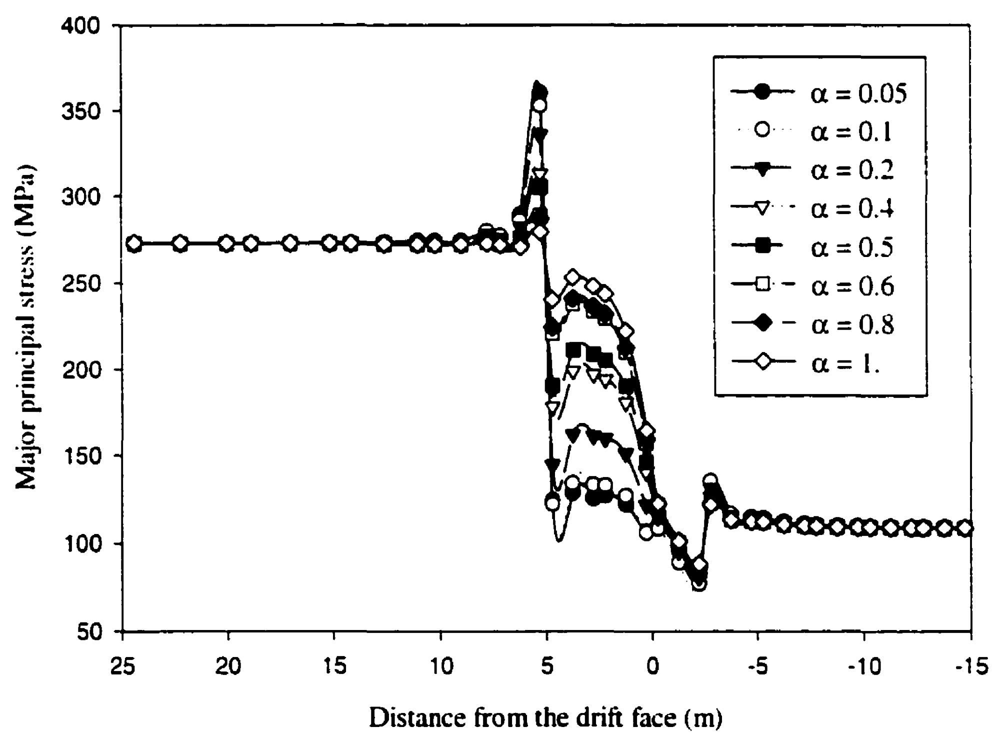

Figure 6.23 Variation of the major principal stress along the line passing by points B_i with α after two face advances

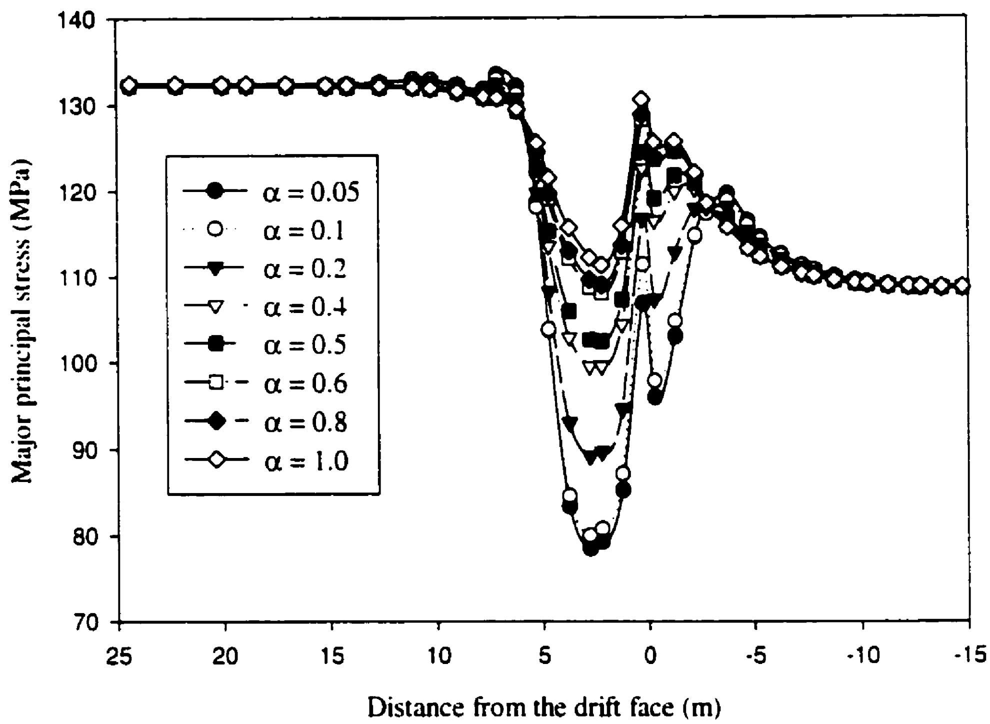

Figure 6.24 Variation of the major principal stress along the line passing by points C, with α after two face advances

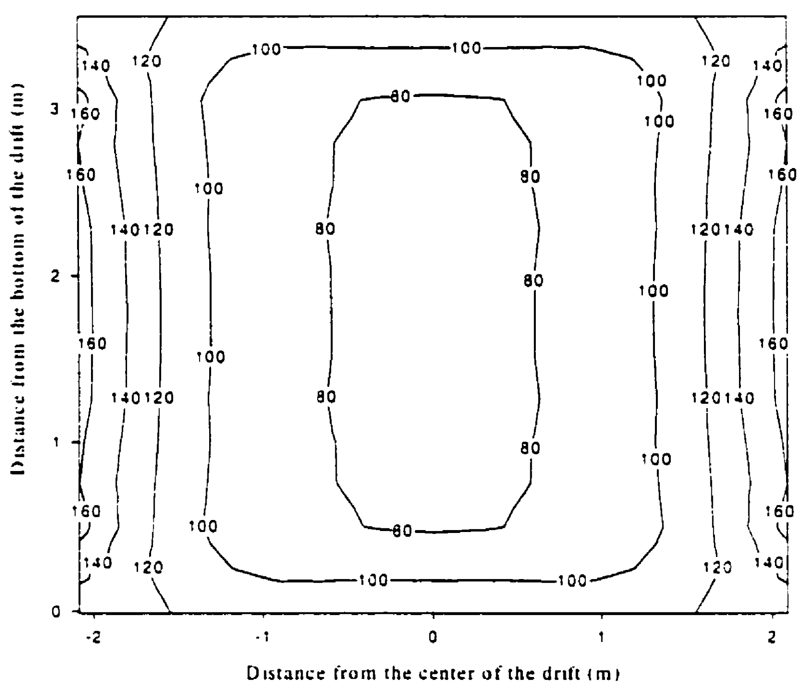

Figure 6.25 Major principal stress contour just in front of the drift face after two face advances

6.5 EFFECT OF STRESS DISSIPATION FACTOR β

In this section, the same finite element model will be used to study the effect of stress dissipation factor to the effectiveness of destress blasting practice. Referring to Table 6.1 the stress dissipation factor β has been varied in the range from 0.1 to 1.0 with constant $\alpha = 0.4$, $\varphi = 0^0$ and $\theta = 90^0$. Also the horizontal to vertical premining stress ratios were kept unchanged.

Table 6.7 Major principal stress changes at feature points vs. stress dissipation factor β just after two face advances while destress blasting

	Points								
	One round behind the drift face			Just behind the drift face			Just in front of the drift face		
β	A6	B6	C6	A7	B7	C7	A8	B8	C8
0.1	87.4	188.9	115.7	146.1	150.2	135.5	114.6	130.4	120.1
0.2	85.6	188.2	112.4	140.3	148.4	130.9	109.9	127.7	119.4
0.3	83.5	184.5	108.3	134.7	144.2	126.7	106.6	123.9	118
0.4	81.2	180.8	104.4	128.7	140.5	122.5	103.6	119.7	116.5
0.5	78.9	174.4	99.3	122.5	134.8	118.5	100.7	115.8	114.5
0.6	76.4	173.3	96.2	115.8	134.5	114.2	98.1	110.5	113
0.8	70.7	164	87.2	101	129	105.1	93.8	99.2	108.6
1.0	65.9	159.8	81.9	87.7	129.2	97.7	87.7	88.5	104.4

The variation of major principal stress distribution vs. stress dissipation factor β after two drift-advances along the lines passing by A_i, B_i, C_i are plotted in Figure 6.26 to 6.28. At feature points on section 3-3 and 4-4, the major principal stresses variation with the increase of the β are shown in Table 6.7.

Referring to Table 6.7, the major principal stress at the feature points on the section 3-3 and section 4-4 have the same trends, and they decrease with the increase of stress dissipation factor β. Figure 6.26, 6.27, and 6.28 show that the value of β has a larger effect on the major principal stress along the corner of the drift when it is larger than 0.4 than when it is less than 0.4. From the major principal stress distribution along the chosen lines, the numerical results show that the stress dissipation factor β has the same important role to the evaluation of the effectiveness of destress blasting as the rock fragmentation factor α. does. Figure 6.29 shows clearly that the stress at three feature points B6, B7, B8 are decrease with the increase of β.

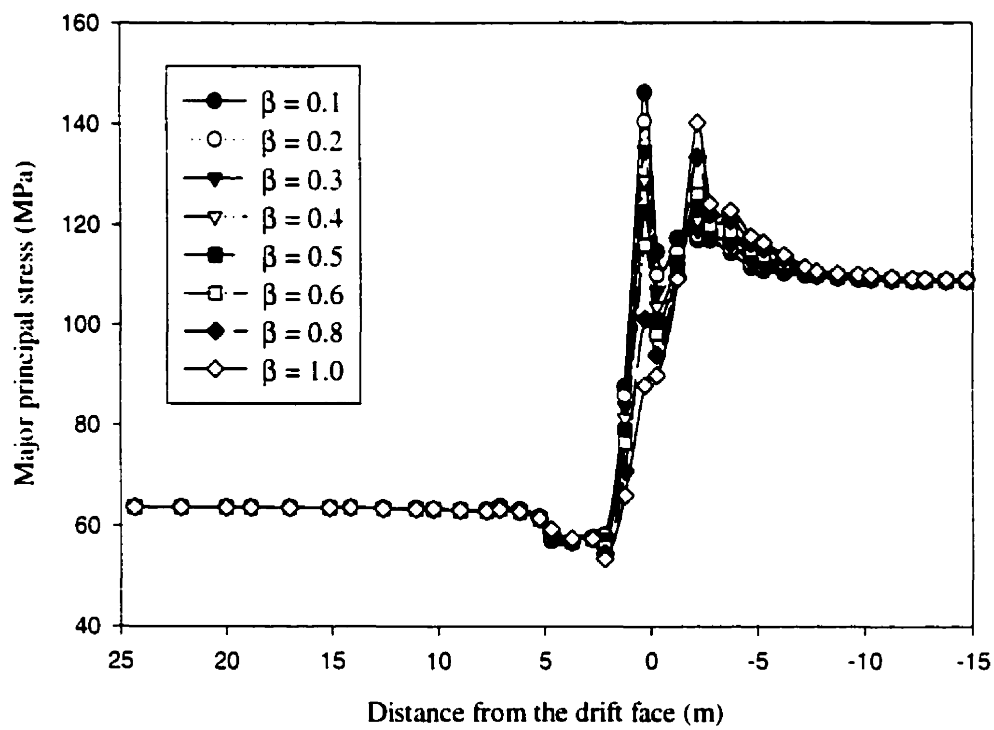

Figure 6.26 Variation of the major principal stress along the line passing by points A_i with β after two face advances

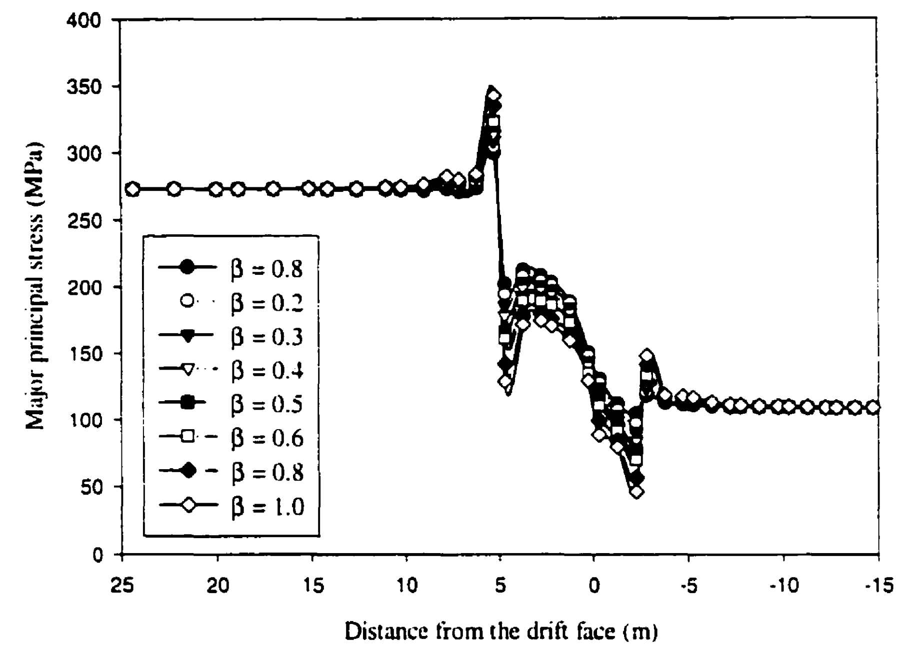

Figure 6.27 Variation of the major principal stress along the line passing by points B_1 with β two face advances

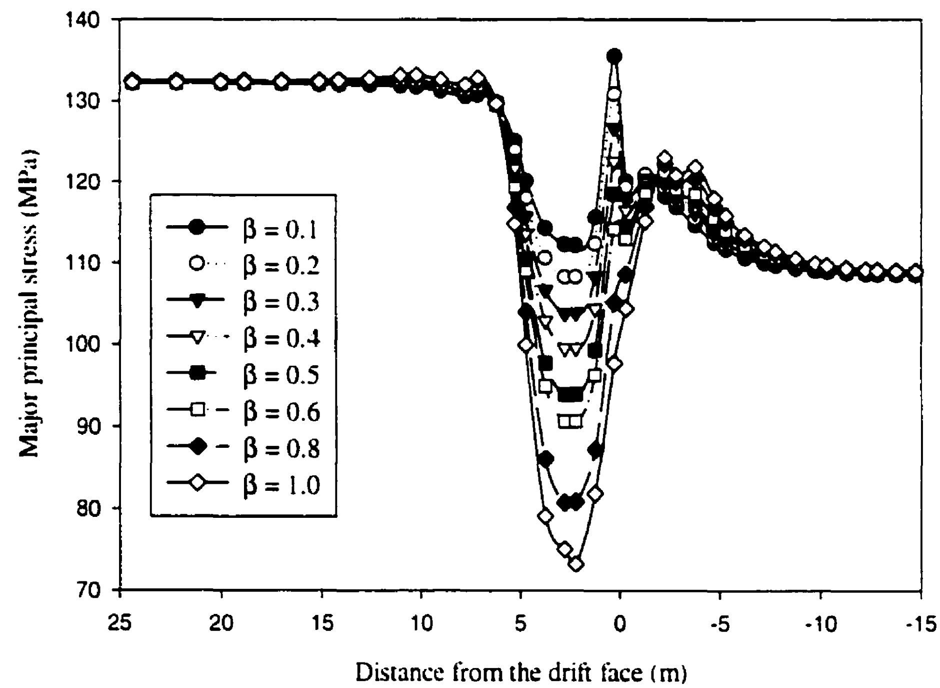

Figure 6.28 Variation of the major principal stress along the line passing by points C_1 with β after two face advances

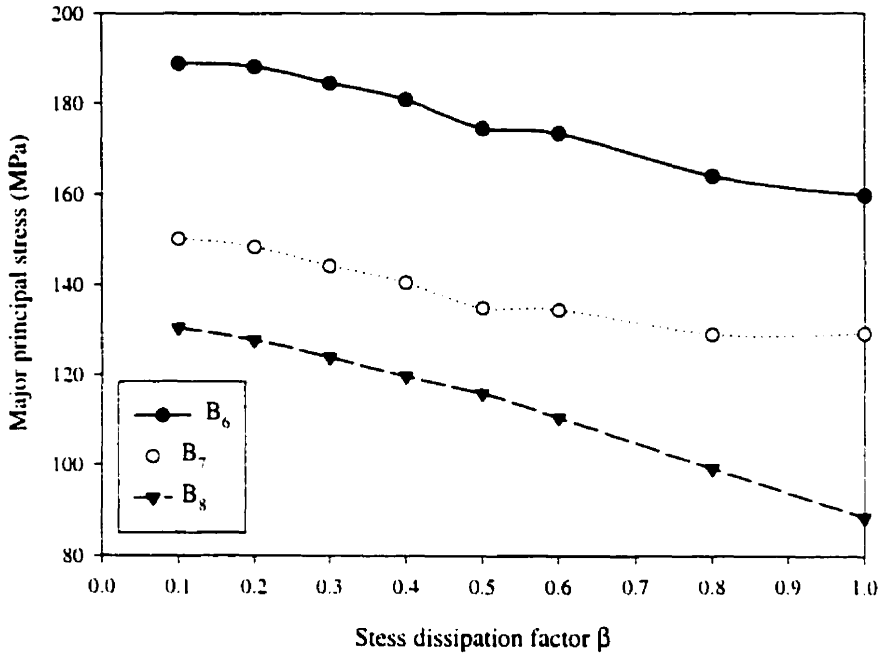

Figure 6.29 Effect of β on stress reduction in the drift corner after two face advances

6.6 EFFECT OF THE ORIENTATION OF THE DRIFT AXIS WITH RESPECT TO THE MAJOR PRINCIPAL IN SITU STRESS

In the previous analyses, the major horizontal in situ stress was assumed to be in a direction perpendicular to the drift longitudinal axis, i.e. in the x-direction. This is not always the case in practice, whereby access ramps, drifts and cross cuts may be driven in different directions thus making an angle with the major horizontal principal in situ stress, σ_1. In this section, the effect of the orientation of the drift axis with respect to σ_1 is examined. For this purpose, the angle θ is defined as the clockwise angle between the drift longitudinal axis (y-axis) and the major horizontal in situ stress σ_1 in its local coordinates (x'); refer to Figure 6.30. Accordingly, the previous analyses were conducted for $\theta = 90^0$. In this section, the values of 0^0, 30^0, 45^0, 60^0 and 90^0 will be analysed.

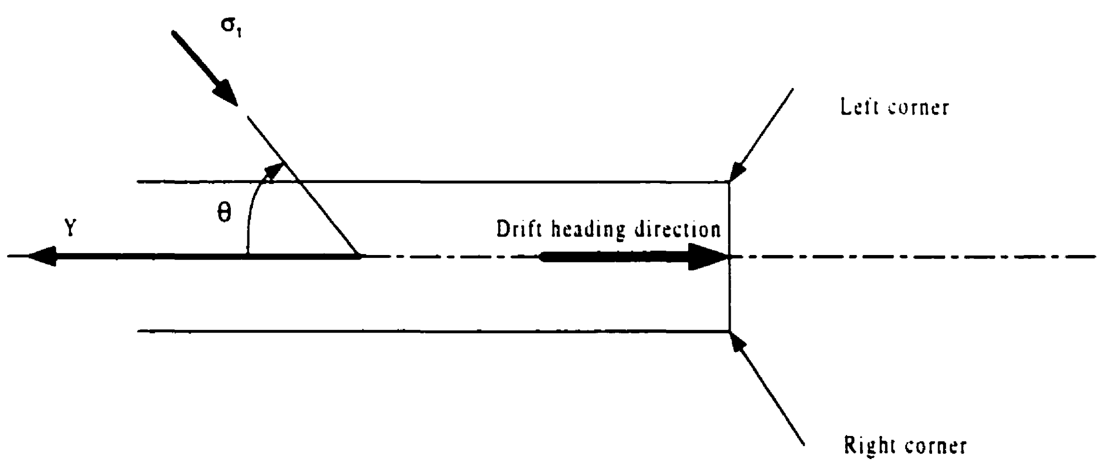

Figure 6.30 Definition of the angle θ in the drift plan view

The problem analysed is the same as before, i.e. the same geometric properties of the drift, and the same material properties are adopted. Due to the unsymmetrical loading condition from in situ stresses on the drift in this case, a new finite element mesh of the entire drift has been constructed. In previous analyses, only half of the drift needed to be modelled due to symmetry.

Modulus of elasticity

Poisson's ratio

Unit weight of the rock mass

Depth below surface

Horizontal –to-vertical ratio, Kx'

Horizontal –to-vertical ratio, Ky'

A total of five models were constructed for θ = 0,30, 45, 60, and 90 degrees. For each model, four mining sequences were simulated, as depicted in Figure 5.2. As mentioned earlier, the comparison of results is made between the first (initial) sequence before destress blasting and the fourth sequence, representing the conditions after two face advances. The numerical results are presented in terms of displacements and stresses. With reference to displacements, two quantities, Floor-to-roof convergence, Horizontal wall closure, have been defined as shown in Figure 6.31.

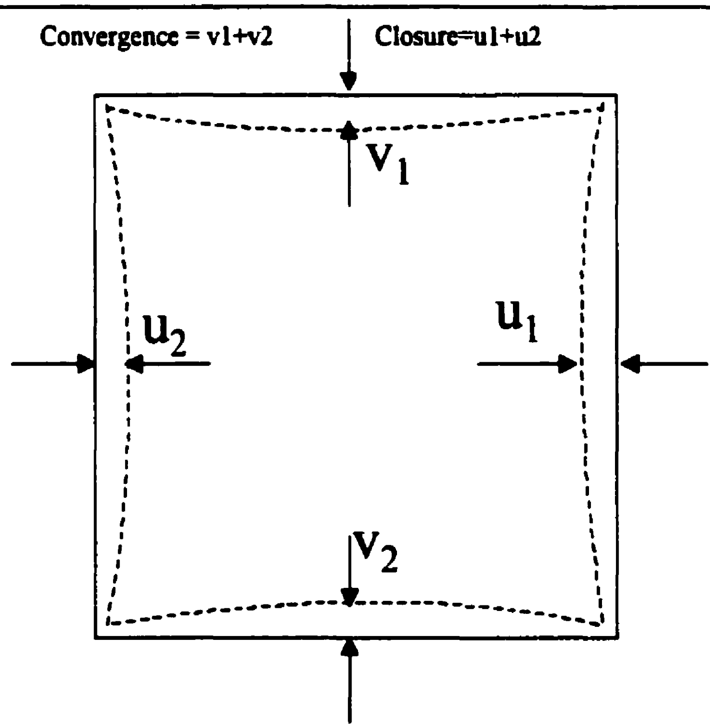

Figure 6.31 Definition of the drift deformation

The stress results are presented in a similar fashion to previous analyses, at the selected locations, A, B and C as per Figure 6.14.

Figure 6.32 to 6.33 respectively show the vertical and horizontal deformation of the drift with the variation of the angle θ before destress blasting and after two face advances one round behind the drift face. The variation of θ from 0^0 to 90^0 has resulted in the decrease of the horizontal closure and almost no change of vertical convergence. Figure 6.34 and Figure 6.38 show the major principal stress distribution along the two top corners, the roof centre and two side-centres of the drift respectively. Figure 6.39 to Figure 6.43 present the major principal stress distribution after two face advances while destressing with the various angle θ.

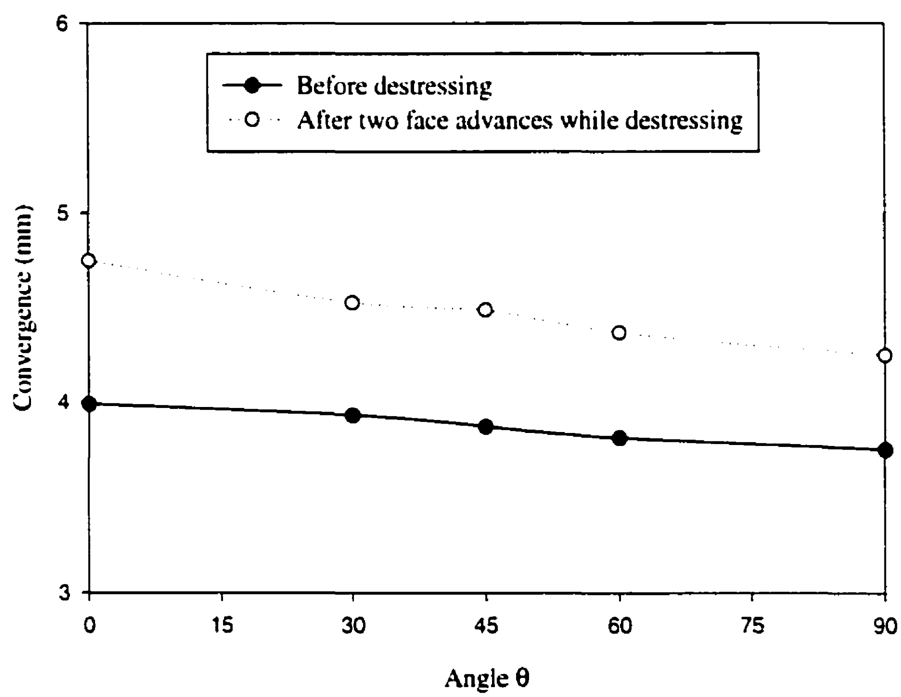

Figure 6.32 Vertical convergence one round behind the face before destress and after two face advances

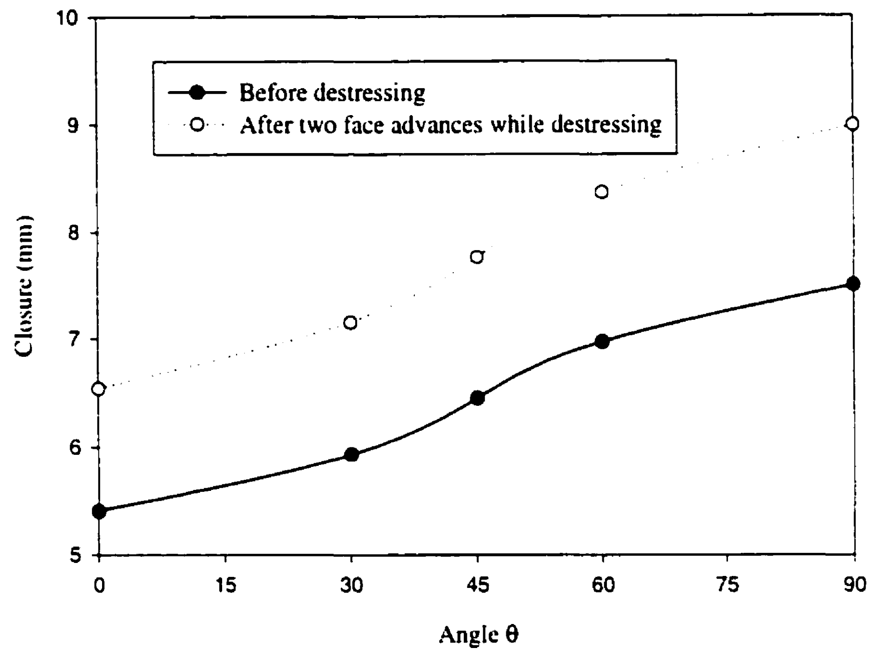

Figure 6.33 Horizontal closure one round behind the face before destress and after two face advances

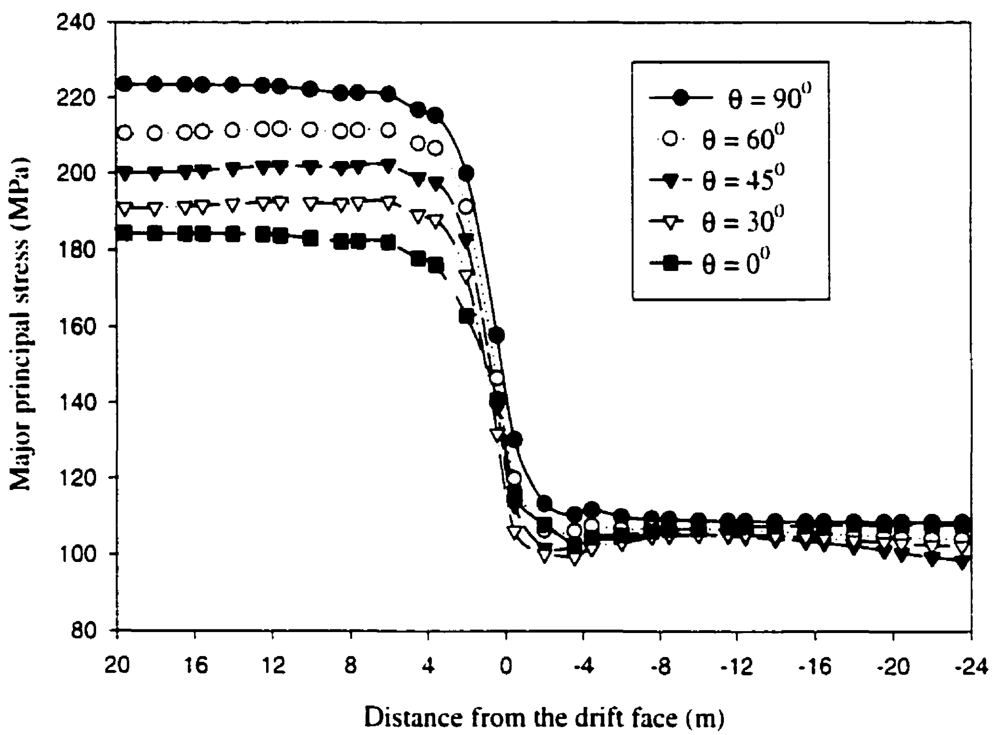

Figure 6.34 Variation of major principal stress distribution vs. strike angle θ along the right corner of the drift

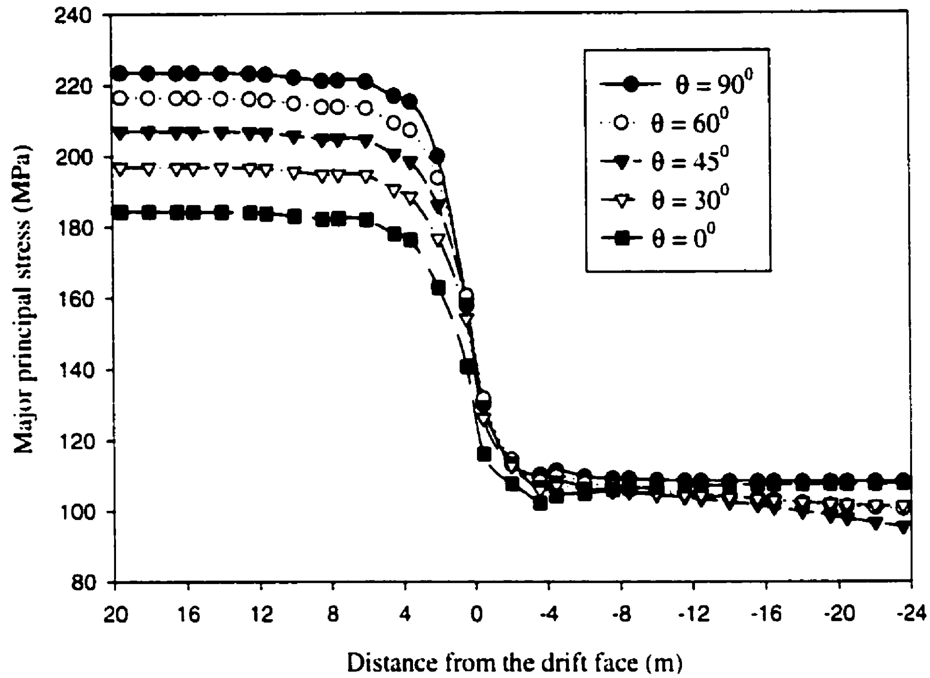

Figure 6.35 Variation of major principal stress distribution vs. strike angle θ along the left corner of the drift

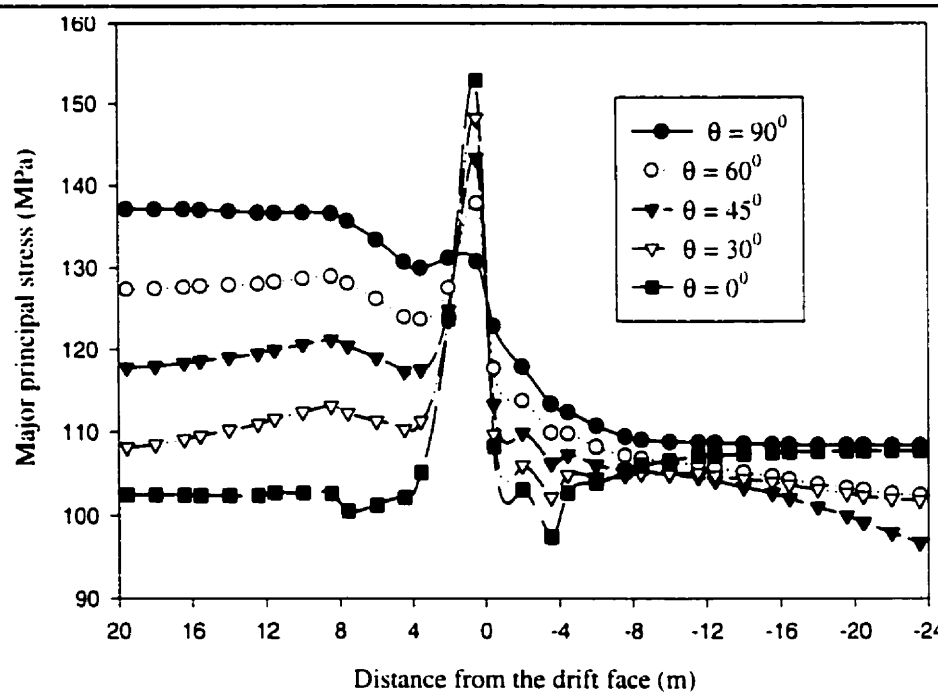

Figure 6.36 Variation of major principal stress distribution vs. strike angle θ along the roof centre of the drift

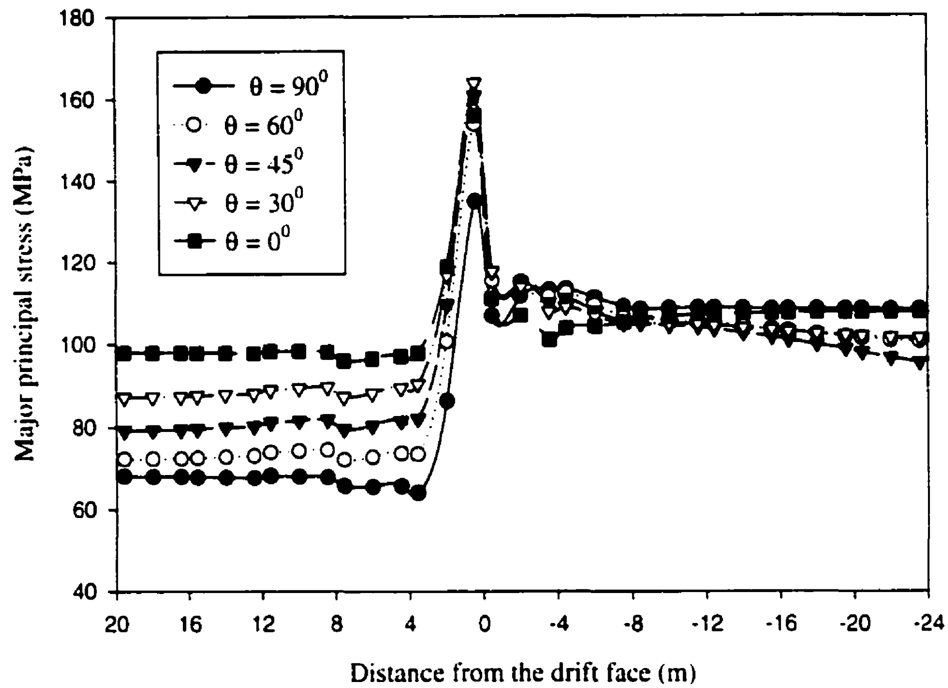

Figure 6.37 Variation of major principal stress distribution vs. strike angle θ along the left-side centre of the drift

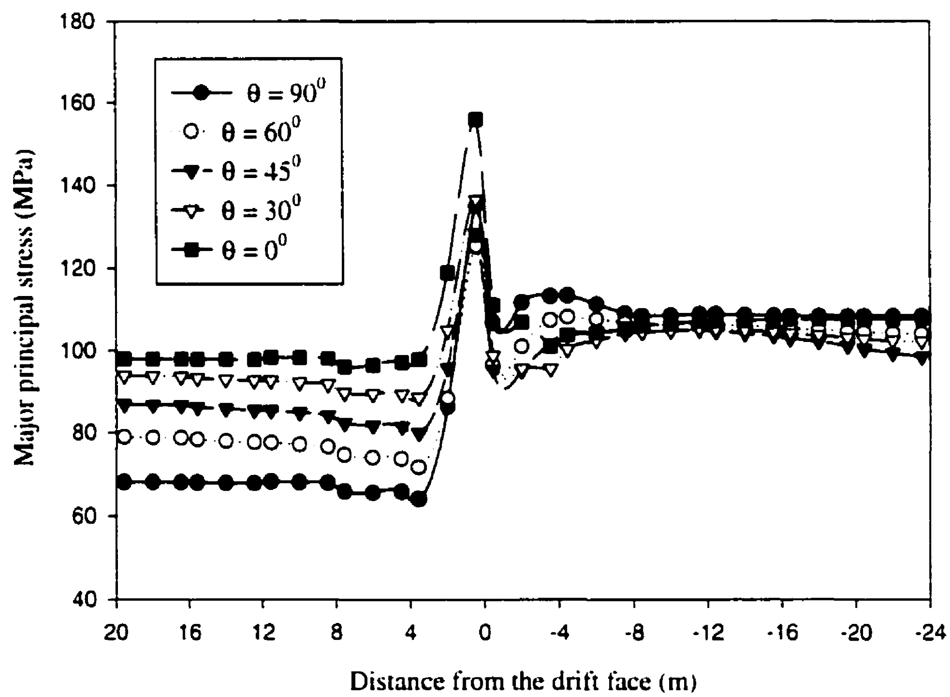

Figure 6.38 Variation of major principal stress distribution vs. strike angle θ along the right-side centre of the drift

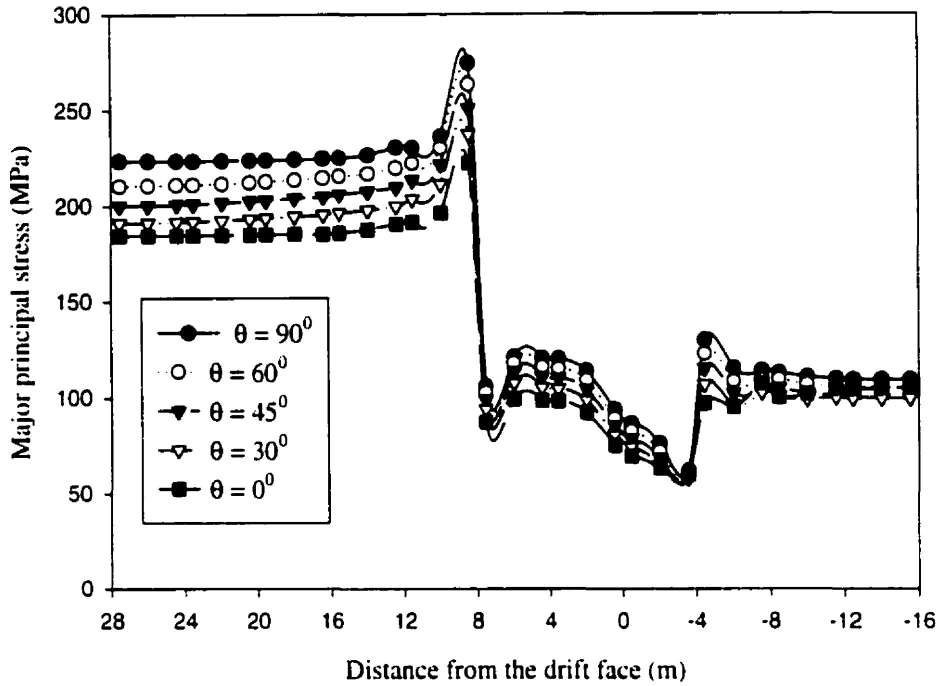

Figure 6.39 Variation of major principal stress distribution vs. strike angle θ along the right corner of the drift after two drift face advance

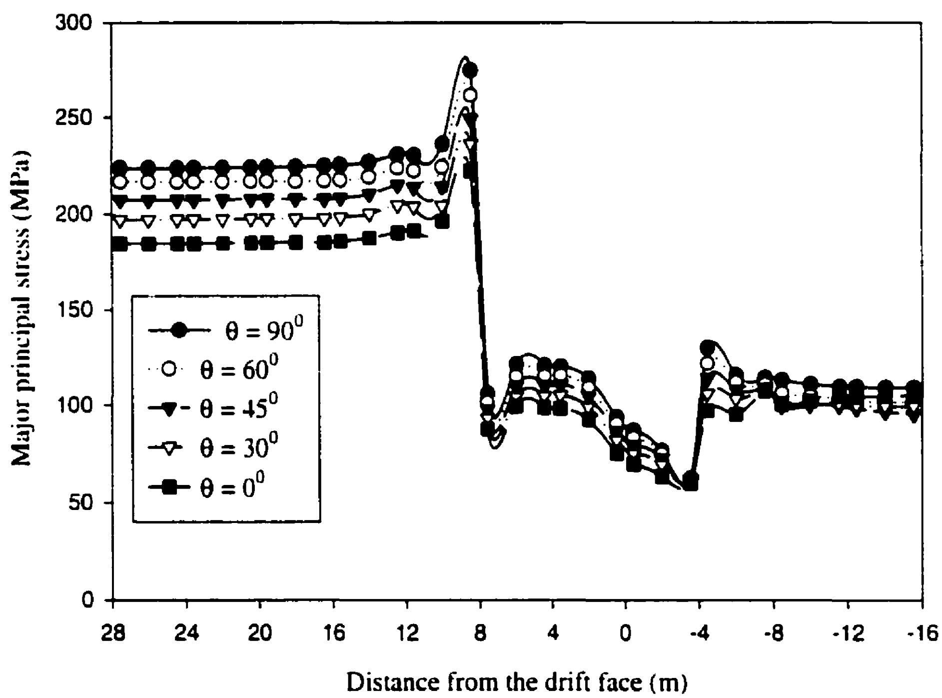

Figure 6.40 Variation of major principal stress distribution vs. strike angle θ along the right corner of the drift after two drift face advance

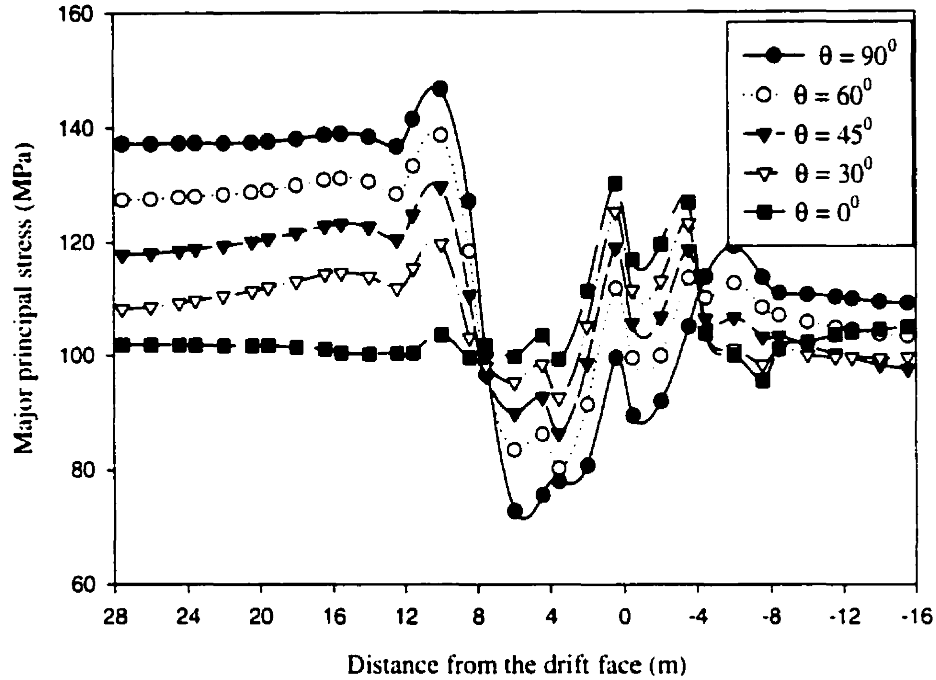

Figure 6.41 Variation of major principal stress distribution vs. strike angle θ along the roof centre of the drift after two drift face advance

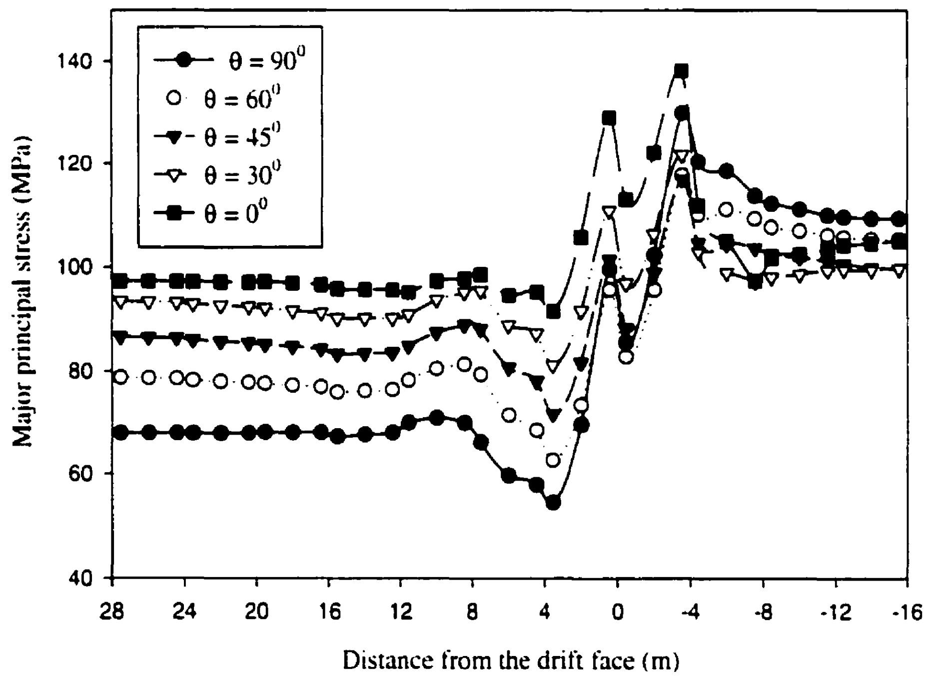

Figure 6.42 Variation of major principal stress distribution vs. strike angle θ along the right side centre of the drift after two drift face advance

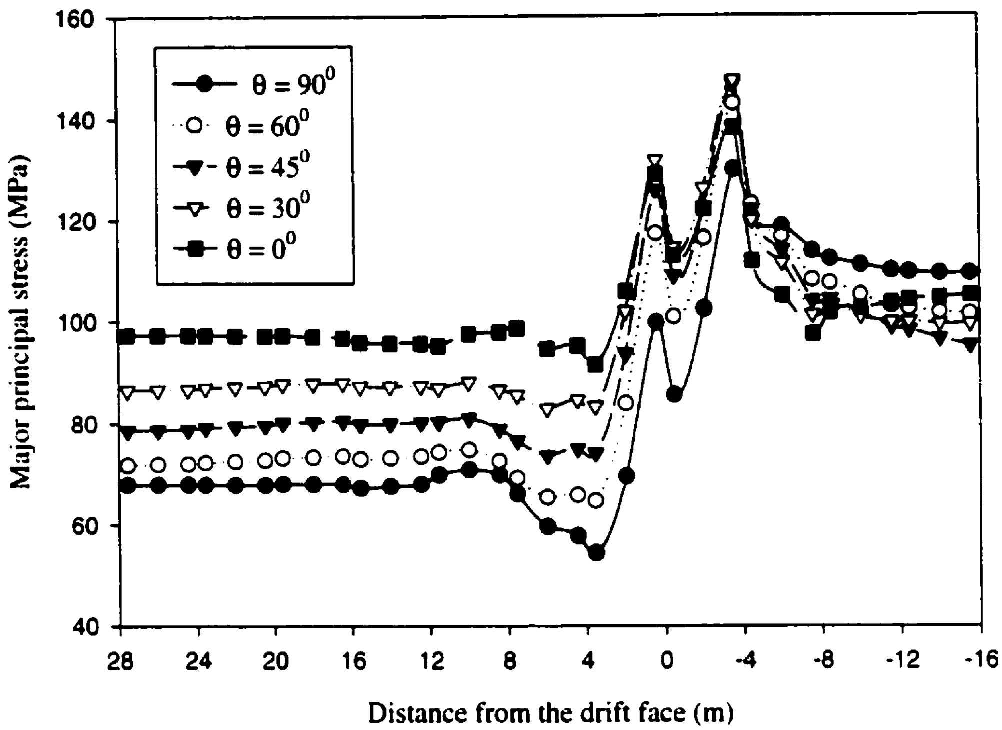

Figure 6.43 Variation of major principal stress distribution vs. strike angle θ along the left side centre of the drift after two drift face advance

From Figure 6.44 to 6.49, the major principal stress contour in front of the initial drift face and in front the drift face after two face advances are presented in pairs with the change of angle θ of 0, 45 and 90 degrees. The major principal stress values on the feature points are collected in Table 6.8 and Table 6.9. Figure 6.50 and Figure 6.51 present the major principal stress changes at the feature points one round behind the drift face before destressing and after two face advances while destressing.

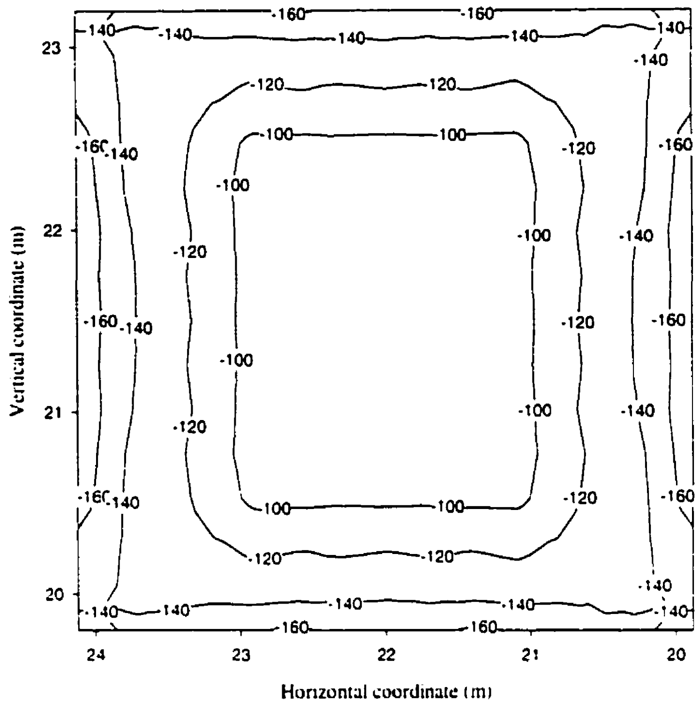

Figure 6.44 Major principal stress contour in front of the initial drift face before destressing for $\theta = 0^0$

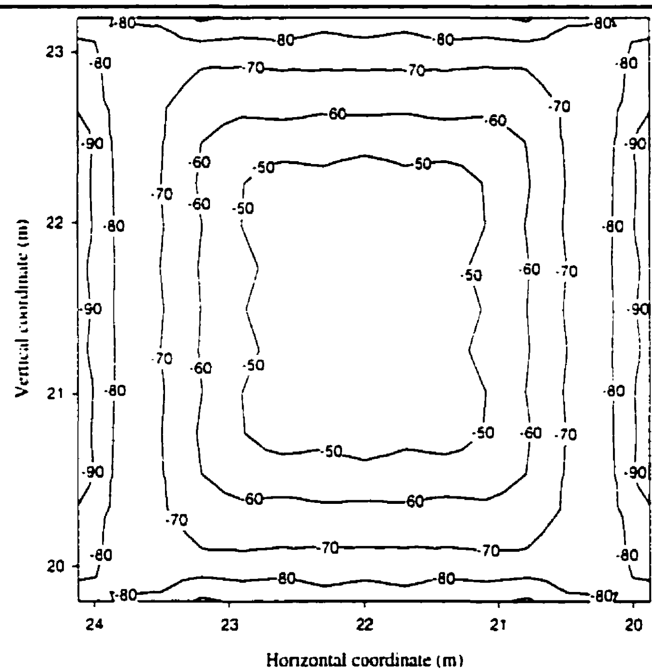

Figure 6.45 Major principal stress contour in front of the drift face after two face advances while destressing for $\theta = 0^0$

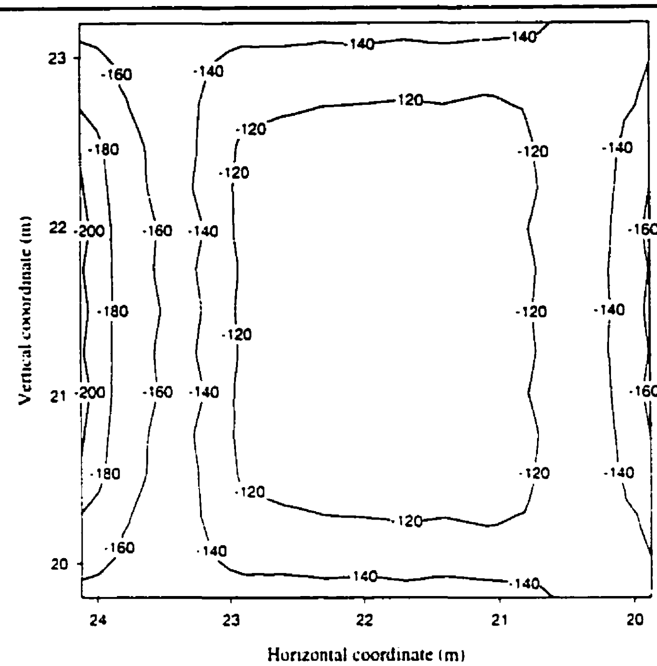

Figure 6.46 Major principal stress contour in front of the initial drift face before destressing for $\theta = 45^0$

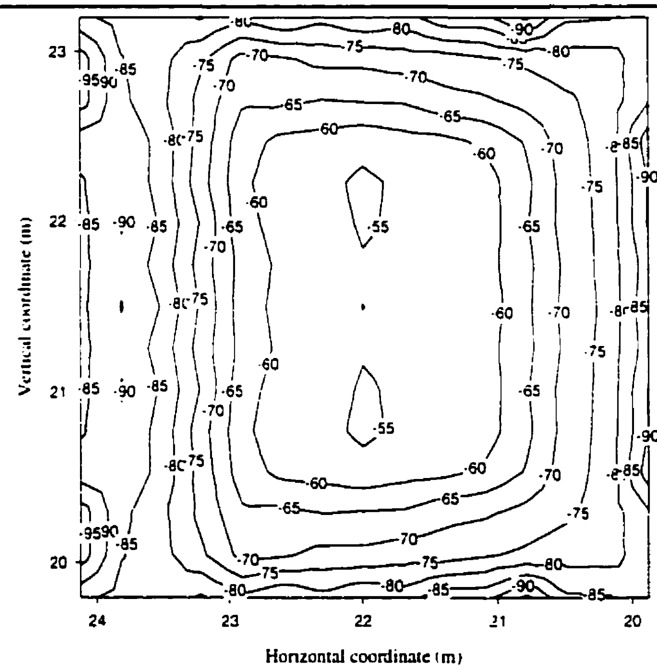

Figure 6.47 Major principal stress contour in front of the drift face after two face advances while destressing for $\theta = 45^0$

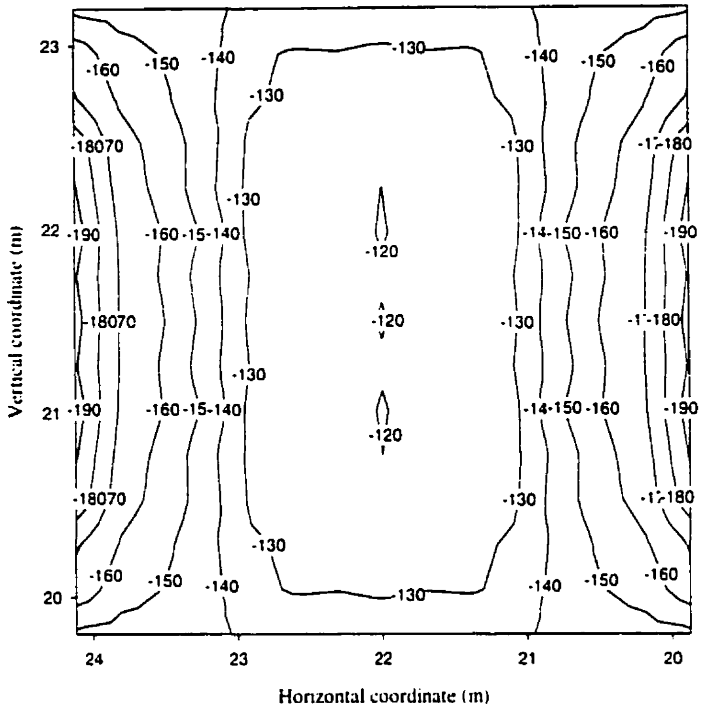

Figure 6.48 Major principal stress contour in front of the initial drift face before destressing for $\theta = 90^0$

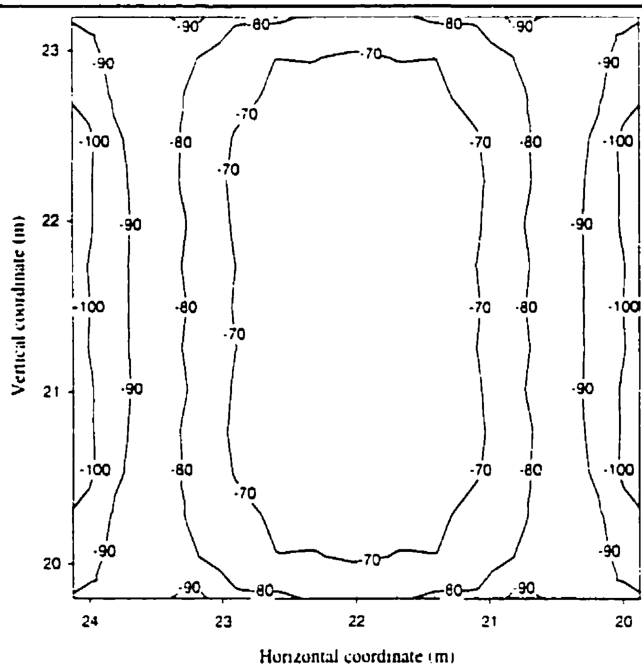

Figure 6.49 Major principal stress contour in front of the drift face after two face advances while destressing for $\theta = 90^0$

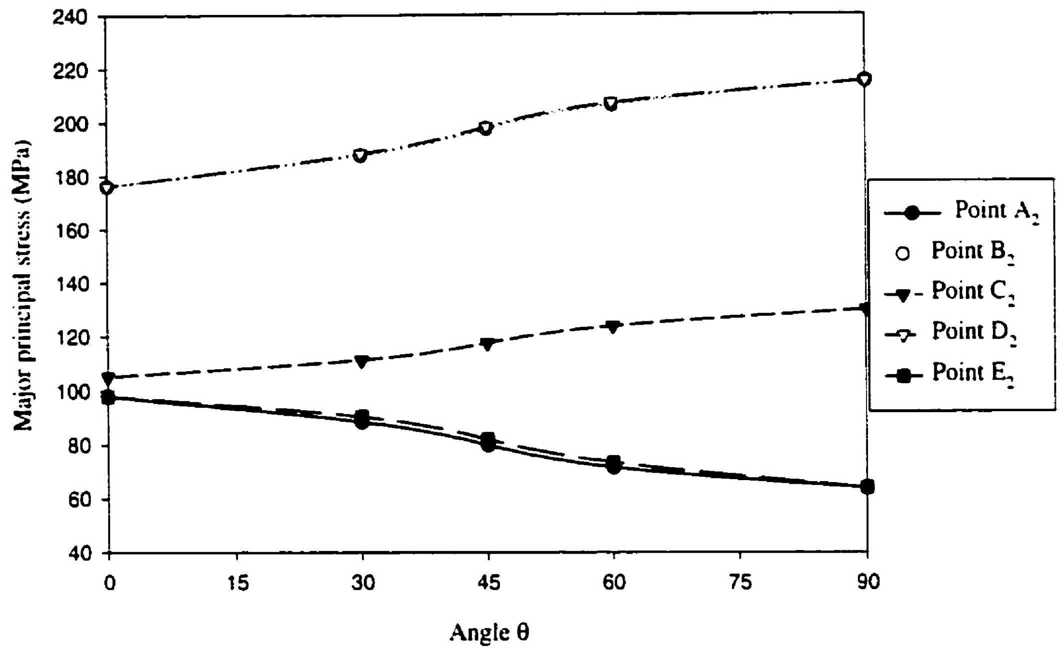

Figure 6.50 Major principal stress at the feature points one round behind the drift face before destressing

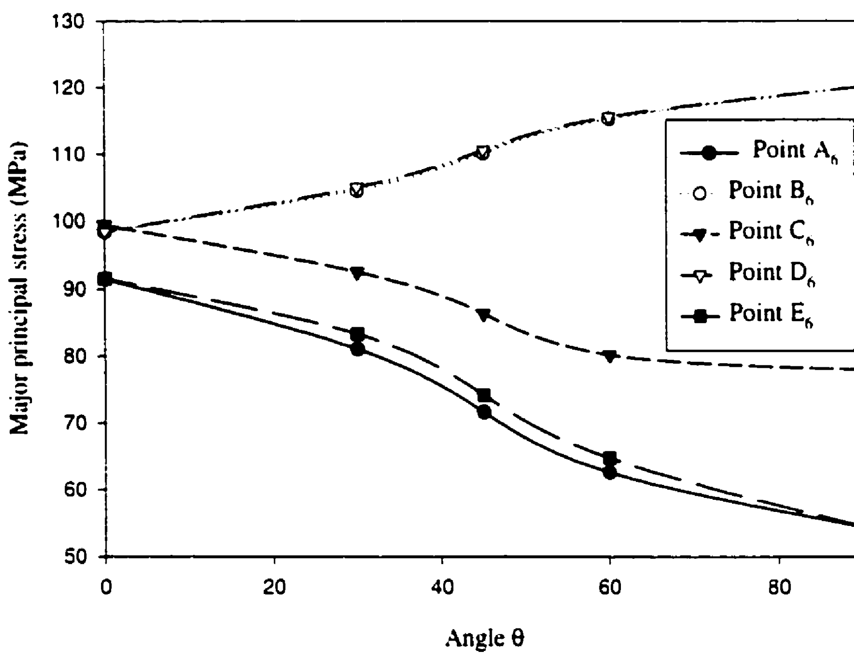

Figure 6.51 Major principal stress at the feature points one round behind the drift face after two face advances while destressing

Table 6.8 Major principal stress changes vs. angle θ on the feature points before destress blasting

Angle θ	One round behind the drift face				
	A2	B2	C2	D2	E2
90	64.0192	215.226	129.996	215.242	64.0125
60	71.6225	206.615	123.729	207.211	73.3625
45	79.9263	197.639	117.48	198.329	82.0007
30	88.5118	187.763	111.251	188.35	90.3541
0	97.8979	176.198	105.134	176.212	97.8951
	Just behind the drift face				
	A3	B3	C3	D3	E3
90	134.98	157.773	130.802	157.745	134.939
60	125.207	146.405	137.929	160.619	153.697
45	128.366	139.076	143.362	158.43	160.694
30	136.351	131.768	148.233	154.115	163.785
0	155.888	140.751	152.951	140.724	155.87
	Just in front of the drift face				
	A4	B4	C4	D4	E4
90	106.838	130.104	122.907	130.1	106.819
60	96.4649	119.862	117.686	131.819	115.359
45	95.2632	112.924	113.254	129.726	117.449
30	98.7059	106.081	109.656	126.242	117.676
0	111.004	116.158	108.223	116.168	111.002

Table 6.9 Major principal stress changes vs. angle θ on the feature points after two face advances

	One round behind the drift face				
	A6	B6	C6	D6	E6
90	54.4011	120.141	78.0118	120.102	54.4156
60	62.5696	115.288	80.1867	115.559	64.7327
45	71.6301	110.161	86.3311	110.582	74.1978
30	81.0522	104.574	92.467	105.048	83.3217
0	91.4626	98.4311	99.3363	98.3939	91.4673
	Just behind the drift face				
	A7	B7	C7	D7	E7
90	99.5896	93.6442	99.4673	93.6248	99.6143
60	95.5981	89.5663	111.746	90.3537	117.187
45	101.394	85.3992	118.97	86.4756	125.915
30	110.793	80.7415	125.212	81.9019	131.668
0	129.003	75.2914	130.234	75.2702	129.007
	Just in front of the drift face				
	A8	B8	C8	D8	E8
90	85.5568	86.7071	89.4832	86.6883	85.5412
60	82.7429	82.7778	99.4093	83.1458	100.743
45	88.2689	78.7433	105.63	79.2606	108.854
30	96.8728	74.3981	111.444	74.95	114.502
0	112.968	69.6242	116.862	69.601	112.96

CHAPTER 7

CASE STUDY OF A CUT-AND-FILL MINE STOPE

7.1 PROBLEM DEFINITION

Model validation is an essential step of its development as an efficient design tool. The model verification serves the purpose of assuming that the model is mathematically correct, whereas its application focuses on its ability to solve mining problems for which it was developed. Therefore, model validation is presented herein in conjunction with data collected through published papers and reports. As the model is developed for the strainburst evaluation, the selected case study must be suitable for it. In this chapter, the numerical model ***e-z tools 3D*** is used through a case study with the data for Placer Dome's Campbell Mine.

Rockbursts or violent pillar failures were first recorded at Campbell Mine in the early 1960's, occurring in crown and boxhole pillars associated with shrinkage mining, from 1983 to 1987, at least 10 rockbursts of magnitude greater than 2.0, and one of 3.1 were recorded (Makuch, 1987).

Destress blasting was used for a number of years to overcome problems of highly stressed ground and rockbursts. It is generally considered that the blast-induced fractures in the rock reduce its deformation modulus and as a result transfer the stress to adjacent rock structures.

Generally, at Campbell Mine, problems occur in the steeply dipping, hard and brittle structures when extraction has reduced the size of the supporting pillars to 20%. Three attempts were made to destress cut-and-fill crown and sill pillars and one attempt in shrinkage boxhole pillars. The report "Destress Blasting At Campbell Red Lake Mine" (Makuch et al, 1987) outlined each of the three destress blasts including background, preparation, instrumentation, hole layouts, powder factors, and the post-blast activities. This provide a good opportunity for the author to undertake the case study.

This study takes the 1902 and 1802 crown and sill pillars at Campbell Mine as the study object. The results obtained from ***e-z tools 3D*** for the case study are presented and discussed.

7.2 CAMPBELL RED LAKE MINE

Campbell Red Lake Mine is a primary gold producer located in Balmertown, Red Lake District of North-western Ontario (Figure 7.1). The mine was brought into production in 1949 at a rate of 350 tonnes per day and eventually mining went down to the 900 metre horizon at a rate of slightly over 1100 tonnes per day.

The mine has had a continual programme of development, the most recent of which was the sinking of the Reid Shaft to a depth of 2150m. The new shaft is to be completed by the second quarter of 1998 and followed by development of the underground infrastructure. The entire system was to be commissioned by January 1999.

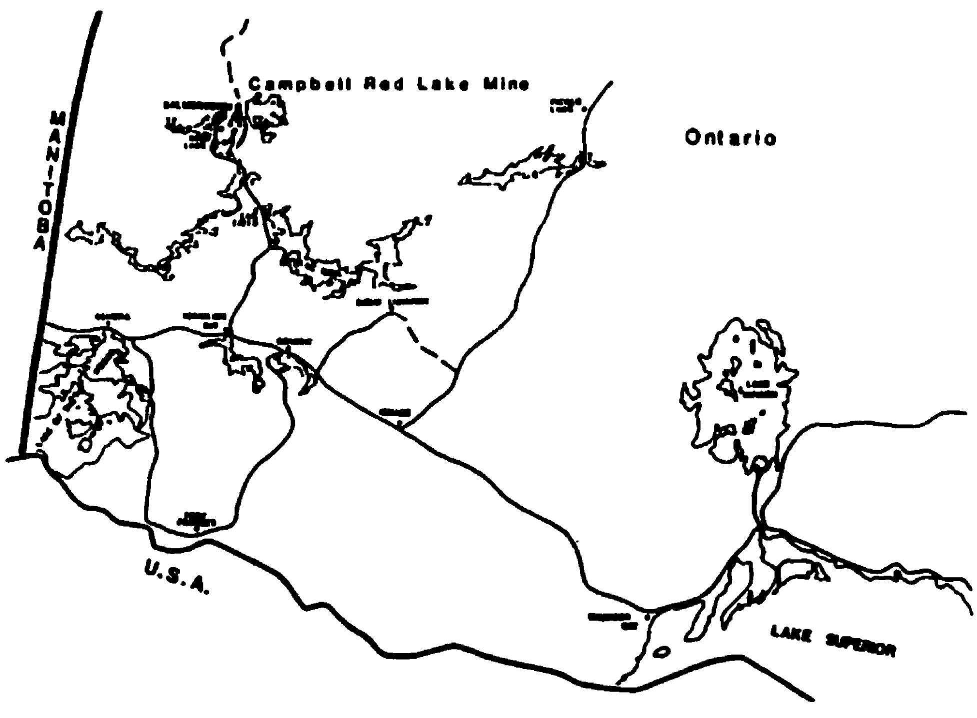

Figure 7.1 Campbell Mine location map (after Cullen, 1988)

The depth development project will cost an estimated $51 million and will allow the mine to maintain or increase its current rate of production well into the next century, potentially increasing annual production from 300,000 to 350,000 ounces of gold per year. Mine access is through a single four compartment shaft sunk to below the 27 Level, a depth of 1,316m below surface. There are 27 levels at 45 metre intervals with an average of 6,000m of development per level. The mine is track based with full haulage facilities on every level. Electric load haul dumps and electric hydraulic longhole drills are used in high tonnage areas of the mine. Mining methods have evolved from shrinkage stope mining through cut and fill and finally to longhole mining. Longhole mining practices include sub-level and crown pillar operations mine-wide.

7.2.1 Rockburst History

Both pillar and strain energy types of bursts have been recognised at Campbell. Pillar bursts occur as violent failure of highly stressed underground rock pillars, while strain energy bursts are a result of high local stress concentrations adjacent to underground openings. Strain energy bursts are more frequent, occurring as rock bumps near production faces, and usually have only minor impact on mining activities. Pillar bursts, although less frequent, are usually more severe in magnitude and can have a greater impact on safety to underground personnel. Crown pillars at Campbell Mine become critically stressed and burst--prone when the pillar thickness approaches 6 m, or at about 80% extraction. To alleviate the rockburst problem and allow safe and efficient recovery of crown pillars, destressing techniques have been adopted at the mine.

Destress blasting has been used for a number of years to overcome problems of highly stressed ground and rockbursts. It is generally considered that the blast fractures the rock, reducing its deformation modulus and transfers the stress to adjacent rock structures.

7.2.2 Mine Geology

The mine is located in the Red Lake Greenstone Belt which includes metavolcanic and sedimentary rocks. The greenstone belt is part of the Birch-Uchi lake subprovince, which in turn is part of the Archean Superior Province (Cullen, 1988).

Ore zones occur in a number of geological settings but are always subparallel to cleavage and major structures such as andesite-altered rock contact. The mine is comprised of 5 main ore zones, F, F2, A, L, and G, as well as a number of secondary distinct types; quartz carbonate fracture filled and replacement type. Quartz carbonate veins are from 0.25 to 1 m in width, replacement veins are 0.6 to 0.9 m wide. The host rocks are andesite and a chlorite schist. Many ore veins occur along the contact of the two. Rockbursting is only a problem in the stiffer andesitic rock. The less stiff chloritic rock may influence whether failure is violent or non violent.

The mine is divided in 27 levels at approximately 45 m intervals (Figure 7.2). Table 7.1 lists level numbers and depth bellow surface.

This pillar destressing was in the 'A' zone near the party wall with Dickenson Mine, as

Table 7.1 Mine levels and elevations (Cullen, 1988)

Level	Elevation (m) Below surface	Level	Elevation (m) Below surface
1	53	15	670
2	91	16	716
3	130	17	762
4	168	18	808
5	213	19	853
6	259	20	899
7	305	21	944
8	351	22	991
9	396	23	1036
10	442	24	1082
11	488	25	1128
12	533	26	1173
13	579	27	1219
14	625		

shown in Figure 7.2. Because of bursting experience in this zone on the upper levels Campbell Red Lake Mine adopted a stair step mining geometry suggested by Professor Morrison in 1961. Mining was started at the lower eastern extremity of the ore and mined by cut-and-fill in small 40 m blocks. Four small sections against the party wall were mined through the level with only minor difficulties. The length of these stopes made mining very slow, and therefore, the stope length was extended to 80 m. When 1902 E. 'C' stope was within 6 m of the level, the decision to destress was made. This was based on the reports of 'Working Ground', visual inspections and, for the first time, an increase in recorded microseismic activity.

On the 18^{th} level the drift was renovated using 1.8 m and 2.4 m resin rebar on walls and back, and welded mesh screen. Initially, all holes were to be drilled 54 mm in diameter from the 18^{th} level using a longhole machine. The plan was changed and spacing adjusted so the same designed powder factor remained when 44 mm upholes were drilled from the 18^{th} level and from inside 1902 E. stope, as shown in Figure 3.10. Since mining was to be done from the 18^{th} level using a benching method, the stope was closed off and tight filled.

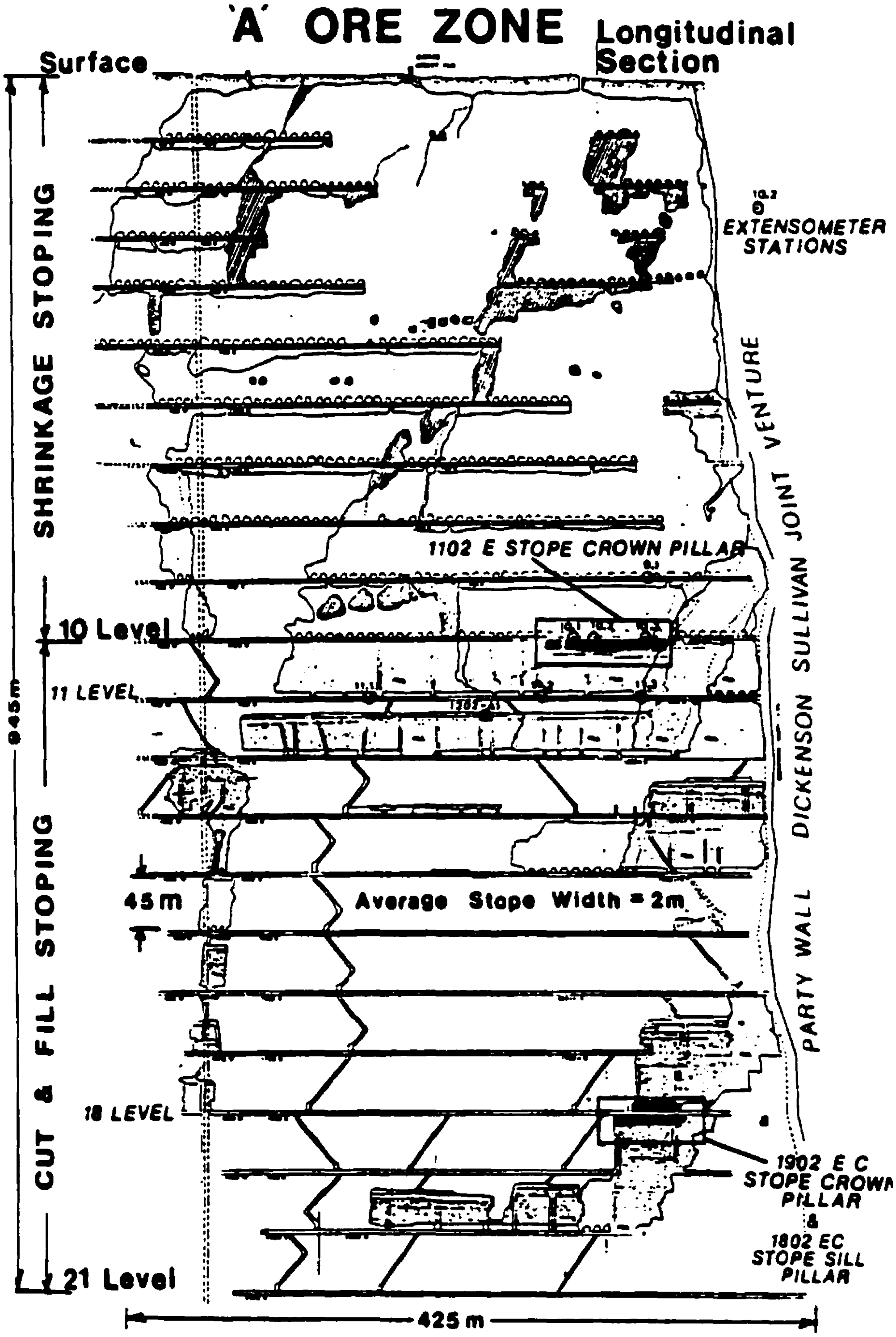

Figure 7.2 Longitudinal section of 'A' ore zone (after Makuch et al, 1987)

7.3 GEOMECHANICAL DATA, PRELIMINARY ANALYSIS AND MODEL PARAMETERS

Mechanical properties of the various rock types are listed in Table 7.2. The values are average obtained from rock samples recovered from throughout the mine.

A number of overcoring type measurements was conducted by CANMET at the mine using CSIR triaxial strain cells. Table 7.3 summarises the results and compares them to expected values based on calculated stress gradients in the Canadian Shield of Northern Ontario. As is common in the Canadian Shield, the major principal stress is horizontal, striking NE-SW. It is almost double the vertical stress, which is slightly greater than that expected from overburden loading alone.

Table 7.2 Results of laboratory test (after Makuch, 1987)

Rock type	Uniaxial Strength (psi)	Elastic Modulus (GPa)	Poisson's Ratio
Andesite	33.0 to 41.0 (230 to 286 MPa)	82.4	0.21
Andesite	Not Done	85.0	0.20
Chloritic Rock	17.0 (117.5MPa)	60.0	0.10

Table 7.3 Field stresses (in MPa), Campbell Red Lake Mine (CRLM) (after Makuch, 1987)

Depth(m)	$\sigma_{lateral}$		$\sigma_{vertical}$ MPa	Lateral to vertical stress ratio	
	Normal to ore veins MPa	Parallel to Ore veins MPa		Normal/ Vertical	Parallel/ Vertical
625 (14L)	27.0	16.0	16.0	1.7	1.0
1000 (22L)	54.0	24.0	26.0	2.0	0.9
1220 (27L)	73.0	43.0	32.0	2.3	1.3

A general analysis of the mining plan for stope 1802E and 1902E is needed for choosing the most suitable principal stresses from the Table 7.3 and Figure 7.2. At the time when destress blasting was carried out, the stopes 1802E and 1902E were almost isolated mined out areas. So the model domain for this case study takes the dimension as 187m×300m× 333m. The 4.5 m wide crown pillar was drilled off with 44 mm holes at 1.8 m spacing, to within 1.5 m of the overlying drift, over a distance of 45 m. The sill pillar, above the level, was drilled off with a 6 m long hole again at 1.8 m spacing over a distance of 25 m. Since mining was to be done from the 18^{th} level using benching method, the stope was closed off and tight filled with 10:1 cemented tailings. ANFO was loaded into the destress holes with a powder factor of 0.2 kg/m^3. After averaging, the principal stresses for the model input for this case study took the following value:

σ_1 = 46.03 MPa, in the normal direction to the ore body;

σ_2 = 25.63 MPa, in the strike direction to the ore body;

σ_3 = 25.63 MPa, in the dip direction to the ore body.

$K_{normal/vertical}$ = 1.8, $K_{parallel/vertical}$ = 1.0.

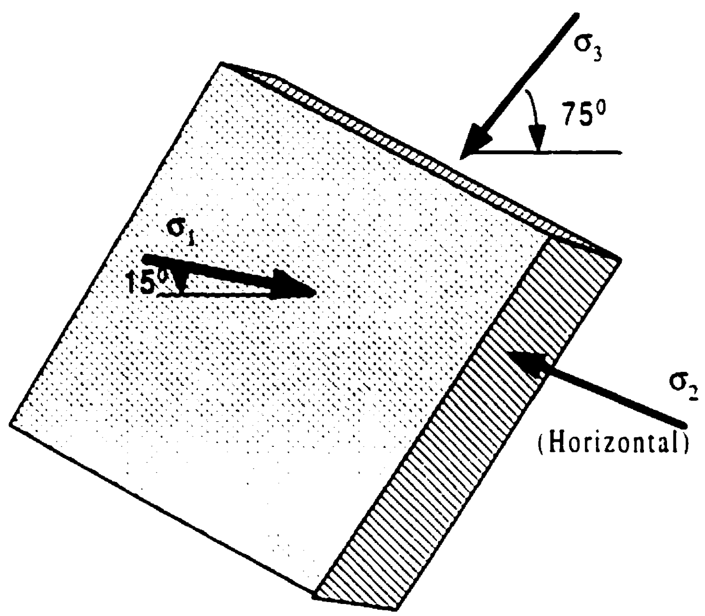

Figure 7.3 Orientation of the premining principal stresses adopted in the case study

The rock mass for the hanging wall and footwall are andesite-dominated. It is decided that the average value of available rock mass properties to be used for the model input are as bellows:

$E_{hangingwall} = E_{footwall} = 80$ GPa, $\nu_{hangingwall} = \nu_{footwall} = 0.21$

$E_{orebody} = 80$ GPa, $\nu_{orebody} = 0.22$,

$\gamma_{rock} = 0.024$ MN/m^3, $\gamma_{ore} = 0.0256$ MN/m^3, $\sigma_c = 230$ MPa.

Based on the test results reported by Scoble et al. (1987) and Cullen (1988), the average modulus in the destressed zone is in the range of 25 to 55 GPa, which means that the rock fragmentation factor $\alpha = 0.3\sim0.7$. Thus, the rock fragmentation factors α_x, α_y, and α_z in the destressed pillars are {0.5, 0.5,0.5}, and the Poisson's ratio factors are {1.4,1.4,1.4}. After preliminary studies with several values of β, the stress dissipation factors β_x, β_y, β_z, β_{xy}, β_{yz}, and β_{zx} used here in this case study are {0.6, 0.6, 0.6, 0.6, 0.6, 0.6} that gave the best correlation with the in situ measured stresses.

7.4 NUMERICAL MODELLING PROCEDURES

e-z tools 3D was first used to evaluate the burst potential of the 1802E sill and 1902E crown pillars. Subsequently, it was used to model the destress blasting process. The

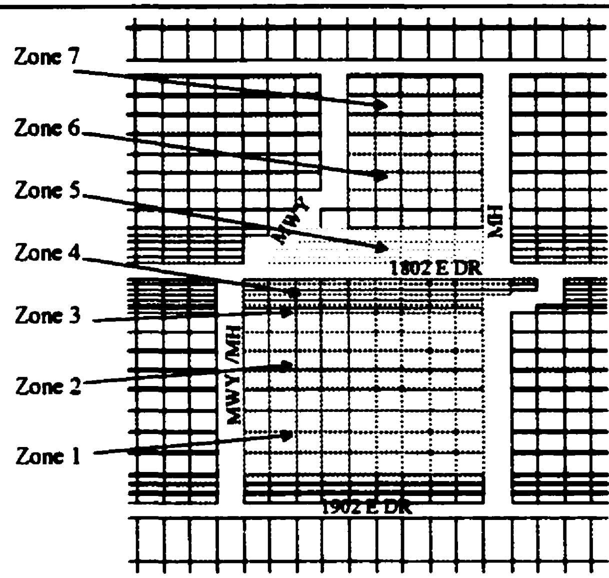

Figure 7.4 Numerical modelling zoning for mining sequence

numerical modelling procedures consisted of seven steps. Referring to Figure 7.4, the seven modelling steps are described in Table 7.4.

Table 7.4 Description of the numerical modelling sequence

Modelling step	Data file	Description
Step1	Cam-18.txt	Initial configuration: drifts and raises
Step 2	Cam18-1.txt	Mining in stope 1802E (zone 6 and zone 7)
Step 3	Cam18-2.txt	Mining lower half of stope 1902E (zone 1) and backfill stope 1802E (zone 6 and zone 7)
Step 4	Cam18-3.txt	Mining upper half of the stope 1902E (zone 2, zone 3, and zone 4) and backfill the lower part of the this stope (zone 1)
Step 5	Cam18-4.txt	Destress 1902E crown and 1802E sill pillars (zone 4 and zone 5) and the same time backfill the zone 2 and zone 3
Step 6	Cam18-5.txt	Destress 1902E crown pillar (zone 4) and backfill the zone2 and zone 3
Step 7	Cam18-6.txt	Destress 1802E sill pillar (zone 5) and backfill zone 2 and zone 3

The finite element mesh was created using a commercial software called HyperMesh® with 78,548 nodes and 52,221 elements. The output file from HyperMesh® was translated to the ***e-z tools 3D*** required format. Based on this file, the input file was created for each mining step as shown in Table 7.4. The calculation of following step2 needs to input the preceding step's output files. For example, the calculation of step5 needs the output files from step 4, for step6 and step 7 also need the input of step 4's output files. The running of these files on Pentium II/233MHz PC computer took 15 hours each.

7.5 DISCUSSION OF THE NUMERICAL MODELLING RESULTS

Simplification of mining sequences to the modelling step 4, focused on the major principal stress and burst potential index distributions in the 1802E sill and 1902E crown pillars. Figure 7.5 defines the feature points on 1802E sill and 1902E crown pillars. As can be seen, the point A, B, C, and D lie on the lower skin of the crown pillar. The major principal stress and burst potential index (BPI) distributions are presented in Figures 7.6 to Figure 7.17.

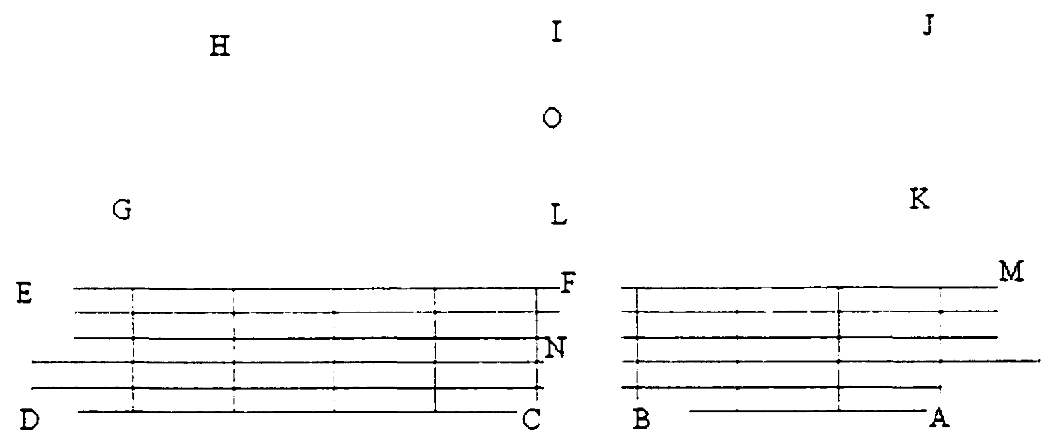

Figure 7.5 Definition of the feature points on the sill and crown pillars

Figure 7.6 to Figure 7.11 present the major principal stresses and burst potential (BPI) distributions in the 1902E crown pillar. These figures show that the major principal stress in the crown pillar at the lower skin are higher than at the top, and near the footwall are higher than near the hanging wall, with the centre of the pillar being the lowest. The stress values at the feature points are collected in Table 7.5 and Table 7.6.

Table 7.5 Major principal stresses at the feature points on 1902E crown pillar (MPa)

	A	B	C	D	E	F	M	N
Near H.W.	189	230	233.3	188.5	161	126.5	125.9	99.2
Centre of the pillar	150.1	168.2	171.8	153.2	115.7	92	99.2	107.5
Near F.W.	214.1	260.2	264.5	214	182	126.5	163.9	95.4

Note: H.W.---Hanging wall, F.W.---Foot wall

Table 7.6 Burst potential index (BPI) at the feature points on 1902E crown pillar (%)

	A	B	C	D	E	F	M	N
Near H.W.	93.2	140.7	144.7	92.7	84.3	38.9	38.4	23.7
Centre of the pillar	60.5	76.3	80	58.7	34.4	19.5	23.6	26.5
Near F.W.	97	140.5	145.8	98.9	90.3	32.3	30.7	20.5

Note: H.W.---Hanging wall, F.W.---Foot wall

Figure 7.12 to Figure 7.17 present the major principal stresses and burst potential (BPI) distributions in the 1802E sill pillar. Stress values at the feature points are compiled in Table 7.7 and Table 7.8. In the 1802E sill pillar the situation is different from in the crown pillar. At the top of the sill pillar (points H, I , and J), the major principal stress and burst potential index (BPI) are higher than at the bottom, and near the hanging wall are higher than near the footwall.

Table 7.7 Major principal stresses at the feature points on 1802E sill pillar (MPa)

	G	H	I	J	K	L	O
Near H.W.	132.4	162	169	198.6	137	110	67
Centre of the pillar	120.5	115.9	126.6	147.1	108.9	82	70.4
Near F.W.	152.2	140.3	156.6	173.6	149.4	110.4	70.6

Note: H.W.---Hanging wall, F.W.---Foot wall

Table 7.8 Burst potential index (BPI) at the feature points on 1802E sill pillar (%)

	G	H	I	J	K	L	O
Near H.W.	43.2	66.9	73.4	102.9	47.3	28.9	8.5
Centre of the pillar	36.3	33.8	40.1	57	28.9	13.9	9.2
Near F.W.	58.1	49.5	60.6	78	56	28.3	9.8

Note: H.W.---Hanging wall, F.W.---Foot wall

Upon examination of the model results, it is found that the burst potential index (BPI) in the 1902E crown and 1802E sill pillars is higher than 100%, suggesting the need for destress blasting.

7.5.1 Destress Blasting of the 1802E Sill and 1902E Crown Pillars

The modelling step 5 was implemented, in which the 1902E crown and 1802E sill pillars were destressed at the same time. The major principal stress distributions in the crown and sill pillar are presented in Figures 7.18 to Figure 7.23, whereas the stress values at the feature points are compiled in Table 7.9 and Table 7.10 respectively. The results show that after destress blasting the major principal stress at the feature points A, B, C, D, and E was reduced to 40~50%, however by not as much at point N and point M for the 1902E crown pillar. In the 1802E sill pillar, after destress, the major principal stress at points G, H, I, J, and K got 25~35% decrease, but not very few changes at point L and point O.

Table 7.9 Major principal stresses at the feature points on 1902E crown pillar (MPa) after modelling step 5 (MPa)

	A	B	C	D	E	F	M	N
Near H.W.	121	148.6	138.2	116.9	109.5	109.8	97.4	95.4
Centre of the pillar	97	110.7	113.1	97	82.3	85	76.8	99
Near F.W.	140.6	173.2	158.3	136.5	129.4	102.1	103.8	93.1

Note: H.W.---Hanging wall, F.W.---Foot wall

Table 7.10 Major principal stresses at the feature points on 1802E sill pillar (MPa) after modelling step 5 (MPa)

	G	H	I	J	K	L	O
Near H.W.	89.5	104.7	125.0	128.3	94.7	89.4	69.3
Centre of the pillar	82.9	72.3	90.5	89.9	78.9	70.8	70.4
Near F.W.	109	80.4	109	107.2	109.8	97.9	71.6

Note: H.W.---Hanging wall, F.W.---Foot wall

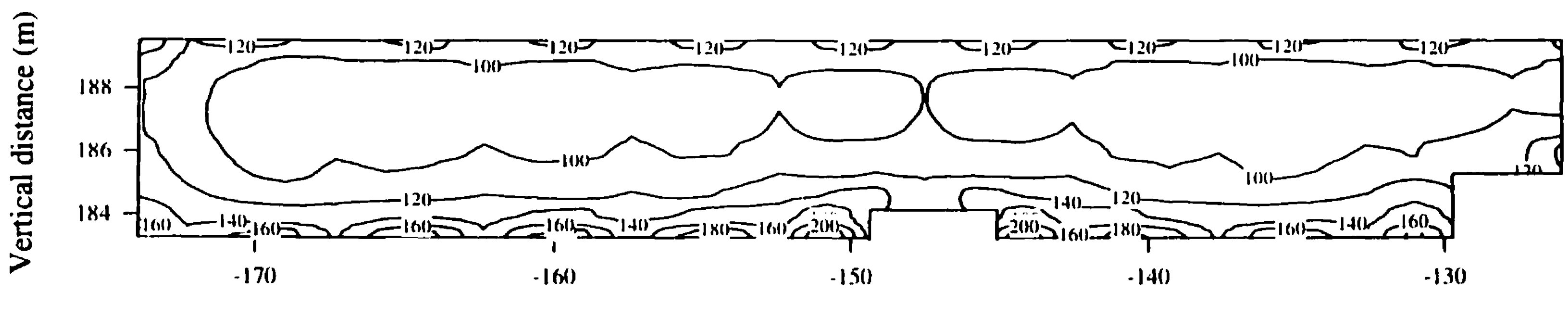

Figure 7.6 Major principal stress distribution in the crown pillar near the hanging wall before destressing

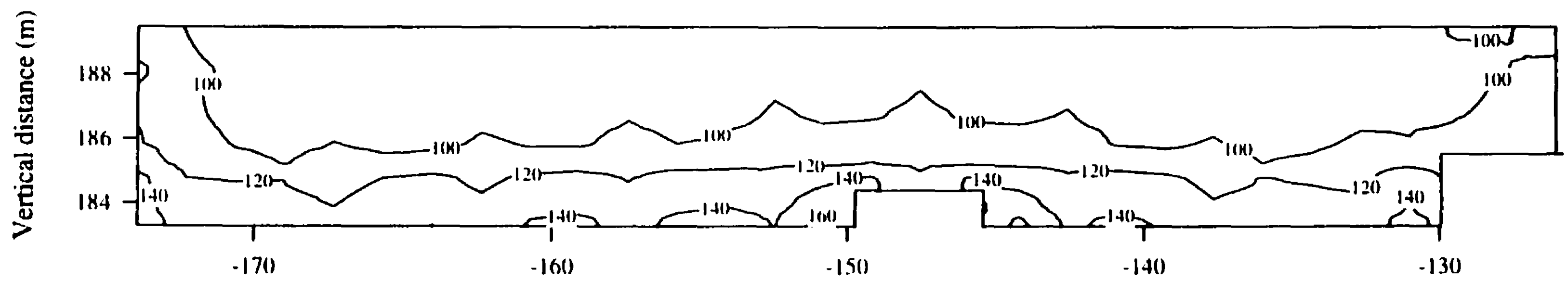

Figure 7.7 Major principal stress distribution in the centre of crown pillar before destressing

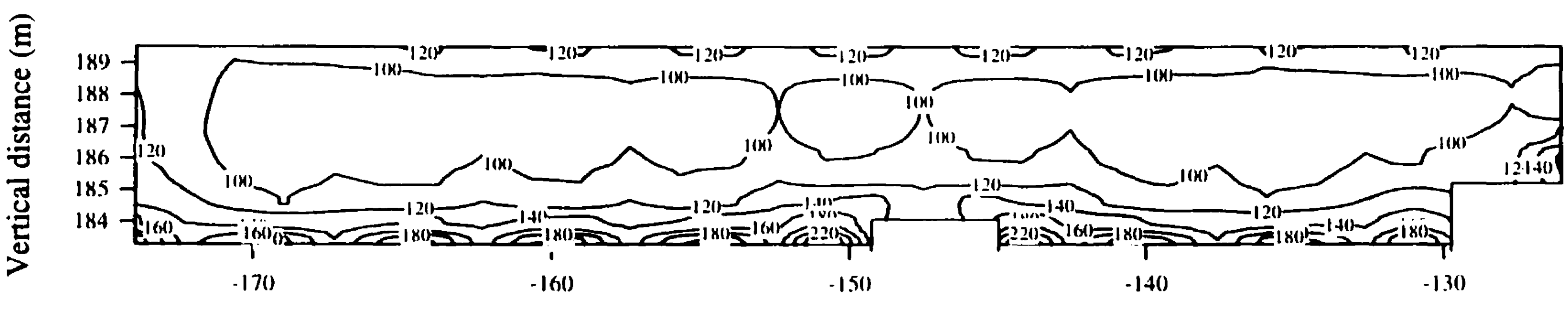

Figure 7.8 Major principal stress distribution in the crown pillar near the footwall wall before destressing

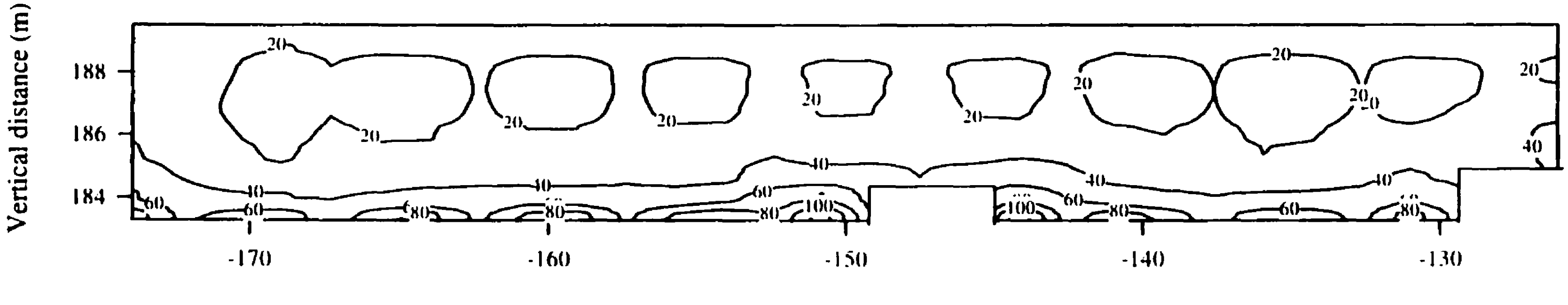

Figure 7.9 Burst potential index (BPI) distribution in the crown pillar near hanging wall before destressing

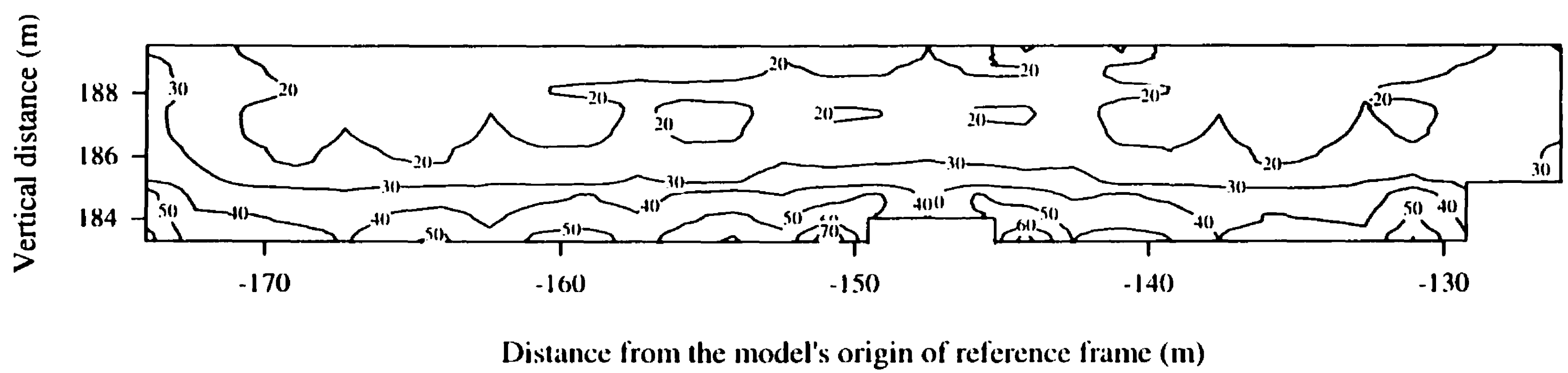

Figure 7.10 Burst potential index (BPI) distribution in the centre of crown pillar before destressing

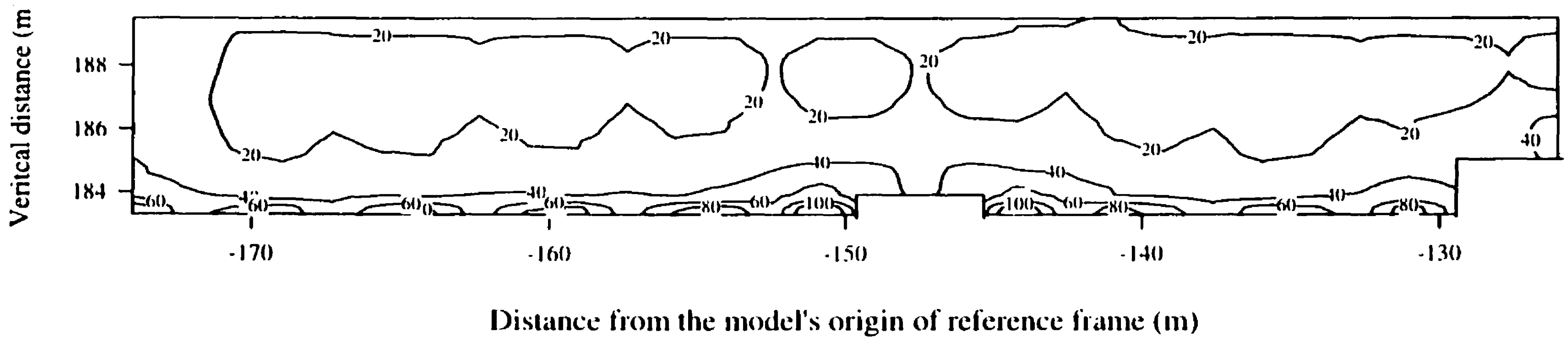

Figure 7.11 Burst potential index (BPI) distribution in the crown pillar near footwall before destressing

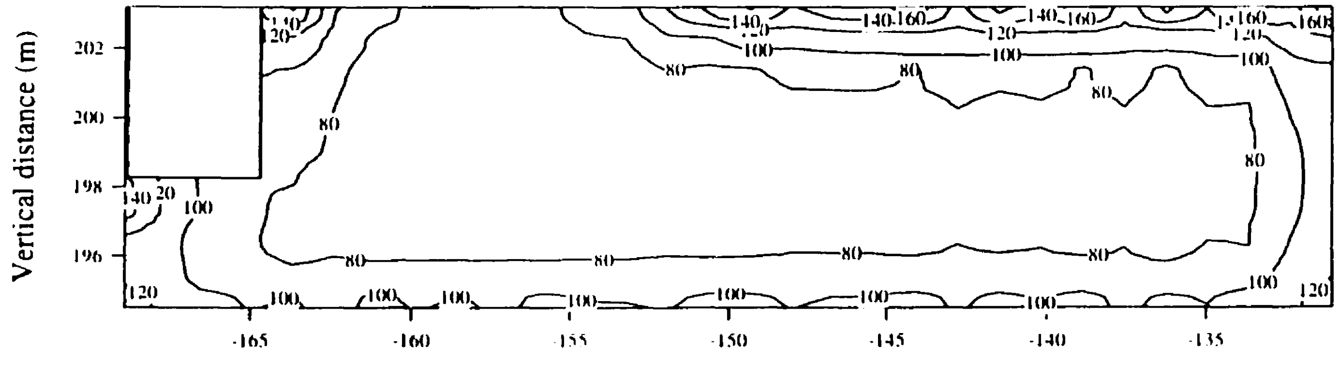

Figure 7.12 Major principal stress distribution in the sill pillar near the hanging wall before destressing

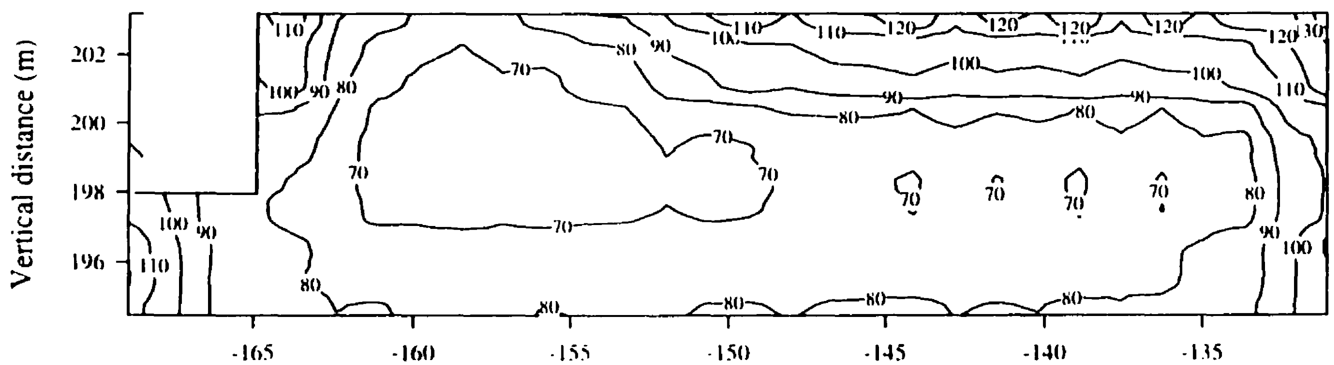

Figure 7.13 Major principal stress distribution in the centre of sill pillar before destressing

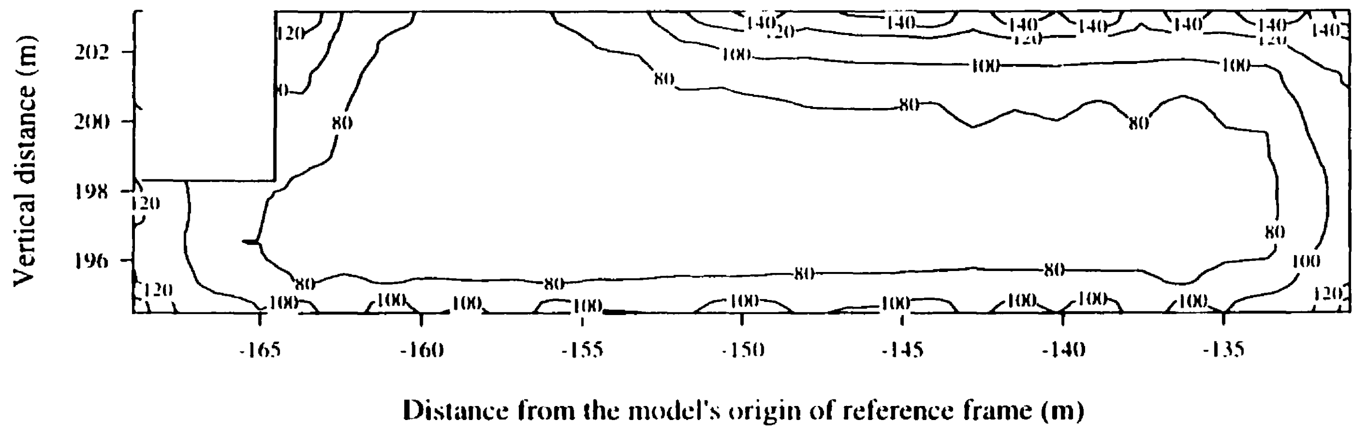

Figure 7.14 Major principal stress distribution in the sill pillar near the footwall wall before destressing

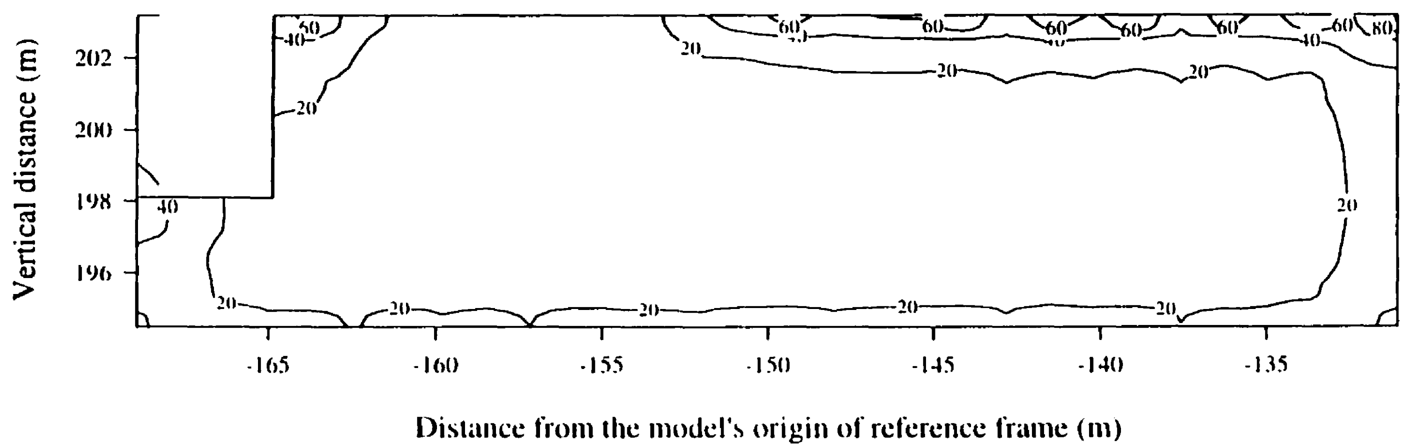

Figure 7.15 Burst potential index (BPI) distribution in the sill pillar near hanging wall before destressing

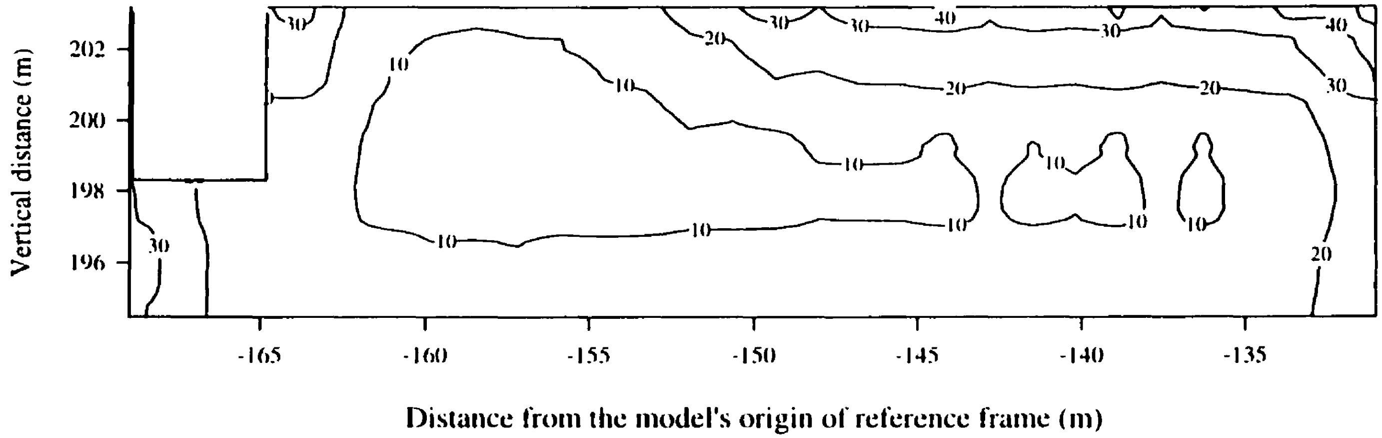

Figure 7.16 Burst potential index (BPI) distribution in the centre of sill pillar before destressing

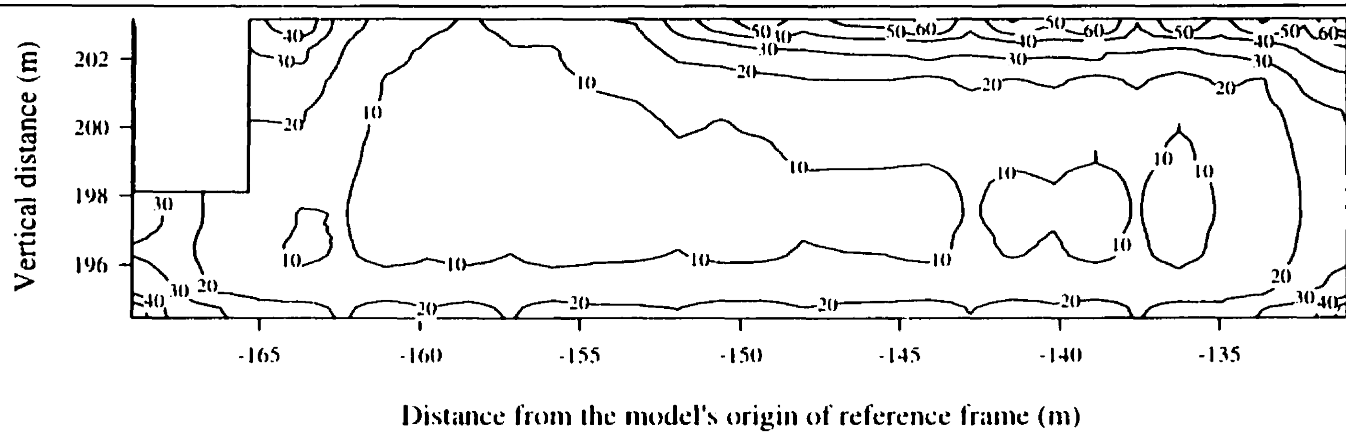

Figure 7.17 Burst potential index (BPI) distribution in the sill pillar near footwall before destressing

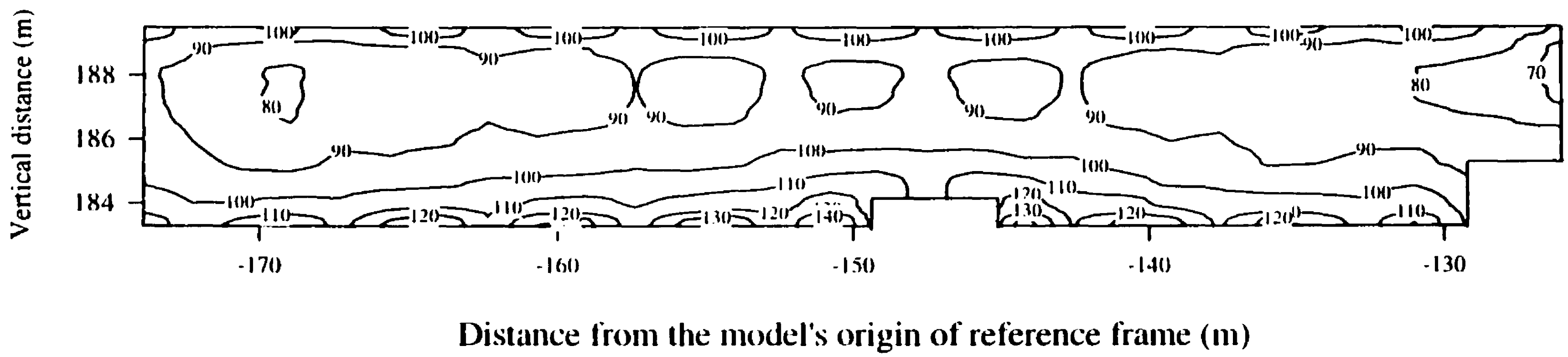

Figure 7.18 Major Principal stress distribution in the crown pillar near hanging wall after destress

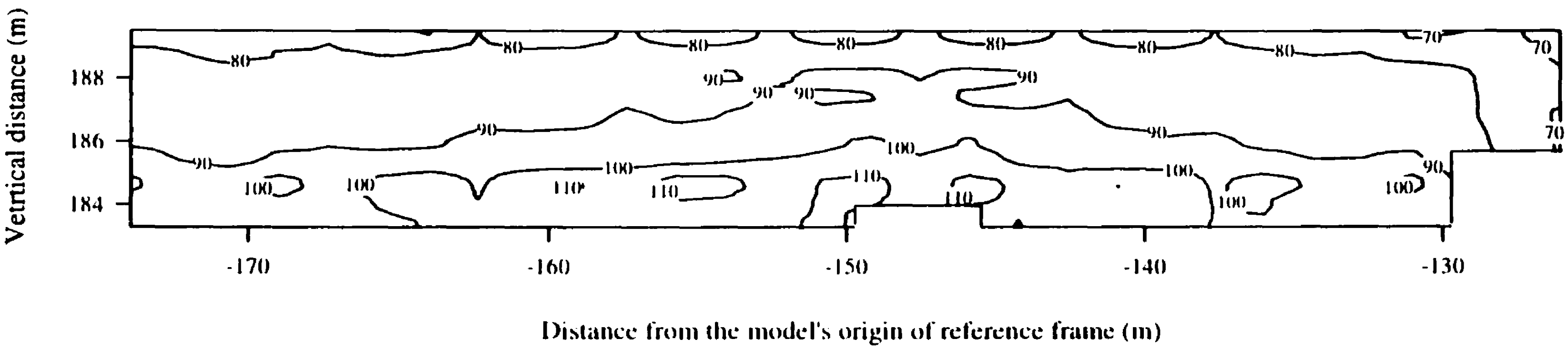

Figure 7.19 Major Principal stress distribution in the centre of the crown pillar after destress

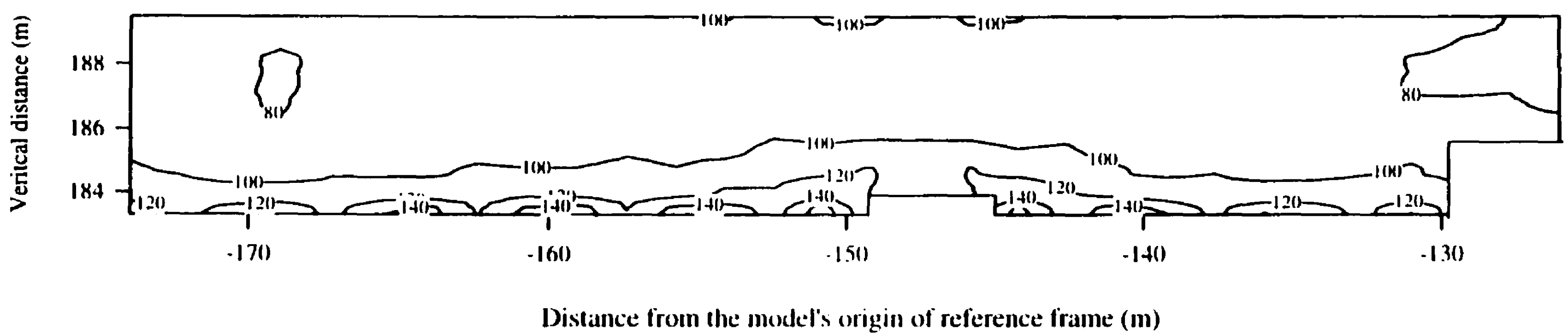

Figure 7.20 Major Principal stress distribution in the crown pillar near footwall after destress

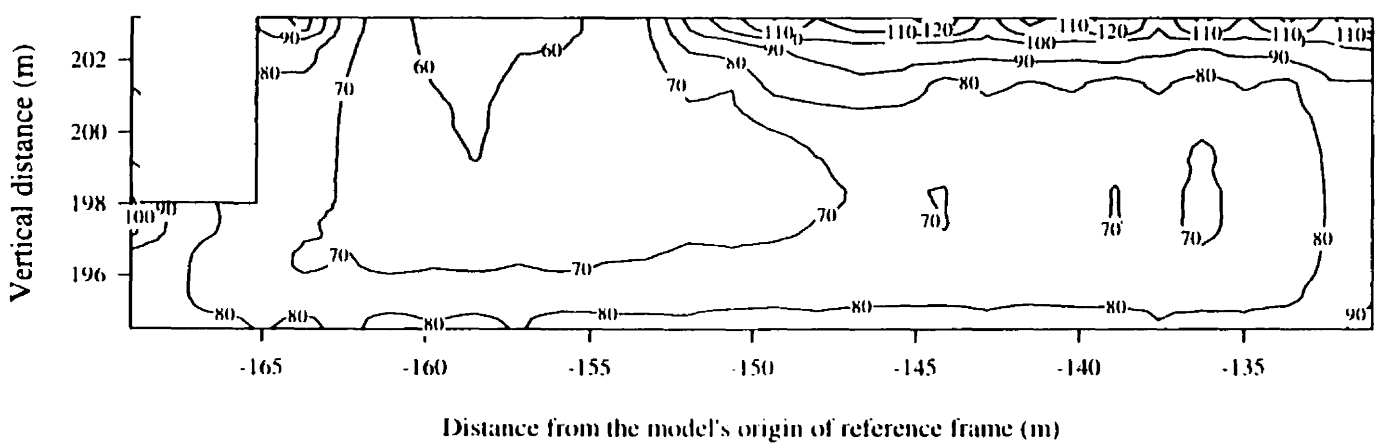

Figure 7.21 Major Principal stress distribution in the sill pillar near hanging wall after destress

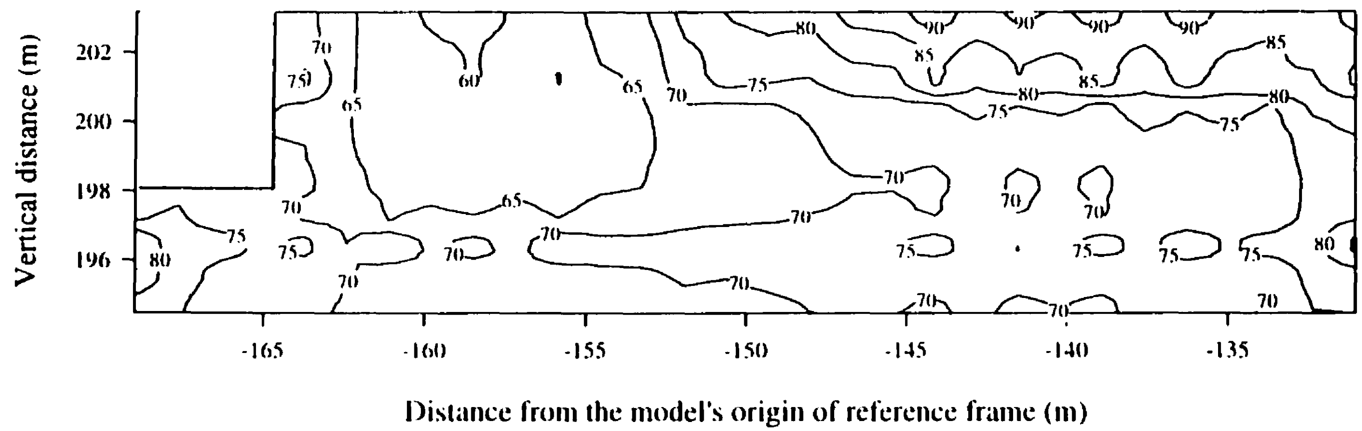

Figure 7.22 Major Principal stress distribution in the centre of the sill pillar after destress

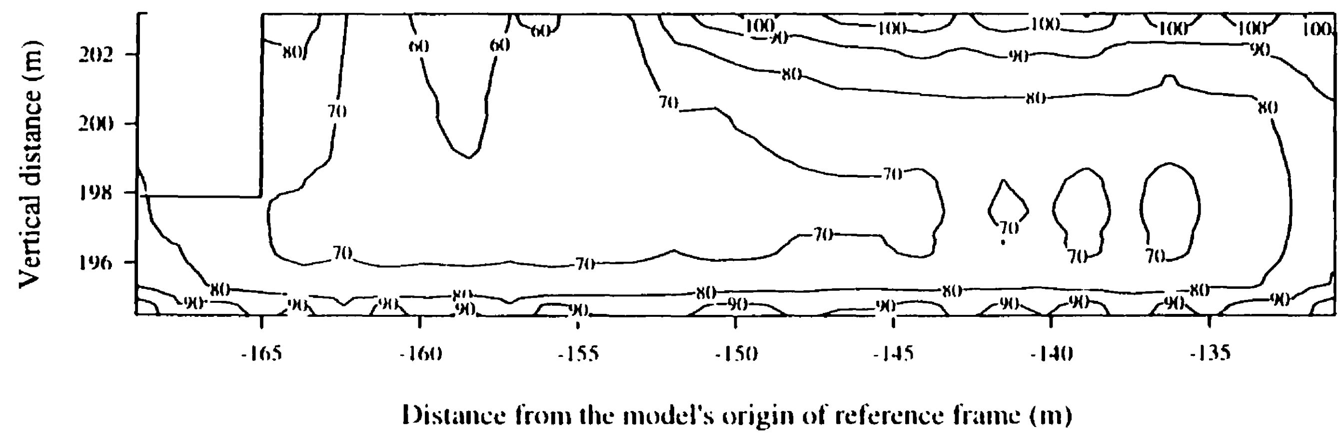

Figure 7.23 Major Principal stress distribution in the sill pillar near footwall after destress

7.5.2 Modelling the Destressing of 1902E Crown Pillar Only

To compare the results for different destressing scenarios, the modelling step 6 was implemented which assumed that only the 1902E crown pillar is destressed. In this step, the same destressing factors ($\{\alpha\}$, $\{\beta\}$) as step 5 were used. The preceding modelling step to this step is No. 4.

Figures 7.24 to Figure 7.29 present the major principal stress distributions in the 1902E crown and 1802E sill pillars after only destressing the 1902E crown pillar (step6). The correspondent feature point values are given in Table 7.11 and Table 7.12.

Table 7.11 Major principal stress distribution in the 1902E crown pillar after its destress blasting (MPa)

	A	B	C	D	E	F	M	N
Near H.W.	117.5	143.7	146	114.6	92.5	98.4	90	91.3
Centre of the pillar	94.6	108.1	110.5	95.4	79.2	77.9	65	94.8
Near F.W.	137	148.7	171.4	134.1	105.6	90.9	100.7	89

Note: H.W.---Hanging wall, F.W.---Foot wall

Table 7.12 Major principal stress distribution in the 1802E sill pillar after destressing the 1902E crown pillar (MPa)

	G	H	I	J	K	L	O
Near H.W.	148.6	165.6	172.3	201.7	152	125.7	73.2
Centre of the pillar	131.9	118.2	128.6	131.9	121.6	94.7	73.4
Near F.W.	170.9	144.4	160.3	177.3	165.6	126.4	75.4

Note: H.W.---Hanging wall, F.W.---Foot wall

The results show that, with the 1902E crown pillar being destressed, the stress level in the 1902E crown pillar is lower than the stress level after step 5, however, the stress level in the 1802E sill pillar increased by 5~15%.

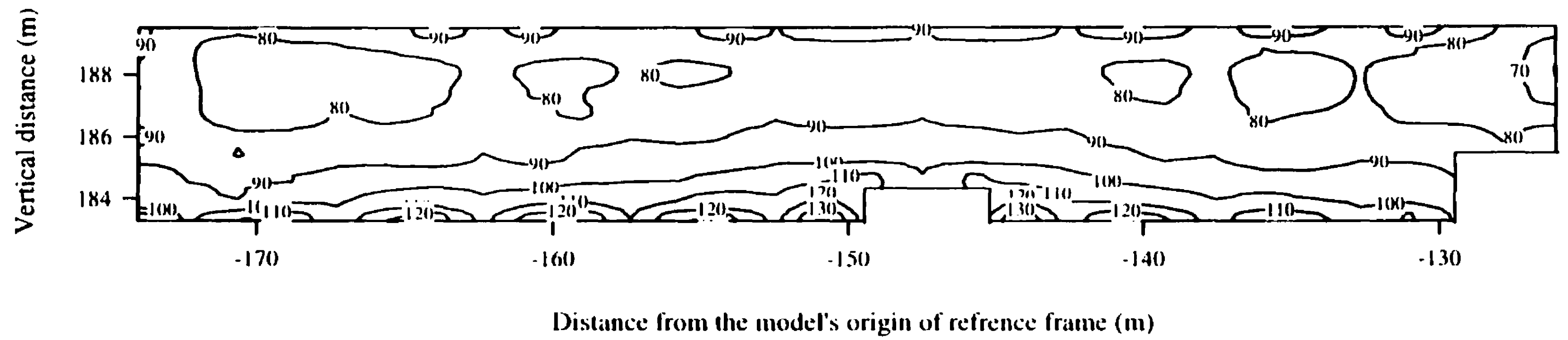

Figure 7.24 Major principal stress distribution in the crown pillar near hanging wall after destress the crown pillar

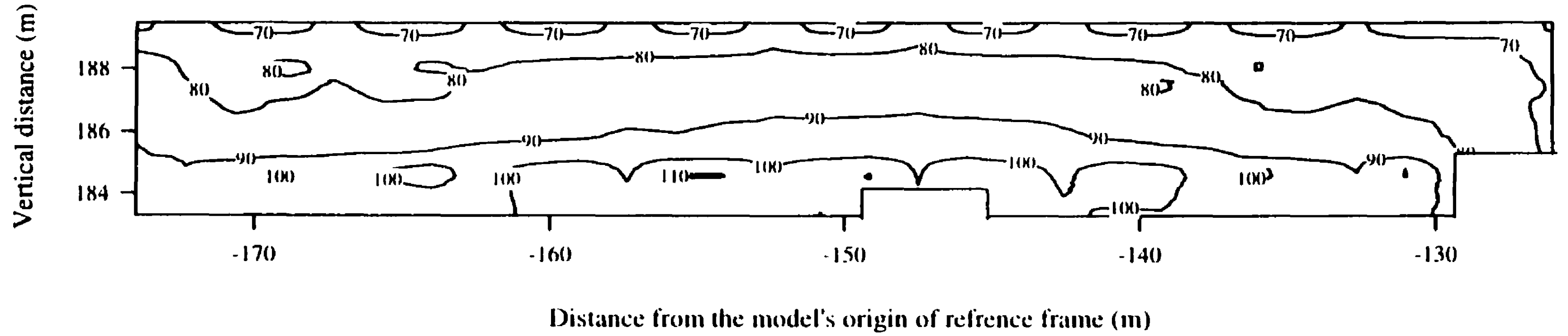

Figure 7.25 Major principal stress distribution in the centre of the crown pillar after destress the crown pillar

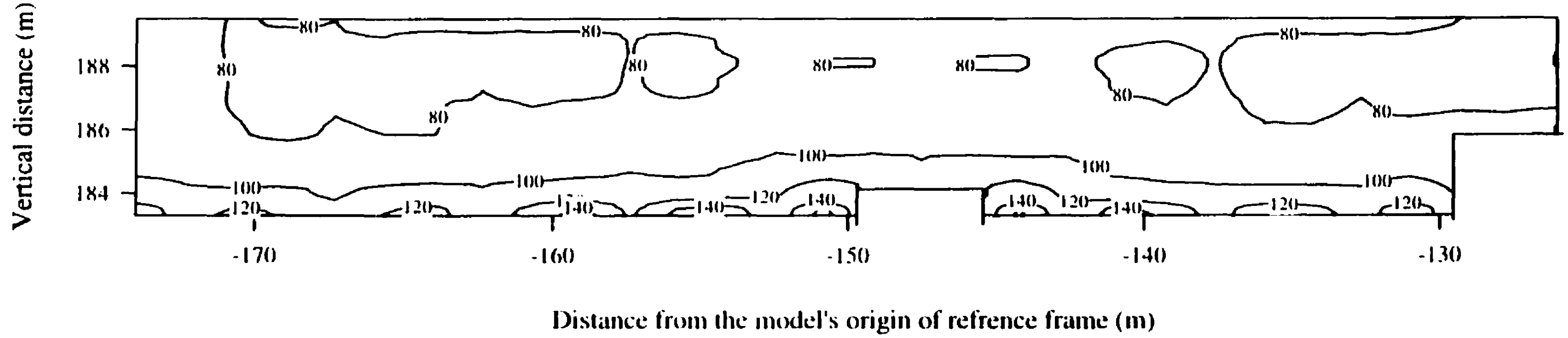

Figure 7.26 Major principal stress distribution in the crown pillar near foot wall after destress the crown pillar

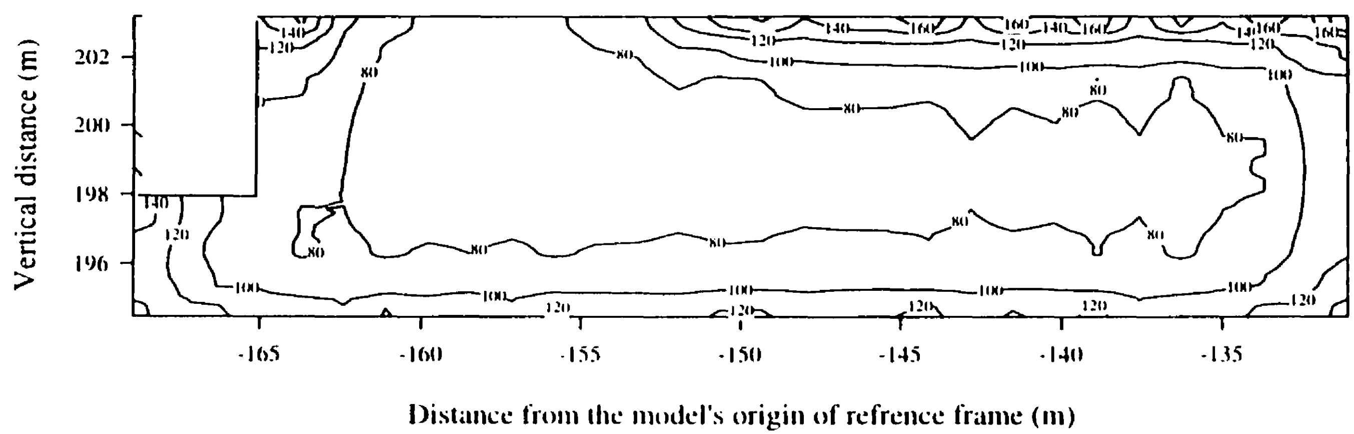

Figure 7.27 Major principal stress distribution in the sill pillar near hanging wall after destress the crown pillar

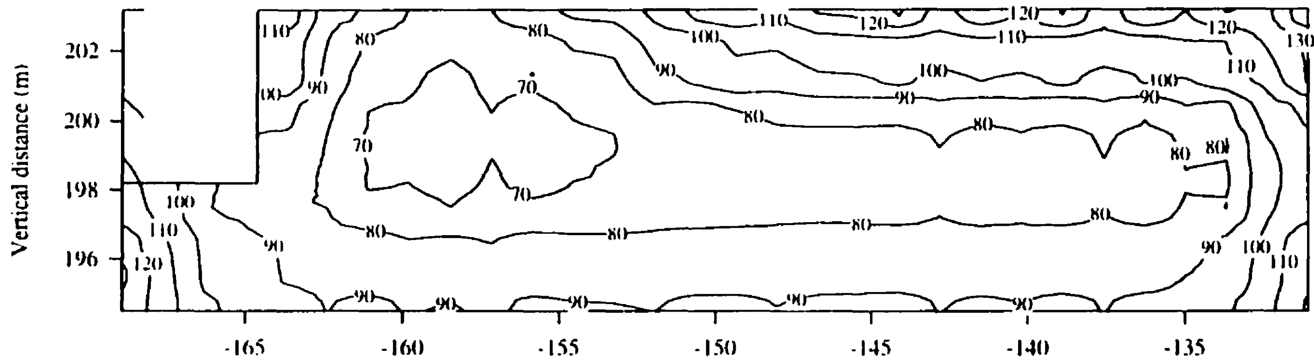

Figure 7.28 Major principal stress distribution in the centre of the crown pillar after destress the sill pillar

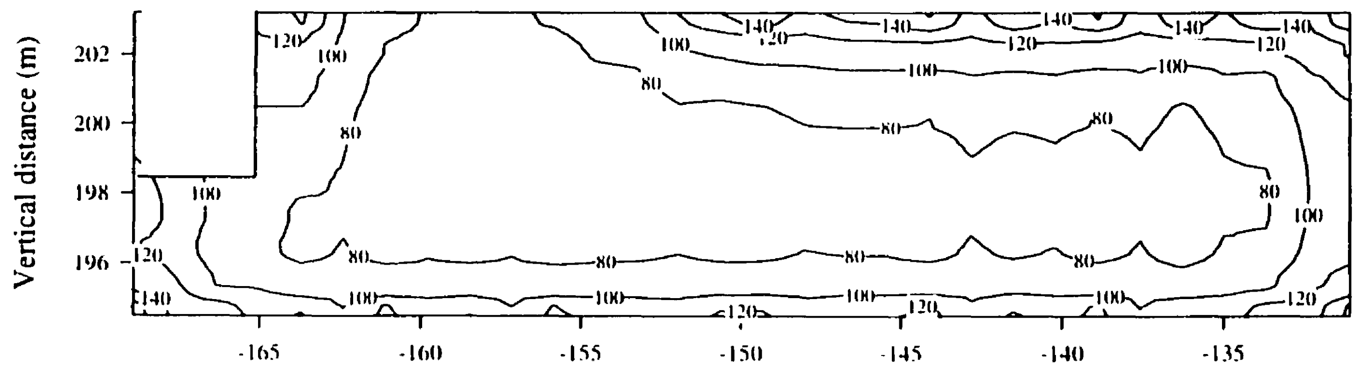

Figure 7.29 Major principal stress distribution in the crown pillar near foot wall after destress the crown pillar

7.5.3 Modelling the Destressing of 1802E Sill Pillar Only

As stated in section 7.5.2, to compare the results for different destressing scenarios, the modelling step 7 was implemented which considers destressing the 1802E sill pillar only. In this step, the same destressing factors ($\{\alpha\}$, $\{\beta\}$) as step 5 were used. The preceding modelling sequence for this step is No. 4. The results from the model step 7 are presented. The major principal stress distribution in 1902E crown and 1802E sill pillars are shown in the Figure 7.30 to Figure 7.35. The major principal stresses at the feature points are given in Table 7.13 and Table 7.14.

Table 7.13 Major principal stress distribution in the 1902E crown pillar after destressing the 1802E sill pillar only (MPa)

	A	B	C	D	E	F	M	N
Near H.W.	192.8	235.4	238.4	191	167.3	140.5	135.2	102.9
Centre of the pillar	152	171.3	174.9	154.1	121.4	100.8	104.6	113.
Near F.W.	218.2	265.8	270.1	216.9	180.3	140.1	130.9	102.1

Note: H.W.---Hanging wall, F.W.---Foot wall

Table 7.14 Major principal stress distribution in the 1802E sill pillar after destressing the 1802E sill pillar only (MPa)

	G	H	I	J	K	L	O
Near H.W.	77.8	101.4	122.3	125.4	84	77.2	66
Centre of the pillar	76.7	68.1	87.7	88.3	73.9	64.8	67.2
Near F.W.	84.2	76.1	97.2	95.6	75.4	75.6	67.2

Note: H.W.---Hanging wall, F.W.---Foot wall

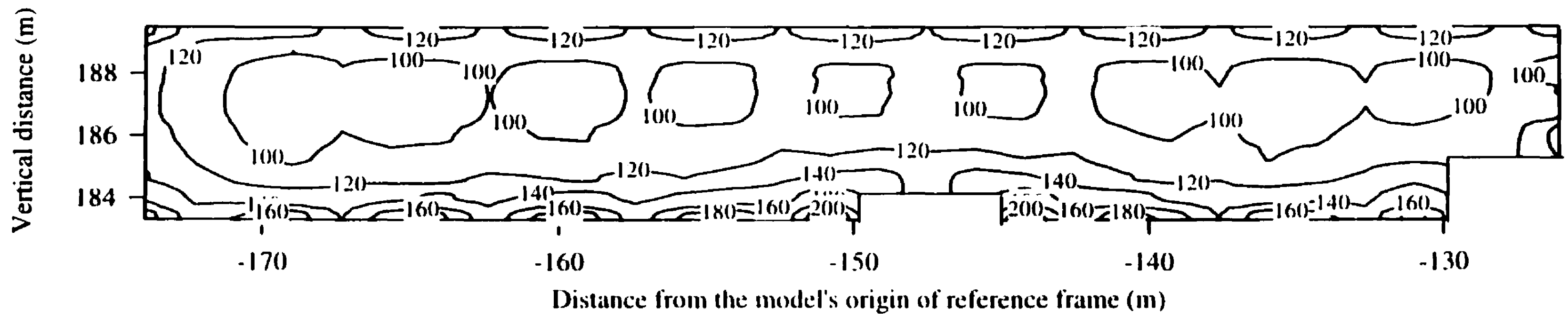

Figure 7.30 Major principal stress distribution in the crown pillar near hanging wall after destress the sill pillar

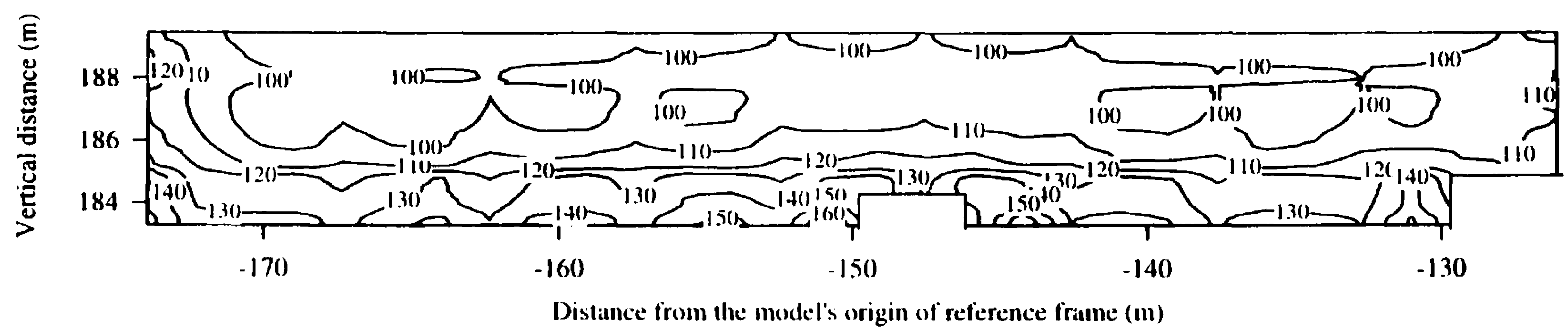

Figure 7.31 Major principal stress distribution in the centre of the crown pillar after destress the sill pillar

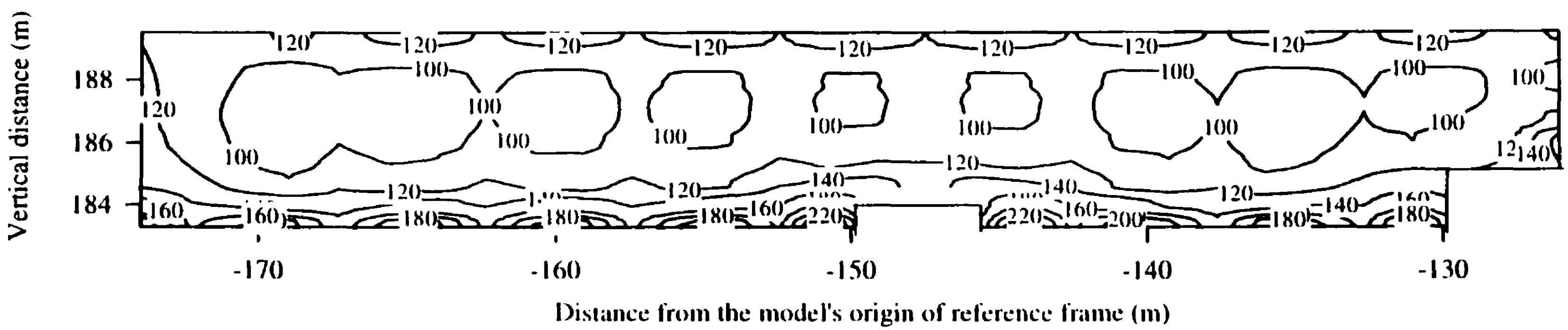

Figure 7.32 Major principal stress distribution in the crown pillar near foot wall after destress the sill pillar

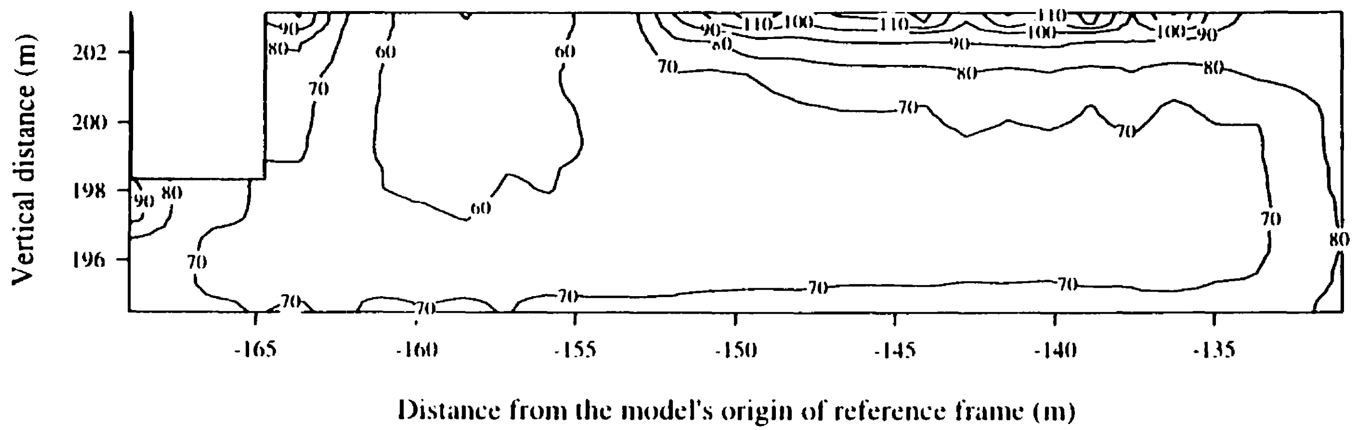

Figure 7.33 Major principal stress distribution in the sill pillar near hanging wall after destress the sill pillar

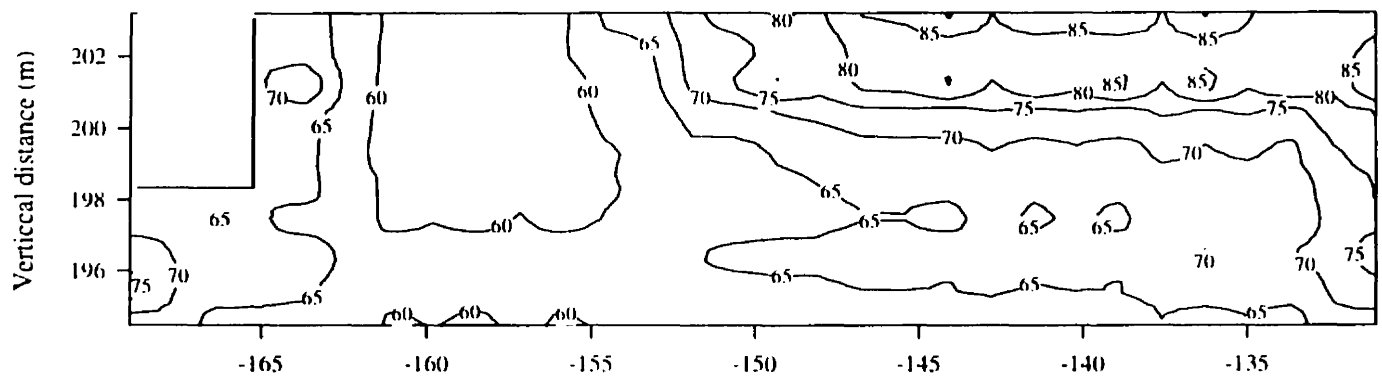

Distance from the model's origin of reference frame (m)

Figure 7.34 Major principal stress distribution in the centre of the sill pillar after destress the sill pillar

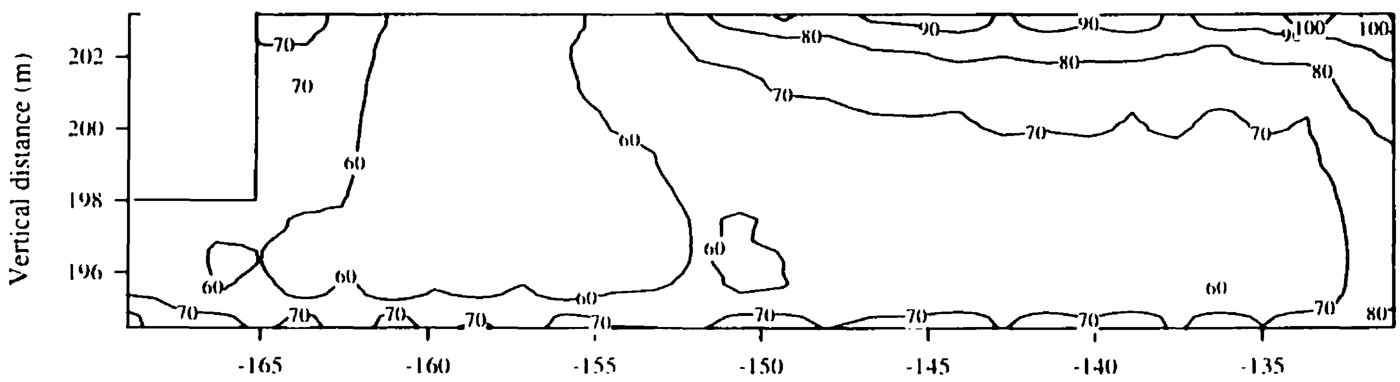

Distance from the model's origin of reference frame (m)

Figure 7.35 Major principal stress distribution in the sill pillar near foot wall after destress the sill pillar

7.5.4 Discussion

In this case study, three destress blasting scenarios for the 1802E sill and 1902E crown pillars have been modelled. From the modelled results shown in this section, the following conclusions of this case study are made.

The major principal stress in the 1902E crown and 1802E sill pillars is lowest in the centre parts of pillars. For the 1902E crown pillar the area near the footwall is subjected to higher stress, but in 1802E sill pillar the area near the hanging wall has higher stress. In the 1902E crown pillar the principal stress near the lower skin of the pillar is higher than that near the top of the pillar, but in the 1802E sill the top of the pillar has higher stresses than the bottom of the pillar.

The highest stress concentration occurred at the centre bottom of 1902E crown pillar where the thinner part of the pillar located.

Destressing of 1902E crown and 1802E sill pillars at the same time shows the most favourable results for the subsequent mining of the 1902E crown pillar.

Destressing of 1902E crown pillar only decreases the stress level in the 1902E crown pillar, however, it increases the stress level in the 1802E sill pillar, which makes the mining of 1902E crown pillar using bench down method very dangerous.

Destressing of 1802E sill pillar only increases the stress level in the 1902E crown pillar which increases the burst potential in the crown pillar.

Comparing the three destress blasting scenarios the destressing of 1902E crown and 1802E sill scenario appears to be the best choice.

CHAPTER 8

CONCLUSIONS

8.1 SUMMARY AND COCLUSIONS

An energy based rockburst potential evaluation method, burst potential index (BPI), was proposed. This new method relies on the mining induced strain energy storage rate and the uniaxial compressive strength of the rock. The Burst Potential Index (BPI) is calculated based on energy considerations, to help estimate the potential for face burst in mine development headings. When BPI exceeds 100%, the situation calls for destress blasting. And then the model was employed to assess the strainburst potential in a cut-and-fill mine stope. From the results obtained, it can be seen that the BPI is a useful tool in predicting crown pillar strainburst in cut-and-fill mining. It was shown that as the mining sequence progresses upwards thus reducing the size of the pillar, the magnitudes of ESR and BPI increase. Those were particularly highest at the corners of the stope back, which indicates a possible shear failure mechanism.

A numerical modelling technique for the simulations of destress blasting in hard rock mining operations at depth was developed and implemented in a newly developed 3-dimensional finite element code, ***e-z tools 3D*** by the author. The technique employs two newly introduced parameters, $\{\alpha\}$, rock fragmentation factor, and $\{\beta\}$, stress dissipation factor, inside the modelled, fractured zone. The model is based on the burst potential theory to help assess strainburst potential and hence, the needs for a remedial solution such as drift destressing. Basically, when the burst potential index (BPI) approaches or exceeds 100%, the method suggests that rockburst is imminent and destress blasting may be required. Destress blasting is simulated by modifying the deformation properties of the rockmass and the post-blast state of stress in the destressed zone using the above mentioned parameters $(\alpha\}$ and $\{\beta\}$. The technique, based on incremental analysis, permits the simulation of actual mining activities, i.e. mining and destressing.

Comparison of results between analytical solutions and numerical predictions of stresses around circular opening shows excellent agreement, sewed to verify the numerical model.

Model parametric study regarding the destress blasting patterns, the variation of the rock fragmentation factor $\{\alpha\}$, the stress dissipation factor $\{\beta\}$, and the initial stresses orientations have shown that each parameter has a significant effect on the rock mass response in terms of stresses and deformations. No parameter could be neglected.

A case study of a cut-and-fill mine stope on the destress blasting of 1802E sill and 1902E crown pillars at Campbell Red Lake Mine, Berlmertown, Ontario was undertaken using the developed finite element model. The geomechanical data were collected from the published papers and reports. The model input data used are the average values. Mine backfill is modelled as a construction material, in which no initial stresses existed. The results indicated that the destress blasting of 1802E sill and 1902E crown pillars is necessary. The modelling results show that after destressing of the 1902E crown and 1802E sill pillars the stress levels in the crown and sill pillars are reduced substantially.

It is shown through case studies of underground Canadian mines that the new method can be particularly useful in the assessment of deep drift face burst potential and the crown pillar burst potential in cut-and-fill mine stopes.

8.2 RECOMMENDATIONS FOR FURTHER RESEARCH

The research work presented in this thesis can be extended in the following directions:

1. Further refinement of the current numerical model may prove useful. The development of an interface with as much available commercial graphic software as possible to make the ***e-z tools 3D*** more versatile.
2. Investigate the behaviour and failure of brittle rocks under versatile loading to improve the burst potential index theory.
3. The numerical model can be developed to account for the non-linear behaviour of the rock mass. And furthermore, the time effect can be incorporated in the model to permit the simulation of time-dependent viscoplastic behaviour of rock structure..
4. More case studies conducted with the new model will be very important for the validation of the proposed approach and the numerical model.

STATEMENTS OF CONTRIBUTIONS

A 3-dimensional linear elastic finite element model is developed to evaluate the rockburst potential and to model destress blasting. An index called the Burst Potential Index (BPI) is calculated based on energy considerations, to help estimate the potential for face burst in underground openings. When BPI exceeds 100%, the method suggests destress blasting is required. The proposed destress blasting simulation technique is implemented with the help of two sets newly introduced parameters: $\{\alpha\}$, rock fragmentation factors, and $\{\beta\}$, stress dissipation factors. The algorithm is based on an incremental methodology. Verification of the implementation was done by comparing the analytical and model results. A comprehensive model parametric study was done through a typical drift in Canadian hard rock mines, then a case study on a cut-and-fill mine stope was carried out. The effects of the destress blasting patterns, initial ground stresses configuration, and the two factors (rock fragmentation, and stress dissipation) on destress blasting are studied. It is shown that the new method can be particularly useful in the assessment of deep drift face burst potential and the crown pillar burst potential in cut-and-fill mine stopes.

REFERENCES

Adams, D.J., Gay, N.C. and Cross, M., 1993, Preconditioning - A Technique for controlling rockbursts, Rockbursts and Seismicity in Mines, Young (ed.), pp.29-33, Balkema, Rotterdam, ISBN 9054103205.

Al-Heib M., Bigarre P. and Josien J.P. Principe, 1994, choix et parametres de la methode de saignee. Laboratoire de mecanique des Terrains. INERIS - Ecole des Mines.

Arjang, B., 1986, Field and stress determination at Campbell Red Lake Mine, Ontario, CANMET M&ET/MRL 86-57 TR.

Aubertin, M., Gill, D.E., 1988, Une méthodologie d'évaluation du potentiel de coups de terrain dans les mines d'Abitibi, Colloque sur le Contrôl de terrain (AMMQ), Val d'Or.

Aubertin, M., Gill, D.E., Simon, R., 1994, On the use of brittleness index modified (BIM to estimate the post-peak behaviour or rocks, Proc. First North American Rock Mech. Symp., Balkema, 945-952.

Beghoul, M.N., Lauriault, R.A., Plouffe, M., 1996, Relation spatio-temporelle du taux d'extraction et al réponse séismique minière induite, C.R. du 11[e] Colloque en Contrôl de Terrain, AMQ (ed.), Val d'Or.

Bigarre P., 1996, Rapport de synthese bibliographique et de recommandation sur les methodes de détente. Laboratoire de mecanique des Terrains. INERIS - Ecole des Mines.

Bieniawski, Z.T. , 1966, Stable and unstable fracture propagation in rock, Report of the South African Council of Scientific and Industrial Research, No. MEG 493.

Bieniawski, Z.T., 1967, Mechanism of brittle fracture of rock, Part I Theory of fracture process; Part II Experimental studies; Part II Fracture in tension and under long-term loading, Int. J. Rock Mech. And Min. Sci., 4, 395-430.

Bigarré, P., 1996, Rapport de synthèse bibliographique et de recommendations sur les méthodes de détente. Insritut national de l'environnement industriel et des risques (INERIS)-Ecole nationale supérieure des mines de Nancy.

Blaha, F., 1990, Some principles of rock mass failure in the case of rockbursts, Mechanics of Jointed and Faulted Rock, Rossmanith (ed.), 757-762.

Blake W. and Cuvelier, D.J, 1988, Developing reinforcement requirements for rockburst conditions at Hecla's Friday Mine, Proc. 2nd Int. Symp. Rockbursts and Seismicity in Mines, Minneapolis, pp. 589-598.

Blake, W., 1971, An automatic Rock Burst Monitor for Mine Use, Proc. Confr. on the Underground Mining Environment, Uni. of Missouri, Rolla, MO, pp. 69-82

Blake, W., 1972, Rockbursts Mechanics, Quarterly of the Colorado School of Mines, vol. 67, No.1, pp.1-64.

Blake, W., 1982, Rock preconditioning as a seismic control measure in mines, Rockbursts and Seismicity in Mines, Johannesburg, S. Afr. Min. Metall., Symp. Series No. 6.

Board, M.P. and Fairhurst, C., 1983, Rockburst control through destressing- a case example, Symp. Rockbursts: Prediction and Control, IMM, London, pp. 91-102.

Bolstad, D.D., 1990, Keynote lecture: Rockburst control research by the US Bureau of Mines. Rockburst and Seismicity in Mines, Fairhurst (ed.), Balkema, pp371-375.

Brady, B.H.G., and Brown, E.T., 1985, Rock Mechanics for Underground Mining, George Allen & Unwin.

Brown, E.T., 1984, Rockbursts: Prediction and control, Tunnels and Tunnelling, April, pp.17-19.

Brummer, R.K. and Kaiser, P.K., 1995, Risk-cost-benefit analysis for support design in burst prone mines, Transactions of the Institution of Mining and Metallurgy, 104(A), A71-A75.

Budavari, S., 1983, Response of the rock mass to excavations underground, Rock Mech. in Mining Practice, S. Afr. Inst. Min. Metall., Monograph Series, Vol. 5, pp. 55-76.

Calder, P.N., Archibald, J.F., Moroz, B., Semadeni, T., Korenberg, M., Mcilroy, P., 1986, Rockburst prediction studies at Queen's University, Can. Min. J., 107, 33-39.

Chavan, S.A., Raju, N.M, and Srivastava, S.B., 1993, Rockburst prediction-An empirical approach, Rockbursts and Seismicity in Mines, Young(ed.), Balkema, Rottedam, ISBN 9054103205, pp.163-167.

Chen,Z.H., Tang, C.A., Huang, R.Q., 1997, A double rock sample model for rockbursts, Int. J. Rock Mech. Min. Sci., Vol. 34, No. 6, pp.991-1000.

Comeau, W., Mitri, H.S., Mohanimed, M. and Tang, B., 1998, World-wide survey of destress blasting, practice in deep hard rock mines, In the Proc of the 25th Annual Conf. on Explosives and Blasing, Nashville, TN (1999), Sponsored by Int. Soc. Explosives Engineers, pp.189-205.

COMRO, 1988, An Industry Guide to Methods of Amelioration of the Hazards of Rockfalls and Rockbursts, Chamber of Mines Research Organization of South America, Johannesburg.

Cook, N.G.W., 1978, An Industry Guide to the Amelioration of Hazards of Rockbursts and Rockfalls, Chamber of mines of South America.

Cook, J.F. and Bruce, D., 1983, Rockbursts at Macassa Mine and the Kirkland lake mining area, Symp. Rockbursts: Prediction and Control, IMM, London, pp.81-90.

Cook, N.G.W, 1965, The failure of rock, Int. J. Rock Mech. Min. Sci., 2: 389-403.

Cook, N.G.W., 1963, The basic mechanics of rockburst, Journal of South African Institute of Mining & Metallurgy, vol. 64, pp71-81.

Cook, N.G.W., Hoek, E., Pretorius, J.P.G.,Ortlepp, W.D., Salamon, M.D.G., 1966, Rock mechanics applied to the study of rockbursts, J.S. Afr. Inst. of Min. Metall., 66, pp.435-528.

Cox, S.J.D., Meredith, P.G., 1993, Microcrack formation and material softening in rock measured by monitoring acoustic emissions, Int. J. Rock Mech. Min. Sci. and Geomech. Abstr., 30, 11-24.

Crouch, S.L., 1974, Analysis of rockbursts in cut-and-fill stopes, Trans. SME-AIME, vol.256, pp.298-303.

CRRP, 1996, A comprehensive summary of five years of collaborative research on rockbursting in hard rock mines, CAMIRO Mining Division, Canadian Rockburst Research Program.

Cullen, M., 1988, Studies of Destress Blasting at Campbell Red Lake Mine, M.Sc. Thesis, McGill University.

Daihua, Z., Miller, H.D.S., 1987, A proposed mechanism of rock failure and rockbursting, Proc. 6th Int. Cong. On Rock Mech., Montreal, 1357-1362.

Davidge, G.R., Martin, T.A. and Steed, C.M., 1988, Lacing support trial at Strathcona Mine, Proc. 2nd Symp. Rockbursts and Seismicity in Mines, Minneapolis.

Dickout, M.H., 1962, Ground control at Creighton Mine of the International Nickel Company of Canada Limited, Proc. 1st can. Rock Mech. Symp., McGill University, Montreal, pp.121-139.

Diest, F.H., 1965, A non-linear continuum approach to the problem of fracture zones and rockburst, J.S.Afr. Inst. Min. Metall., 65, pp.502-522.

Evan, B., Fredrich, J.T., Wong, T, 1990, The brittle-ductile transition in rocks: Recent experimental and theoretical progress, The Brittle-Ductile Transition in Rocks: The Heard Volume, Duba, et al. (eds), American Geophysical Union, Washington, D.C.

Filcek, H., 1980, Geomechanical criteria of rockburst hazard, Zeszyty Naukowe AGH, Górnictwo no. 4, Kraków, (cited from Tajdus et al. 1997).

Gay, N.G., Spencer, D., Van Wyk, J.J., Van Der Heever, P.K., 1982, The control of geological and mining parameters on seismicity in the Klerksdorp Gold Mine District, Proc. of Symp. On Seismicity in Mines, S. Afr. Nat. Group on Rock Mech., paper 3.

Gibowicz, S.J., 1990, Keynote lecture: The mechanism of seismic events induced by mining-A review, Rockbursts and Seismicity in Mines, Fairhurst (ed.), Balkema, 3-27.

Gibowicz, S.J., Kijiko, A., 1994, An Introduction to Mining Seismology, Academic Press Inc., International Geophysics Series, Vol. 55, ISBN 0122821203.

Gill, D.E., Aubertin, M. and Simon, R., 1993, A practical engineering approach to the evaluation of rockburst potential, Rockbursts and Seismicity in Mines, Young(ed.), Balkema, Rottedam, ISBN 9054103205, pp.63-68.

Gill, D.E., Aubertin, M., 1988, Évaluation du potentiel de coups de terrain dans les mines d'Abitibi, Rapport de recherche de l'URSTM présenté à l'Institut de Recherche en Santé et Sécurité du Travail (IRSST).

Glazer, S.N., 1997, Applied mine seismology: A Vaal Reef perspective, Rockbursts and Seismicity in Mines, Gibowicz and Lasocki (eds), Balkema, 69-73.

Hakami, H., 1988, Post-failure behaviour of brittle rock, Doctoral Thesis, Luleå University of Technology, Suède.

Hakami, H., Kankkunen, J., O'Flaherty, T. and Olsson, M. , 1990, Destress Blasting Experiments at the Pyhäsalmi Mine, Finland, Report DS 1990 :3, SveDeFo, Stockholm, Sweden.

Hanson, D., Quesnel, W., and Hong, R., 1987, Destressing a rockburst prone crown pillar, CANMET MRL 87-82(TR).

Hasegawa, H.S., Wetmiller, R.J., Gendzwill, D.J., 1989, Induced seismicity in mines in Canada-An overview, Pure and Appl. Geophysics, 129, 423-453.

Hedley, D.G.F., 1991, A five-year review of the Canada-Ontario industry rockburst project, CANMET Special Report SP90-4E.

Hedley, D.G.F., 1992, Rockburst Handbook for Ontario Hardrock Mines, CANMET Special Report SP92-1E, ISBN0-660-14549-9.

Hedley, D.G.F., and Whitten, N., 1983, Performance of bolting systems subject to rockbursts, CIM Seminar Underground Support Systems, Sudbury, CIM Special volume 35, pp.73-79.

Hedley, D.G.F., Udd, J.E., 1987, The Canada-Ontario-industry rockburst project, Fred Leighton Memorial Workshop on Mining Induced Seismicity, ISRM-CIM, Montreal, 115-127.

Hill, F.G., and Plewman, R.P., 1957, Destressing: a means of ameliorating rockburst conditions: Part2: implementing destressing with a discussion of the results so far obtained, J.S. Afr. Inst. Min. Met., October, 1957.

Hoek, E., & Bieniawski, Z.T., 1965b, Fracture propagation in hard rock, Technical Report- Rock Mech, Div., South African Council for Scientific and Industrial research.

Hoek, E., & Bieniawski,Z.T., 1965a, Brittle fracture propagation in rock under compression, Int. J. Frac. Mech., 1, 137-155.

Hoek, E., and Brown E.T., 1980, Underground Excavations in Rock, Inst. Min. and Metall., London.

Hodgson, K. and Joughin, N.C. 1967, The relationship between energy release rate, damage and seismicity in deep mines. Proc 8th Symp. on Rock Mech., University of Minnesota, In Failure and Breakage of Rock, C. Fairhurst (Ed), pp.194-203.

Hucka, V., Das, B., 1974, Brittleness determination of rocks by different methods, Int. J. Rock Mech. Min. Sci. & Geomech. Abstr., 30, 257-269.

Hueckel, T., 1987, Hysteresis evolution and failure in cyclic loading of dilatant rocks, Constitutive Laws for Eng. Materials: Theory and Applications, Desai C.S. et al. (ed.), Elsevier Science Pub., 565-572.

Jeager, J.C., Cook,N.G.W., 1976, Fundamentals of Rock Mechanics, 2nd Edition, Champman and Hall, ISBN 0-470-15063-7.

Karwoski, W. J., McLaughin, W. C. and Black, 1979, Rock preconditioning to prevent rock bursts-report on a field demonstration. Report of investigations 8381, United States Department of the Interior, Bureau of Mines.

Krauland, N., Söder, P-E., 1991, Rock stabilisation by destress blasting – experiences from Boliden mines (in Swedish), Rock Mechanics Meeting, BeFo, Stockholm, Sweden.

Kidybinski, A., 1981, Bursting Liability indices in coal, Int. J. Rock Mech. Min. Sci., 18, 295-304.

Kijko, Andrzej, 1997, Keynote: Seismic hazard assessment in mines, Rockbursts and Seismicity in Mines, Gibowicz & Lasocki(eds.)© Balkema, Rotterdam, ISBN 9054108908.

Landriault, D., and Oliver, P., 1992, The destress slot concept for bulk mining at depth, Rock Support in Mining and Underground Construction, Kaiser & McCreath (eds.)© Balkema, Rotterdam, ISBN 9054100443, pp.211-217.

Lekhnitskii, S.G., 1963, Theory of Elasticity of an Anisotropic Elastic Body, Julius J. Brandstatter (ed.), Holden-Day, Inc., San Francisco.

Lightfoot, N., 1993, The use of numerical modelling in rockburst control, Rockbursts and Seismicity in Mines, Young(ed.), Balkema, Rotterdam, ISBN 9054103205, pp.355-360.

Lightfoot, N., Goldbach, O.D., Kullmann, D.H., and Toper, A.Z., 1996, Rockburst control in the South African deep level gold mining industry, Proceedings of the 2nd North American Rock Mechanics Symposium (NARMS 96), pp.295-303, Montreal, Canada.

Lu, J.Y., Wang, B. and Wang, C.M., 1993, Application of numerical methods in rockburst prediction and control, Rockbursts and Seismicity in Mines, Young (ed.), Balkema, Rotterdam, ISBN 9054103205, pp361-366.

MacDonald, P., Wiles, T. and Villeneuve, T., 1988, Rock mechanics aspects of vertical retreat mining at 2000m depth at Creighton Mine, CARE Univ. Newcastle-upon-Tyne, Pub. IMM., London.

Martin, C. Derek, 1996, Brittle failure of rock materials: Test results and constitutive model, Canadian Geotechnical Journal, vol. 33, No. 2, p378.

McCreath, D.R. and Kaiser, P.K., 1992, Evaluation of current support practices in burst-prone ground and preliminary guidelines for Canadian hardrock mines, Rock Support in Mining and Underground Construction, Kaiser & McCreath (eds.), © Balkema, Rotterdam, ISBN 9054100443, pp.611-619.

McGarr, A., and Wiebols, G.A., 1977, Influence of mine geometry and closure volume on seismicity in a deep level mine, Int. J. Rock Mech. Min. Sci. Geomech., 14, pp.139-145.

Mei, J., Lu, J., 1987, The phenomena, prediction and control of rockburst in China, Proc. 6th Int. Cong. Rock Mech., ISRM, Vol. 2, pp.1135-1140.

Mitri, H. S., Hassani, F.P. and Kebbe, R.1993, A strain energy approach for the prediction of rockburst potential in underground hard rock mines, Proc., 1st Canadian Symp. on Numerical Modelling Applications in Mining and Geomechanics, Montreal, March 27-30, pp. 228-239.

Mitri, H.S., 1996a, Numerical modelling of mining-induced energy in rockburst problems, Workshop notes of 2nd North American Rock Mechanics Symposium 1996, Mitri et al. (ed.), Montreal, pp.1-1~1-19.

Mitri, H.S., 1996b, Study of rockburst potential at Sigma Mine, Val d'Or, Quebec using numerical modelling, Final Report, p.129.

H.S. Mitri, B. Tang and R. Simon, 1999, FE modelling of mining-induced energy release and storage rates. Transactions of SAIMM (South African Institute of Mining and Metallurgy) Journal, Vol. **99(2)**: 103-110.

Morrison, R.G.K., 1942, Report on rockburst situation in Ontario mines, trans. Can. Inst. Min. and Met., 45, pp225-272.

Moruzi, G.A. and Pasieka, A.R., 1964, Evaluation of a blasting technique for destressing ground subject to rockbursting, 6th U.S. Rock Mech. Symp., Rolla, Missuri.

Moruzi, G.A., and Pasieka, A.R., 1969, Evaluation of a Blasting Technique for Destressing Ground subject to Rock Bursting, Proc. 5th Canadian Symp. on Rock Mech., Mines Branch, Queens Printer, Ottawa, pp. 185-204.

Makuch, A., 1987, Rock mechanics at Campbell Red Lake Mine. Workshop on Mining Induced Seismicity, Montreal, pp. 181-188.

Makuch A., Neumann M., Hedley D.G.F., and Blake W., 1987, Destress blasting at Campbell Red lake mine. Part 1: Rock Mechanics concepts of destressing pillars, Part 2: Practical applications of pillar destressing at Campbell Mine, Part 3: An instrumented destress blast of the 1604E crown pillar. CANMET, Elliot Lake Laboratory, Report produced for Canada/Ontario/industry Rockburst Research Project, Report SP 87-8E.

Neyman, B., Szecowka, Z., Zuberek, W., 1972, Effective methods for fighting rockburst in Polish collieries, Proc. 5th Int. Strata Control Conf., 23.1-23.9.

O'Donnell, J.D.P., 1992, The use of destress blasting at Inco's Creighton Mine, MASSMIN 92, Johannesburg, SAIMM, pp.71-74.

Obert, L., Duvall, W.I., 1967, Rock Mechanics and the Design of Structures in Rock, John Wiley.

Oliver, P., Wiles, T., MacDonald, P. and O'Donnell, D., 1987, Rockburst control measures at Inco's Creighton Mine, Proc. 6th Conf. on Ground Control in Mining, West Virginia.

Ortlepp, W.D., 1982, Rockbursts in South African Gold Mines: A Phenomenological View, Proceedings of the 1st international Congress on Rockbursts and Seismicity in Mines, Gay & Wainwright(ed.), Johannesburg, 1982, pp165-178.

Ortlepp, W.D., 1983. The Mechanism and Control of Rockbursts: Chapter 12: Rock Mechanics in Mining Practice", Budavari (ed.), S. Afr. Inst. Min. Met., Mono series No. 5, pp. 257 - 282.

Ortlepp, W.D., 1984, Rockbursts in South African gold mines: a phenomenological view, Int. Symposium on Rockbursts and Seismicity in Mines, South African Institute of Min. Metall. Symp. Series No. 6, Johannesburg, pp.165-178.

Ortlepp, W.D., 1992, Invited lecture: The design of support for the containment of rockburst damage in tunnels-An engineering approach, Rock Support in Mining and

Underground Construction, Kaiser & McCreath (eds.)© Balkema, Rotterdam, ISBN 9054100443, pp.593-609.

Ortlepp, W.D., Stacey, T.R., 1994, Rockburst mechanisms in tunnels and shafts, Tunnelling and Underground Space Technology, Vol. 9, No.1, pp.59-65.

Pande, G.N., Beer, G., and Williams, J.R., 1990, Numerical Method in Rock Mechanics, John Wiley & Sons Ltd., ISBN 047192022l5.

Paterson, M.S., 1978, Experimental Rock Deformation-The Brittle Field. Spinger-Verlag.

Petukhov, I.M., 1987, Forecasting and combating rockbursts: recent developments, Proc. 6th Cong. IRSM. Vol. 2, pp.1207-1210.

Petukhov, I.M., 1990, Theory of rockbursts and their classification, Rockburst-global experience, paper presented at Fifth Plenary Scientific Session of Working Group on Rockbursts of International Bureau of Strata Mechanics, pp.1-10.

Plouffe, M., Mottahed, P., Lebel, D., Côté, M., 1993, Monitoring of large mining induced seismic events-CANMET/MRL's contribution, Rockbursts and Seismicity in Mines, Young (ed.), Balkema, 393-397.

Roberts, M.K.S. and Brummer, R.K., 1988, Support requirements in rockburst conditions, J. South African Inst. Min. Met., vol.88, No.3, pp97-104.

Robson, W.T., Adamson, J.C. and Selnes, W.E., 1940, Rock-burst at Lake Shore Mines, Trans. C.I.M., vol.43, pp7-30.

Rorke, A.J. and Brummer, R.K., 1988, The use of explosives in rockburst control techniques, Proc. 2nd Int. Symp. Rockbursts and Seismicity in Mines, Minneapolis, A.A. Blkema, Rotterdam, pp.377-386.

Rorke, A.J., Cross, M., Van Antwerpen, H.E.F., and Noble, E., 1990, The mining of a small up-dip remnant with the aid of preconditioning blasts. Int. Deep Mining Conf., Johannesburg, s.afr. Inst. Min. Met., Symposium Seires 10. pp. 765-774.

Roux, A.J.A., Leeman, E.R.,and Denkhaus, H.G., 1957, Destressing: a means of ameliorating rockburst conditions. Part I: The concept of destressing and the results obtained from its applications, J. S.Afr. Inst. Min. Met., October 1957.

Ryder, J.A., 1987, Excess shear stress (ESS): an engineering criterion for assessingunstable slip and associated rockburst hazard, Proc. 6th Cong. Rock Mech., IRSM, Montreal, vol.2, 1211-1215.

Ryman-Lipinsky, W.K., Bakker, D., 1997, The development of government rockburst and rockfall hazard monitoring system for South African mines, Rockburst and Seismicity in Mines, Gibowicz and Lasocki (eds.), Balkema, 371-376.

Salamon, M.D.G., 1964a, Elastic analysis of displacements and stress induced by the mining of seam or reef deposits—Part I, J. S. Afr. Inst. Min. Metall., 64, pp.129-149.

Salamon, M.D.G., 1964b, Elastic analysis of displacements and stress induced by the mining of seam or reef deposits—Part II, J. S. Afr. Inst. Min. Metall., 64, pp.197-218.

Salamon, M.D.G., 1964c, Elastic analysis of displacements and stress induced by the mining of seam or reef deposits—Part III, J. S. Afr. Inst. Min. Metall., 64, pp.468-500.

Salamon, M.D.G., 1970, Pillar stability/ instability and design of pillar workings, Int. J. Rock Mech. Min. Sci., 7, pp613-631.

Salamon, M.D.G., 1974, Rock Mechanics of Underground Excavations, Advances in Rock Mechanics, Proc. 3rd Cong. Int. Soc. Rock Mech., Vol. 1-B, pp.951-1099.

Salamon, M.D.G., 1984, Energy considerations in rock mechanics: fundamental results, J. S.Afr. Inst. Min. Metall., Vol. 84, No. 8, pp.233-246.

Salamon, M.D.G., 1993, Keynote address: Some applications of geomechanical modelling in rockburst and related research, Rockbursts and Seismicity in Mines, Young(ed.), Balkema, Rotterdam, ISBN 9054103205, pp.297-309.

Salamon, M.G.D., 1983, Rockburst hazard and the fight for its alleviation in South African gold mines, Rockbursts: Prediction and Control, IMM, London, pp. 11 - 36.

Scoble, M.J., Cullen, M. And Makuch, A., 1987, Experimental studies of factors relating to destress blasting. 28th U.S. Symposium on Rock Mechanics, Tucson, Arizona, USA

Scott, D.F., 1990, Relationships of geological features to seismic events, Lucky Fridy Mine, Mullan, Idaho, Rockbursts and Seismicity in Mines, Fairhurst(ed.), Balkema, Rotterdam.

Shao, J.F., Khazraei, R., 1996, A continuum damage mechanics approach for time independent and dependent behaviour of brittle rock, Mechanics Research Communications, Vol.23, No. 3, pp.257-265.

Simon, R., 1999, Analysis of Fault-Slip Mechanisms in Hard Rock Mining, Ph.D. Thesis, McGill University.

Simon, R., Aubertin, M. and Mitri, H. S., 1995, Evaluation of rockburst potential in hard rock mines, 97th AGM of C.I.M. and Rock Mechanics and Strata Control Session, Halifax, Nova Scotia, Canada.

Simon, R., Aubertin, M., Auer, L., Gill, D.E., Labrie, D. and Mitri, H.S, 1998, A study of destress blasting effect on the rockburst potential of an underground mine in hard rock. 3rd North Amer. Rock Mech. Symp. NARMS'98, Cancun, 285-294.

Singh, S.P., 1989, Classification of mine workings according to their rockburst proneness, Mining Science and Technology, 8, 253-262.

Spottiswoode, S.M., 1990, Volume excess shear stress and cumulative seismic moments, Rockbursts and Seismicity in Mines, Fairhurst (ed.), Balkema, pp. 39-43.

Srinivasan, C., Arora, S.K., and Yaji, R.K., 1997, Use of mining and seismological parameters as premonitors of rockbursts, Int. J. Rock Mech. Min. Sci., Vol. 34, No.6, pp1001-1008.

Stacey, T.R. and Page, C.H., 1986, Practical Handbook for Underground Rock Mechanics, Trans-Tech. Publ.

Stacey, T.R., Ortlepp, W.D., and Kirsten, H.A.D., 1995, Energy-absorbing capacity of reinforced shotcrete, with reference to the containment of rockburst damage, J.S.Afr. Inst. Min. Metall., V. 95, n. 3, p137, 4p.

Starfield, A.M., Fairhurst, C., 1968, How high-speed computers advance design of practical mine pillar systems, Engng. Min. J., 169, 78-84.

Starfield, A.M., Wawersik, W.R., 1968, Pillars as structural components in room-and-pillar mine design, Proc. 10th US Sym. On Rock Mech., Austin, 783-809.

Stewarski, E., 1987, Energetic indicator of liability of rocks to burst during shock loading with Hopkin's bar, Stanislaw Staszic Acad. Min. Metall., Cracow, Min. Bul., 129, 263-269.

Stopinski, W., Dmowska, R., 1984, Rock resistivity in the Lubin (Poland) Copper Mine and its relation to variations of strain field and occurrence of rockbursts, Proc. 1st Int. Cong. Rockbursts and Seismicity in Mines, Johannesburg, S.Afr. Inst. Min. Metall., 297-307.

Tajdus, A. Flisiak, J., and Cala, M., 1997, Estimation of rockburst hazard basing on 3D stress field analysis, Rockbursts and Seismicity in Mines, Gibowicz & Lasocki(ed.), Balkema, Rotterdam, ISBN 9054108908, pp272-277.

Tan, T.K., 1986, Hypothesis on rockbursts, Proc.Int. Symp. On Rock Stress and Stress Measurements, pp515-520.

Tang CA., 1997, Numerical simulation of progressive rock failure and associated seismicity, Int. J. of Rock Mech. & Min. Sci. & Geomech. Abs., 34(2): 249 ff

Tao, Z.Y., 1988, Support design of tunnels subjected to rockbursting, Rock Mechanics and Power Plants, Romana (ed.), Balkema, 407-411.

Taube, A., Krauland, N., Ouchterlony, F. and Hakami, H. , 1991, Destress blasting in Centralmine's (Boliden Group) Laisvall orebody (in Swedish), Report DS 1991 : 3G, SveDeFo, Stockholm, Sweden.

Toper, A.Z., Grodner, M., Stewart, R.D., Lightfoot, N., 1997, Preconditioning: A rockburst control technique, Rockbursts and Seismicity in Mines, Gibowicz & Lasocki(ed.), Balkema, Rottedam, ISBN 9054108908, pp.267-272.

Toper, A.Z., Srewart, R.D., Kullmann, D.H, Grodner, M., Lightfoot, N., Janse van, Rensburg, A.L. and Longmore, P.J., 1998, Develop and implement preconditioning techniques, CSIR, Division of Mining Technology, SIMRAC report, GAP 336.

Walsh, J.B., 1977, Energy changes due to mining, Int. J. Rock Mech. Min. Sci., Vol. 14, pp. 25-33.

Wawersik, W.R., Rudnicki, J.W., Olsson, W.A., Holcomb, D.J., Chau, K.T., 1990, Localisation of deformation in brittle rocks: Theoretical and laboratory investigations, Micromechnics of Failure of Quasi-brittle Materials, Elsevier Appl. Sci., 115-124.

Williams, T.J., and Cuvelier, 1988, Report on a field trial of an underhand longwall mining method to alleviate rockburst hazards, Proc. 2nd Int. Symp. Rockbursts and Seismicity in mines, Minneapolis, A.A. Balkema, Rotterdam, pp. 349 - 354.

Wittaker, B.N., Singh, R.N., and Sun, G.X., 1992, Rock Fracture Mechanics: Principle, Design and Applications, ELSEVIER, Amsterdam-London-New York-Tokyo.

Wu, Y.K., and Zhang, W.B., 1997, Prevention of rockbursts in coal mines in China, Rockbursts and Seismicity in Mines, Gibowicz & Lasocki(ed.), Balkema, Rotterdam, ISBN 9054108908, pp.361-366.

Zipf, R.K., 1996, Simulation of cascading pillar failure in room-and-pillar mines using boundary element method, Proceedings of 2nd North American Rock Mechanics Symposium, Aubertin, Hassani, and Mitri (eds), Montreal, June 19-21, pp. 1887 – 1892

Yu, Y.S, Toews, N.A., Boyle, R., Vongpaisal, S., Wang, B., and Thomson, S, 1996, Very large-scale 3-D modelling of mine structures using the finite element technique. Rock Mechanics Tools and Techniques (NARMS'96), vol. 2, pp. 1871-1878.

APPENDIX A

BRICK ELEMENT SHAPE FUNCTION

For each corner node, it has its connection mid-side nodes. We put this relation into a matrix NK(8,3). For ξ_i, η_i, ζ_i, we also can put them into a matrix CEZ(20,3) for 20-node and a matrix CEZ1(8,3) for 8-node element. Corresponding to Figure 5.6, the matrices can be arranged as follows:

$$CEZ(20,3) = \begin{bmatrix} -1. & -1. & 1. \\ -1. & 1. & 1. \\ 1. & 1. & 1. \\ 1. & -1. & 1. \\ -1. & -1. & -1. \\ -1. & 1. & -1. \\ 1. & 1. & -1. \\ 1. & -1. & -1. \\ -1. & 0. & 1. \\ 0. & 1. & 1. \\ 1. & 0. & 1. \\ 0. & -1. & 1. \\ -1. & -1. & 0. \\ -1. & 0. & 1. \\ 1. & 1. & 0. \\ 1. & -1. & 0. \\ -1. & 0. & -1. \\ 0. & 1. & -1. \\ 1. & 0. & -1. \\ 0. & -1. & -1. \end{bmatrix} \qquad NK(8,3) = \begin{bmatrix} 12 & 9 & 13 \\ 10 & 9 & 14 \\ 10 & 11 & 15 \\ 12 & 11 & 16 \\ 20 & 17 & 13 \\ 18 & 17 & 14 \\ 18 & 19 & 15 \\ 20 & 19 & 16 \end{bmatrix} \qquad (A.1)$$

$$CEZ1(8,3)=\begin{bmatrix}-1 & -1 & 1\\ -1 & 1 & 1\\ 1 & 1 & 1\\ 1 & -1 & 1\\ -1 & -1 & -1\\ -1 & 1 & -1\\ 1 & 1 & -1\\ 1 & -1 & -1\end{bmatrix} \qquad (A.2)$$

For example,

i=1: ξ_1=CEZ(1,1)= -1., η_1=CEZ(1,2)= -1.,ζ_1=CEZ(1,3)= -1.

$$A=9\begin{cases}\xi_9=0.\\ \eta_9=-1.,\\ \zeta_9=-1.\end{cases} \quad B=12\begin{cases}\xi_{12}=-1.\\ \eta_{12}=0.\\ \zeta_{12}=-1.\end{cases} \quad ,C=17\begin{cases}\xi_{17}=-1.\\ \eta_{17}=-1.\\ \zeta_{17}=0.\end{cases}$$

$N_1=\frac{1}{8}(1-\xi)(1-\eta)(1-\zeta)-\frac{1}{2}[\frac{1}{4}(1-\xi^2)(1-\eta)(1-\zeta)+\frac{1}{4}(1-\eta^2)(1-\xi)(1-\zeta)+\frac{1}{4}(1-\zeta^2)(1-$

$\xi)(1-\eta)]$

$=\frac{1}{8}(1-\eta)(1-\xi)(1-\zeta)[1-(1+\xi)-(1+\eta)-(1+\zeta)]$

$=\frac{1}{8}(1+\xi_1\ \xi)(1+\eta_1\ \eta)(1+\zeta_1\ \zeta)[\xi_1\ \xi+\eta_1\ \eta+\zeta_1\ \zeta-2]$

For i=6: $\xi_6=CEZ(6,1)=1.$ $\eta_6=CEZ(6,2)=-1,$ $\zeta_6=CEZ(6,3)=1$

$$A=13\begin{cases}\xi_{13}=0.\\ \eta_{13}=-1.\\ \zeta_{13}=1.\end{cases} , \quad B=14\begin{cases}\xi_{14}=1.\\ \eta_{14}=0.,\\ \zeta_{14}=1\end{cases} \quad C=18\begin{cases}\xi_{18}=1.\\ \eta_{18}=-1.\\ \zeta_{18}=0.\end{cases}$$

$N_6=\frac{1}{8}(1+\xi)(1-\eta)(1+\zeta)-\frac{1}{2}[\frac{1}{4}(1-\xi^2)(1-\eta)(1+\zeta)+\frac{1}{4}((1-\eta^2)(1+\xi)(1+\zeta)+\frac{1}{4}1-$

$\zeta^2)(1+\xi)(1-\eta)]$

$=\frac{1}{8}(1+\ \xi)(1-\eta)(1+\zeta)[\xi-\eta+\zeta-2]$

$$=\frac{1}{8}(1+\xi_6\xi)(1+\eta_6\eta)(1+\zeta_6\zeta)[\xi_6\xi+\eta_6\eta+\zeta_6\zeta-2]$$

After calculated each corner node's shape function we find that

$$N_i=\frac{1}{8}(1+\xi_i\xi)(1+\eta_i\eta)(1+\zeta_i\zeta)[\xi_i\xi+\eta_i\eta+\zeta_i\zeta-2] \qquad (A.3)$$

Now we can get the derivatives of shape function to ξ,η,ζ respectively

For i =1, 8

$$N_{i,\xi}=\frac{1}{8}\xi_i(1+\eta_i\eta)(1+\zeta_i\zeta)[2\xi_i\xi+\eta_i\eta+\zeta_i\zeta-1]$$

$$N_{i,\eta}=\frac{1}{8}\eta_i(1+\xi_i\xi)(1+\zeta_i\zeta)[\xi_i\xi+2\eta_i\eta+\zeta_i\zeta-1] \qquad (A.4)$$

$$N_{i,\zeta}=\frac{1}{8}\zeta_i(1+\xi_i\xi)(1+\eta_i\eta)[\xi_i\xi+\eta_i\eta+2\zeta_i\zeta-1]$$

For i =13,16

$$N_{i,\xi}=-\frac{1}{2}\xi\ (1+\eta_i\eta)(1+\zeta_i\zeta)$$

$$N_{i,\eta}=\frac{1}{4}\eta_i(1-\xi^2)(1+\zeta_i\zeta) \qquad (A.5)$$

$$N_{i,\zeta}=\frac{1}{4}\zeta_i(1-\xi^2)(1+\eta_i\eta)$$

For i = 10, 12, 20, 18

$$N_{i,\xi}=\frac{1}{4}\xi_i(1-\eta^2)(1+\zeta_i\zeta)$$

$$N_{i,\eta}=-\frac{1}{2}\eta\ (1+\xi_i\xi)(1+\zeta_i\zeta) \qquad (A.6)$$

$$N_{i,\zeta}=\frac{1}{4}\zeta_i(1-\eta^2)(1+\xi_i\xi)$$

For i = 9, 11, 19, 17

$$N_{i,\xi}=\frac{1}{4}\xi_i(1-\zeta^2)(1+\eta_i\eta)$$

$$N_{i,\eta} = \frac{1}{4}\eta_i(1-\zeta^2)(1+\xi_i\xi) \tag{A.7}$$

$$N_{i,\zeta} = -\frac{1}{2}\zeta(1+\xi_i\xi)(1+\eta_i\eta)$$

APPENDIX B

USERS GUIDE TO *e-z tools 3D*

A.1 STRUCTURE OF THE INPUT DATA FILE

In this appendix, the preparation of input data file is explained in detail. When the input data are prepared, all the information needed is all well arranged into the input data file with the following format.

Card 1: NND, MM, NEC, NCUT, NIS, NGW, NCA:

- **NND**: total number of nodes;
- **MM**: total number of the elements;
- **NEC**: total number of materials;
- NCUT: number of cut sequences;
- NIS: initial stress indicator: 0-without initial stress, 1-with initial stress;
- NGW: gravity indicator:

  0-without gravity,

  1-gravity along Z-positive,

  2-Y-positive,

  3-X-positive,

  4-Z-negtive,

  5-Y-negtive,

  6-X-negtive;
- NCA: local node numbering system. 1--normal 20-node. 2--HyperMesh 20-node. 3--8-node element.

Card 2: IGS, IDS, IMS, NCOM, NSR

- IGS: indicator for the equation solver, 1-GS-Seidel, 2-Skyline;
- IDS: indicator for destress blasting, 0-without destress, 1 with destress blasting;

- IMS: indicator for the material number in the destressed zone, it should always equal to the material number for the destressed zone;
- NCOM: total number of components.
- NSR: surface traction indicator, 0-without surface traction, 1-with surface traction.

Card 3: NMAT (NCOM):

Array used to define the number of material for each component, when it equals to zero that means the element is being cut in the cut.

Card 4: NK, X (NK), Y (NK), Z (NK):

- NK: node number;
- X(NK), Y(NK), Z(NK)-coordinate of the node

Card5: MAN, (ECS (I), I=1,10):

- MAN: material number,
- ESC(1): E_x Elastic modulus on x direction;
- ESC(2): E_y Elastic modulus on y direction;
- ESC(3): E_z Elastic modulus on z direction;
- ESC(4): G_{xy} Shear Modulus on xoy plane;
- ESC(5): G_{yz} Shear Modulus on yoz plane;
- ESC(6): G_{xz} Shear Modulus on zox plane;
- ESC(7): ν_{xy} Poisson's ratio on xoy plane;
- ESC(8): ν_{yz} Poisson's ratio on yoz plane;
- ESC(9): ν_{zx} Poisson's ratio on zox plane;
- ESC(10): γ unit weight of the rock material.

Card 6: (SIGMA(I),I=1,6), θ, φ:

- SIGMA(I): initial stresses array at the original point

  θ: strike describes the direction of a contour

  φ: dip describes the slope of the line of the dip on the local plane relation to the global coordinate system, refer to Figure 5.3.

Card 7: (FB(I), I=1,6):

Coefficient array for stress ratio: normally **FB(1)**=0.5-2.5, FB(2)=0.5-2.,FB(3)=1., FB(4) = FB(5) = FB(6) = 0.

Card 8: CC, SM, SS, FAI, SIGC:

- CC: Coherent force of the material;
- SM: geomechanical constant m for RMR,
- SS: geomechanical constant s for RMR,
- FAI: friction angle;
- SIGC: uniaxial compress strength

Card9: ALPHA(I),I=1,9): (Rock fragmentation factors array, 0. to 1.0), (if necessary):

Card 10: (BETA(I),I=1,6): (stiffness factors array, 1.0 to 0.0), (if necessary):

Card 11: (ME, MAN, (NN(I), I=1,m): (m=20 for 20-node element, m = 8 for 8-node element)

- ME: element number;

- MAN: material number;
- NN(I): element node number connectivity array

Card 12: NK, (NCON(I),I=1,3):

- NK: node number,
- NCON(I): node constraints array,0-free, 1-fixed

Card 13: NTOT (if necessary):

- NTOT: total number of node suffering surface traction

Card 14: NK, (P (i), i =1,3) (if necessary):

- NK: node number
- P(I): Nodal surface stress suffered

B.2 SCENARIO FOR THE GLOBAL STIFFNESS MATRIX

In skyline format, the global stiffness matrix will be stored in three arrays: S(NMT), MDIA(N+1), and MHT(N), in which the NMT is the total size of the skyline format global stiffness matrix, N is the total number of rows or columns of the matrix, and MDIA(I) is the diagonal element position in the skyline format for global stiffness matrix, MHT(I) is the column height in skyline format for global stiffness matrix. Referring to Figure A-1, the upper triangle of a symmetric matrix will be store in the format as in Table A-1, and the lower triangle of it will be stored in the format as in Table A-2.

Table B-1 Skyline format for the upper triangle symmetric matrix

	1	2	3	4	5	6	7	8	9	10	11	12	13	14	15	16	17	18	19	20	21	22	23
S(I)	x	x	x	0	0	x	x	0	0	0	x	x	x	0	x	x	x	x	x	x	x	x	x
MDIA(I)	1	3	7	12	16	18	21	23	24														
MHT(I)	1	3	4	3	1	2	1	0															

Table B-2 Skyline format for the lower triangle symmetric matrix

	1	2	3	4	5	6	7	8	9	10	11	12	13	14	15	16	17	18	19	20	21
S(I)	x	x	0	0	x	x	0	x	x	x	x	x	0	0	x	x	0	x	x	x	x
MDIA(I)	1	6	9	10	12	16	19	21	22												
MHT(I)	4	2	0	1	3	2	1	0													

The Sparse Linear Algebra Package (SLAP) utilizes two matrix data structures: 1) the SLAP Triad format or 2) the SLAP Column format. In the ***e-z tools 3D*** the SLAP TRIAD format has been used.

In the SLAP Triad format, only the non-zeros are stored. They may appear in ANY order. Three arrays of length NELT, where NELT is the number of non-zeros in the matrix: (IA(NELT), JA(NELT), A(NELT)) are employed. For each non-zero the row and column index of that matrix element will be stored in the IA and JA arrays. The value of the non-zero matrix element is placed in the corresponding location of the array. This is an extremely easy data structure to generate. On the other hand it is not too efficient on vector computers for the iterative solution of linear systems. Hence, SLAP changes this input data structure to the SLAP Column format for the iteration (but does not change it back). Here is an example of the SLAP Triad storage format for a 5x5 Matrix. Recall that the entries may appear in any order.

5x5 Matrix

$$\begin{bmatrix} 11 & 12 & 0 & 0 & 15 \\ 21 & 22 & 0 & 0 & 0 \\ 0 & 0 & 33 & 0 & 35 \\ 0 & 0 & 0 & 44 & 0 \\ 51 & 0 & 53 & 0 & 55 \end{bmatrix}$$

SLAP Column format for 5x5 matrix on left

	1	2	3	4	5	6	7	8	9	10	11
A:	11	21	51	22	12	33	53	44	55	15	35
IA:	1	2	5	2	1	3	5	4	5	1	3
JA:	1	1	1	2	2	3	3	4	5	5	5

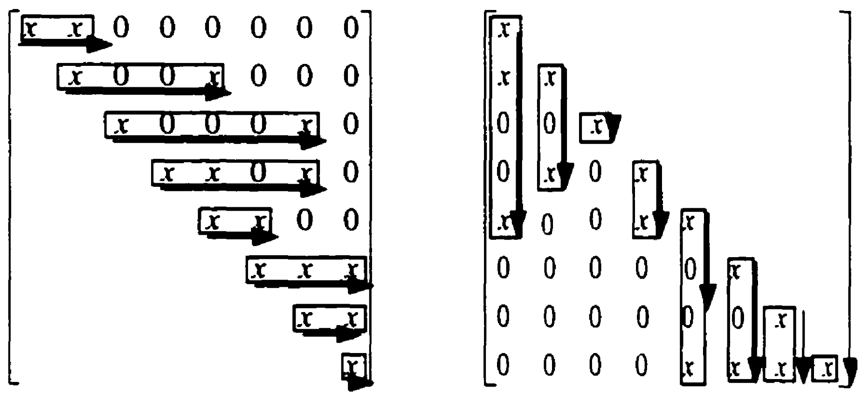

a) Upper Triangle Skyline

b) Lower Triangle Skyline

Figure B-1 Skyline storage strategy for global stiffness matrix

APPENDIX C

POTENTIAL ENERGY

Based on the relationship between the stresses and the strains in the element and the nodal point displacements, the equation of condition for the nodal point displacements can be established.

The potential energy of an element π^e is comprised of the elastic strain energy and the work of the bulk, distributed and point loads on the element. The elastic strain energy in relation to an element of volume is obtained from half of the product of the stress and the elastic strain. Thus the following is obtained for the element for the element under consideration:

$$\pi^e = \frac{1}{2}\int_{V^e}\{\Delta\sigma\}^T \cdot \{\varepsilon\} \cdot dV - \int_{V}\{\delta\}^T \cdot \{p\} \cdot dV - \int_{S^e}\{\delta\}^T \cdot \{q\} dS - \{\delta^e\}^T \{F^*\} \qquad \text{(C.1)}$$

The quantities in Equation 5.43 are defined as follows:

$\{\Delta\sigma\} = \{\sigma\}-\{\sigma^0\}$, $\{\sigma^0\}$ is the initial stress vector in the element.

$\{\delta\} = \{u, v, w\}^T$ — Displacement vector

$\{p\} = (p_x, p_y, p_z\}^T$: — bulk force per unit volume, e.g. dead weight.

$\{q\} = (q_x, q_y, q_z\}^T$: — distributed load per unit area.

$\{F^*\} = \{ F^*_{x_1}, F^*_{y_1}, F^*_{z_1}, F^*_{x_2}, F^*_{y_2}, F^*_{z_2}, \cdots, F^*_{x_m}, F^*_{y_m}, F^*_{z_m} \}^T$:

point loads applied to nodal points of element.

V_e = volume of element. S_e = surface of the element.

Using Equation 5.37. Equation 5.43 can be changed into Equation 5.44 which the only unknowns are the nodal displacements u_i, v_i, w_i, $i = 1, m$.

$$\begin{aligned}\pi^e = &\frac{1}{2}\left(\int_{V^e}\{\delta^e\}^T[B]^T[D]\cdot[B]\cdot\{\delta^e\}\cdot dV - \int_{V^e}\{\delta^e\}^T[B]^T\{\sigma^0\}\cdot dV\right)\\ &-\int_{V}\{\delta^e\}^T[N]^T\cdot\{p\}\cdot dV - \int_{S^e}\{\delta^e\}^T\{N'\}^T\cdot\{q\}dS - \{\delta^e\}^T\{F^*\}\end{aligned} \qquad \text{(C.2)}$$

Applying the minimum potential energy theory here, the following vector can be obtained:

$$\frac{\partial \pi^e}{\partial\{\delta^e\}} = \begin{Bmatrix} \dfrac{\partial \pi^e}{\partial u_1} \\ \dfrac{\partial \pi^e}{\partial v_1} \\ \dfrac{\partial \pi^e}{\partial w_1} \\ \vdots \\ \dfrac{\partial \pi^e}{\partial w_m} \end{Bmatrix} = 0 \tag{C.3}$$

Carrying the differentiation gives

$$\begin{aligned} \frac{\partial \pi^e}{\partial\{\delta^e\}} &= \int_{V^e} [B]^T [D] \cdot [B] \cdot dV \{\delta^e\} - \int_{V^e} [B]^T \{\sigma^0\} dV \\ &- \int_{V^e} [N]^T \{p\} \cdot dV - \int_{S^e} \{N'\}^T \{q\} \cdot dS - \{F^*\} = 0 \end{aligned} \tag{C.4}$$